Deciphering the relevance of background changes to extreme rainfall events in southern India

A thesis submitted to the University of Hyderabad

For the degree of

Doctor of Philosophy

In

Earth and Space Sciences

By

Alugula Boyaj

Reg. No: 15ESPE07

Under the supervision of

Prof. Karumuri Ashok

Centre for Earth, Ocean and Atmospheric Sciences
School of Physics
University of Hyderabad
Hyderabad - 500046
Telangana, India

2021

Declaration

I hereby declare that this PhD thesis entitled **"Deciphering the relevance of background changes to extreme rainfall events in southern India"** is the result of an investigation carried out by me in the Centre for Earth, Ocean and Atmospheric Sciences, School of Physics, University of Hyderabad, Hyderabad under the guidance/supervision of Prof. Karumuri Ashok. This work is a bonafide research work and free from plagiarism. I also declare that the thesis has not been submitted previously in part or in full to this or any other University or Institution for the award of any degree or diploma.

A report on the plagiarism statistics from the University of Hyderabad librarian is enclosed.

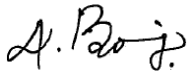

Place: Hyderabad

Date:

Alugula Boyaj
Reg.No. 15ESPE07
Scholl of Physics
University of Hyderabad
Hyderabad, Gachibowli-500046.

Certificate

This is to certify that the PhD thesis entitled **"Deciphering the relevance of background changes to extreme rainfall events in southern India"** by Mr. Alugula Boyaj bearing the Reg. No. 15ESPE07 in partial fulfillment of the requirements for the award of Doctor of Philosophy in the Centre for Earth, Ocean and Atmospheric Sciences (CEOAS), School of Physics, University of Hyderabad is a bonafide work carried out by him under my supervision/guidance. This thesis has not been submitted previously in part or in full to this or any other University or Institution for the award of any degree or diploma. Any text, illustration, tables, figures, etc., used in the thesis from other sources have been duly cited.

He has completed the following requirements as per PhD regulations of the University:

(a) Completion of the course work as per the University rules.

(b) Regular submission of six months progress report.

(c) Presentation of his work to the PhD doctoral committee members.

(d) Publication of at least one research paper in a refereed research journal.

Prof. Karumuri Ashok
(Supervisor)

(Head, CEOAS)

(Dean, School of Physics)

Exams/1301
31/5/17

UNIVERSITY OF HYDERABAD
NOTIFICATION OF RESULTS

Course Work: Ph.D., Centre for Earth and Space Sciences,

Month & Year: April'2017
Semester -II

Sl. No	Regn.No.	Name of the Student	CORE/COMPULSORY COURSES & NO OF CREDITS AND GRADES				
			ES 801 Credits 4	ES 805 Credits 3	ES 806 Credits 4	ES 807 Credits 3	ES 811-830 Credits 2
1	13ESPE01	KONETI SUNITHA	Pass	Pass	Pass	Pass	Pass
2	13ESPE03	DEBASHRI GARAI	Pass	Pass	Pass	Exempted	Pass
3	15ESPE01	FABA FRANCIS	Pass	Pass	Pass	Pass	Pass
4	15ESPE02	HEMADRI BHUSHAN AMAT	Pass	Pass	Pass	Fail	Pass
5	15ESPE03	K. MALLESH	Pass	Pass	Pass	Exempted	Pass
6	15ESPE04	CHENNU RAMU	Pass	Pass	Pass	Pass	Pass
7	15ESPE05	GOVARDHAN DANDU	Pass	Pass	Pass	Pass	Pass
8	15ESPE07	BOYAJ ALUGULA	Pass	Pass	Pass	Pass	Pass
9	15ESPE09	TEJAVATH CHARAN TEJA	Pass	Pass	Pass	Pass	Pass
10	15ESPE10	BILLINGI TARUN KUMAR	Pass	NA	Pass	NA	Pass
11	16ESPE01	RESHMA M.R.	Pass	NA	Pass	Exempted	Pass
12	16ESPE02	SEEDABATTULA V BALAJI MANASA RAO	Pass	NA	Pass	NA	Pass
13	16ESPE04	SUNIT MOHANTY	Pass	NA	Pass	NA	Pass
14	16ESPE05	TARUN THOMAS T.	Pass	NA	Pass	NA	Pass

Course No.	Title of the Course
ES 801	Earth system sciences -4
ES 805	Research Mehtodology -3
ES 806	Mathematics for Earth Sciences -4
ES 807	Interdisciplinary course -3
ES 811-830	Special Paper on Specified Research Topic -2

NA - NOT APPEARED

Dated: 29.05.2017

Controller of Examination 30-5-17

To

Head, Centre for Earth and Space Sciences
Dean School of Physics

31/05/2017

Dedicated to my family

Contents

Acknowledgements

During my thesis work, I have been supported, encouraged, and motivated by many people. It is my pleasure to convey wholehearted gratitude to all of them.

First and foremost, I am sincerely grateful to my supervisor ***Prof. Karumuri Ashok****. I consider myself blessed for getting his guidance. His immense knowledge, motivation as a teacher, and his integral view on high-quality research have made a deep impression on me. He has always motivated and taught me to work hard, think, critically evaluate my work, develop a scientific temperament, and importance of using every opportunity. I am indebted to him for his patient guidance and support, which helped me to overcome difficulties throughout my PhD work.*

I would like to thank my PhD doctoral committee members, ***Dr. S. Maqbool Ahmed,*** *Principal Scientific Officer and Head of Central Instruments Laboratory, UoH,* ***Dr. S. Sri Lakshmi,*** *and* ***Dr. Vijay P. Kanawade,*** *CEOAS, UoH, for their valuable suggestions/comments, encouragement, and thought-provoking questions.*

I wish to thank ***Prof. K. S. Krishna,*** *the current Head, CEOAS, UoH, and former Head* ***Prof. M. Jayananda,*** *for the facilities made available to me for my research work. I also sincerely thank the other faculty of CEOAS****, Prof. V. Chakravarthi, Dr. T. Devleena Mani, Dr. M. Ismaiel****, Dr. Aliba Ao****, and visiting faculty* ***Dr. Y. V. Rama Rao,*** *TSPDS, for their encouragement. Special thanks to* ***Prof. A. C. Narayana*** *for his constant encouragement since I joined the university as a masters student.*

I want to express my immense gratitude to ***Prof. Ibrahim Hoteit,*** *KAUST, for giving me an opportunity to visit KAUST, Saudi Arabia, for six months. My sincere thanks are also to* ***Dr. Hari Prasad Dasari****, KAUST, to mentor me during the stay at KAUST and set up the model experiments.*

I gratefully acknowledge the Council of Scientific and Industrial Research for the Senior Research Fellowship (CSIR-SRF).

I would like to express my heartfelt thanks to ***Dr. Nagaraju Chilukoti,*** *Assistant Professor****,*** *NIT, Rourkela, for his help in model installation and technical support. I am also happy to acknowledge* ***Dr. Krishna Kishore Osuri,*** *NIT, Rourkela,* ***Dr. V. S. Prasad****, NCMRWF, for their discussions and advice during my visits to the respective laboratories. I thank Dr.* ***Srinivas Rao Karri,*** *NRSC, for his guidance and technical support.*

I gratefully acknowledge the help and encouragement received from ***Dr. N. Sravanthi, Dr. Rama Krishna Karumuri, Mr. G. Naga Raju, Dr. Yagnesh****, and* ***Mr. Anjaih.***

*I thank my lab-mates****, H. B. Amat, D. Govardhan, T. Charan Teja, Feba Francis, S. Bidyabati,*** *and* ***Vikas Kumar Kushwaha,*** *for all the happy and constructive times we had at the CEOAS. I particularly acknowledge Govardhan for his discussions and collaboration on a different research problem. I would like to extend my warm thanks to all my other research scholars of the CEOAS****.*** *I also place on record my heartfelt thanks to the non-teaching staff of the CEOAS.*

I am also thankful to my friends ***Dr. P. Kiran Kumar, K. Anand Rao, Srikanth Dora, Adharsh Dube, Stella, Ch. Ramu,*** *and* ***P. Praveen Kumar.***

I am also grateful to ***Pastor. Ch. Israel anna, Pastor. B. Raju anna*** *and church co-believers for their prayers and encouragements.*

Last but not least, I would like to express my deep sense of gratitude to my loving family, my parents ***Mr. Jemesh and Smt. Rosemary****, sister* ***Leya,*** *brothers* ***Paul*** *and* ***Joseph,*** *their unconditional love and encouragement throughout my thesis work. I am grateful to my brother* ***Joseph*** *for his encouragement to pursue the PhD and have financially supported through a major portion of my post-graduate education. I also special thanks to* ***Roseleen****. Finally, I bow my head humbly before the almighty God for making me capable of completing my PhD.*

Thank you all…

Alugula Boyaj

List of Publications:

Research papers published in peer-reviewed journals

1. **Boyaj, A.**, Ashok, K., Ghosh, S., Devanand, A., and Dandu, G. (2018). The Chennai extreme rainfall event in 2015: the Bay of Bengal connection. Climate Dynamics. 50, 2867–2879, doi:10.1007/s00382-017-3778-7. *(Impact factor=4.08)*

2. **Boyaj, A.,** Dasari, H. P., Hoteit, I., Ashok, K. (2020). Increasing heavy rainfall events in south India due to changing land use and land cover. Q. J. R. Meteorol. Soc., 146, 1–22, doi.org/10.1002/qj.3826. *(Impact factor=3.47)*

3. **Boyaj, A.,** Dasari, H. P., Rama Rao, Y. V., Hoteit, I., Ashok, K. (2020). Assimilation of Global Positioning System Radio Occultation refractivity for enhanced prediction of extreme rainfall events over southern India . ***(Under Review in Weather and Forecasting)***

Papers presented in the International/National conference/seminars:

- **Boyaj, A.,** Ashok, K: Fidelity of regional models in deciphering the relevance of Indo-Pacific SST for extreme events: a case study. International Tropical Meteorology-2017 (INTROMET-2017) during 7-10 November 2017 organized at SAC, Ahmedabad, India.

- **Boyaj, A.,** Ashok, K: Fidelity of regional models in deciphering the relevance of boundary signatures for extreme events: Tale of two. National workshop on "Ocean-Atmosphere Processes and Applications" organized by the CEOAS-INCOIS at the UoH on 18th February 2019.

- **Boyaj, A.,** Dasari, H. P., Hoteit, I., and Ashok, K: Increasing heavy rainfall events in South India due to changing land use land cover. National Symposium on "Land, Ocean and Atmosphere Interactive Processes in the Context of Weather and Climate" during 11 to 14 December, 2019 at Andhra University, Visakhapatnam, Andhra Prades.

List of Abbreviations

ARW : Advanced Research WRF

AVHRR : Advanced Very High-Resolution Radiometer

AWiFS : Advanced Wide Field Sensor

AZM : Atlantic Zonal Mode

AZMI : Atlantic Zonal Mode Indiex

BoB : Bay of Bengal

BSS : Brier Skill Score

CAPE : Convective available Potential Energy

CCL : Convective Condensation Level

CMIP5 : Coupled model Intercomparison Project phase 5

EMI : El Niño Modoki Index

ENSO : El Niño Southern Oscillation

ERA : European Centre for Medium-Range Weather Forecasts Reanalysis

GFS : Global Forecasting System

GISST : Global Sea Ice and Sea Surface Temperature

GTS : Global Telecommunications System

HadISST : Hadley Centre's Monthly Sea Ice and Sea Surface Temperature

IAV : Interannual Variability

IITM : Indian Institute of Tropical Meteorology

IMD : India Meteorological Department

IOD : Indian Ocean Dipole

IODMI : Indian Ocean Dipole Mode Index

IPCC : Intergovernmental Panel on Climate Change

ISM : Indian Summer Monsoon

ISMR : Indian Summer Monsoon Rainfall

ISRO : Indian Space Research Organization

JJAS : June, July, August and September

LBC : Lower Boundary Conditions

LCL : Lifting Condensation Level

LLJ : Low Level Jet Stream

LULC : Land-Use Land-Cover

MDB : Marine Data Bank

MM5 : Fifth generation Mesoscale Model

MODIS : Moderate Resolution Imaging Spectroradiometer

NASA : National Aeronautics and Space Administration

NCAR : National Center for Atmospheric Research

NCEP : National Centre for Environmental Prediction

NIO : North Indian Ocean

NOAA : National Oceanic & Atmospheric Administration

OISST : Optimum Interpolation Sea Surface Temperature

RCM : Regional Climate Model

RCP8.5 : Representative Concentration Pathway 8.5

SST : Sea Surface Temperature

SSTA : Sea Surface Temperature Anomalies

TRMM : Tropical Rainfall Measuring Mission

USGS : United States of Geological Survey

VIM : Vertical Integrated Moisture

WRF : Weather Research and Forecasting

List of Figures

List of Tables

Abstract

In this thesis, I investigated the potential roles of background changes in the tropical Indo-Pacific SSTs and land-use land-cover (LULC) on the intensity and frequency of extreme rainfall events (EREs) in southern India. Toward this end, I conducted several sensitivity experiments using the Weather Research and Forecasting (WRF) regional climate model with various combinations of observed and climatological SST, and those to evaluate the importance of lower boundary LULC conditions. I also explore the importance of assimilating the satellite-based product of Global Positioning System (GPS) Radio Occultation (RO) dataset in improving the prediction skills of the EREs.

At the outset, I investigated the influence of the important individual tropical ocean climate drivers, specifically, the El Niño Southern Oscillation (ENSO), ENSO Modoki, Indian Ocean Dipole (IOD) and the Atlantic Zonal Mode (AZM), on the EREs over India during the ISM from 1980 to 2019. My results suggest that the statistics related to summer monsoon, such as, the mean rainfall, rainy days, normal, moderate, and heavy rainfall events, and 75, 99, and 95 percentile of rainfall magnitudes increased by 10%-30% mainly over northwestern regions of India. Interestingly, the EREs increased about 40% over Gujarat, some places in central India, and Odisha during the 2000-2019 period compared to 1980-1999 period. In addition, the IOD and AZM indices also show significantly increasing trends since the year 2000. My composite and partial correlation analyses show that, since then, the strengthening of positive IODs is significantly increasing the seasonal mean rainfall, heavy rainfall events, 95 and 99 percentile rainfall magnitudes over northwestern, and the ERE frequency over Gujarat, central India, and Odisha regions of India. The El Niño, El Niño Modoki, and positive AZM events do not show any significant association of these changing characteristics in these regions. An increasing SST in the equatorial Indian Ocean maximized in its west, and consequent strengthening of

low-level monsoonal westerlies over the Arabian Sea during the positive IOD events may be the possible reason for increasing EREs and magnitudes over aforementioned regions of India.

The eastern Bay of Bengal (BoB) SST shows an increasing trend since 1980s, and said to be causing the intensification of the tropical cyclones in the NEM. In addition, the concurrent El Niños have a positive association with the northeast monsoon rainfall (NEMR). Importantly, the Tamil Nadu region was buttressed with a heavy rainfall event in December 2015, leading to huge above 350 deaths and economic loss. This event co-occurred with the peak period of extreme El Niño of 2015, which was as strong as that in 1997. In addition, the eastern BoB experienced above normal SSTs. Given such a combination, and the possibility that both the co-occurring El Niño and a warm BoB contributed to the extremity of the event. I have explored the relative contributions of a strong El Niño and the increasing BoB SSTs to the intensity of ERE that occurred over Chennai on 01 December 2015. My results show that the eastern BoB SST anomalies and El Niño SST anomalies are positively and significantly correlated with the NEMR, especially over Chennai region. My results from various sensitivity experiments I have carried out with the WRF model at 25 km resolution suggest that, the strong concurrent El Niño conditions contributed to about 21.5% of the intensity of the extreme Chennai rainfall through its signals in the local SST as well as its signature in the local atmospheric circulation over the NIO. The increased SST in BoB associated with background warming also contributed almost equally to the extremity of the Chennai event.

In addition, I have explored the potential role of LULC changes on the EREs. I noticed increasing in heavy rainfall events and 99 percentile rainfall magnitudes that are coincident with and considerable changes in the LULC/urbanization over three major states of southern India, namely, Tamil Nadu, Telangana, and Kerala in the recent decades. Unlike the SST which is a large-scale field, the LULC has a very high spatial variation. Therefore, using the WRF

model at 2 km horizontal resolution, I investigated the potential roles of these local LULC changes on EREs over the three southern Indian states. For a detailed spatial validation, I focused on the peak days of one major ERE each from each of these states. These representative events are, (i) the ERE over Chennai on 01 December 2015, (ii) over Telangana on 26 September 2016, and (iii) over Kerala on 15 August 2018. The results show the simulated rainfall is more realistic with the use of the most recent (2017) LULC boundary conditions from the ISRO, as compared to their older (2005) LULC boundary conditions, and the default MODIS LULC conditions 2002. Based on the analysis of these simulations, and outputs from additional nine extreme rainfall simulations, I suggest that the recent LULC changes result in higher surface temperatures, sensible heat fluxes, and a deeper and moist boundary layer. These causes a relatively higher convective available potential energy and, consequently, heavier rainfall. The LULC changes in the three regions, dominated by the increasing urbanization in Telangana and Tamil Nadu, may be conjectured to have enhances the rainfall during the EREs by 20% - 25%.

Prediction of the EREs in southern India is an outstanding issue. Therefore, towards eventually improving the prediction skills of EREs, I explored importance of assimilating the observed GPS RO refractivity data using the WRF model and its three-dimensional variational (WRF-3DVar) techniques. For this exercise, I choose the three EREs which I aforementioned, and used the 2017 LULC conditions. My results, based on the three prediction experiments, demonstrate that assimilation of GPS RO refractivity profiles into the model improves the predictability of all three EREs in terms of location, areal extensions, and associated extreme conditions.

Chapter – 1

Introduction

In this chapter, I have presented the brief introduction of the variability, trends, and mechanisms of the extreme rainfall events (EREs) in the Indian southwest and northeast monsoon seasons, based on the literature survey of relevant previous studies. This chapter also briefly describes the impact of tropical ocean climate drivers and land-use land-cover changes on the frequency and intensity of EREs over India. Besides, I have briefly reviewed available literature on the prediction of EREs through the use of dynamical regional climate models. The objectives of the thesis introduced in this chapter.

1.1 Monsoons over India

The word "monsoon" comes from the Arabic term "Mausam," which means season. The term monsoon is commonly used in meteorology to define the seasonal reversal of annual mean wind patterns associated with precipitation over tropical and subtropical regions. The world monsoon regions lie between 25°S-35°N, and 30°W-170°E (Ramage, 1971). However, as far as the Indian sub-continent is concerned, along with the circulation, the rainfall and its variability are important (e.g., Rao, 1976).

The Indian subcontinent is one of the most monsoon dominates countries. It faces primarily two monsoon seasons, one is summer/southwest monsoon, and another one is winter/northeast monsoon. The Indian monsoonal rainfall plays a crucial role in the economy of the country, as the majority of the Indian population depends on the rain-related agricultural activities for their daily lives. The Indian summer monsoon (ISM), which is the chief rainy season for India, accounts for 70% - 80% of annual rainfall between June and September (JJAS; Rao, 1976; Parthasarathy et al., 1994). Figure 1.1a shows the spatial distribution of climatology of ISM rainfall (ISMR) from 1980- 2019. High amount of seasonal mean rainfall occurs over the Western Ghats, north-eastern, and central parts of India (Rao, 1976; Parthasarathy et al., 1994).

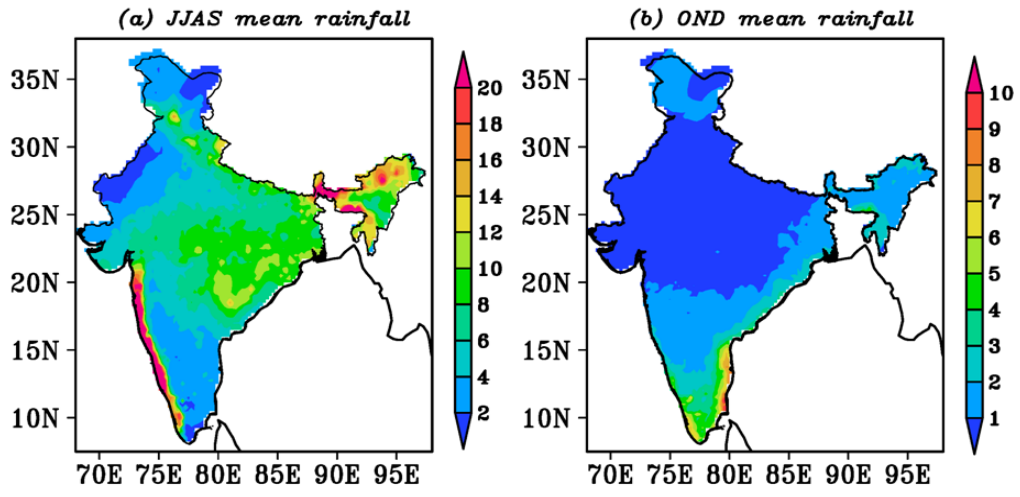

Figure 1.1: Spatial distributions of observed seasonal mean rainfall (mm/day) during the (a) southwest (JJAS), and (b) northeast (OND) monsoon seasons across India. The figures have been generated using 0.25°×0.25° resolution of IMD gridded daily rainfall dataset from 1980-2019.

Figure 1.2a indicates the spatial distribution of the climatological of wind vectors and magnitude (shaded) at 850 hPa during the ISM from 1980 to 2019. The seasonal mean winds blow from southwest direction (Figure 1.2a); thus, it is known as the southwest monsoon. Several physical processes facilitate the ISM. For example, during the northern hemisphere summer (March-May), the incoming solar radiation heats up the central Asian landmass, mainly over Iran, northern India, and Tibetan plateau. As a result of this, a low-pressure associated with vertical ascending airflow arises over the Tibetan plateau. At the same time, we have the seasonal high-pressure area over southern Indian Ocean, known as Mascarene High (~30°S, 50°E). Thus, the land-sea temperature gradient manifests as a pressure gradient as well. The atmospheric pressure gradient between the Asian landmass and southern Indian Ocean causes a large-scale meridional circulation, mainly during the onset phase. As these winds enter the western part of the Indian Ocean, they rotate into south-westerly winds (Figure 1.2a) due to the Coriolis Effect. These winds are located near 1.5 km height in the lower-troposphere and often reach a maximum speed of ~50 m/s at the Somali and Madagascar coasts (Hastenrath, 1985; Webster, 1987). These strong low-level winds are also known as the Low-Level Jet stream (LLJ) or Findlater Jet (Joseph and Raman, 1966; Findlater, 1969), and play a crucial role for the ISM rainfall (ISMR). Recent literature suggests that while the land-sea gradient is important for the onset, the maintenance of the seasonal monsoon through June-September months may be attributed to tropospheric temperature gradient (e.g., Goswami and Chakravorty, 2017), mainly due to the diabatic heating associated with convection. At 100 hPa level, the strong meridional temperature gradients between the Asian landmass, mainly the elevated Tibetan Plateau, and the Indian Ocean, results in the strong Tropical Easterly Jet (TEJ) in the upper-troposphere (Koteswaram, 1958). The TEJ is an essential feature of the upper-level monsoon circulation, and is opposite in direction from the surface meridional winds into the Indian region (Rao, 1976; Krishnamurti and Bhalme, 1976). The subtropical westerly jet moves further north (Pant and Rupa Kumar, 1998).

The monsoon trough is a low-pressure system that spreads from the west Africa through southern Bay of Bengal (BoB). It is a semi-permanent synoptic scale system that contributes to the higher precipitation during the ISM (Mooley and Shukla, 1989). The mean position of the monsoon trough over India spreads from the northwest-ward of Rajasthan to the north BoB and extends vertically from the sea level to 500 hPa (Keshavamurty and Awade, 1970). In addition, the active and break monsoon phases are depending on the position of the monsoon trough. Hence, the semi-permanent systems of ISM, such as monsoon trough, LLJ, Tibetan High and associated TEJ have significantly influenced the strength of the ISMR.

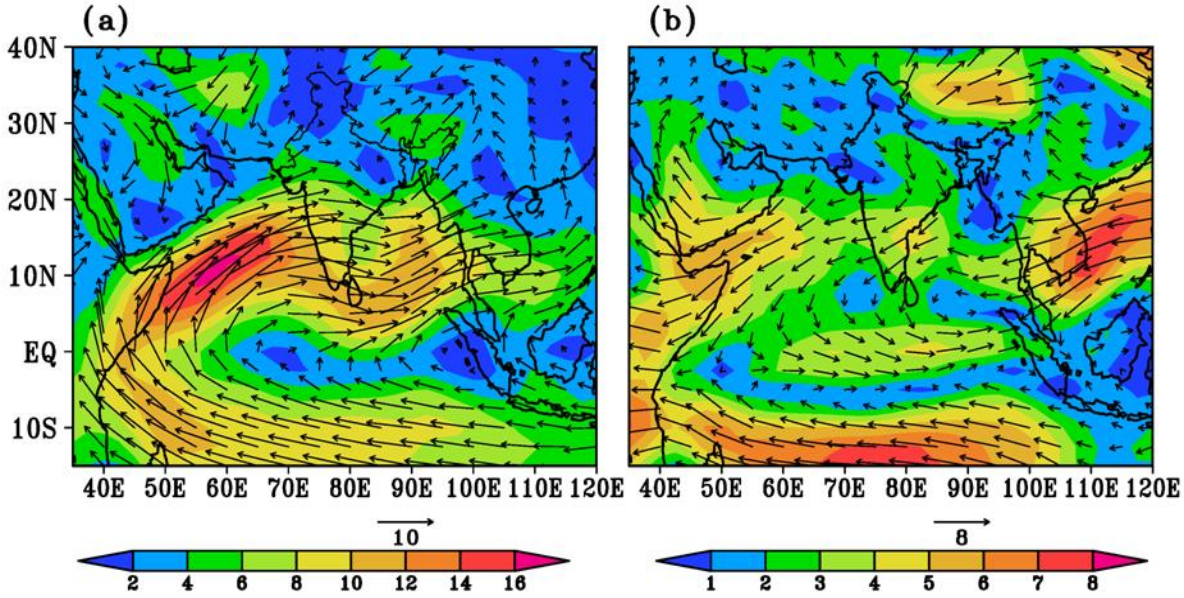

Figure 1.2: Spatial distribution of climatological wind vectors (m/s) and magnitude (shaded) at 850 hPa in the (a) southwest (JJAS) and (b) northeast (OND) monsoon season for the period of 1980-2019. The figures have been generated using the NCEP Reanalysis-2 at 2.5°×2.5° resolution dataset.

In addition to the ISM, the northeast monsoon (NEM) is also a crucial rainy season, but limited to southern peninsular India (IMD, 2010). The NEM season occurs over a span of three months, between October and December (OND); it is limited in extent only to the coastal Andhra Pradesh, Rayalaseema, Tami Nadu, southern-interior of Karnataka, and Kerala states (Rao and Raghavendra, 1971; Srinivasan and Ramamurthy, 1973; De and Mukhopadhyay, 1999). Figure 1.2b shows the climatology of wind vectors and magnitude (shaded) at 850 hPa over India during the NEM season. The seasonal mean winds blow from the northeast direction

(Figure 1.2b); thus, it is known as northeast monsoon. The contribution of the NEM rainfall (NEMR) to the annual rainfall of India is about 10%, while to that, over southeast peninsular India is 30% - 60% of rainfall (Rao Krishna and Jagannathan, 1953; George et al., 2011). Figure 1.1b shows the climatology of NEMR (mm/day) from 1980 - 2019 over India. The coastal Tamil Nadu, Rayalaseema, and southern part of Kerala receive almost all of their annual rainfall (~5 - 8 mm/day) in the NEM season.

1.2 Interannual variability of Indian southwest and northeast monsoon rainfall

The ISMR and NEMR undergo significant interannual variability (IAV). The IAV in the monsoon rainfall significantly influences the agricultural activity, drinking water, droughts, and floods conditions over some regions in India. Several studies have explored the IAV of ISMR (Pramanik and Jagannathan, 1954; Mooley and Parthasarathy, 1984; Rupa Kumar et al., 1992; Webster, 1998; Kripalani and Kulkarni, 2001; Gadgil, 2003, etc.) as well as NEMR (Dhar and Rakhecha, 1983; De and Mukhopadhyay, 1999; Khole and De, 2003; Kripalani and Kumar, 2004). Figures 1.3a and 1.3b show the IAV of ISM and NEM rainfall anomalies for total India from 1980 - 2016. There are some major external tropical ocean drivers such as El Niño Southern Oscillation (ENSO), ENSO Modoki, Indian Ocean dipole (IOD), and Atlantic Zonal Mode (AZM), which are known to influence the IAV of the monsoonal rainfall over India (Sikka, 1980, 1977; Pant and Parthasarathy, 1981; Saji et al., 1999; Saji and Yamagata, 2003; Ashok et al., 2004; Kucharski et al., 2007; Yadav et al., 2016). In addition, the Himalayan and Eurasian snow cover variations are also known to influence the monsoonal interannual variability (Blanford, 1884; Bhanu Kumar, 1987; Bamzai and Kinter, 1997).

The ENSO is an Ocean and atmospheric coupled interannual phenomenon. Its signatures can be prominently seen in the anomalies of sea surface temperature (SST), surface level pressure, sea surface height, and oceanic sub-surface temperatures across the equatorial Pacific Ocean (Figures not shown). As a coupled phenomenon between ocean and atmosphere, it was first documented by Bjerknes (1969).

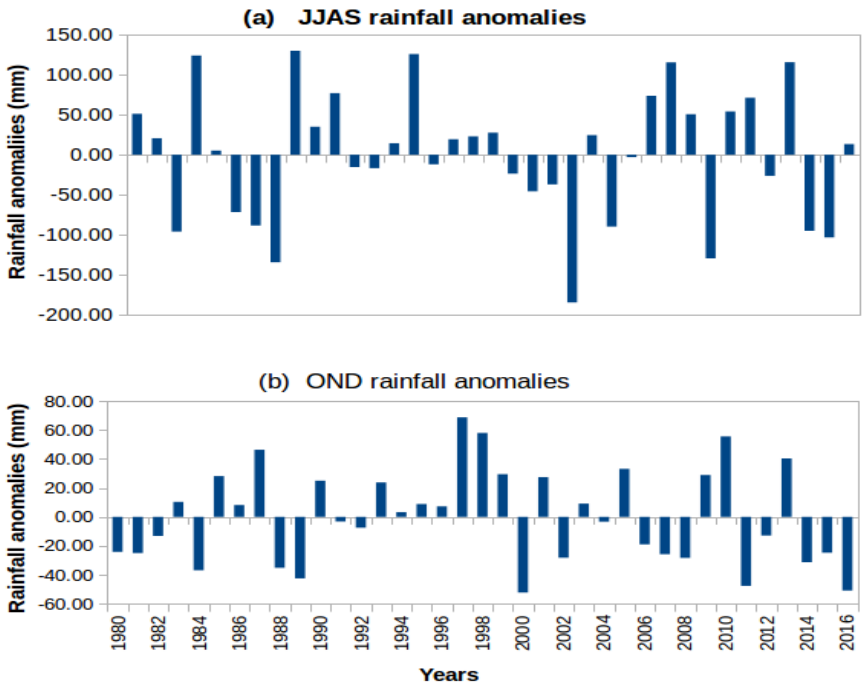

Figure 1.3: Interannual variability of (a) ISMR and (b) NEMR anomalies (mm/year) over a period of 1980 to 2016. Figures have been generated using the IITM sub-divisional dataset.

The El Niño (La Niña) is associated with anomalous warming (cooling) of SST in the tropical eastern-central Pacific Ocean (Box-6 in the Figure 2.1), mainly seen from the April/May months, sustaining through the boreal summer and fall, and peaking around the ensuing the December through February. Due to these periodic changes over the tropical Pacific Ocean, the atmospheric overturning circulation, known as the Southern Oscillation, circulation also changes. Though the ENSO happens in the tropical Pacific Ocean, it impacts the global climate system (Shukla and Paolina, 1983; Keshavamurty, 1982; Wang et al., 2000; Ashok et al., 2007, Weng et al., 2007, etc.). Two types of El Niños have been identified over tropical Pacific Ocean, and are referred to as El Niño and El Niño Modoki (Ashok et al., 2007; Marathe et al., 2015). The El Niño Modoki (La Niña Modoki) is associated with a significantly warmer (colder) SST anomalies over the central equatorial Pacific Ocean through 3 - 4 contiguous seasons, flanked by significantly colder than normal SST anomalies over the western and eastern tropical Pacific Ocean (Ashok et al., 2007). This is different from the canonical El Niños where the eastern tropical pacific is anomalously warm and the western tropical Pacific is anomalously warm. The atmospheric signatures are also consequently different in phase

and/or magnitude. It is also an Ocean-atmosphere coupled phenomenon, quite different from the canonical El Niños with reference to spatial, temporal characteristics, and teleconnection patterns. The El Niño is significantly anti-correlated with ISMR (e.g., Sikka, 1980, Pant and Parthasarathy, 1981, Keshavamurty 1982; Slingo and Annamalai, 2000; Ashok et al., 2019 and references therein), and positively correlated with the NEMR (De and Mukhopadhyay, 1999; Kumar et al., 2007; Yadav et al., 2010; Sreekala et al., 2012, etc.). Interestingly, the relationship between ISMR and ENSO has apparently weakened (Krishna Kumar et al., 1999; Ashok et al., 2001; Kumar et al., 2006; Feba et al., 2017; Ashok et al., 2019), while the NEMR relationship is increasing in the recent decades (Zubair and Ropelewski, 2006; Pankaj Kumar et al., 2007; Yadav, 2012). While the impact of canonical ENSOs is seen more through the monsoon trough, the El Niño Modoki is significantly weakening the ISMR mainly over southern peninsular India (Kumar et al., 2006; Ashok et al., 2019). In addition, strong IOD (Saji et al., 1999; Webster et al., 1999; Murtugudde et al., 2000), which is an Ocean and atmosphere coupled phenomenon in the tropical Indian Ocean (TIO), also affect the monsoons. The positive IOD events have occurred independently in many years such as 1961, 1963, 1994, 2006, 2012, 2017, 2019, etc., as well as co-occurred with ENSOs in some years such as 1972, 1977, 1982, 1983, 1997, etc. The strong positive IOD events influence the IAV of ISMR as well as the NEMR. The strong positive phase of IOD events anomalously enhance the ISMR (Ashok et al., 2001, 2004, Ashok and Saji, 2007; Yamagata et al., 2003; Krishnaswamy et al., 2014), as well as NEMR (Kripalani and Kumar, 2004; Gadgil et al., 2004; Sreekala et al., 2012). The moisture transport from the south-eastern BoB is favourable and intensifies the rainfall activity over the Indo-Gangetic plains in positive phase of IOD events (Behera et al., 1999). Ashok et al. (2001, 2004) show that during the El Niño events, an anomalous divergence over the Indian region, induced by an anomalous convergence over the central equatorial Indian ocean, causes anomalous subsidence over India, leading to the reduced rainfall over India. During the positive IOD events, the anomalous divergence in the eastern equatorial Indian ocean cases an

anomalous convergence over the head BoB and neighbouring region. The associated ascending motion moves causes surplus rainfall over India during ISM (Ashok et al., 2007), as seen in years such as 1997 when the co-occurring El Niño impacts have apparently been reduced. The western pole of positive IOD also facilitates anomalously surplus rainfall over Gujarat, Rajasthan and neighbouring Pakistan. Geethalakshmi et al. (2009) stated that in the extreme El Niño years, the BoB and the Arabian Sea show significantly positive and negative sea level pressure anomalies, respectively. This pressure gradient led to strengthening the north-easterly winds in the southern part of India, resulted in more rain in the NEM.

Several recent studies suggest that the AZM is a potential factor that affects the IAV of ISMR. The AZM is phase-locked to the seasonal cycle and commonly high in the boreal summer from June to August (JJA; Lübbecke et al., 2010). The negative (positive) phase of AZM contributes to enhancement (reduction) of rainfall over the Indian subcontinent. Several studies have well investigated the relationship between the AZM and ISMR variability (Kucharski et al., 2007; Wang et al., 2009; Yadav et al., 2017; Pottapinjara et al., 2016, etc.).

In addition to the interannual variability, the ISMR exhibits a wide spectrum of temporal variability such as the decadal, intraseasonal, and transient scales (Kriplani and Kulkarni, 1997; Chatterjee and Goswami, 2004). Importantly, the monsoons are characterized by a short duration of heavy/extreme rainfall events in various regions of India. These heavy/extreme rainfall events over various parts in India occur during the ISM as well as the NEM seasons and exhibit year-to-year variability (Francis and Gadgil, 2006; Goswami et al., 2006; Revadekar and Kulkarni, 2008; Dash et al., 2009; Pattanaik and Rajeevan, 2010; Krishnan et al., 2016; Kulkarni et al., 2017; Roxy et al., 2017; Sanap et al., 2018, etc.). The following section will explain some of the significant aspects of the spatio-temporal variability of extreme rainfall events and potential background mechanisms.

1.3 Extreme rainfall events during southwest and northeast monsoon seasons

The Indian subcontinent is often affected by weather extremes such as floods, tropical cyclones,

heat and cold waves, lightning, hailstorms, and thunderstorms, etc. Among these, the extreme rains and the ensuing floods are a severe threat to the environment, agriculture, urban transportation, infrastructure, and human life (Mohapatra and Singh, 2003). India is one of the worst-affected countries due to weather extremes, resulting in calamities and casualties. The high number of heavy rainfall events (HREs; ≥ 35.6 to ≤ 124.4 mm/day) occur in the ISM over Western Ghats, central and north-eastern regions of India (Figure 1.4a), in the NEM over south-eastern coastal regions of India (Figure 1.4b). Usually, the heavy/extreme rainfall events (EREs) occur primarily due to the severe synoptic weather systems, etc. over India (Saha, 1974; Rao and Ratna, 2010). Those over the south-eastern part of India (Figure 1.4a) occur mainly due to synoptic-scale disturbances of low-pressure systems, which form over the BoB (Rao, 1976). Recently, India has experienced several severe floods due to EREs. For example, the Uttarakhand state received more than 340 mm/day of rainfall from an extreme rainfall event (ERE) in June 2013, resulting in flood and landslides that led to a loss of ~6000 human lives and ~$3.8 billion economic losses (Mukherjee et al., 2018). A recent ERE which is occurred over Kerala in August 2018, caused inundation of many parts in Kerala due to severe floods; more than 440 people lost their lives (Duncombe, 2018; Vishnu et al., 2019; Viswanadhapalli et al., 2019). Similarly, several severe floods associated with EREs have occurred in the other parts of India in the recent last few decades.

So far, there is no established standard definition for the ERE. According to meteorological point of view, if the rainfall for a particular period exceeds the long-term mean rainfall over that area by one standard deviation, it is considered as an ERE (Sikka, 2000; WMO, 1994).

The IMD has classified various rainfall into categories from light to extreme heavy rainfall events (Table 2.1). Besides, some previous studies have also proposed different thresholds to identify the EREs over different regions in India. For example, using the gridded daily rainfall dataset, Goswami et al. (2006) defined events with rainfall > 100 mm/day, as heavy, and those

with > 150 mm/day as very heavy rainfall events, Roxy et al., (2017) used the threshold of ≥ 150 mm/day to identify the ERE over central India (CI). Pattanaik and Rajeevan et al. (2010), on the other hand, used ≤ 64.4 mm/day and ≥ 124.4 mm/day to distinguish the low and ERE over India. Using station data, Francis and Gadgil (2006) defined 150 - 200 mm/day as a very heavy rainfall event over the Western Ghats.

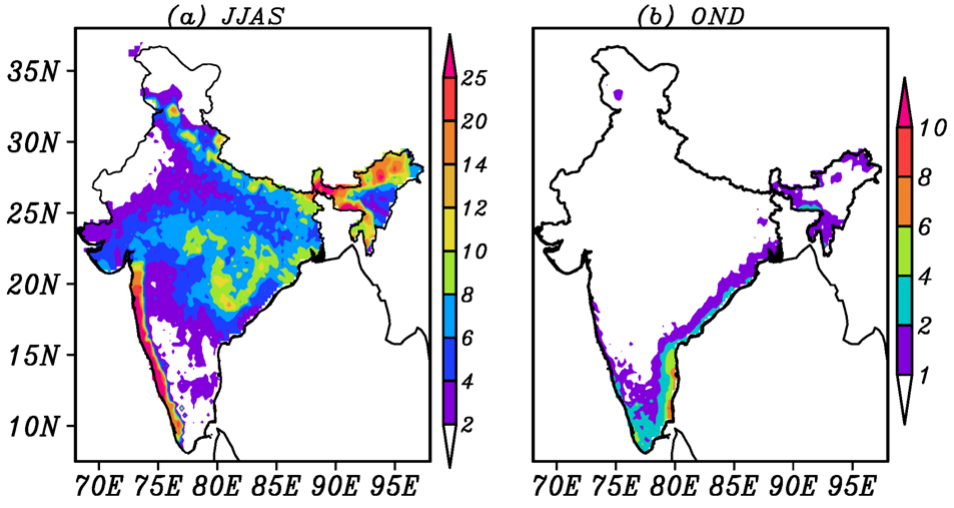

Figure 1.4: Spatial distribution of climatology of heavy rainfall events per year from1980 to 2019 during the (a) southwest (JJAS), and (b) northeast (OND) monsoon seasons across India. As per IMD rainfall calcifications, the rainfall ≥ 35.6 to ≤ 124.4 mm/day is considered as a heavy rainfall event. The figures have been generated using 0.25°×0.25° resolution of IMD gridded daily rainfall dataset.

Several earlier studies have reported that the frequency and magnitude of EREs have significantly increased during ISM over different parts in India, mainly over CI since the 1950s (Goswami et al., 2006; Rajeevan et al., 2008; Pattanaik and Rajeevan, 2010; Guhathakurta et al., 2011; Singh et al. 2014; Malik et al., 2016; Singh et al., 2019; Nikumbh et al., 2019). Increasing frequency of EREs said to be coincident with the decrease of low-intensity rainfall events over CI (Goswami et al., 2006; Dash et al., 2009; Pattanaik and Rajeevan, 2010). Dash et al. (2011) shows that the contribution from HREs to the seasonal rainfall is significantly increasing over the northwest, northeast, central northeast, Uttarakhand, and Telangana, states of India. In contrast, a study by Ghosh et al. (2009) reported that there is no statistically significant spatial trend in the frequency and magnitude of EREs over CI. Studies by Pattanaik and Rajeevan (2010); Singh et al. (2014), through an analysis of the IMD daily gridded rainfall

dataset at 1°×1° resolution for the period of 1951 - 2005, show that an increasing trend in the seasonal mean moisture convective instability may be causing an increase in the frequency of summer monsoon EREs over CI. Roxy et al. (2017) analysed the 0.25°×0.25° IMD's gridded daily rainfall dataset during the period of 1950 – 2015. Their results show a threefold rise in EREs over CI, which the authors claim is due to the strengthening of low-level monsoon westerlies over the Arabian Sea. A study by Rajeevan et al. (2008) reported that the increasing trend of EREs over CI is associated with the increasing trend of sea surface temperatures (SST) and surface latent heat flux in the tropical Indian Ocean in the last few decades. Studies by Varikoden et al. (2013), and Dave and James, (2017) found that due to increasing the cyclonic activity over the Arabian Sea, the frequency of HREs (> 65 mm/day) has increased significantly over the state of Gujarat and north-western part of India in the last decade (2004 - 2013). Analysis of various climate model data outputs, including the historical simulations of the Coupled Model Intercomparison Project 5 (CMIP5), also shows the EREs significantly increased over some parts in India (Rajendran and Kitoh, 2008; Koteswara Rao et al., 2014; Mukherjee et al., 2018). Several observational and model studies suggest that the increased EREs are potentially associated with global warming and anthropogenic activities over some parts in India (Goswami et al., 2006; Rajendran and Kitoh, 2008; Mishra et al., 2012; Malik et al., 2012; Koteswara Rao et al., 2014; Mukherjee et al., 2018). The frequency of EREs is projected to rise significantly over southern and CI under the Representative Concentration Pathway (RCP) 8.5 (Ali and Mishra, 2017; Mukherjee et al., 2018). Interestingly, a study by Ghosh et al. (2009) reported that the spatial variability of regional urbanization associated with industrialization and deforestation might be one of the reasons for increased EREs over some parts in India.

Compared to the ISM, relatively, only a single study has so far explored the spatio-temporal variability in the frequency and intensity of ERE trends during the NEM and potential mechanisms that cause the changes. Revadekar and Kulkarni, (2008) analysed the IMD rain-

gauge station daily rainfall data over southeast peninsular India during NEM from 1901 - 2002. The results show there are no significant trends in the frequency and intensity of EREs.

The following sections will describe the impact of tropical Indo-Pacific Ocean climate drivers and land-use land-cover changes on EREs over India during the ISM and NEM seasons.

1.4 Potential roles of tropical Indo-Pacific Ocean climate drivers on extreme rainfall events

A few studies have examined the potential influences of the ENSO and IOD phenomena won the EREs over India during the ISM. For example, Ajayamohan and Rao, (2007); Krishnaswamy et al. (2015) reported that an increase of EREs (> 100 mm/day) over CI is strongly associated with the co-occurring positive IOD events from 1951 - 2003. Krishnaswamy et al. (2014) analysed the IMD daily gridded rainfall datasets over the 1901 - 2004 period. Their results show that El Niños strongly influences a threshold of < 100 mm/day of rainfall events over India, but the positive IODs seem to. Varikoden and Preethi, (2013) reported that anomalous heavy rainfall was observed over the northern part of the west coast (central India) during the El Niño (La Niña) years.

The occurrence of extreme rainfall activity is also high during the NEM over south-eastern India, mainly over the state of Tamil Nadu. For example, in December 2015, the Chennai capital city of Tamil Nadu and adjoining regions received ~483 mm/day due to an extreme rainfall activity, which is devastating floods, economic loss around $2.2 billion, and above 350 deaths (Chakraborty, 2016, Vishnu and Sridharan, 2016; Srinivas et al., 2018). The frequency of the tropical cyclones (TCs) from the BoB making landfall also peaks in this season over the southeast coast of India (Subbaramayya and Rao, 1981, 1984). A study by Balaguru et al. (2014) analysed the multiple SST datasets from 1981 - 2010, and suggests that SST have significantly increased over 90°E - 95°E, 10°N - 20°N region. Balaguru et al. (2014) claim that an increasing SST in the eastern BoB since the 1980s is causing the intensification of the TCs during the NEM. The IAV of NEM rainfall is also associated with the variability of warm SSTA

over the eastern BoB and cool SSTA over east equatorial Indian Ocean. As per Yadav (2013), the positive SST gradient between these two regions, the tropical depressions and cyclonic storms formed over north Indian Ocean move more zonally and hit the southern peninsular India resulted in surplus NEMR, mainly Tamil Nadu region. Moreover, A study by Yadav (2012) claims that during the El Niño years in the recent decades (1979 - 2008), the SST is warmer as compared to the earlier decades (1949 - 1978) over a warm-pool region of Indonesia; it leads to intensifying the deep convection over the Indian Ocean. The state of Tamil Nadu received extreme rainfall in 1997; the year 1997 was one of the strongest El Niño years (Jayanthi and Govindachari, 1999). Sanap et al. (2018) reported that during the NEM, around 43% of the HREs are occurred in the El Niño, ~31% in the La Niña, and ~26% in the neutral years. During the El Niño years, a strong SST gradient between the BoB and the tropical western Pacific Ocean causes anomalously strong low-level easterly winds, which lead to increases the heavy rainfall events during the NEM (Sanap et al., 2018). The role of enhanced seasonal winds associated with concurrent El Niños has also been pointed during the course of this PhD work (published as Boyaj et al., 2015), and form a part of the current thesis. The details will be provided in subsequent chapter. Interestingly, Girishkumar and Ravichandran, (2012) suggest that the El Niño events reduce the intensity of the tropical cyclones in the BoB during November - December through anomalous high wind shear over the BoB along with reduced tropical cyclonic heat potential.

1.5 Importance of land-use land-cover changes on extreme rainfall events

The monsoon system involves interactions between land, ocean, and the atmosphere. Over the tropics, particularly the Indian subcontinent, land-surface processes are an important driver of the weather and climate variability (Saha et al., 2012, 2016; Halder et al., 2016; Nayak et al., 2019). Some of the anthropogenic activities such as land-use land-cover changes, urbanization, irrigation, deforestation, and greenhouse gases affect the local/regional weather system (Meehl and Washington, 1993; Niyogi et al., 2002; Pielke et al., 2002). The fifth report of the

Intergovernmental Panel on Climate Change (IPCC) noted that since the industrial revolution, urban expansion has increased. The extreme weather events have a certain association with forest and grassland degradation. Land-use land-cover (LULC) and increasing urbanization affect the physical properties of the albedo, surface temperature, surface winds, soil moisture, atmospheric boundary layer, latent heat and sensible heat fluxes (Arnfield, 2003; Goswami et al., 2010; Gogoi et al., 2019). A recent study by Paul et al., (2016) suggested that the weakening of the ISMR may have been due to deforestation and associated decrease in evapotranspiration. Niyogi et al., (2010) show that the land-use changes associated with agricultural intensification could reduce the ISMR over northern India. Moreover, model studies suggest that urbanization plays a vital role in the distribution of precipitation over an urbanized area around the globe (Kumar et al., 2008; Lei et al., 2008; Li et al., 2013 and 2016). Indeed, urbanization is a key parameter, which often causes higher surface temperatures, larger sensible heat fluxes, more water vapour and water-vapor mixing ratio in the boundary layer and hence higher convective available potential energy that triggers the convection and associated heavy rainfall (Zhang et al., 2007; Zhong and Yang, 2015; Yu and Liu, 2015).

Most of the climate change studies have reported the influences of the large-scale dynamics on EREs. However, understanding and studying the potential role of small/regional-scale land surface feedback on the EREs is also important, at least where the LULC is significantly changing (Pielke et al., 2011; Cook et al., 2015; Jain et al., 2015; Paul et al., 2018). As mentioned earlier, Ghosh et al. (2009) indicate that changes in the spatial extent of regional urbanization due to industrialization and deforestation as a potential cause for increased EREs in some parts in India. Kishtawal et al. (2010) analysed the long-term gridded rainfall dataset and reported that over urban areas, the frequency of HREs is high as compared to non-urban areas over India. A few extreme rainfall case studies explored the effect of urbanization on EREs over different parts of India such as over Delhi (Rao et al., 2004; Mohan et al., 2009, 2011), Mumbai (Rao et al., 2004; Kumar et al., 2008; Paul et al., 2018), Bengaluru (Kumar et

al., 2008; Goswami et al., 2010; Jagadeesh et al., 2015; Sahoo et al., 2020), over Uttarakhand (Sahoo et al., 2020). All these studies show that the LULC and urbanization are positively influencing the heavy rainfall activity.

1.6 Prediction of extreme rainfall events using dynamic models

Prediction of high-intensity rainfall events in India has been a challenge to the scientists till recently, but is very important given the implications of an accurate prediction in saving lives, protect agriculture sector, and for all round disaster management. Several global and regional dynamical climate models are available in the research community. Using the Global Climate Models (GCMs), it is very difficult to simulate the extreme weather events, particularly EREs, because of their relatively low resolutions (Koteswara Rao et al., 2014). Compared to GCMs, the Regional Climate Models (RCMs) are better in simulating the EREs, because the RCMs, by virtue of their higher resolution in general as compared to the GCMs, resolve the local land-surface properties such as orography, vegetation, and the associated internal regional climate variability (Jones et al., 1995; De Sales and Xue, 2010; Di Luca et al., 2011). Notwithstanding the improvements in the modelling in the recent period, accurate forecasts of EREs are challenging in real-time, and there are many uncertainties in the dynamical model simulations over Indian regions. For example, a study by Bhatla et al., (2020) suggested that the regional climate model (RegCM-4.3) performance is very poor in predicting/simulating the EREs over some regions in India.

The forecast performance of the RCMs depends on several reasons. An important reason is the poor quality of the initial conditions. Generally, the GCMs provide the initial conditions to mesoscale/regional climate models. These initial conditions have some limitations, such as low-resolution and insufficient representation of local mesoscale features. Therefore, assimilation of observed conventional (synoptic, radiosonde), and non-conventional (satellite radiance) datasets can improve the initial conditions and reduce the uncertainties in model simulations (Daley, 1991; Govindankutty and Chandrasekar, 2011; Srinivas et al., 2012).

In the recent past, several studies have assimilated different weather variables from the satellite, RADAR, GPS RO, and other ground observations using three/four-dimensional variational (3DVar/4DVar) assimilation techniques into the Weather Research and Forecasting (WRF) model, a state-of-the-art regional model used for weather forecasting all over the world. A few recent case studies reports that assimilation of different observed variables using WRF-3DVar techniques significantly improves the weather prediction skills over different parts in India (Abhilash et al. 2007; Routray et al. 2010, 2013; Srivastava et al. 2010; Bhowmik et al. 2011, etc.). A study by Routray et al., for example, (2010) suggests that assimilation of satellite oceanic surface wind and cloud top temperature, data from surface weather stations, buoys, ships, and radiosondes datasets significantly improve the ability to predict patterns of convective HREs. The assimilation of reflectivity and radial wind from Doppler Weather Radar data has also been reported to enhance the ability to predict the spatial patterns leading to thunderstorms (Prasad et al., 2014), heavy rainfall events, and monsoon depressions (Abhilash et al., 2007; Routray et al., 2013) over several regions of the Indian continent.

With the advent of satellites that retrieve moisture and rainfall information, assimilation of moisture parameters from various remote sensing retrievals has been suggested as a potential technique to improve the forecast quality. Indeed, Kumar and Varma (2016) indicate that assimilation of INSAT-3D derived rainfall makes a good improvement in temperature and wind speed forecasts, in case of the heavy rainfall episode over the Ahmedabad, India. Apart from the INSAT datasets, another satellite-derived observed dataset, called Global Positioning System (GPS) Radio Occultation (RO) refractivity, is available. These soundings are particularly useful for providing atmospheric moisture information with global coverage (Ware et al., 1996; Rocken et al., 1997). The GPS RO refractivity data is retrieving based on the atmospheric pressure and temperature profiles (Ware et al., 1996). Previous studies have shown that the assimilation of GPS RO refractivity has a positive influence on regional as well as global weather predictions (Kursinski et al., 2000; Healy et al. 2005; Huang et al. 2005;

Cucurull et al. 2006; Healy and Thepaut 2006, etc.). Several case studies demonstrated that the uncertainties in the model forecast could be significantly minimized by assimilating the GPS RO refractivity data (Kuo et al. 2004, 2005; Chen et al. 2006; Cucurull et al. 2006). Huang et al., (2005) assimilated GPS RO refractivity soundings into the MM5 model with 3DVar system for two typhoons on Taiwan, namely, Nari in 2001 and Nakri in 2002, the results show that both typhoons track and rainfall predictions have improved with the assimilation of GPS RO refractivity dataset. Huang et al., (2007) examined the impact of assimilating the GPS RO refractivity data on the prediction of rainfall in the west coast of India using the WRF-3DVar model; they reported that the assimilation of GPS RO data has improved the prediction skills in terms of rainfall locations and amounts. From the context of southern India, Madhulatha et al. (2017) have assimilated the satellite radiance observations and found improvement in the prediction of mesoscale convective systems over southern India.

1.7 Gaps, Objectives and scope of the study

From the brief literature survey presented above, it is evident that the frequency and intensity of the EREs have been significantly increasing over different parts of India during the ISM including southern peninsular India in the recent decades. The past studies explored a few possible mechanisms for increased EREs over India. In addition, we also know that the tropical ocean drivers such as ENSO, ENSO Modoki, IOD, and AZM are affecting the IAV of the Indian ISM as well as NEM rainfall. Interestingly, no comprehensive study is available on the impact of changing large scale tropical Indo-pacific climate drivers, e.g., changing frequencies and/or intensities, reduction of canonical El Niños and increasing El Niño Modokis, etc., on the EREs in India during the ISM. Therefore, it is worth to investigating the changes in the potential role of tropical SSTs on EREs over India during the ISM in recent decades.

In addition, very few studies over southern Indian states, which explore the potential role of changes in urbanization on the EREs are available. It is also very important to investigate to catalogue local LULC and urbanization changes over southern Indian states, and their

implications for the local EREs. In this context, we focus on the three southern states of Tamil Nadu, Telangana, and Kerala. All three states are different from one another either in the annual cycle of the climate or the distance from the oceans. The Tamil Nadu and Kerala are the coastal regions that receive a copious amount of rainfall during the NEM and ISM season, respectively. But the state of Telangana, on the other hand, is a land-locked region and far away from the oceans. These three states, more or less represent the variability of the other regions in southern India as well.

From the perspective of the dynamical prediction of the EREs, so far, no other studies assimilated the GPS RO refractivity data to potentially improve the predictability of EREs over southern India regions.

Based on the above discussion, I propose the following specific objectives, which will be addressed in the present thesis:

1. To document the observed spatial trends in the frequency and intensity of EREs in India, and potential causal roles of various tropical Indo-Pacific Ocean climate drivers.

2. Assess the relative contributions of extreme El Niños vis a vis and the recent warming of the Bay of Bengal SST to the intensity of EREs during the northeast monsoon using a regional model.

3. Explore the importance of LULC changes on extreme rainfall events in southern India using a regional model.

4. Applying the radio occultation (RO) refractivity assimilation in improving the prediction skills of extreme rainfall events in southern India in a regional model.

The thesis is organized into 7 chapters, including the current one. The organization of the contents of the thesis in the remaining chapters follow.

A detailed description of the various observed and reanalysis datasets used is presented in Chapter 2. The chapter also espouses on the methodologies; briefly, I present a brief discussion of the regional model used, and statistical equations that I used in this study. In Chapter 3, I have studied the spatial variability of the EREs and the long-term trends therein and the relative impacts of tropical ocean drivers such as ENSO, IOD, and ENSO Modoki across two sub-

periods 1980 - 1999, and 2000 - 2019. In Chapter 4, I report on my investigation from various sensitivity experiments I carried out using the WRF model version 3.6, the relative contributions of BoB warming SST anomalies, and the effect of the strong co-occurring El Niño on the intensity of Chennai 2015 ERE. In Chapter 5, I have examined the relative role of LULC and urbanization changes on EREs over southern India using observations in the recent two decades along with several modelling experiments. In Chapter 6, by employing the WRF version 3.8.1, I have explored the importance of assimilating the GPS RO refractivity dataset for predictability of several representative EREs over southern India. The summary of the thesis and future scope have been presented in Chapter 7.

Chapter – 2

Datasets and Methodology

In this chapter, I present a brief introduction of different observational and reanalysis datasets that I have used in this thesis. In addition, I also describe my research methodology, including the statistics used, and a short narrative of the Weather Research and Forecasting (WRF) model I have used.

In this thesis, various observational as well as reanalysed gridded atmospheric and oceanic parameter datasets at hourly, daily, and monthly resolutions, and rainfall datasets from measurements by rain-gauges at various stations, have been analysed. The analysis has been carried out to understand, among other things, rainfall variability over peninsular India and the teleconnections from the tropical Oceans. In addition, I have also studied the trends in the frequency and the intensity of EREs in India in general, and the relative roles of background changes in the sea surface temperature (SST) and LULC on the climate statistics of the EREs in three representative states of southern India during the local principal monsoon seasons. Furthermore, sensitivity experiments have been conducted to explore the potential background mechanisms with the Weather Research and Forecasting (WRF) model. I also use some of the observational and reanalysis datasets to validate the outputs from my various WRF sensitivity simulation experiments.

The details of all the observational and reanalysis datasets have been described in Section 2.1 of this chapter. Section 2.2 describes the statistical equations and methodologies, which I used for various analyses in this thesis. Sections 2.3 provide a brief description of the WRF model and its 3DVar assimilation process and physical parameterization schemes.

2.1 Observational and reanalysis datasets

2.1.1 Rainfall datasets

I mainly used the daily gridded rainfall datasets of the India Meteorological Department (IMD) dataset from 1901 to 2019 (Pai et al., 2014 for primary analysis).

The dataset has a spatial resolution of with 0.25°×0.25° and has been prepared using the daily rainfall records from a higher density of 6955 rain-gauge stations all over India, and was generated after making standard quality controls for the rain-gauge stations all over India. For more details see Pai et al., 2014). Given the uncertainties in the gridded rainfall datasets (e.g., Jourdain et al., 2013; Collins et al., 2013), wherever possible, I have used available station observations, and other observational rainfall datasets described below, particularly while

validating my model simulations. In this context, I used rainfall datasets from the IMD rain gauge network and those from the Automatic Weather Station (AWS) of the Bureau of Economics and Statistics, Government of Telangana (Reddy et al., 2007). The gridded daily rainfall datasets from the Asian Precipitation-Highly-Resolved Observational Data Integration Towards Evaluation (APRHRODITE) at 0.25°×0.25° spatial resolution available between 2000 and 2015 (Yatagai et al., 2012) have also been used. The APHRODITE datasets are available since 1951; these are based on the data from a "dense" network about 12000 rain-gauge stations, available through the Global Telecommunication System network. These gridded datasets are available for only four sub-domains, specifically, the Middle East, Asia, Russia, and Japan. I also used the satellite-based daily gridded rainfall datasets from the Tropical Rainfall Measurement Mission (TRMM) version 07, available at 0.25°×0.25° spatial resolution from 2000 to 2017 (Huffman et al., 2010). The TRMM dataset is a joint mission of the National Aeronautics and Space Administration (NASA) and Japan Aerospace Exploration Agency; it was launched in 1997 to study the weather and climate applications. It provides precipitation data for the tropical and subtropical regions (35°S - 35°N). Besides, I used Global Precipitation Measurement Integrated Multi-Satellite Retrievals for GPM (GPM - IMERG) version 05, level 3 hourly gridded rainfall dataset (Huffman, 2015), which was developed by the NASA. The advantage of use this dataset is that it has a high spatial resolution of 0.1°×0.1° and half an hourly temporal resolution. However, it is available only for the period 2014 - present. I used these datasets to validate the rainfall outputs of WRF sensitivity simulation experiments.

The advantages of use various gridded rainfall datasets, we quantified the regional climate change spatial trends and made evidence on the basis of various rainfall datasets.

2.1.2 Sea surface temperature datasets

In this study, I used the Hadley Centre Sea Ice and Sea Surface Temperature (HadISST) monthly gridded SST datasets at 1°×1° spatial resolution from 1901 to 2019 (Rayner et al., 2003) to generate the time series of the ENSO activity, IOD, AZM, and also to quantify the

observed trends in SST. These data have been developed by the U. K. Met Office Hadley Centre for Climate Prediction and Research. The HadISST dataset is an updated version of the Global Sea Ice and Sea Surface Temperature (GISST) datasets, available for the period 1870-present. The HadISST datasets have been developed by assimilating the various in-situ ocean observations, also including the SST data from the Met Office Marine Data Bank (MDB), which is available from 1982 onwards, and data received from the Global Telecommunications System (GTS). In addition, I used the National Oceanic and Atmospheric Administration (NOAA) daily spatial resolution Optimum Interpolation Sea Surface Temperature Version 2 (OISSTV2, henceforth OISST) dataset, available from 1986 to 2015 (Reynolds et al., 2007) at 0.25°×0.25° resolution. The OISST is based on the assimilation of ocean temperature observations from satellite and in-situ observations from ships and buoys, etc. Among other datasets, the Advanced Very High-Resolution Radiometer (AVHRR) infrared instruments are used to estimate the OISST fields and provide global SST fields. The OISST dataset has been primarily used in my study as lower boundary conditions for various WRF sensitivity simulation experiments.

2.1.3 Wind (circulation) datasets

I used the daily gridded, multi-level zonal, meridional winds, and specific humidity datasets from the National Center for Environmental Prediction and National Center for Atmospheric Research (NCEP/NCAR) reanalysis-1, available from 1950 to 2019 (Kalnay et al., 1996). In this thesis, the NCEP/NCAR reanalysis-1 zonal and meridional winds datasets have also been used as lateral boundary conditions for various WRF sensitivity simulation experiments. This dataset is available from 1948 to date at 6-hourly, daily, and monthly temporal scales at 2.5°×2.5° spatial resolution and 17 vertical pressure levels from the surface. To generate this reanalysis product, observations have been assimilated into the first guess fields from the global numerical model of the National Centres for Environmental Prediction Global Forecasting System (NCEP-GFS) by means of the ensemble Kalman filter data assimilation method. In

addition, I have also used the reanalysed gridded multi-level zonal and meridional winds, sea level pressure, and specific humidity datasets, which were developed by the European Centre for Medium-Range Weather Forecasts Reanalysis (ERA5) and available from 1979 - present (Hersbach and Dee, 2016). As these ERA5 datasets are available for hourly-scale and high spatial resolution at 0.25°×0.25°, unlike the NCEP/NCAR datasets available at 6 - h resolution, I used these datasets to validate the outputs of WRF sensitivity simulation experiments.

2.1.4 Land-use land-cover (LULC) datasets

To investigate the impact LULC changes on the intensity of extreme rainfall events, I have used the LULC datasets generated by the Indian Space Research Organization (ISRO) for the years 2005 and 2017. In addition to some analysis of the LULC datasets itself, I used these datasets as lower boundary conditions of the WRF model while carrying out LULC sensitivity experiments. The datasets have been obtained from the Advanced Wide Field Sensor (AWiFS) aboard the Indian Remote-Sensing Satellite (IRS P6) of the ISRO. This LULC dataset is available with 24 categories (Table 4.1), at three different spatial resolutions such as 5m (~9 km), 2m (~3.5 km), and 30s (~0.9 km) on an annual basis from the year 2005 onwards for the Indian region only (Biswadip et al., 2014). These datasets are freely available at "Bhuvan" web-portal (https://bhuvan-app3.nrsc.gov.in/data/download/index.php).

2.1.5 Satellite-based GPS RO dataset

I have used the Global Positioning System (GPS) Radio Occultation (RO) refractivity soundings dataset (NCEP, 2008) to explore the predictability of EREs over southern India. It is a UCAR-led first concept of GPS RO refractivity soundings mission, known as GPS/MET, which has launched in 1995 (Ware et al., 1996). This was followed by the Constellation Observing System for Meteorology, Ionosphere, and Climate/Formosa Satellite Mission 3 (COSMIC/FORMOSAT-3; henceforth COSMIC). Since April 2006, the COSMIC has been a joint mission of the United States and Taiwan (Anthes et al., 2008). The GPS RO is an active satellite-to-satellite limb sounding technique in which the transmitter and receivers are placed

in GPS and Low-Earth-Orbiting (LEO) satellites, respectively. Nearly 4000 GPS RO soundings in a day are uniformly distributed worldwide and made it available for the users. With an all-weather sounding capability on board, the soundings have high vertical resolutions of temperature and humidity profiles, and highly accurate (Yunck et al., 2000; Anthes et al., 2008; Ha et al., 2017). The GPS RO soundings agree with the conventional radiosonde soundings even in the middle and upper troposphere (Rocken et al., 1997). Several studies have established the usefulness of these datasets for various weather and climate applications (Kuo et al. 2004, 2005). Along with satellite GPS RO refractivity profiles, we used available upper-air and surface weather observations (NCEP, 2008).

2.2 Methodology

2.2.1 Statistical methods

In this thesis, I used various statistical methods to understand the variability and trends in the frequency and intensity of EREs, and the relevance of background changes to the intensity of EREs over southern India during the ISM and NEM season, the details follow.

To identify the daily EREs, I follow a slightly modified classification of the IMD categorization methodology, which was described in Chapter 1. Briefly, the IMD has categorized eight various rainfall classes based on the accumulated daily rainfall amount, which can be accessed at (Table 2.1, http://www.imdpune.gov.in/Weather/Reports/glossary.pdf). According to the IMD classified rainfall classifications, if the rainfall amount during an event is ≥ 244.4 mm/day, it is considered as an extreme heavy rainfall event. But these extreme heavy rainfall events (≥ 244.4 mm/day) are not common all over the entire Indian region. So, I have merged the IMD categorized classes of extreme heavy (≥ 244.4 mm/day) and very heavy (≥ 124.5 to ≤ 244.5 mm/day) rainfall events into a single class as ‘extreme rainfall event (≥ 124.5 mm/day)’ in this thesis. In the same way, the IMD classes of heavy (≥ 64.5 to ≤ 124.4 mm/day) and rather heavy (≥ 35.6 to ≤ 64.4 mm/day) rainfall events are regrouped into the heavy (> 35.5 to < 124.4 mm/day) rainfall events. My definition of moderate rainfall events is the same as

that of the IMD (≥ 7.6 to ≤ 35.5 mm/day). The light (≥ 2.5 to ≤ 7.5 mm/day) and very light (> 0.1 to ≤ 2.4 mm/day) rainfall events are regrouped into a single class of as normal rainfall events (> 0.1 to ≤ 7.5 mm/day). Moreover, if the rainfall amount in a day exceeds 0.1 mm, i.e., if the rainfall rate is at least 0.1 mm/day, then I classify it as a rainy day (Table 2.1).

While analysing the variability and trends in the rainfall magnitude over India, I considered the 99, 95, and 75 percentiles rainfall magnitudes as those for extreme, heavy, and moderate rainfall.

Table 2.1: Classification the different rainfall categories based on magnitude of accumulated rainfall.

S. No	IMD rainfall categories	Rainfall (mm/day)	Our rainfall categories	Rainfall (mm/day)
1			Rainy day	> 0.1
2	Very light	> 0.1 - 2.4	Normal	0.1 - 7.5
3	Light	2.5 - 7.5		
4	Moderate	7.6 - 35.5	Moderate	7.6 - 35.5
5	Rather heavy	35.6 - 64.4	Heavy	35.6 - 124.5
6	Heavy	64.5 - 124.4		
7	Very heavy	124.5 - 244.4	Extreme	≥ 124.6
8	Extreme heavy	≥ 244.5		

To study the spatial distribution of long-term trends in the rainfall of various categories of rainfall events and magnitudes over India, I used the Mann-Kendall trend test (Kendall, 1975; Mann, 1945), and evaluated the statistical significance at 5% level. The Mann-Kendall trend test is a non-parametric approach, commonly used in the climate studies to identify statistically significant trends of rainfall events over India (Yadav et al., 2014; Ahmad et al., 2015; Hussain et al., 2015; Ghosh et al., 2016; Soraisam et al., 2018). In this test, the null hypothesis (H_0) assumes that there is no trend in the data over time, and the alternate hypothesis (H_1) assumes that there is a trend in the data (either increasing or decreasing) over time.

The Mann-Kendall trend test statistic 'S' is computed as follows

$$S = \sum_{i=1}^{n-1} \sum_{j=i+1}^{n} sign(X_j - X_i), \quad (2.1)$$

$$sign\left(X_j - X_i\right) = \begin{cases} 1 & if\ X_j - X_i > 0 \\ 0 & if\ X_j - X_i = 0 \\ -1 & if\ X_j - X_i < 0 \end{cases} \quad (2.2)$$

$$Var\ (S) = \frac{1}{18}\left[n(n-1)(2n+5) - \sum_{p=1}^{q} t_p(t_p-1)(2t_p+5)\right] \quad (2.3)$$

$$Z = \begin{cases} \frac{S-1}{\sqrt{Var\ (S)}} & if\ S > 0 \\ 0 & if\ S = 0 \\ \frac{S-1}{\sqrt{Var\ (S)}} & if\ S < 0 \end{cases} \quad (2.4)$$

Where (i = 1, 2, ... n-1) and (j = i + 1, 2, ... n), X_i and X_j are the time series of observation, n is the number of time steps, t_p is the number of ties for p^{th} value, and q is the number of tied values. The positive and negative Z values are representing an increase and decrease trends.

Moreover, I used the well-known linear trend equation to estimate the trends of individual time series of SST datasets for tropical ocean climate drivers.

$$Y = mX + C \quad (2.5)$$

Where m is the slope and c is an intercept of Y, X is an independent variable, and Y is a dependent variable.

I used the following equation (2.6) to calculate the linear anomaly correlation between the interannual relationship of the NEM with and that with Niño3 index, which represents the variability of ENSO and that with an index of the BoB SST. The linear correlation is a standard linear method to estimate the linear association between two variables.

$$r = \frac{\sum_{i=1}^{n}(X_i - \bar{X})\,(Y_i - \bar{Y})}{\sqrt{(\sum_{i=1}^{n}(X_i - \bar{X})^2)(\sum_{i=1}^{n}(Y_i - \bar{Y})^2)}} \quad (2.6)$$

Where, r is the correlation between X and Y variables. $\bar{X}$ and $\bar{Y}$ denote the mean of each of these variables. n represents the number of time steps over which the correlation is obtained.

In addition, I used the partial correlation technique to linearly isolate the individual correlation

of local rainfall with one of the seasonally co-occurring events, such as the ENSO, ENSO Modoki, IOD, and AZMs, etc. As the phenomena such as the IOD and ENSO are known to co-occur (e.g., Yamagata et al., BAMS, 2004), the method is widely used for such purpose (e.g., Nicholls 1989; Ashok et al., 2001, 2007).

The partial correlation is obtained by using the below equation.

$$r_{ab.c} = \frac{r_{ab} - r_{ac} r_{bc}}{\sqrt{(1 - r_{ac}^2)(1 - r_{bc}^2)}} \qquad (2.7)$$

Where $r_{ab.c}$ is the partial correlation between variables a & b after removing the compound effect of c. r_{ab} is the correlation between a & b, r_{bc} is a correlation between b & c, r_{ac} is the correlation between a & c.

In complement to the correlation analysis, to evaluate the impact of significant anomalous warming of the BoB and that of the ENSO on the northeast monsoon rainfall, I used the below regression equation.

$$A = a + bX \qquad (2.8)$$

$$a = \frac{\sum Y - b \sum X}{N}, \quad b = \frac{N \sum XY - (\sum X)(\sum Y)}{N \sum X^2 - (\sum X)^2}$$

Where, N = Number of observations/years, X is a year index, and Y is a population size for given census years.

I used Student's t-test to find the confidence level of correlations, with degrees of freedom equalling to n-1 (n-2) for the one-tailed (two-tailed) test (Wilks, 2011), where n is the number of independent sample size. I used one -tailed Student's t-test when the sample size was rather small.

$$t = r \sqrt{\frac{n-2}{1-r2}} \qquad (2.9)$$

Where r is the correlation and n is the independent sample size.

As can be seen in latter chapters, I have carried out several experiments to evaluate the impact of the assimilation of GPSO RO datasets in improving the prediction skills for EREs; I have used the Brier Skill Score (BSS) index (Von Storch and Zwiers, 1999; Wilks, 2006; Desamsetti

et al., 2018), a common statistic used in weather prediction.

The BSS index is derived from the Brier Score (BS), which is the mean-square error between the forecast–observation pair at each grid point/station

$$BS = \frac{1}{n}\sum_{i=1}^{n}(F_t - O_t)^2 \quad (2.10)$$

The BSS is then obtained as

$$\text{BSS} = \begin{cases} 1 - \frac{BS_{(ALLOBS,Obs)}}{BS_{(CTL,Obs)}}, & if\ BS_{(ALLOBS,Obs)} < BS_{(CTL,Obs)}, \\ \frac{BS_{(ALLOBS,Obs)}}{BS_{(CTL,Obs)}} - 1, & if\ BS_{(ALLOBS,Obs)} > BS_{(CTL,Obs)}, \end{cases} \quad (2.11)$$

In the above, F_t and O_t are the forecast and observed (Obs) parameters, say, rainfall at a grid point, $BS_{(CTL,Obs)}$, and $BS_{(ALLOBS,Obs)}$ are the mean-square of CTL-Obs and ALLOBS-Obs rainfall.

The BSS values vary between -1 and +1. Positive and negative values indicate a better performance of the assimilated and the control experiments, respectively (Von Storch and Zwiers, 1999).

2.2.2 Dynamical analysis

For the purpose of evaluating the improvements of the forecast skills for extreme events in assimilation experiments, I have also carried out a vorticity budget analysis to diagnose the dynamical processes of each simulated or predicted extreme rainfall event (e.g., Dasari et al., 2017; Luong et al., 2020). The well-known vorticity equation in an isobaric coordinate system (Charney et al., 1950), also used for the tropics (Sardeshmukh a nd Hoskins, 1988), is presented in Equation (2.12). The contribution from each term in the vorticity equation towards the rate of change of vorticity is computed as

$$\frac{\partial \zeta}{\partial t} = -\left(u\frac{\partial}{\partial x} + v\frac{\partial}{\partial y}\right)(\zeta + f) - \omega\frac{\partial \zeta}{\partial P} - (\zeta + f)\left(\frac{\partial u}{\partial x} + v\frac{\partial v}{\partial y}\right) + \left(\frac{\partial u}{\partial P}\frac{\partial \omega}{\partial y} - \frac{\partial v}{\partial P}\frac{\partial \omega}{\partial x}\right) + \left(\frac{\partial F_y}{\partial x} - \frac{\partial F_x}{\partial y}\right) \quad (2.12)$$

where $\frac{\partial \zeta}{\partial t}$ represents the tendency of relative vorticity. On the right-hand side of the equation, the first and second terms account for the contributions from the horizontal advection of

absolute vorticity and vertical advection of relative vorticity. The third term represents the divergence acting on absolute vorticity, also known as the stretching term. The penultimate term represents the tilting associated with the vertically sheared horizontal flow, and the last term represents the contribution from the horizontal gradients of friction. The analysis of these terms provides comprehensive information to explain the different physical and dynamical processes necessary for the intensification of an extreme rainfall event.

I also computed the apparent heat source (Q), following Yanai et al. (1973). These terms briefly represent the diabatic heat; it is obtained the sum of the latent heat associated with the phase changes, vertical transport, sub-grid diffusion, and radiative heat. The distribution of the apparent water vapor provides the heat sink and source regions (Yanai et al., 1973; Schumacher et al., 2007; Shige et al., 2007) according to

$$Q(x,y,p,t) = \left(\frac{\partial T}{\partial t} + u\frac{\partial T}{\partial x} + v\frac{\partial T}{\partial y} + \omega\frac{\partial T}{\partial p}\right) - \frac{k\omega T}{P} \qquad (2.13)$$

Where, T is the temperature, and u, v, and ω are the horizontal, meridional, vertical velocity components. p is the pressure, $k = \frac{R}{C_p}$, where R and C_p are the gas constant and the specific heat capacity at constant pressure.

I have computed out the vertical wind shear (Xavier and Joseph, 2000) by subtracting the $wind_{500}$, the wind at 500 hPa, from $wind_{1000}$, the wind at 1000 hPa. Studies suggest that the vertical wind shear between the lower and mid-troposphere provides crucial information for the maintenance and duration of the convective storms (Coniglio et al., 2010; Taylor et al., 2017; 2018). Strong wind shear and vertical wind represent the development of deep moist convection associated with heavy precipitation (Rao and Ratna, 2010; Srinivas et al., 2018). I also conducted a Skew-T Log-P analysis using the vertical profiles of moisture and temperature outputs of the WRF model. A Skew-T Log-P analysis was carried out through the use of an NCAR Command language algorithm. This routine also generates various parameters such as the lifting condensation level (LCL), convective condensation level (CCL), the convective available potential energy (CAPE), which are also analysed.

The well-known Niño3 index, defined as the area-averaged SST anomalies (SSTA) over 150°W - 90°W, 5°S - 5°N region of eastern Pacific Ocean, is employed to represent the variability of the ENSO (Box-6 in Figure 2.1). The ENSO Modoki Index (EMI) defined by the below Equation (2.14, Ashok et al., 2007), represents the variability of the ENSO Modoki.

$$EMI = (SSTA)_A - 0.5(SSTA)_B - 0.5(SSTA)_C \quad (2.14)$$

The bracket in Equation (2.14) denotes the area-average SSTA over each of the regions $(SSTA)_A$ *= 165°E - 140°W, 10°S - 10°N,* $(SSTA)_B$ *= 110°W - 70°W, 15°S - 5°N, and* $(SST)_C$ *= 125°E - 145°E, 10°S - 20°N.*

The IOD mode index (IODMI) defined the area-averaged SSTA difference between western of 50°E - 70°E, 10°S - 10°N and south-eastern of 90°E - 110°E, 10°S - 0° over tropical Indian Ocean (Box-2 and 3 in Figure. 2.1, Saji et al. 1999) represents the variability of the Indian Ocean Dipole.

The Atlantic Zonal Mode index (AZMI) is the area-average of the SSTA over a region of 20°W - 0°, 3°S - 3°N considered as an AZM region (Zebiak, 1993). AZM is phase-locked to the seasonal cycle and typically peaks in the boreal summer between June and August (JJA; Lübbecke et al., 2010, Box-1 in Figure 2.1).

The area-averaged SSTA over the domain bound by 8°N - 15°N, 85°E - 95°E has been adopted as the Bay of Bengal (BoB) SST index, and for convenience, simply referred to as the BoB index. This region has been chosen because (1) it has been experiencing a warming trend since the late 1980s (Figure 4.2a), and (2) many tropical cyclones influence this region, as can be seen from the digital tropical cyclone tracks provided by the IMD (http://www.rmc-chennaieatlas.tn.nic.in) (figure not shown).

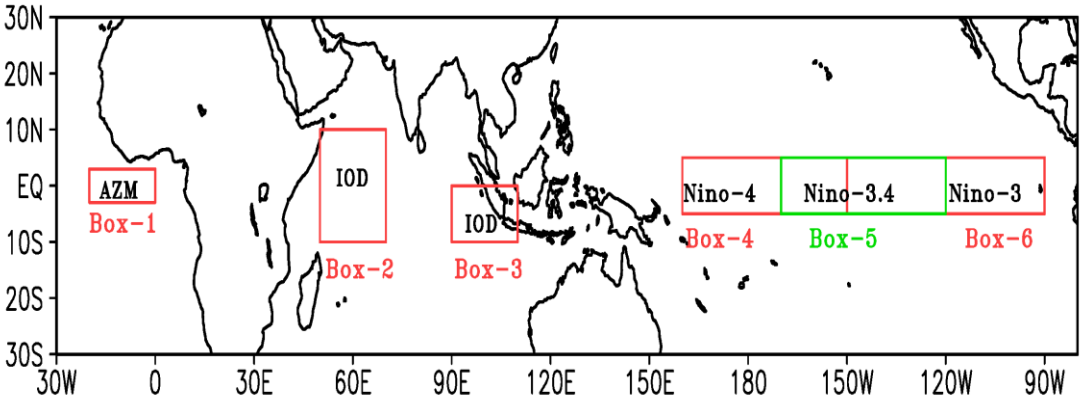

Figure 2.1: Schematic diagram represents the different SST index regions over the tropical Indo-Pacific and Atlantic Oceans.

2.3 The WRF model description

The Weather Research and Forecasting (WRF) is a mesoscale climate model system. It has been developed by a collaborative partnership of the National Center for Atmospheric Research (NCAR), the National Oceanic and Atmospheric Administration (NOAA), the United States. Air Force, the Naval Research Laboratory, the University of Oklahoma, and the Federal Aviation Administration (FAA). The Advanced Research WRF (ARW) model is designed for both atmospheric research and operational forecasting applications purpose. It has capable of simulating all the meteorological parameters at small/regional scales ~1 km also. In WRF model, it is very flexible to set up the horizontal and vertical resolutions, interactive nested domains, and choosing several parameterization schemes such as cumulus convection, radiation, microphysics, boundary layer, surface fluxes, and boundary layer turbulence, explicit moisture, and soil processes, etc. The WRF model has several prognostic variables such as three-dimensional pressure, wind, potential temperature, geo-potential height, surface pressure, turbulent kinetic energy and etc. The WRF model can assimilate several meteorological parameters from the conventional and non-conventional observational datasets, through three/four-dimensional variational (3D/4DVar) techniques. The comprehensive details of the WRF model are given in Skamarock et al., (2008).

2.3.1 The Governing equations of the WRF model

The regional or global atmospheric models have a set of primitive equations for weather forecasts and climate simulations. These primitive equations are derived from the three fundamental conservation laws, such as conservation of mass, conservation of momentum, and conservation of moisture. Moreover, the dynamical models require the equation of state of dry air, which is generally use ideal gas law. The WRF model is a fully compressible non-hydrostatic dynamical core model; but it can also perform as a hydrostatic model. The equations are in the WRF model formulated using the terrain-following mass vertical coordinate (Laprise, 1992).

The terrain-following mass vertical coordinate system of dry air in the WRF is denoted by η, defined by the following equation.

$$\eta = [P_{dh} - (P_{dh})_t]/\mu_d \quad \text{with} \quad \mu_{d=}(P_{dh})_s - (P_{dh})_t \qquad (2.15)$$

Where the P_{dh} refers to the hydrostatic pressure of dry air, the $(P_{dh})_s$ and $(P_{dh})_t$ denote the pressure of dry air values at the surface and top of the atmosphere. The η refers to the mass of the dry atmospheric air column between the surface and top. The value of η varies from surface (η = 1) to the model top (η = 0) vertical distribution.

From the law of conservation of momentum and the thermodynamic equation, we can derive four equations, the flux form of four equations for the three components (U, V, and W) of velocities and the potential temperature (θ) by considering the continuity equation.

$$\frac{\partial U}{\partial t} + m_x\left[\frac{\partial (U_u)}{\partial x} + \frac{\partial (V_u)}{\partial y}\right] + \frac{\partial (\Omega_u)}{\partial \eta} + \frac{m_x}{m_y}\left[\mu_d \alpha \frac{\partial p}{\partial x} + \frac{\alpha}{\alpha_d}\frac{\partial p}{\partial \mu}\frac{\partial \emptyset}{\partial x}\right] = F_U \qquad (2.16)$$

$$\frac{\partial V}{\partial t} + m_y\left[\frac{\partial (U_v)}{\partial x} + \frac{\partial (V_v)}{\partial y}\right] + \frac{m_y}{m_x}\left[\frac{\partial (\Omega_u)}{\partial \eta}\right] + \frac{m_y}{m_x}\left[\mu_d \alpha \frac{\partial p}{\partial y} + \frac{\alpha}{\alpha_d}\frac{\partial p}{\partial \eta}\frac{\partial \emptyset}{\partial y}\right] = F_V \qquad (2.17)$$

$$\frac{\partial W}{\partial t} + \frac{m_x m_y}{m_y}\left[\frac{\partial (U_w)}{\partial x} + \frac{\partial (V_w)}{\partial y}\right] + \frac{\partial (\Omega_w)}{\partial \eta} - \frac{1}{m_y} g\left[\frac{\alpha}{\alpha_d}\frac{\partial p}{\partial \eta} - \mu_d\right] = F_W \qquad (2.18)$$

$$\frac{\partial \Theta}{\partial t} + m_x m_y\left[\frac{\partial (U_\theta)}{\partial x} + \frac{\partial (V_\theta)}{\partial y}\right] + m_y\left[\frac{\partial (\Omega_\theta)}{\partial \eta}\right] = F_\Theta \qquad (2.19)$$

In the above equations, $\emptyset$, θ, and g are represents geopotential, potential temperature, and acceleration due to gravity, respectively. p is the total pressure for moist air $p = p_0(R_d\theta_m/p_o \propto_d)^\gamma$. Where $\gamma = c_p/c_v = 1.4$ is the ratio of the specific heats at constant pressure and volume. The $\theta_m = \theta[1 + (R_\vartheta/R_d)q_\vartheta]$ is a moist potential temperature, R_ϑ and R_d represent

perfect gas constants relative to dry air and water vapor. Th $\alpha = 1/\rho$ is an inverse of density, α_d is an inverse of the density of dry air, and those satisfy a relation $\alpha = \alpha_d(1 + q_\vartheta + q_c + q_r + q_i + \cdots)^{-1}$, where $q_\vartheta, q_c, q_r, q_i$ ...etc., are the mixing ratios of hydrometeors.

In equations (2.16) to (2.18), the quantities of $F_U, F_V, and\ F_W$ contain the Coriolis force components, the curvature terms, and mixing terms for the three components of momentum. By considering the isotropic projections such as Lambert, Polar, and Mercator by considering $m_x = m_y$ = m the Coriolis and curvature terms can be written as

$$F_{U_c} = +\left(f + u\frac{\partial m}{\partial y} - v\frac{\partial m}{\partial x}\right)V - eW\cos\alpha_r - \frac{uW}{r} \quad (2.20)$$

$$F_{V_c} = -\left(f + u\frac{\partial m}{\partial y} - v\frac{\partial m}{\partial x}\right)U - eW\sin\alpha_r - \frac{vW}{r} \quad (2.21)$$

$$F_{W_c} = +e(U\cos\alpha_r - V\sin\alpha_r) + \left(\frac{uU+vV}{r}\right) \quad (2.22)$$

Where α_r is the angle of rotation between the ordinate axis and meridian, r is the radius of the Earth (6371 km), $f = 2\Omega\sin\varphi$ and $e = 2\Omega\cos\varphi$ (Ω standing for the angular velocity of rotation of the Earth (7.272×10^{-5} rad/s) and φ for latitude).

2.3.2 WRF-3DVar data assimilation method

In this thesis, to study the impact of assimilating GPS RO refractivity data on the prediction of EREs over southern India, I used the three-dimensional variational (3DVar) data assimilation technique available with the WRF model (Barker et al., 2004). The data assimilation is a technique, which combines the observations with numerical weather prediction output from a previous time step (first guess), and by minimizing their relevant error statistics, to give better estimate of the atmospheric state (Ide et al., 1997). The 3DVar assimilation method has been widely used for assimilation purpose due to its practicability in terms of computational efficiency (Sugimoto et al., 2009). Various research institutes are focus on the assimilation of conventional observations using the 3DVar assimilation method for improving the initial state of mesoscale models (Gao et al., 2004; Xiao et al., 2005; Xiao and Sun, 2007; Thiruvengadam et al., 2019). The 3DVar data assimilation method provides a minimization of a prescribed cost

function (J) as follows (Ide et al., 1997).

$$J = \frac{1}{2}(x - x_b)^T B^{-1}(x - x_b) + \frac{1}{2}(y^0 - H(x))^T R^{-1}\left(y^0 - H(x)\right) \quad (2.23)$$

Where, y^0, x_b and x indicates the observation, background and analysis variables. R and B represent the error covariance matrices for observation and background. H is used to map the variables from model space to observation space.

2.3.3 WRF model physical parameterization schemes

One of the biggest challenges in the regional climate model is to setup the model with an appropriate configuration for a specific region. Each region has been characterized by different unique conditions and problems due to its geographical position and properties. The optimal model set-up for one region could produce good results, which could lead to poorer results for another region. In addition, one of the most important aspects in configuring the model is to pick the correct physical parameterization schemes. The major advantage of the WRF model is that we can select different physical mechanism schemes such as microphysics, land-surface, planetary boundary layer, radiation, cumulus parameterization and so on. The comprehensive information about several physics options and their mechanisms can be found at Skamarock et al. (2008). The brief summary of the parameterization schemes that I used in this thesis is described below.

2.3.3.1 Microphysics scheme

In the WRF model, microphysics may directly resolve the water vapor, cloud and rainfall processes. Any number of mass mixing-ratio variables and particle number concentrations can be held by the WRF model. Among the various microphysics schemes, I chose Goddard Cumulus Ensemble (GCE) microphysics scheme (Tao et al., 2016) to achieve the realistic simulation of rainfall. This microphysics scheme has been used for many weather applications purposes in several studies (Huang and Wu, 2020; Sahu et al., 2019; Barros et al., 2019, Tao et al., 2017, etc.).

Goddard Cumulus Ensemble microphysics scheme

Goddard Cumulus Ensemble (GCE) Microphysics scheme has recently been improved by introducing a fourth ice class (frozen drops/hail). This enhances the cloud ice, snow, graupel, and frozen drops/hail and can simulate extreme and moderate convection (Lang et al., 2014). The GCE microphysics scheme allows for better performance in ice supersaturation, ice concentration formula and snow size mapping, including a new snow breakup effect, and a good aggregation signature with radar distributions (Tao et al., 2016).

2.3.3.2 Short and long wave radiation schemes

Radiation schemes play a crucial role in numerical weather prediction models and provide atmospheric heating due to radiative flux divergence and long-wave surface and short-wave radiation for the surface heat budget. The longwave radiation contains infrared/thermal radiation which is absorbed and emitted by the various atmospheric gases and Earth surfaces. The upward longwave radiative flux from Earth surfaces is direct by the surface emissivity which depends upon the land-use type and surface temperature. Shortwave radiation includes the incoming visible, ultraviolet radiation from the Sun, but some of the incoming radiation is reflected, absorbed and scattered by the atmosphere and the surface of the Earth. In the atmospheric NWP models the radiation schemes responds to clouds, water vapour, carbon dioxide, ozone, and trace gas concentrations. In the WRF model various longwave and shortwave radiation schemes are available, based on the earlier studies I chose the Rapid Radiative Transfer Model for longwave and Dudhia for shortwave radiation in this study (e.g., Routray et al., 2010; Liu et al., 2013; Dodla et al., 2016).

Rapid Radiative Transfer Model longwave radiation scheme

The Rapid Radiative Transfer Model (RRTM) longwave radiation (Mlawer et al., 1997) is a spectral-band scheme which is derived by using the correlated-k method. It uses predetermined tables to perfectly denote the longwave processes due to water vapor, ozone, carbon dioxide, trace gases, and accounting the cloud optical depth.

Dudhia for shortwave radiation scheme

The Dudhia shortwave radiation (Dudhia, 1989) has simple downward integration of solar flux. The Rayleigh atmosphere, the absorption of water vapour, and cloud albedo and absorption are considered.

2.3.3.3 Planetary Boundary Layer scheme

The planetary boundary layer (PBL) is the bottom layer of the lower troposphere and the average thickness of the layer is around 1-1.5 km from the Earth surface. Strong convective air motions and intense turbulent mixing occurs within this layer. In this PBL, weather variables such as temperature, wind speed and humidity show major variations with deep vertical mixing. The PBL is responsible for vertical sub-grid scale fluxes due to eddy transport in the entire atmospheric column and resolves flux profiles within the well-mixed boundary layer as well as the stable top layer. The selection of most appropriate horizontal diffusion scheme shall be based on horizontal deformation or constant eddy viscosity (K_h) values with separate treatment for horizontal and vertical mixing. The surface flux values for the PBL scheme derive from the surface layer as well as from land-surface schemes. I chose the Yonsei University (YSU) PBL system from several PBL schemes, which can well represent boundary layer parameters and is best, suited to regional climate simulation across the Indian region (Rao and Ratna, 2010; Srinivas et al., 2013).

Yonsei University PBL scheme

The Yonsei University (YSU) PBL (Hong et al., 2006) is the next generation of the Medium Range Forecast Model (MRF) PBL scheme that simulates deeper vertical mixing in the PBL with greater precision. A critical bulk Richardson number of zero (0.5 was used in the MRF PBL scheme) is used to describe the PBL top, which is efficiently based on the buoyancy profile. The YSU PBL counter-gradient mixing value is also smaller, which produces a well-mixed profile of the boundary layer.

2.3.3.4 Land-surface scheme

One of the key components of climate models is the land-surface scheme (LSS). It is used to provide heat and moisture flow over land-surface and sea-ice information obtained from the land-surface layer scheme of the model. These fluxes of heat and moisture provide a lower boundary condition that is useful in the PBL schemes for vertical transport. The LSS have different degrees of sophistication in handling heat and moisture fluxes in multiple soil layers, vegetation, root and canopy effects and surface snow-cover prediction. LSS do not provide tendencies but which update the land's state variables such as the ground, and soil temperature profiles, soil moisture profiles, snow cover and canopy properties. In the WRF model, there are several LSS available, among these, I chose the Noah unified LSS that is commonly used in regional climate simulations in Indian regions (Warrach-Sagi et al., 2013; Chawla et al., 2018).

Noah land-surface scheme

NCAR and NCEP jointly developed the Noah land-surface scheme (Chen and Dudhia, 2001). This has the advantage of being compatible with the time-dependent soil fields given in the research datasets. This is a 4-layer soil temperature and moisture model with canopy moisture and snow cover forecast. The thickness of the layer is 10, 30, 60 and 100 cm from the top to the bottom. It includes root zone, evapotranspiration, soil drainage and runoff, taking into account categories of vegetation, monthly vegetation fraction and soil texture. The scheme provides the boundary layer scheme with sensible and latent heat fluxes. In addition, the Noah land-surface scheme forecasts soil ice and fractional snow cover impacts, has enhanced urban treatment, and considers the properties of surface emissivity.

2.3.3.5 Cumulus parameterization scheme

The cumulus parameterization scheme is responsible for the sub-grid scale effects of convective and/or shallow clouds. The schemes are intended to represent vertical fluxes due to unsolved updrafts and downdrafts and to compensate for motion outside the clouds. They only operate on individual columns where the scheme is triggered and provide vertical heating and moistening

profiles. All schemes have a convective portion of surface rainfall. Theoretically, cumulus parameterizations are only valid for larger grid sizes (>10 km) where it is necessary to properly release latent heat on a realistic time scale in convective columns. Although assumptions about convective eddies being entirely sub-grid scales break down for finer grid sizes, often these schemes have been found to be helpful in triggering convection in 5–10 km grid applications. Generally, it should not be used when the model can solve the convective eddies itself (≤ 5 km grid). Based on the previous studies, I chose the Kain-Fritsch scheme in this study (Osuri et al., 2013; Srinivas et al., 2018; Lekhadiya and Jana, 2018; Swain et al., 2020).

Kain-Fritsch cumulus parameterization scheme

The updated version of the Kain-Fritsch scheme (Kain, 2004) is based on Kain and Fritsch (1990) and Kain and Fritsch (1993) but has been modified on the basis of the Eta model. It uses a basic cloud model with moist updrafts and downdrafts, including the effects of detrainment, entrainment, and relatively simple micro-physics, as with the original KF scheme. In the following respects, it varies from the original KF scheme.

• A minimum entrainment rate is imposed to suppress widespread convection in marginally unstable, relatively dry environments.

• Shallow (non-precipitating) convection is permitted for any updraft that does not exceed a minimum cloud depth for precipitating clouds; this minimum depth varies depending on the temperature of the cloud base.

• The entrainment rate is allowed to vary as a function of low-level convergence.

Chapter – 3

To document the observed spatial trends in the frequency and intensity of EREs and potential roles of various tropical Indo-Pacific Ocean climate drivers over India

In this chapter, I investigated the potential relative roles of tropical ocean climate drivers on various classes of rainfall events over India during the ISM, especially the extreme rainfall events during the 1980 to 2019 period. I also explore the trends in the extreme rainfall events and magnitudes over the 1980 to 2019 period.

3.1 Introduction

The extreme rainfall events are one of the most catastrophic natural disasters in many parts of the world including over the Indian subcontinent. As mentioned in the Chapter 1, though the ISMR has been decreasing since 1950s (Krishnan et al. 2012; Roxy et al., 2017; Samanta et al., 2020), the frequency and intensity of EREs significantly increasing over some parts in India during the ISM (e.g., Joshi and Rajeevan, 2006; Malik et al., 2016; Ghosh et al., 2016; Roxy et al., 2017; Nikumbh et al., 2019; Singh et al., 2019; Boyaj et al., 2020).

Several previous studies suggested the various factors that affecting the EREs. In addition, very few studies have investigated the relationship between ENSO, IOD, and EREs over India (Ajayamohan and Rao, 2007; Krishnaswamy et al., 2014). Figure 5 of Krishnaswamy et al. (2014) shows an interesting non-linear relationship between ENSOs and EREs over India. While the La Niñas impact the EREs with above 100 mm/day, the rainfall events below this magnitude apparently increase with increasing strength of El Niños. They also point out that non-linear and positive relationship of the IOD events with the ISMR as well as with the frequency of EREs with rainfall above 100 mm/day. Rajeevan et al., (2008) reported that the increasing trends in the EREs are associated with the increasing trend of SST over the tropical Indian Ocean. In addition, the recent studies suggested that the AZM as a factor affecting the IAV of ISMR (Kucharski et al., 2007; Yadav et al., 2016; Pottapinjara et al., 2016, references therein). But no study presented the impact of the AZM on the EREs over India during ISM.

Using the IMD gridded rainfall datasets at 1°×1° resolution for the 1951 - 2005 period, Pattanaik and Rajeevan, (2010) indicated that EREs increasing in central India. Roxy et al. (2017), by analysing the IMD daily gridded rainfall dataset at 0.25°×0.25° resolution for the 1950 - 2015 suggested that EREs with a minimum threshold of 150 mm/day are increasing in number over the central India. Despite several studies indicating a mild weakening trend in the ISMR since 1950s, as shown above, a recent study by Jin and Wang et al. (2017) suggest an increasing ‘trend’ in summer monsoon over north central India between 2002 - 2013. While such a trend over a decade may be just due to sampling, it at least matches with the increasing

EREs in the region. It will be worthwhile to document any trends in multiple categories of the summer monsoon rainfall events across India.

In this present chapter, using the 0.25°×0.25° resolution of IMD daily gridded rainfall dataset for 1980 to 2019 period, I have accordingly investigated the trends in frequencies of multiple categories of rainfall events across India during summer monsoon, with emphasis on those in the EREs. A similar exercise for trends in magnitude of various categories of rainfall magnitudes have also been carried out. Specifically, we examined the trends in 99, 95, and 75 percentiles of rainfall magnitude. Besides, we investigated the potential roles of tropical ocean climate drivers on the frequency of various categories of rainfall events and 99, 95, and 75 percentiles rainfall magnitude over India during the ISM from 1980 - 2019. The primary reason for choosing this time period is that the ENSO-ISM teleconnections have changed since the year 1980 (Aneesh and Sijikumar, 2018; Kucharski and Abid, 2017).

3.2 Spatial trend analysis of various categories of rainfall events and magnitudes over India

In Figure 3.1, we present the linear trends in seasonal mean rainfall, rainy days, and those in various categories of rainfall events, which were defined in Table 2.1 throughout India during the ISM from 1980 - 2019.

In the Figure 3.1, we see significantly increasing trends in the seasonal mean rainfall at 95% confidence level (Figure 3.1a) over the northernmost state of Jammu and Kashmir, a significant portion of the coastal state of Odisha, and north-western states of Rajastahan, Gujarat, and north-western Maharashtra state. The increase in mean rainfall is apparently due to significant increasing trends in number of rainy days and that in moderate and heavy rainfall categories over north-western India and Jammu and Kashmir at 95% confidence level (Figures 3.1b, 3.1d, 3.1e). One need to be careful in the state of Jammu and Kashmir given the data quality issues. The 95 and 75 percentiles of rainfall magnitude have also increased (Figures 3.2b, and 3.2c). The frequency of normal rainfall events (Figure 3.1c), and that of 99 percentile of rainfall magnitude (Figure 3.2a) also show an increasing trend over north-western part of India and

Odisha; this increasing trend in normal rainfall events and that in 99 percentile of rainfall magnitude is statistically significant at 95% confidence level only in Gujarat and in a region around Mumbai. Earlier, Dave and James, (2017) also suggested an increasing trend in EREs over Gujarat regions through an analysis of the IMD rainfall datasets from 1971 to 2005. We observed mixed trends in the respective frequencies of heavy and extreme rainfall categories over the southern states of Andhra Pradesh and Telangana during summer monsoon. However, the frequency of rainy days and normal rainfall events show significantly increasing trend over some places in southern India.

Except for a few places, we see decreasing trends in seasonal rainfall to the west of Western Ghats, with an opposite signal to their east. The potential role of the Western Ghats in this context needs further investigation, but beyond the scope of the current thesis.

Figure 3.1a show a significant decreasing trend in seasonal mean rainfall at 95% confidence level over central northeast and north-eastern parts of India. This mean decrease in seasonal rainfall is apparently due to significantly decreasing trends in the frequencies of rainy days (Figure 3.1b), percentile of rainfall magnitudes (Figures 3.2a-c), and all categories of rainfall events (Figures 3.1c-f). The normal rainfall events show a significantly decreasing trend over central India. However, the trends in corresponding in the moderate, heavy, extreme categories of rainfall events and various percentiles of rainfall magnitudes, and even the rainy days show mixed responses. This was also noticed earlier by Ghosh et al., (2009). Recalling that Roxy et al., (2017) reported that the EREs with rainfall > 150 mm/day show increasing trend over central India, the difference of our conclusion with Roxy et al. (2017) may be due to the fact that Roxy et al. (2017) carries out the analysis for a longer period, i.e., from 1950 to 2015.

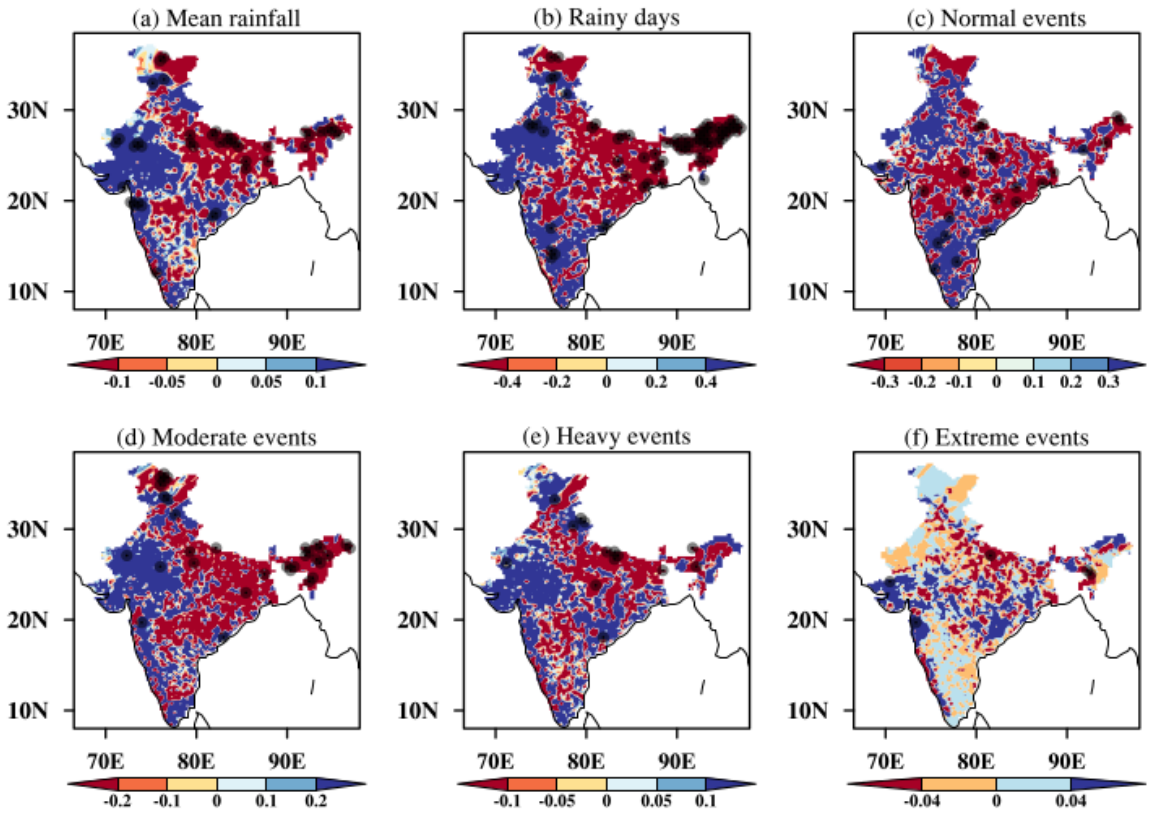

Figure 3.1: Spatial distribution linear trends in seasonal (a) mean rainfall, (b) rainy days, (c) normal (c) moderate, (d) heavy, and (e) extreme rainfall events over the India during the ISM from 1980 to 2019, using the IMD daily gridded rainfall at 0.25°×0.25° resolution dataset. The blue and red color shades show positive and negative trends, the black dots (.) indicate 95% confidence level.

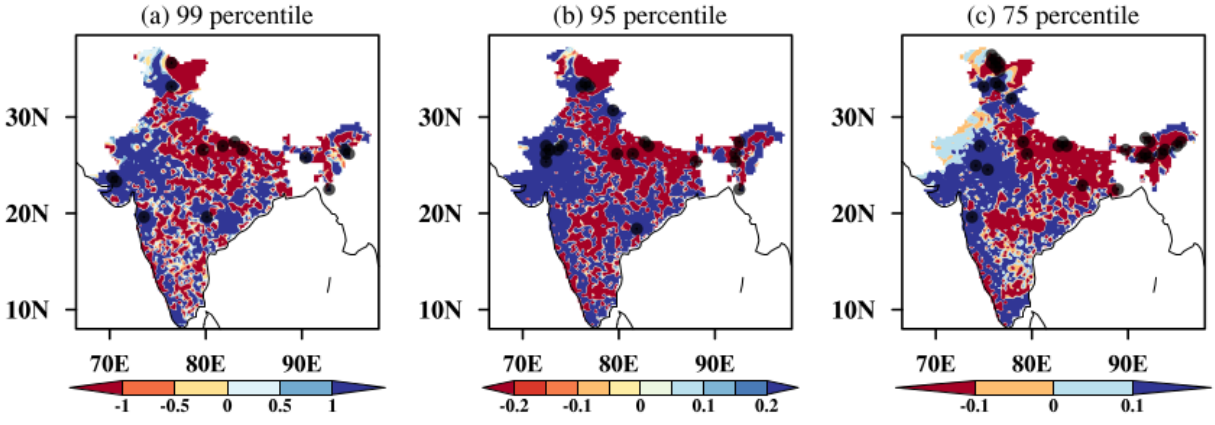

Figure 3.2: Same as Figure 3.1 but it is for (a) 99, (b) 95, and (c) 75 percentiles of rainfall magnitude.

We qualitatively obtain similar results when we generate difference in various statistics between Pre-2000 (1980 - 1999) and Post-1999 (2000 - 2019) periods. To this end, we subtracted the Pre-2000 mean values from the mean of Post-1999 values ($Mean_{Post\text{-}1999} - Mean_{Pre\text{-}2000}$) for each statistic. We observe that the seasonal mean rainfall, rainy days, normal,

moderate, and heavy rainfall events have increased by ~10% - 30% over north-western, Jammu and Kashmir, eastern parts of the Western Ghats and some places in southern Indian regions in the Post-1999 years (Figures 3.3a-e). Similarly, the 99, 95, and 75 percentile of rainfall magnitudes (Figures 3.4a-c) have also increased by ~10% - 30% over same and Odisha regions. Interestingly, the EREs have increased by ~40% over north-western state of Gujarat, north-eastern of Maharashtra, some places in central India, and Odisha regions of India in the Post-1999 years (Figures 3.3f). Given that the trends in the central India do not see any significant trends over the 40 years (Figures 3.1 and 3.2), this EREs increase in central India must be only due to such a signal in the recent few years.

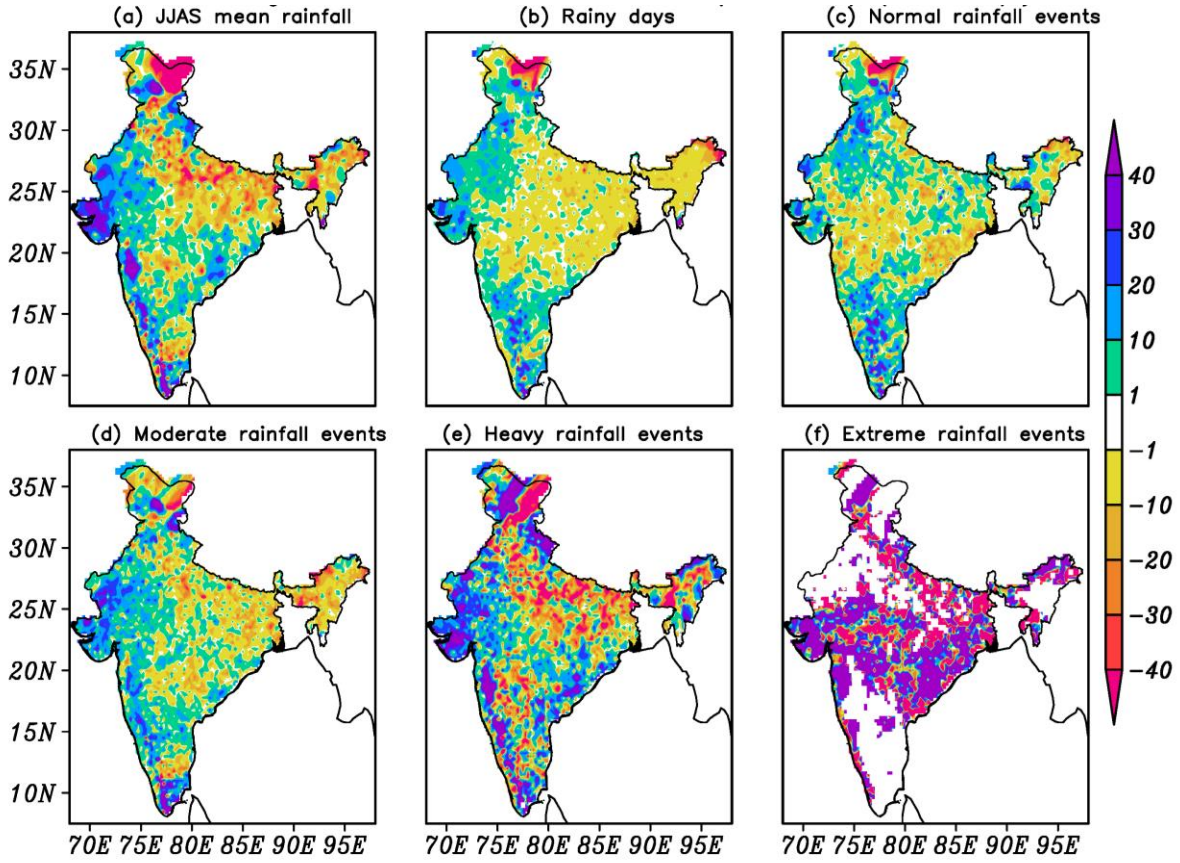

Figure 3.3: Difference in percentage in seasonal (a) mean rainfall, (b) rainy days, (c) normal (c) moderate, (d) heavy, and (e) extreme rainfall events between the Post-1999 and Pre-2000 years. We subtracted the mean of 2000-2019 period from the mean of 1980-1999 period [Mean $_{(Post\text{-}1999)}$-Mean $_{(Pre\text{-}2000)}$] for this purpose.

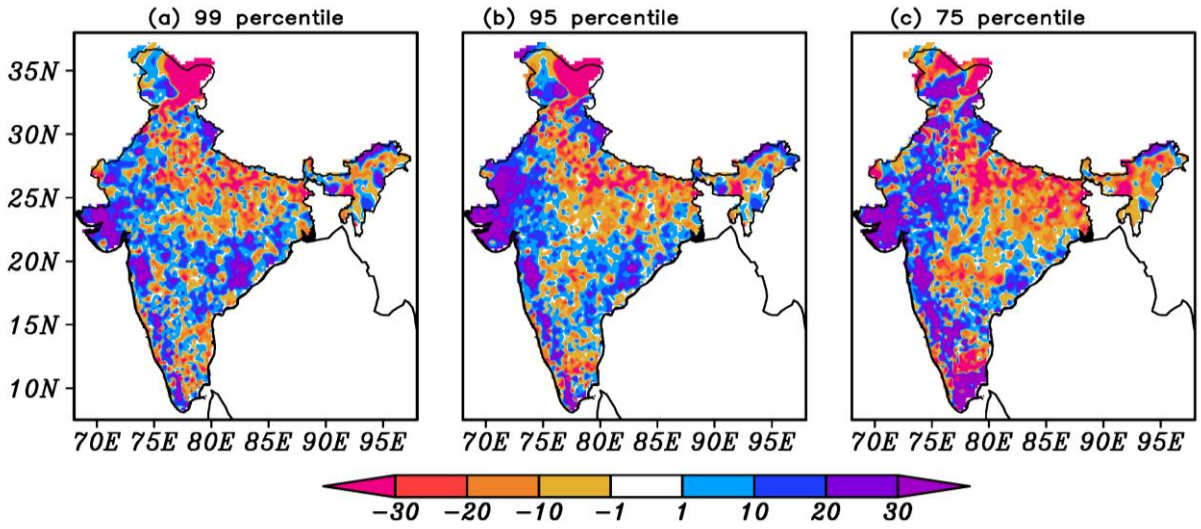

Figure 3.4: Same as Figure 3.3 but it is for seasonal (a) 99, (b) 95, and (c) 75 percentiles of rainfall magnitude.

3.3 Trend analysis for various tropical ocean climate drivers

Figure 3.5 shows the time series of the IODMI, NINO3 index, EMI, and AZMI over the period 1980 - 2019 (Figure 2.6). Among the four SST indices, the IODMI and AZMI (Figures 3.5a and b) are showing significantly increasing trends at 99% and 94% confidence level respectively, in agreement with Ajayamohan and Rao, 2008. We noticed that the trends change phase around the year 2000. The NINO3 index and EMI do not show any significant trends (Figure 3.5c and d).

From the section 3.2 and 3.3, we demonstrated that the seasonal mean rainfall has increased by 10% - 30% mainly over north- western states of India in the Post-1999 period compared to Pre-2000 period, and in fact, so have the frequency all categories of rainfall events and the 99, 95, and 75 percentiles of rainfall magnitudes. We have also shown that EREs have increased by ~40% over north-western state of Gujarat, central, and Odisha regions of India. While this appears to be associated with a potential climate change due to increased anthropogenic activity or a is just a natural decadal variability signal, it is possible that such a change is manifested through changes in the frequency and/or magnitudes of the tropical ocean drivers such as the positive IOD, which increase the ISM rainfall (e.g., Ashok et al., 2001, 2004; Krishnaswamy et al., 2014). Indeed, the positive IOD, and positive AZM events have

significantly strengthened since the year 2000 (Figure 3.5a and b). Interestingly, the average of 19 global coupled models showed an upward trend in the IOD index over the 1950 - 1999 period (Cai et al., 2009). Ma rathe et al. (2021) through an analysis of the future projections of frequencies of the tropical Indo-pacific drivers suggest that the IOD events may strengthen due to increased global warming. In contrast, no significant trend is seen in the NINO3 index and EMI (Figure 3.5). Motivated by these factors, we have investigated the changes in the ISM rainfall, from the Pre-2000 to Post-1999 periods, during concurrent IOD events, and those with other co-occurring drivers. The results are shown in the next section.

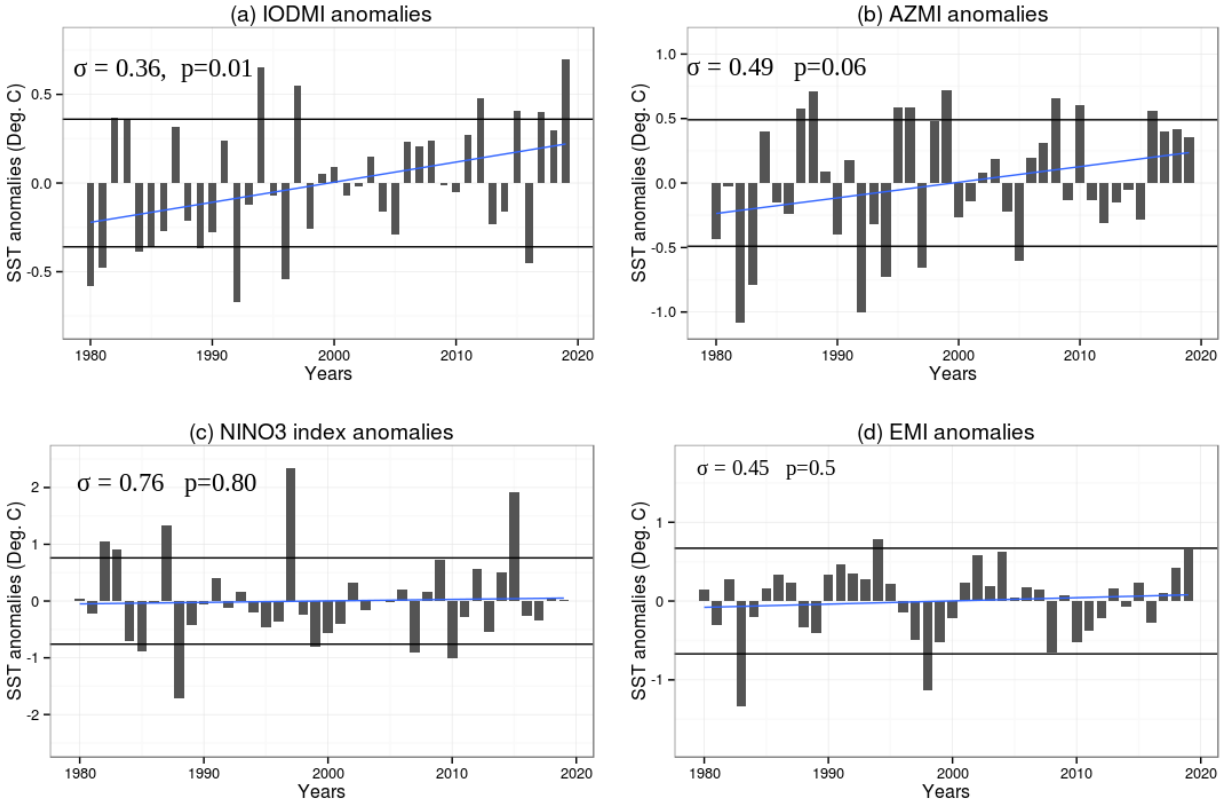

Figure 3.5: Time-series of area-averaged seasonal SSTA over (a) IOD, (b) AZM, (c) NINO3, and (d) EM index for the period of 1980-2019 using the HadISST at 1°×1° resolution dataset. The blue and black color lines show the linear trend line and standard deviation. The sigma (σ) and p-value indicate the standard deviation and trend values for the respected region.

3.4 Potential association of extreme rainfall events over India with various tropical ocean climate drivers

3.4.1 Composite analysis

A composite analysis of the JJAS rainfall anomalies throughout the Indian region during co-

occurring strong positive IOD events prior to the year 2000, and that for the negative IOD events Post-1999 were carried out (Figures not shown). The composite summer monsoon rainfall distribution for the Pre-2000 was subtracted from the composite of Post-1999 period. The difference gives us the summer monsoon rainfall changes associated with the changes in the positive intensity and spatial distribution from the Pre-2000 period to Post-1999 period. Similar analysis has also been carried out to evaluate the summer monsoon rainfall changes during Pre-2000 and Post-1999 concurrent with El Niño, El Niño Modokis, and positive AZM events. In this context, it is to be noted that any of these positive-phased events is catalogued as a 'strong event' whenever the magnitude of the representative index equals or exceeds its one standard deviation, obtained for the 1980 - 2019 period (see table 3.1 for the details). For example, the standard deviation of the JJAS IODMI for the 1980 - 2019 period is 0.36°C. Therefore, we catalogue all IODMI events with a magnitude of ≥ 0.36°C SSTA values as strong positive IOD.

Table 3.1: Strong summers associated with tropical ocean climate drivers positive SSTA years of all for the 1980-2019 years.

Period	Positive IOD years	Positive AZM years	El Niño Modoki years	El Niño years
Pre-2000	1982, 1983, 1994, 1997	1987, 1988, 1995, 1996, 1999	1991, 1994	1982, 1983, 1987, 1997
Post-1999	2012, 2015, 2017, 2019	2008, 2010, 2016	2002, 2004, 2019	2015

Figure 3.6a shows the differences of Post-1999 period composite of ISMR anomalies associated with concurrent strong positive IODs relative to those during the Pre-2000 period. For comparison, similar differences associated with the other positively phased events, i.e., the El Niño, El Niño Modoki, and AZM years are shown in Figures 3.6a-d. The aforementioned recent increase in summer monsoon rainfall anomalies over north-western and western part of central India is significantly, associated mainly with concurrent positive IOD years (Figure 3.6a). Seasonally too, positive summer monsoon rainfall anomaly in these regions is seen during only positive IOD events, but not with other positive-phased climate drivers from the

tropical oceans (Ashok et al., 2004; Ashok and Saji 2007). The increasing concurrent rainfall during positive IODs in recent period also conforms to the indication from Figure 3.5a that positive IOD events have strengthened Post-1999. While a similar increase in concurrent rainfall signal is also seen in these regions during co-occurring El Niños, El Niño Modoki events, and positive AZM events, the signal is not statistically significant (Figures 3.6d, c, and b). During the Post-1999 period, significant strengthening of negative rainfall anomalies is noticed over north-western India during concurrent El Niño Modokis with an opposite signal north-eastern region of India (Figure 3.6c).

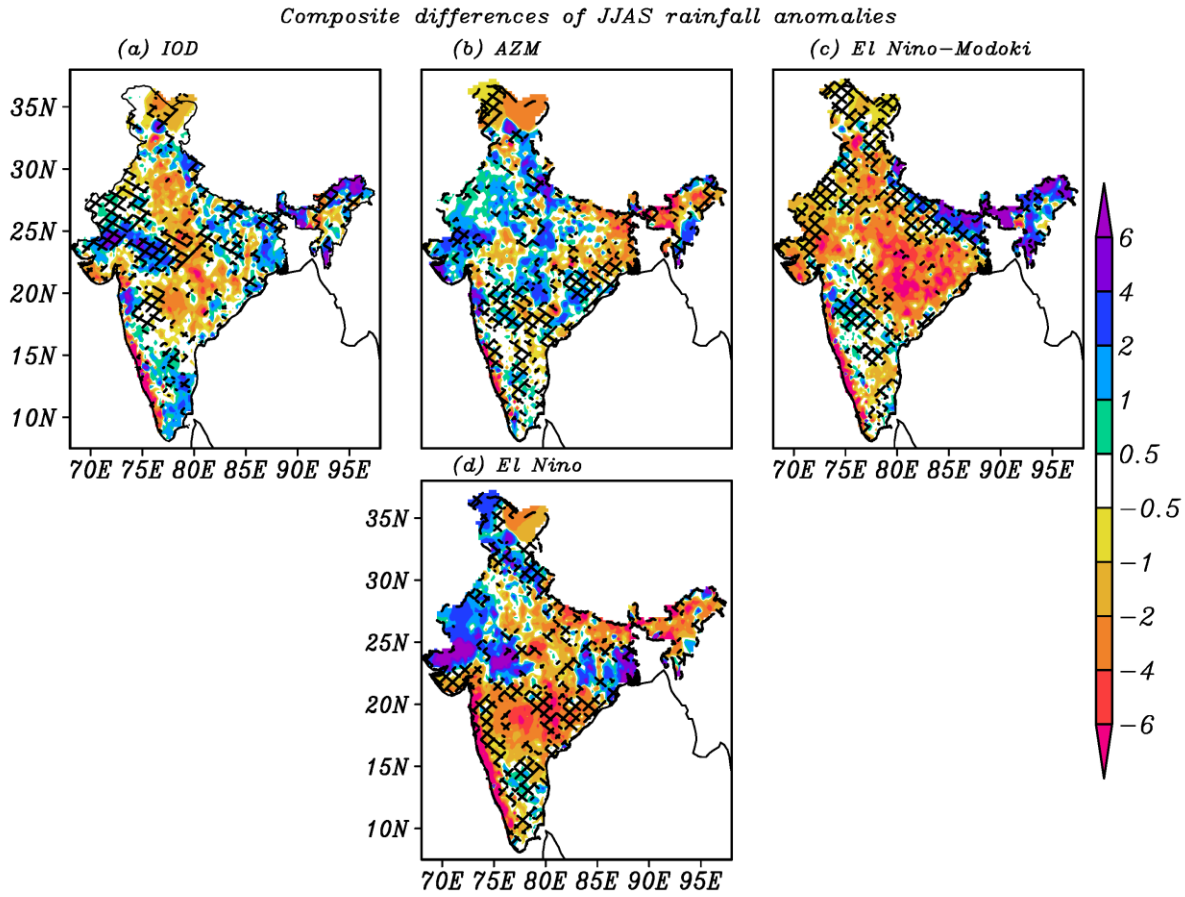

Figure 3.6: The ISMR anomalies differences between the composite of Pre-2000 and Post-1999 period of strong positive (a) IOD, (b) positive AZM, (c) El Niño Modoki, and (d) El Niño years. Hatched areas are significant at 95%confidence level from a one-tailed Student's t-test.

It is also noteworthy that the EREs associated with positive IODs have significantly increased by ~40% over broad regions in north-western state of Gujarat, western central India, and Odisha regions during the Post-1999 period (Figure 3.7a). While the co-occurring EREs also

increased during Post-1999 during strong El Niño, El Niño Modoki, and positive AZM years (Figure 3.7b-d), it was only at a few sporadic points.

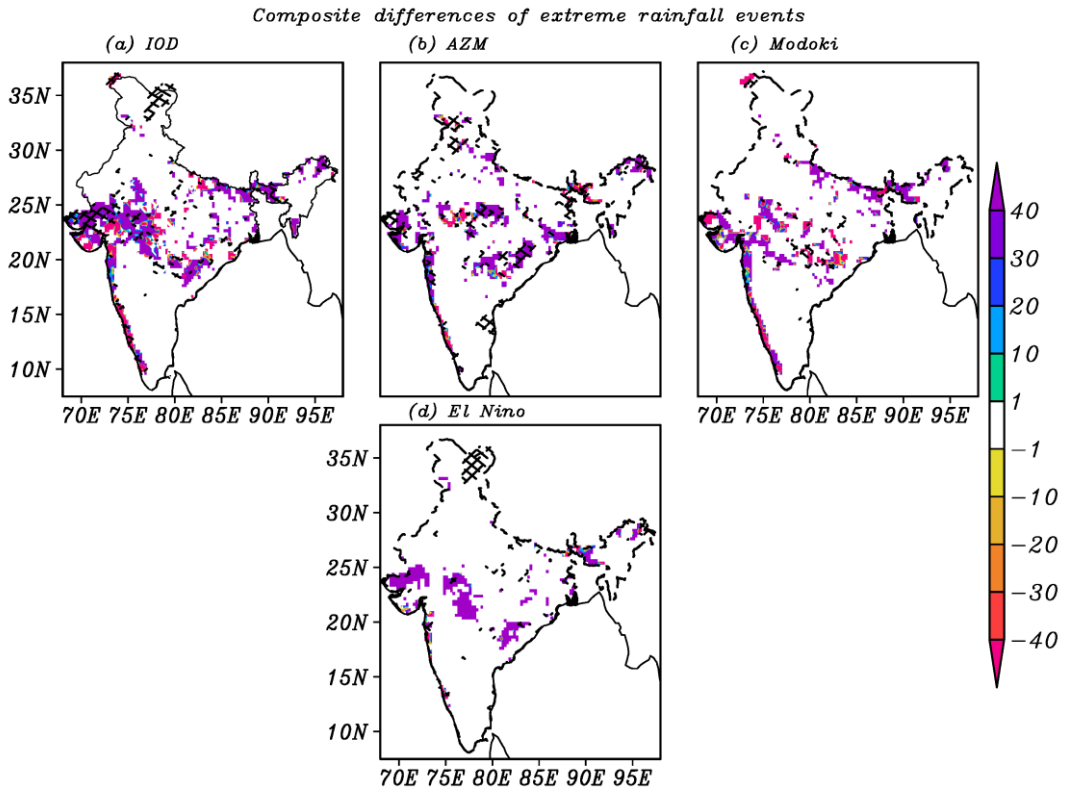

Figure 3.7: Same as Figure 3.6 but it represents the extreme rainfall events.

A similar conclusion about the prominence of the IODs can also be drawn in case of the changes in the heavy rainfall class of events as well as the 99 and 95 percentiles rainfall magnitude (Figures 3.8, 3.9, and 3.10). Such an increases in these features co-occurring with other tropical ocean climate drivers is only sporadic. Also, we noticed that the heavy rainfall events, 99, and 95 percentile of rainfall magnitude significantly increased over Odisha regions in the Post-1999 strong positive AZM years.

The above results also conform to the finding that the number of rainy days, moderate and normal rainfall events, and 75 percentile rainfall magnitudes significantly decreased during the co-occurring strong positive IOD years over north-western regions of India (Figures not shown). On the other hand, these statistics show an insignificant increase over north-western regions of India during the co-occurring strong El Niño and strong positive AZM years.

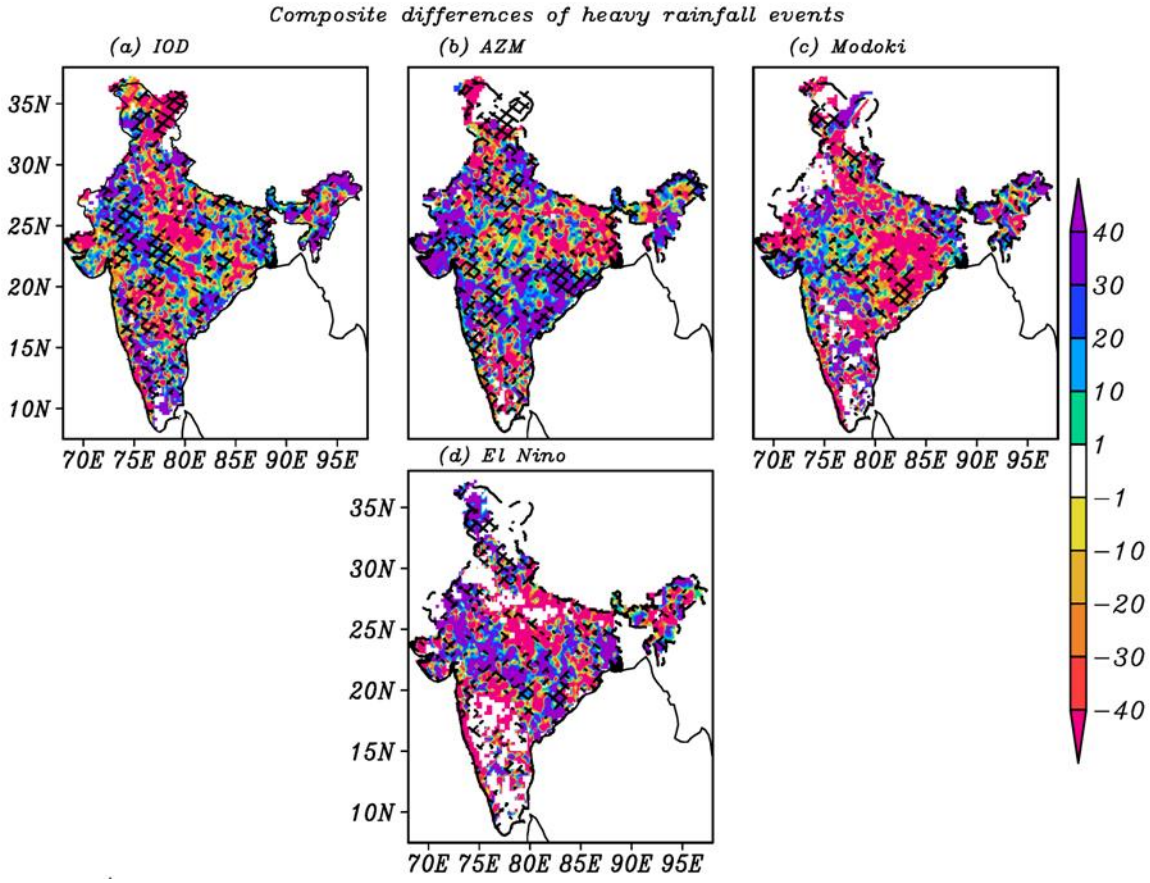

Figure 3.8: Same as Figure 3.6 but it represents the heavy rainfall events.

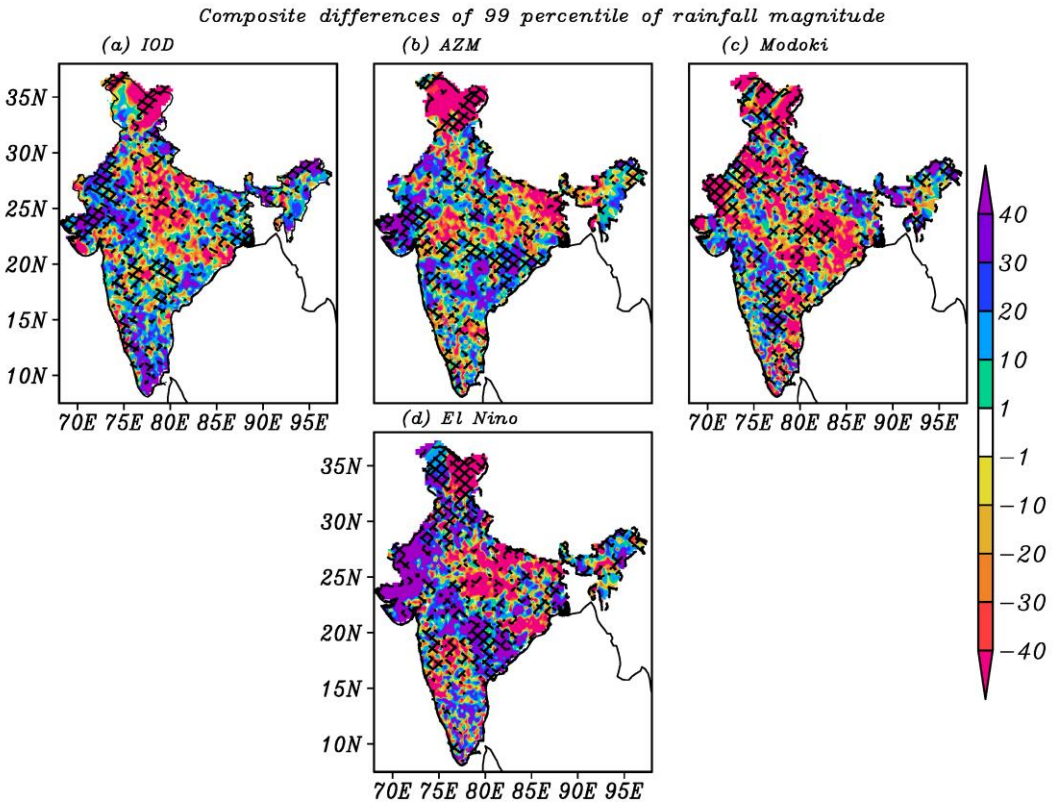

Figure 3.9: Same as Figure 3.6 but it represents the 99 percentile of rainfall magnitude (mm).

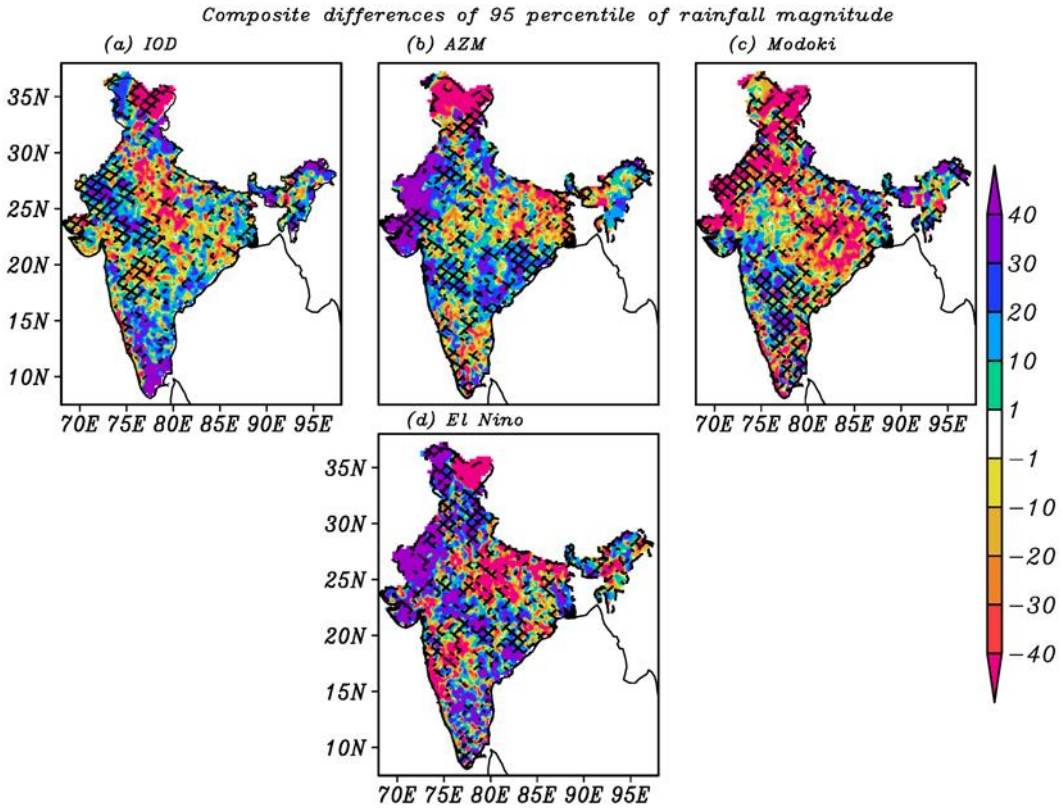

Figure 3.10: Same as Figure 3.6 but it represents the 95 percentile of rainfall magnitude.

Besides, we find that the moderate rainfall events, 75 percentile rainfall magnitude, and rainy days have increased significantly over few regions such as Telangana in southern India during strong El Niño Modokis in the Post-1999 period. Such signals associated with the positive IOD years, but statistical significance only during El Niño Modoki years. On the whole, no strong conclusions can be drawn on the association of changing rainfall statistics in southern India with co-occurring ocean drivers.

3.4.2 Partial correlations analysis

In addition, we performed a partial correlation analysis for the period 1980 - 1999 (Pre-2000) and 2000 -2019 (Post-1999) to ascertain our conclusions from the composite analysis (section 3.4.1) on the relationships between tropical ocean climate drivers and various rainfall categories and magnitudes across India. Briefly, the results from our partial correlation analysis broadly support the conclusions from our composite analysis, as shown in the next few paragraphs.

The summer rainfall in north western India, west central India and southeast regions of

India was weakly but positively correlated with the IODMI Pre-2000 (Figure 3.11a). Importantly, the positive correlation has become significant at 90% confidence level during Post-1999 period (Figure 3.11a). The summer monsoon rainfall anomalies in the north-western, west central India and southeast regions of India have been negatively and significantly correlated with NINO3 index as well as with the EMI during Pre-2000 and Post-1999 periods (Figures 3.11c and d). The AZMI had a weak negative association with the summer monsoon rainfall in these regions prior to 2000, but now significantly and positively associated (Figure 3.11b). The ISM rainfall anomalies over north-eastern regions were positively influenced by EMI in the Post-1999 period. This result supports our previous composite analysis (Figure 3.5).

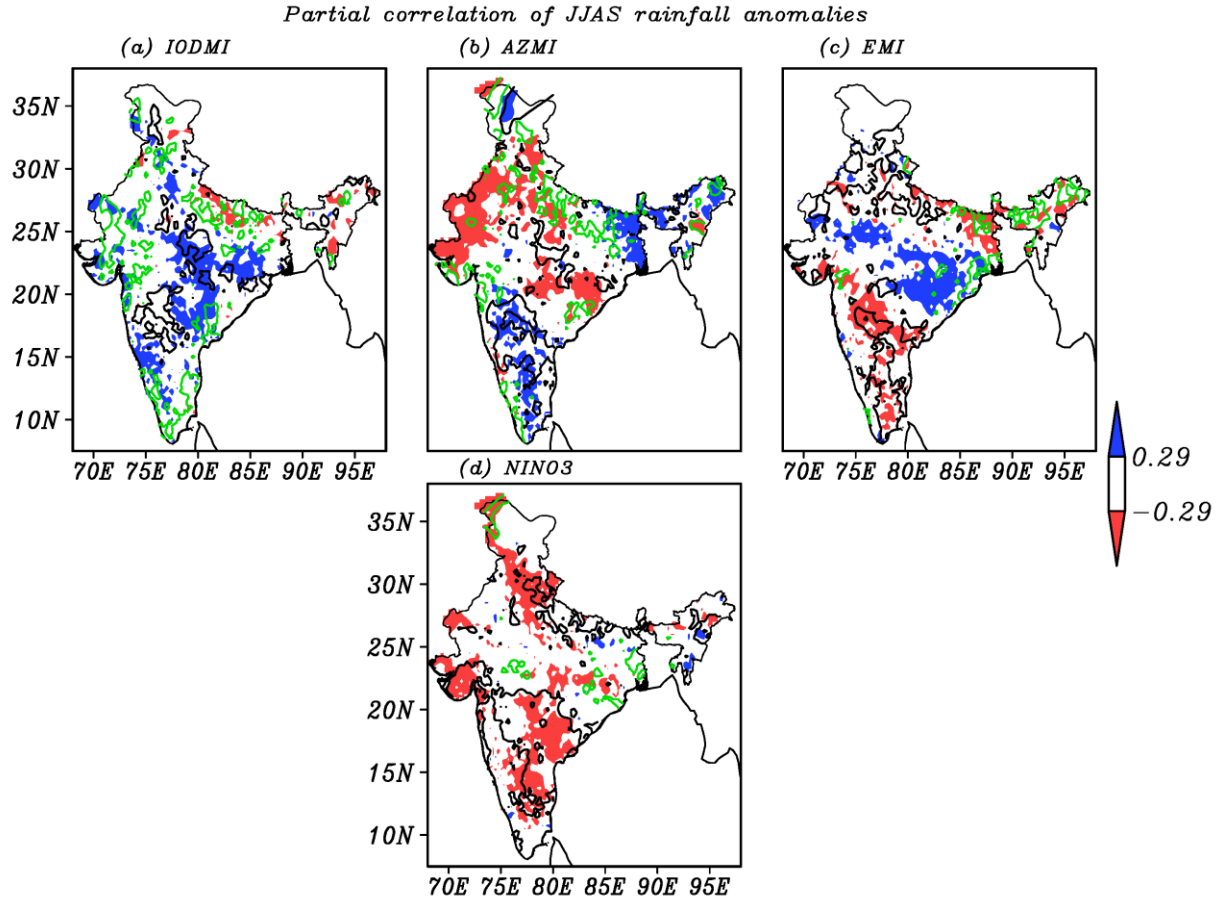

Figure 3.11: Partial correlation of (a) IODMI, (b) AZMI, (c) EMI, (d) NINO3 index with JJAS rainfall anomalies during Pre-2000 and Post-1999 years. The blue (positive) and red (negative) shaded area represents the partial correlation during the Pre-2000 years. The green (positive) and black (negative) contours represent the partial correlation during the Post-1999 years. All positive and negative values (shaded and contours) indicate at 90% of confidence level from one-tailed Student's t test.

Figure 3.12 shows that during the Post-1999 period, the frequency of EREs over the north-western state of Gujarat, west central India, and Odisha regions are positively correlated with the IODMI at 90% confidence level (Figure 3.12a). But, the NINO3 index, EMI, and AZMI are not showing positive relationship. Likewise, during the Post-1999 period, heavy rainfall events, 99, and 95 percentiles rainfall magnitude in the north-western, Odisha, and southern regions, mainly the east and west coasts of India, were significantly correlated with the IODMI. The NINO3 index, EMI, and AZMI were negatively correlated, except for the 99 percentile of rainfall magnitude in some regions of north-western India. Moreover, we noted that the frequency of extreme, heavy rainfall events, 99, and 95 percentiles of rainfall magnitude in some regions in central India has a positive relationship with NINO3 index, EMI, and AZMI in the recent periods (Figure 3.12d- c, 3.13d-c, 3.14d-c, and 3.15d-c). With the exception of IODMI, the moderate, normal rainfall events and 75 percentile rainfall magnitude in some places in southern Indian have negatively correlated the NINO3 index, EMI, and AZMI (Figures not shown).

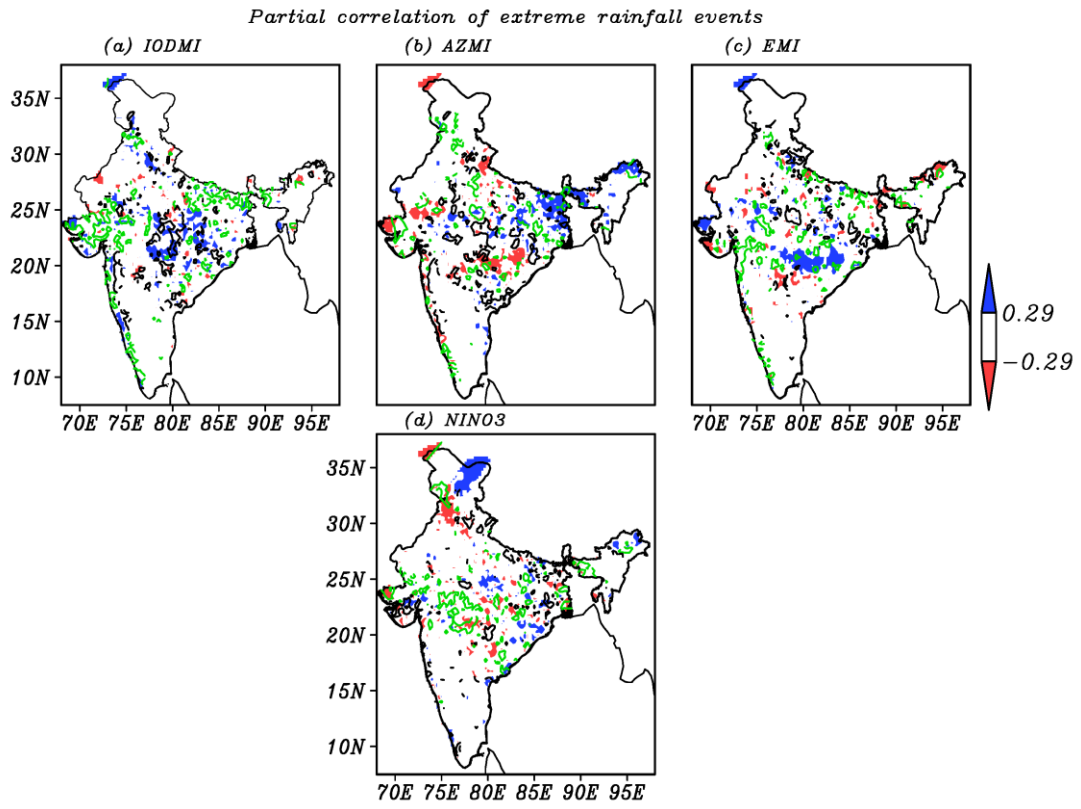

Figure 3.12: Same as Figure 3.11, but it represents the extreme rainfall events.

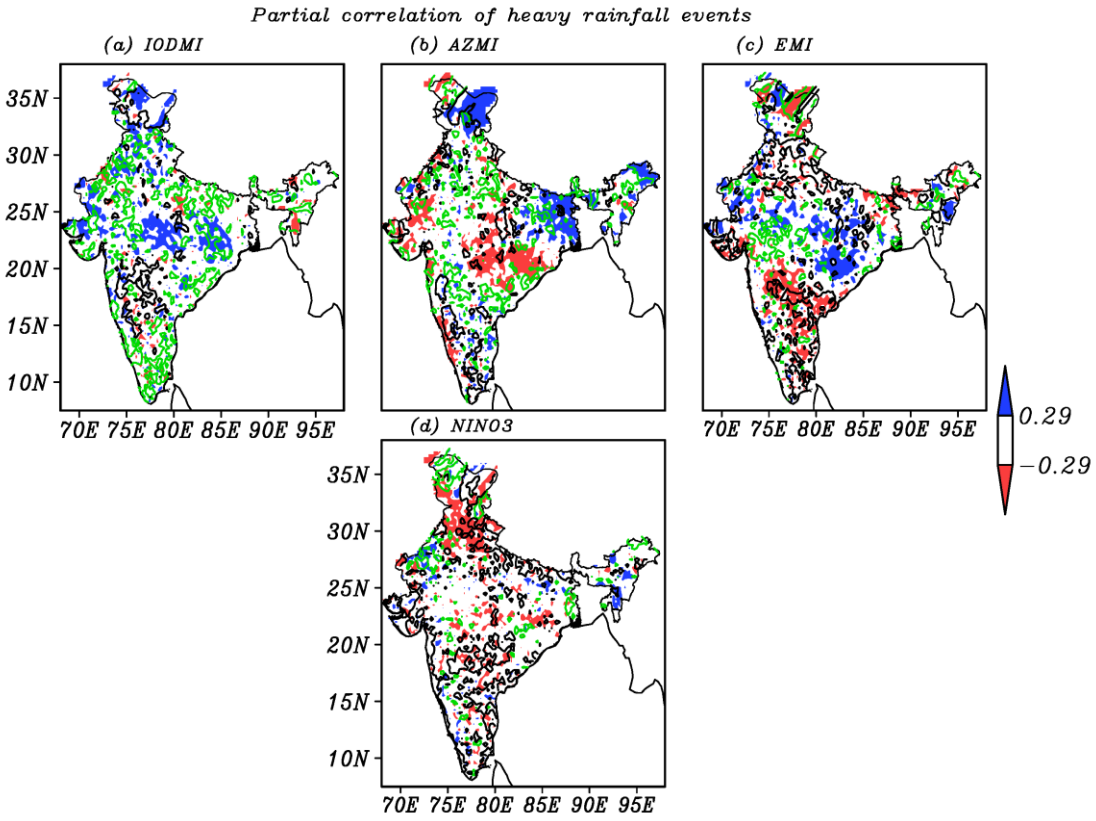

Figure 3.13: Same as Figure 3.11, but it represents the heavy rainfall events.

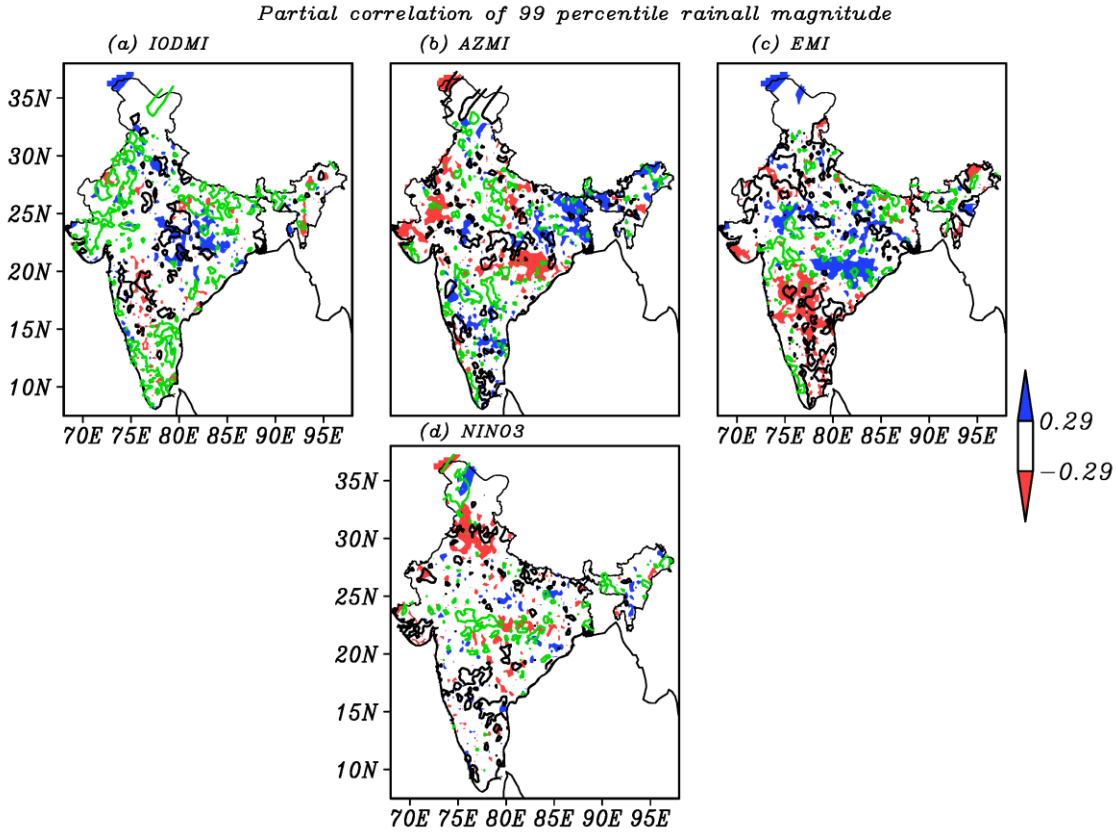

Figure 3.14: Same as Figure 3.11, but it represents the 99 percentile of rainfall magnitude.

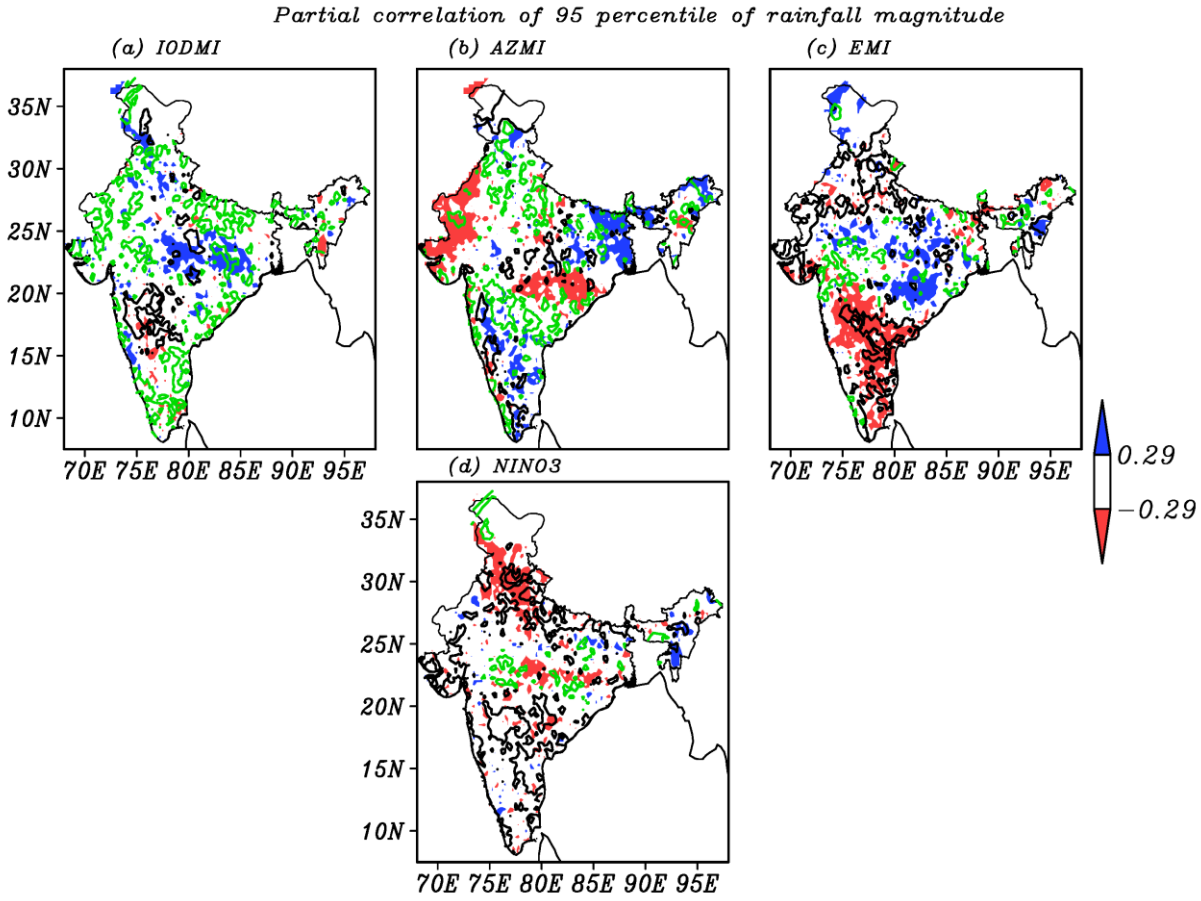

Figure 3.15: Same as Figure 3.11, but it represents the 95 percentile of rainfall magnitude.

3.5 Possible mechanism for increasing extreme, heavy rainfall events and 99, 95 percentiles of rainfall magnitudes due to positive IODs

Figures 3.16a, 3.16b and 3.16d indicate the differences in the untrended and detrended SSTA during the strong positive IOD years between the Post-1999 and Pre-2000 and those in the concurrent wind anomalies. Figure 3.16c shows the JJAS mean SST differences between the Post-1999 and Pre-2000 periods. The mean SST increased up to 1°C mainly over western part of Indian Ocean (45°E - 70°E, 5°S - 10°N) and north western part of Arabian Sea (50°E - 65°E, 15°N - 25°N), but decreased (~0.5°C) over the west and east coasts of India during the Post-1999 period compared to Pre-2000 period (Figure 3.16c). Interestingly, we see that the SSTA in the western box region of the positive IOD have strengthened during the Post-1999 relative to the earlier period (Figure 3.16a). This increase is mainly due to the background warming (Figure 3.16b). This is easily ascertained from Figure 3.18b, which shows the detrended SSTA during positive IOD events post-1999. Importantly, Cai et al. (2014) show, using analysis of

several coupled model outputs, that he increasing SST over the north Indian Ocean during the positive IODs potentially increases the moisture content over that regions. Also, we observed that the wind magnitude at 850 hPa anomalously increased (0.5 - 1.5 m/s) over western part of equatorial Indian Ocean, northern Arabian Sea, southern and western part of Indian subcontinent during Post-1999 strong positive IOD years (Figure 3.16d). The strengthening of these westerlies transports the more moisture from the Arabian Sea towards the Indian subcontinent resulted in more precipitation (Roxy et al., 2017). Indeed, all these mechanisms apparently work in brining increased anomalous moisture convergence into Indian region, particularly the northwest and central India, during Post-1999 strong positive IODs.

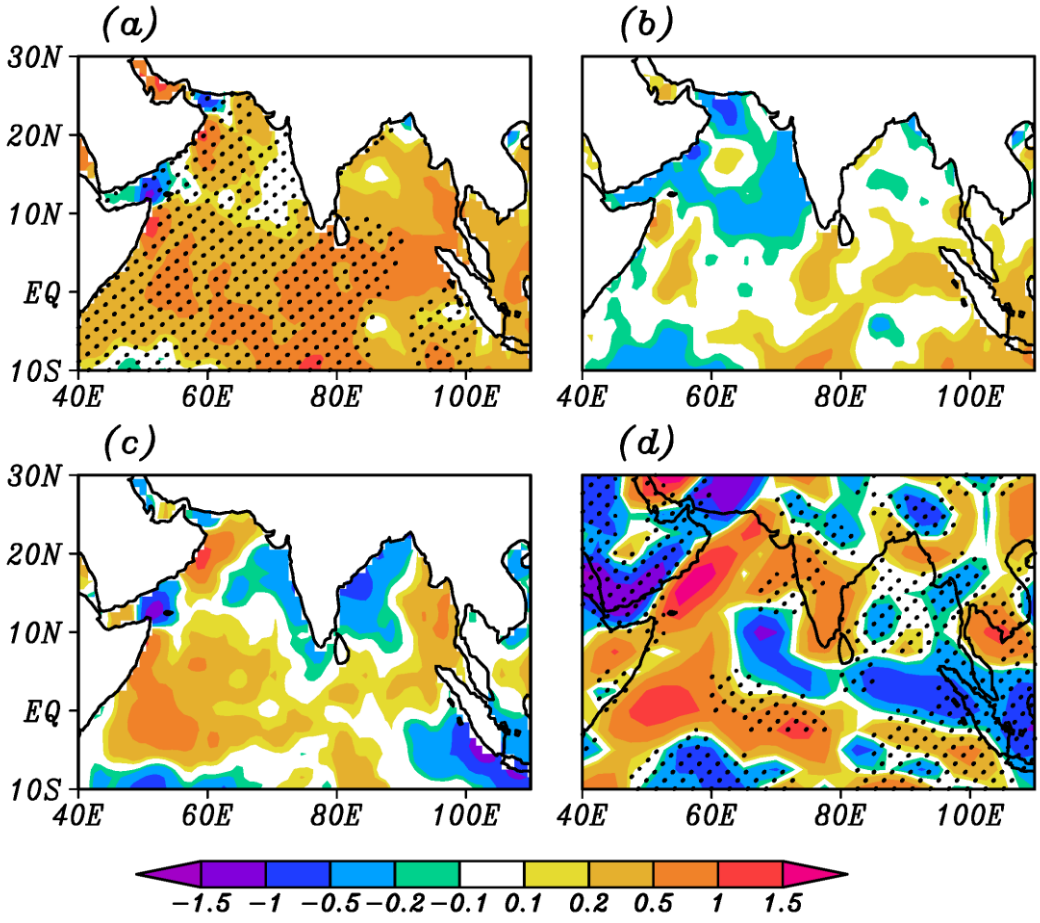

Figure 3.16: Spatial distribution of (a) untrended SSTA, (b) detrended SSTA, and (d) at 850 hPa wind magnitude (m/s) differences between the Post-1999 and Pre-2000 periods in the strong positive IOD years. (c) mean of Post-1999 and Pre-2000 SST differences, regardless of any ocean climate drivers. The black dots represent at 95% confidence level from one-tailed Student's t-test.

To understand how the strong positive IOD events influencing high intensity rainfall events and magnitudes in the Post-1999 period, we carried out at 850 hPa velocity potential (m^2/s) composite differences between the Pre-2000 and Post-1999 periods in the strong positive IODs (Figure 3.17). In the Figure 3.17, significantly more convergence can be seen over the western (10°S - 5°N, 45°E - 65°E) and equatorial Indian Ocean, western Arabian Sea, and over the head BoB. Also, the convergence increased over Pakistan and north-western parts of Indian regions in the Post-1999 period. The divergences weaken over the eastern Indian Ocean (Figure 3.17). It may be due to the increase SSTs over these regions in the Indian Ocean during the Post-1999 compared to Pre-2000 period (Figure 3.16a).

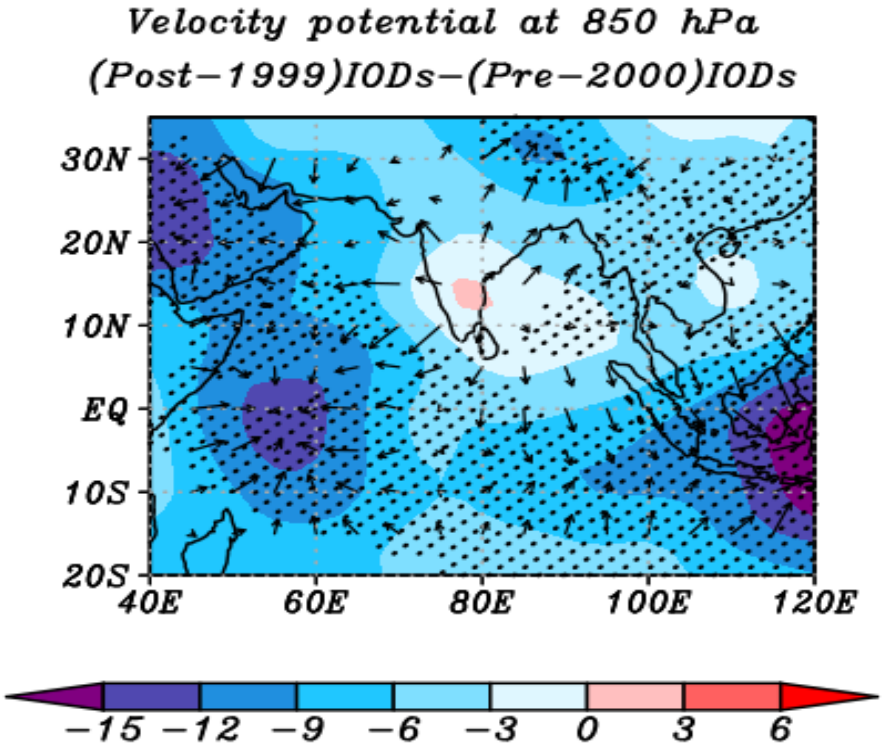

Figure 3.17: The 850 hPa velocity potential (m^2/s) anomalies differences between composite of Pre-2000 and Post-1999 strong positive IODs [Composite $_{(Post-1999)}$–Composite $_{(Pre-2000)}$]. Black dots indicate the 95% confidence level from the one-tailed Student's t-test.

3.6 Summary

In this chapter, we analysed trends in the frequency of various categories of rainfall events, magnitudes over India, using the IMD rainfall datasets over the 1980 - 2019 period. The trends in the magnitudes of the indices of the tropical oceanic drivers, namely ENSO, ENSO Modoki,

IOD, and AZM, were also examined using the HadISST datasets for the same period. We proposed a slightly modified classification of the IMD rainfall categories to identify the daily extreme and other categories of rainfall events over India. We explored the potential roles of tropical ocean climate drivers on the frequency of various categories of rainfall events magnitudes.

Our results show that. in the Post-1999 period, various seasonal rainfall related statistics, namely, the seasonal mean rainfall, number of rainy days, normal, moderate, heavy rainfall events and 99, 95, and 75 percentile of rainfall magnitudes have increased by ~10% - 30% mainly over north-western and Odisha regions of India. Interestingly, the EREs have increased by ~ 40% over north-western state of Gujarat, northeast of Maharashtra, some places in central India and Odisha in the Post-1999 period. In addition, the IOD and AZM SST indices have also significantly increased since the year 2000. In this context, we examined the influence of tropical ocean climate drivers on the ISM mean rainfall, number of rainy days and multiple categories of rainfall events and magnitudes during the Pre-2000 and Post-1999 periods. The composite analysis shows that the during the strong positive IOD (AZM) events the seasonal mean rainfall, frequency of extreme, heavy rainfall categories, 99, and 95 percentiles rainfall magnitude significantly increase over north-western and west central Indian regions (northern Andhra Parades and Odisha regions) in the Post-1999 period compared to Pre-2000 period. Besides, the partial correlation analysis indicate that compared to NINO3 index, EMI, and AZMI, the IODMI has significantly correlated with where the extreme, heavy rainfall events, 99, and 95 percentiles rainfall magnitude increased over India during the Post-1999 years compared to Pre-2000 years. Finally, our results show that, in the last two decades, the IOD events are significantly influencing the different rainfall events and magnitudes, especially the EREs over north-western state of Gujarat, west central and Odisha regions of India compared to the El Niño, El Niño Modoki, and positive AZM events. An increasing SST trend in the mainly in the equatorial western Indian Ocean (Alory et al., 2007; Rao et al., 2012; Roxy et al., 2014)

and consequent strengthening of low-level monsoonal westerlies over the Arabian Sea (Roxy et al., 2015) during the positive IODs may be a possible reason for increasing EREs and magnitudes over these regions.

In this chapter, I have examined the relative roles of tropical ocean climate drivers on the various rainfall categories and magnitudes, using various observational and reanalysed datasets, mainly for the 1980 to 2019 period. In addition, I have also described the features of the WRF models I have used. The specific sensitivity experiments, however, are discussed in relevant chapters where the results from the experiments are discussed.

Chapter - 4

Assess the relative contributions of extreme El Niño, and the recent warming of the Bay of Bengal SST to the intensity of EREs during the northeast monsoon: A regional modelling approach

---

In this chapter, I examined the impact of SST background changes in the BoB on the intensity of EREs. In this regard, as a case study, I have evaluated the relative contributions of the strong El Niño during 2015 and the warming trend in the Bay of Bengal SSTs to the intensity of ERE, which occurred over Chennai and adjoining regions on December 01, 2015, using the WRF model simulations.

4.1 Introduction

During the last day of November and early December 2015 south-eastern India, especially Chennai, the capital city of Tamil Nadu (see Figure 4.1 for the geographical location) and the adjoining regions experienced extreme rainfall activity, which led to devastating flood over Tamil Nadu. As per the regional meteorological centre, Chennai, of the IMD the rainfall recorded on December 01, 2015 over the state of Tamil Nadu was 35 mm against the daily normal daily seasonal mean rainfall of 4.5 mm. Importantly, the IMD also stated that Chennai city received 276 mm rainfall on that particular day alone against the seasonal normal rainfall of 361 mm over the Chennai. The extreme rainfall of 218.1 mm rainfall over the neighbouring union territory city of Pondicherry on December 01, 2015 suggests that the extreme rainfall on that day was widely distributed. Tamil Nadu received 570.4 mm of rainfall from October 01 to December 02, 2015, that is, in excess of 58% of the seasonal normal of 361 mm over the Tamil Nadu. The corresponding seasonal rainfall amounts received by Chennai and Pondicherry were 1487.3 mm and 1249.2 mm, which are 129% and 53% in excess of their respective seasonal normal rainfall values. Chakraborty (2016) carried out a synoptic and dynamical analysis relevant to this event. This work suggests that convective weather systems from the west Pacific Ocean propagated into the warm Indian Ocean. Due to the warm temperatures, these intensified, and then veered intensified further over the north towards the Tamil Nadu coast, steered by two mid-troposphere highs of that lay to the east and west of the Indian region. Chakraborty et al (2016) also suggest that the high to the east was typical of the El Niño year that the 2015 was. that the high to the west was suggested to be associated with a phase shift of an upper tropospheric global Rossby wave.

Interannual through decadal changes in the tropical oceans influences the northeast monsoon rainfall (NEMR) and the tropical cyclones (TCs) in the northeast monsoon season (NEM). In this context, while it is well-known that the NEM season of the year 2015, eastern BoB experienced strong above normal SSTA (Figure 4.3). Importantly, 2015 was one of the

strongest El Niño years, Hu and Fedorov, (2017; also see Figure 4.4c). A recent and relevant study by Van Oldenborgh et al. (2016) examines the relative importance of aerosols and tropical SSTs for the occurrence of extreme events such as the Chennai event by analysing observed and climate change projection datasets, coupled model simulations. They also carry out a suite of 13-month long multiple ensemble simulations with a 0.5°×0.5° resolution regional model covering the CORDEX South Asia domain; all the experiments start with perturbed initial conditions of December 01, 2014. They suggest that a small but clear increase in the probability of extremes in the SST-forced regional model, associated with El Niño and other SST anomalies, but statistically insignificant signal associated with ENSO.

However, there are no studies that explore the relative contributions of a strong El Niño, and the BoB warming trend, to the intensity of an ERE such as the Chennai event, and understand the background mechanisms. For example, it can be easily discerned that ENSO events influence the seasonal evolution of the concurrent NEM through anomalous changes in circulation. However, in determining the intensity of a tropical cyclone or an ERE occurring off the coast of the BoB, the ENSO-induced SST in the BoB (Alory et al., 2007) may also be critical in controlling the local convection anomalies as compared to the ENSO-induced circulation changes. In this chapter, we evaluate these gaps.

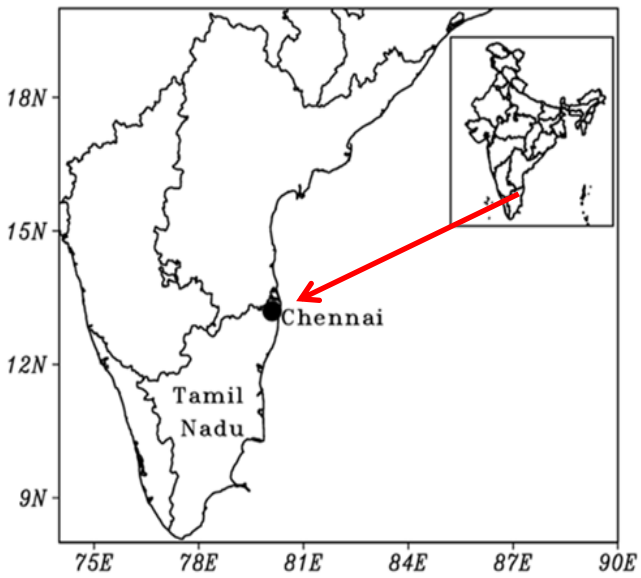

Figure 4.1: Represents the geographical location of Chennai (Tamil Nadu).

4.2 Relevance of the tropical Indo-Pacific SSTs on NEMR from observations

We carried out a correlation analysis to understand the relative importance of the potential teleconnections from the tropical Pacific and BoB SSTs. A trend analysis carried out on the time series of the BoB index indicates an increasing trend in the SST over the southern BoB (85°E - 95°E, 8°N - 15°N) since the 1980s, which is particularly prominent for the last two decades (Figure 4.2a). We also verify, using the OISST datasets that such a trend exists since 1980s (Figure 4.3). The result is in agreement with studies that show a recent warming of the TIO in the last few decades (Alory et al., 2007; Rao et al., 2012; IPCC report, 2013; Roxy et al., 2014). The result is also in general conformation with the findings of Balaguru et al. (2014), whose region of study falls into the region of our selection. Notably, the 2015 was a strongest El Niño year (see Figures 4.4c and 4.5; Hu and Fedorov, 2017), comparable to those seen in 1982 and 1997 (Figure. 4.4a and 4.4b) in terms of its strength (Figure 4.5). A study by Yadav (2012) claims that during the El Niño years in recent decades after 1978, the zonally elongated warm SSTs of the warm-pool region along the tropical Indo-Pacific Ocean is much warmer than the earlier decades. This resulted in intensified the deep convections over the Indian Ocean during recent El Niños. Consequently, north-westward propagating trailing Rossby-gyres formed in the western portion of the equatorial deep convection, and intensified as tropical storms and cyclones over NIO during the El Niño years in the recent decades.

Figure 4.6a shows temporal anomaly correlations between the NEMR with the BoB SSTA index for the 1901 - 2013 period for the NEM season. The result indicates that the NEMR over the Chennai region is positively correlated with BoB SSTA index for the period; the correlation is modest but statistically significant at 90% confidence level from a two-tailed Student's t-test. Our correlation analysis between NEMR and Niño3 index for the NEM during the period 1901-2013, however, indicates a statistically significant but modest positive correlation (Figure 4.6b).

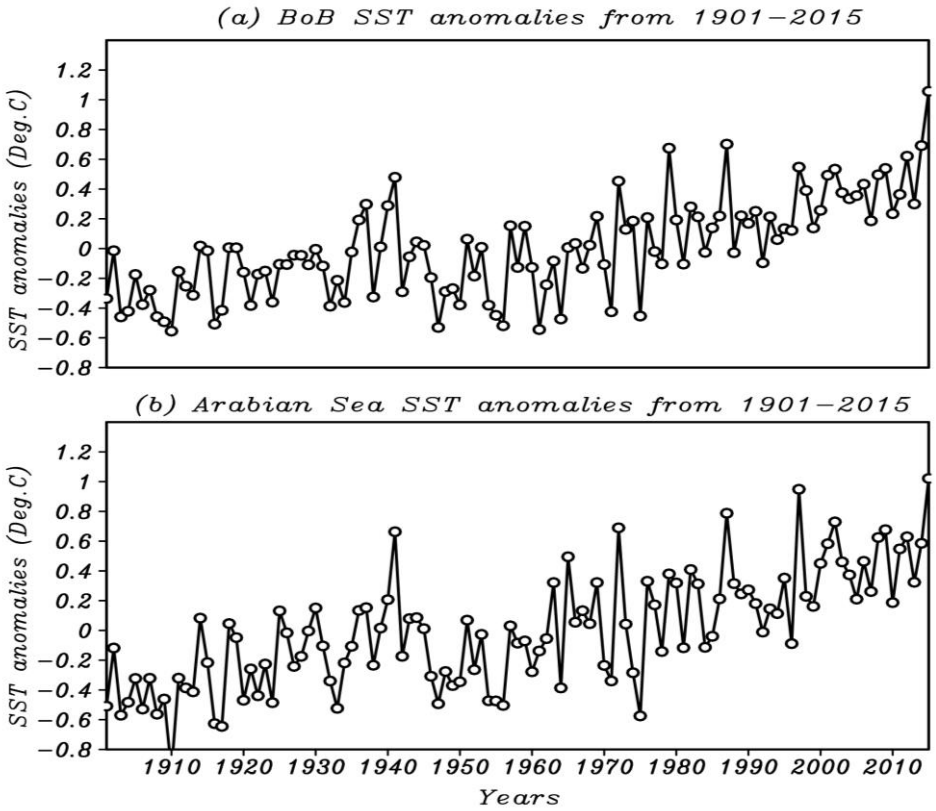

Figure 4.2: Time series of area-average SST anomalies over (a) eastern BoB (85°E to 95°E, 8°N to 15°N) and (b) over Arabian Sea (65°E to 75°E, 8°N to 15°N) form the HadISST dataset during OND season for the period of 1901-2015.

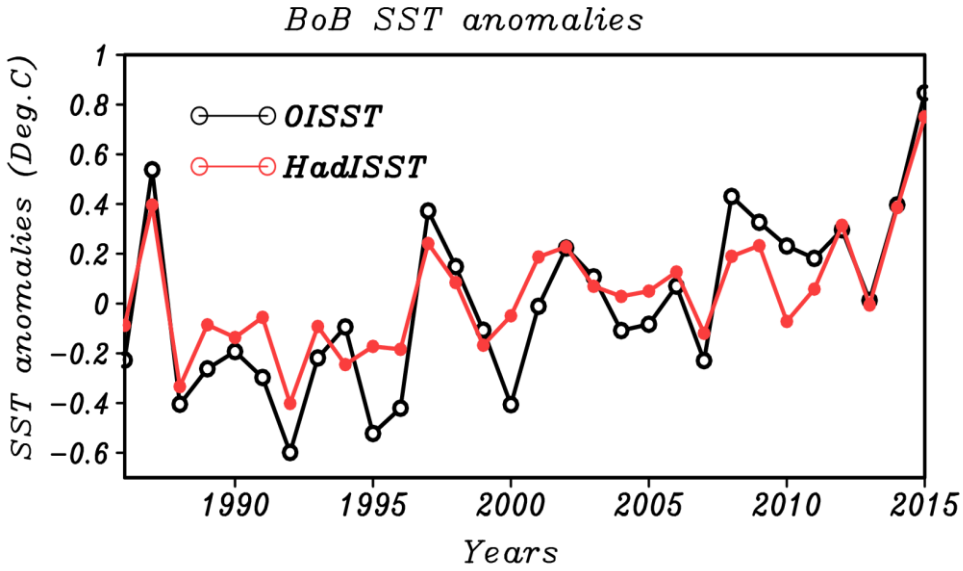

Figure 4.3: Time series of area-average of eastern BoB (85°E to 95°E, 8°N to 15°N) SST anomalies during the OND season form the OISST (black color line) and HadISST (red color line) datasets during the period from 1980-2015.

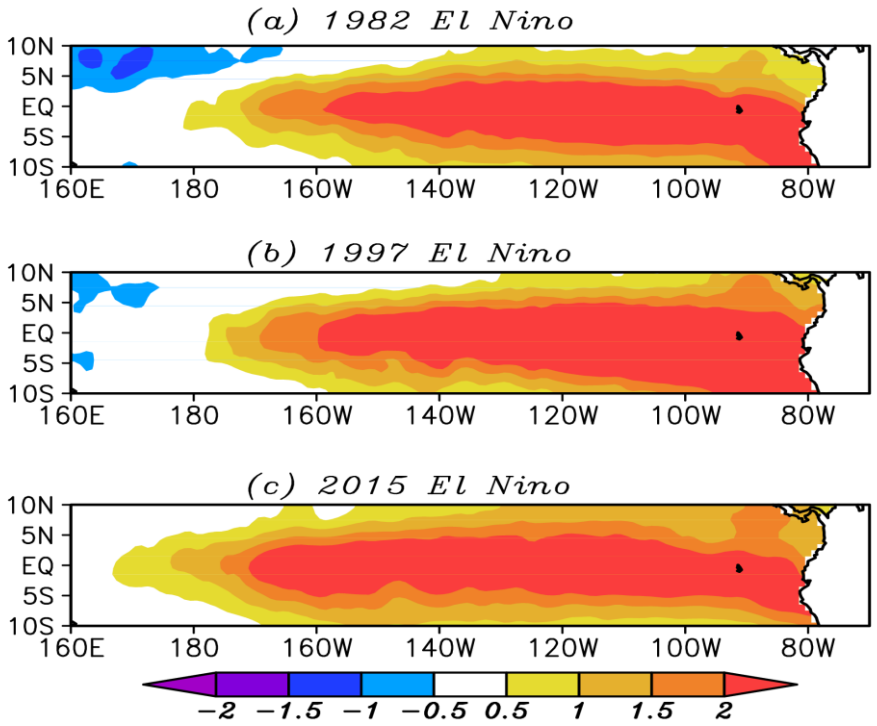

Figure 4.4: Spatial distribution of strong El Niño conditions in (a) 1982, (b) 1997, and (c) 2015 during the OND season using the HadISST dataset.

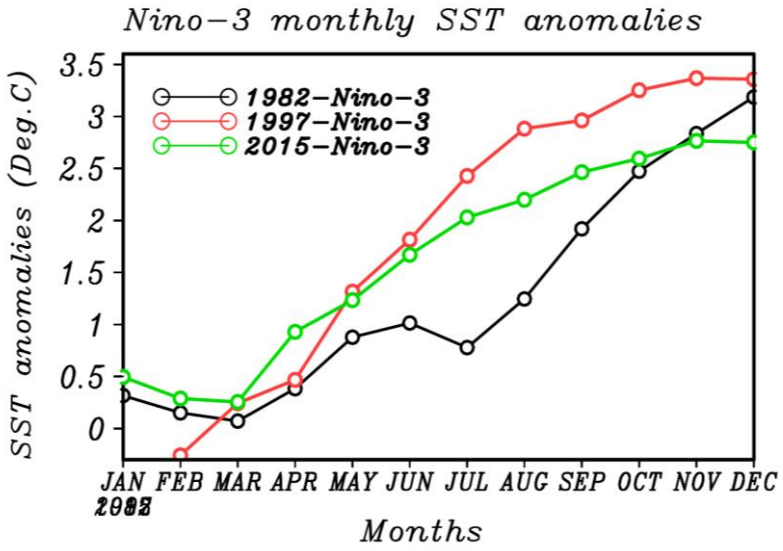

Figure 4.5: Time series area-average of Niño3 index monthly anomalies for the year 1982, 1997, and 2015.

The correlation of the NEMR with the eastern BoB is also positive. Its magnitude is similar to that of the correlation between the Niño3 index and NEMR. This, along with a strengthening warming trend in the BoB SST (Figure 4.3), motivates us to focus on the relevance of the concurrent BoB SST for the Chennai event in this study, and also make a conjecture about the

potential role of the SST trend in the BoB. Interestingly, we find that the Arabian Sea is also experiencing a warming trend (Figure 4.2b). But for all practical purposes, the BoB SSTs will be more relevant for formation and intensification of a synoptic event in the BoB. A warming trend in the Arabian Sea SST, of course may have implications for the background atmospheric circulation in the BoB as well. I focus on the importance of the BoB SST by carrying two sensitivity simulations of extreme rainfall over the Chennai during the period of November 29 to December 04, 2015 using the WRF model at 25 km resolution.

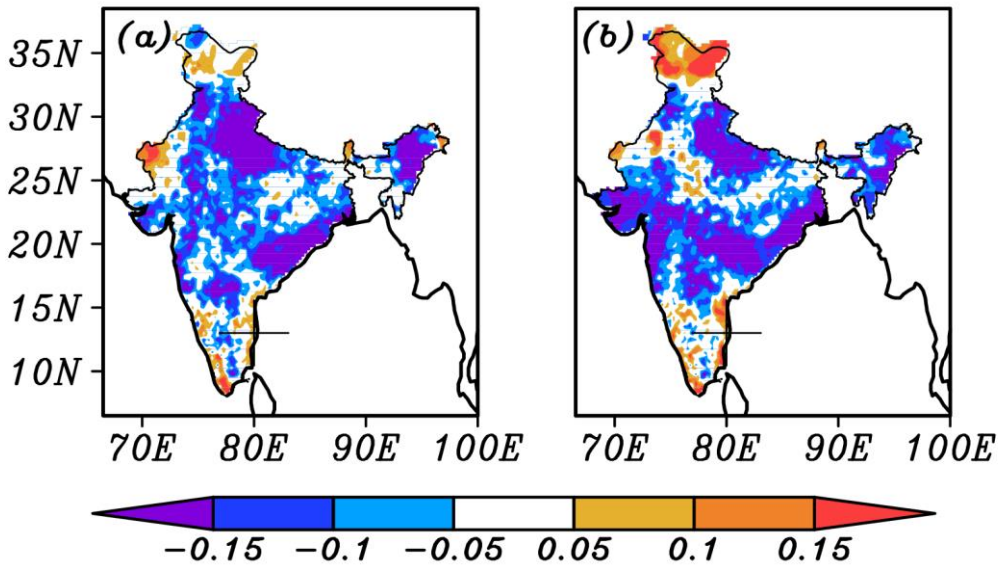

Figure 4.6: (a) Correlations between NEMR and BoB SSTA index (b) correlation between NEMR and Niño-3 index for the season OND during the period of 1901-2013. The orange (blue) colour areas denote positive (negative) correlations, statistically significant at 90% confidence level from a two-tailed t-test. '+' mark indicates the location of the Chennai city.

4.3 Experimental design of sensitivity tests for evaluation of BoB and El Niño SSTs impacts on Chennai 2015 extreme rainfall event using WRF model

To investigate the impact of BoB and El Niño SSTA on Chennai ERE on December 01 2015, I used the regional climate WRF model version 3.6 (Skamarock et al., 2008). Several studies have used the WRF model to simulate, forecast, and diagnose the dynamics of as EREs over India (Jenamani, 2006; Kumar et al., 2008; Kirtsaeng et al., 2010; Rao and Ratna, 2010; Routray et al., 2010; Hariprasad et al., 2011; Mohanty et al., 2012; Srinivas et al., 2013, etc.).

Various physics options chosen in the WRF model to address this problem are, the WSM 3-class simple ice scheme for microphysics (Hong et al., 2004), the Rapid Radiative Transfer Model (RRTM) scheme for long-wave radiation (Mlawer et al., 1997), the Dudhia scheme for short-wave radiation (Dudhia, 1989), the Monin-Obukhov similarity scheme for surface layer (Monin and Obukhov, 1954), the Thermal diffusion scheme for land-surface (Dudhia, 1996), the Yonsei University (YSU) scheme for planetary boundary layer (Hong et al., 2006), and the Kain-Fritsch (new Eta) scheme for cumulus parameterization (Kain, 2004). For this analysis, all the sensitivity experiments are carried out at 0.25°×0.25° horizontal resolution and with default 30 vertical levels. All the experiments carried out in this study have been detailed in Table 4.1 and Table 4.2. We carried out two preliminary experiments to select the domain for our simulations (Figure 4.7). For the first of these experiments, named as the Tropical Indian Ocean-GFS (TIO-GFS), we choose this domain mainly covering the Tropical Indian Ocean (TIO) bound by 60°E - 100°E zonally and 10°S - 30°N meridionally (Figure 4.7a).

4.3.1 Optimal domain selection

While we are mainly interested in confining ourselves to the north Indian Ocean, we have extended the domain southward to 10°S in order to avoid any artefacts associated with a model boundary very close to the study region. In this experiment, starting with the initial boundary conditions representing 0000 UTC on November 29, 2015, the model was integrated for 144 hours, i.e., up to 2400 UTC on December 4, 2015, with a 3-hours interval. Importantly, the initial conditions were obtained from the Global Forecast System (GFS) model at 0.5°×0.5° horizontal resolution developed by the National Centres for Environmental Prediction (NCEP, 2015). Note that the lower boundary conditions (LBC) of the SST were also from the GFS model. Just to make sure that the domain used in the TIO-GFS experiment is sufficient to capture the evolution of a weather event in the regional model, we carry out our second experiment, henceforth referred to as the Indo-Pacific-GFS (Figure 4.7b), a changed the zonal domain, specifically by moving the eastern boundary of the domain all the way from 60°E to

90°W; that is, in this experiment, the domain covers through the eastern tropical Pacific region where the maximum SSTA associated with the 2015 El Niño event was manifested. Finally, we find that the results are more realistic from the TIO-GFS experiment. Therefore, we carry our sensitivity experiments with the same domain (Figure 4.7a) as that used in the other experiments.

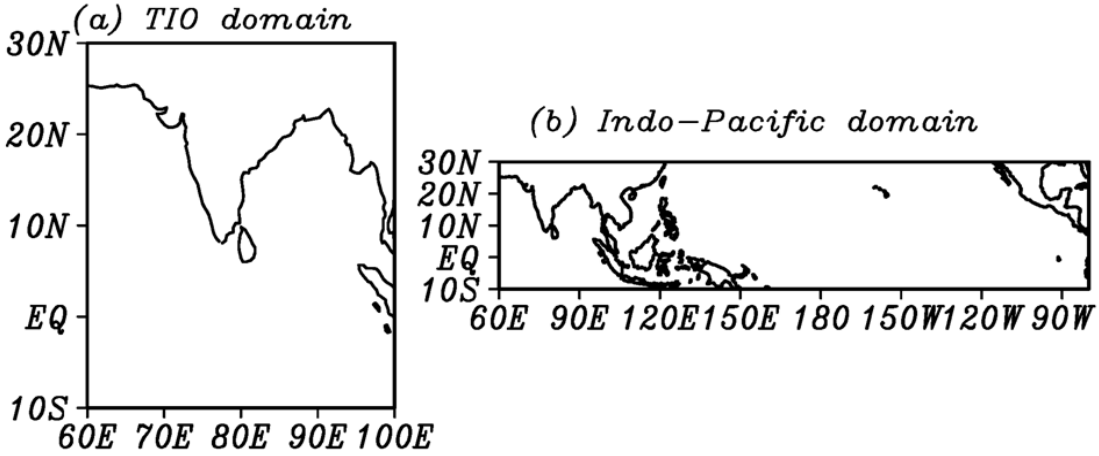

Figure 4.7: Represents the sensitivity experimental domains of (a) tropical Indian Ocean-GFS and (b) Indo-Pacific Ocean-GFS.

The TIO-GFS experiment is an attempt to explore the ability of the GFS SST, which are necessarily forecast, in at least qualitatively predicting the Chennai event. In addition, we also carry out a series of experiments with the LBC SST derived from the OISST. Unlike the GFS SST, which is forecast, the OISST is based on the observations, and therefore, more "realistic." Using long-term OISST data gives information about the ability and changes associated with background SST conditions. LBC gives relevance to the concurrent El Niño-induced SST in the TIO, etc., with better confidence.

The nomenclature and details of all the other four experiments with the LBC SST derived from the OISST are provided in Table 4.1. The experiment TIO-OISST-real, which is our control experiment, is similar to the TIO-GFS experiment, but with the OISST during the event period as the LBC in place of the GFS SST used in the previous two experiments. Besides, we carry out three sensitivity experiments to understand the "remote" impact of the 2015 El Niño passed

to the North Indian Ocean (NIO) through atmospheric circulation. Similarly, the experiment TIO-real-Winds is similar to the TIO-GFS experiment, but with the NCEP winds during the event period as the LBC in place of the GFS winds. The details of the configurations, and nomenclature, of these different winds experiments are listed in Table 4.2.

Table 4.1: Explains the different sensitivity experiments with different SSTs.

S. No	Name of the experiment	The domain of the experiment	SSTs
1	TIO-GFS	10°S to 30°N, 60°E to 100°E	GFS
2	Indo-Pacific-GFS	10°S to 30°N, 60°E to 100°E	GFS
3	TIO-OISST-real (referred to as the control experiment)	10°S to 30°N, 60°E to 100°E	Daily real OISST
4	TIO-OISST-Clima	10°S to 30°N, 60°E to 100°E	Daily climatological OISST (1986-2015)
5	TIO-OISST-BKG	10°S to 30°N, 60°E to 100°E	Daily OISST anomalies (2006-2015) added to daily old climatological OISST (1986-1995)
6	TIO-No-ENSOSST	10°S to 30°N, 60°E to 100°E	Same as the control, but the LBC SST has been obtained by regression the Niño3 related signal in the lower boundary SST through regression analysis.

Table 4.2: Explains the different sensitivity experiments with different winds.

S. No	Name of the experiment	The domain of the experiment	Winds
1	TIO-real-Winds	10°S to 30°N,60°0E to100°E	NCEP_daily real winds
2	TIO-Clima-Winds	10°S to 30°N, 60°E to100°E	NCEP_daily_climatological winds
3	TIO-No-ENSO-Winds	10°S to 30°N, 60°E to 100°E	Same as the control, but the LBC winds have been obtained by regression the Niño3.

4.4 Results from model sensitivity experiments

We discuss the results from observations and simulations mainly for the three peak days of Chennai rainfall, i.e., from November 30 through December 02, 2015. Figure 4.8a shows a

spatial map of accumulated daily rainfall data from the TRMM observation. On November 30, the rainfall was ~80 mm/day over the Chennai and the surrounding regions adjoining the western BoB. On December 01, the region recorded a peak rainfall of above ~120 mm/day. Interestingly, the TRMM rainfall indicates strong rainfall of about ~100 mm/day in Chennai and adjoining coastal regions on December 02, 2015, with the dominant rainfall zone having shifted slightly southward as compared to the day before.

Figures 4.8b and 4.8c show the spatial maps of simulated rainfall from the TIO-GFS (Figure 4.2a) and Indo-Pacific-GFS (Figure 4.2b) experiments, respectively, for the November 30 - December 02, 2015, these both runs are forced with the LBC SST from the GFS. Note that the day-to-day changes and spatial distribution of the simulated rainfall in our experiments prior to the advent of the extreme event are qualitatively realistic. Notwithstanding that the model is forced by the GFS SST, the experiments successfully capture the observed extreme rainfall event activity and the spatial extent of the Tamil Nadu coast in both experiments (Figure 4.8b and 4.8c). Having said this, the locations of the simulated maximum rainfall in both experiments are somewhat south of the Chennai region (Figures 4.8b and 4.8c), where it was actually located (Figure 4.8a). Also, while the peak rainfall in the Chennai region occurred on December 01, 2015 as seen from the TRMM data, both experiments simulate the peak rainfall on December 02, 2015 (Figure 4.9). The amount of simulated rainfall is on the day of peak rainfall from the TIO-GFS experiment is somewhat lower than that from the observed rainfall (Figure 4.9), while that from the Indo-Pacific-GFS experiment is significantly lower. Between these two simulations, the amount of rainfall simulated was more in the TIO-GFS experiment from December 01 onwards. Specifically, the area-averaged (10°N - 14°N, 79°E - 82°E) peak rainfall, as seen from the TRMM datasets, on December 01 is 100 mm/day, the corresponding simulated values on December 02 from the TIO-GFS and Indo-Pacific-GFS experiments are ~89 and ~67 mm/day, respectively. From this sense, between the two simulations, the one from the TIO-GFS experiment is relatively nearer to the TRMM observations.

We now discuss the moisture convergence feature from the observation and simulations for the three peak days of Chennai rainfall. Figure 4.10a shows a spatial distribution of observed moisture convergence at 1000 hPa for the November 30 - December 02, 2015 period, and Figures 4.10b and 4.10c the corresponding the spatial distributions from our TIO-GFS and Indo-Pacific-GFS experiments. Figure 4.10a shows low-level moisture convergence at Chennai and adjoining regions, which peaks on December 01, 2015, in agreement with the local rainfall changes during these days. The peaking of the moisture convergence on December 01, 2015 is also reflected in the weakened north-easterlies east of the coastal Tamil Nadu on this day as compared to the previous day (Figure 4.10d and c).

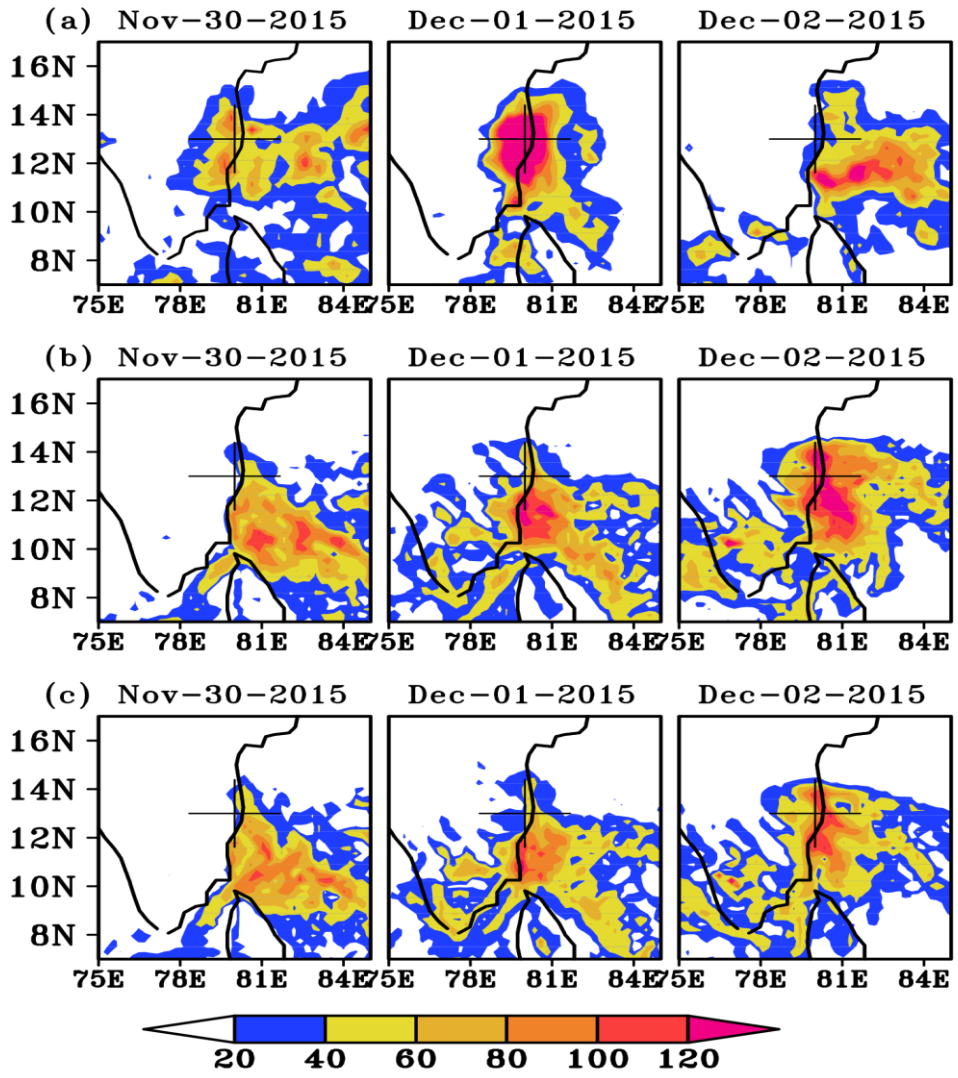

Figure 4.8: Spatial map of daily accumulated rainfall (mm/day) from first panels (a) TRMM observations, second and third panels simulated rainfall from (b) TIO-GFS experiment, and (c) Indo-Pacific-GFS experiment. Panels depict signals during November 30, December 01, and December 02, 2015, respectively, from left to right.

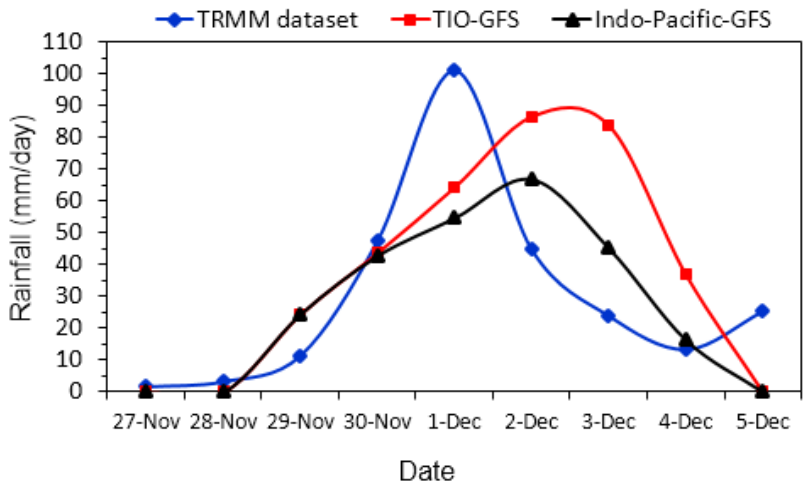

Figure 4.9: Time series of area averaged (10°N-14°N, 79°E-82°E) of daily rainfall (mm/day) from TRMM observations (blue line), TIO-GFS experiment (red line), and Indo-Pacific-GFS experiment (black line).

Both the simulations (Figure 4.10b and 4.10c) qualitatively reproduce the observed moisture convergence though they overestimate the convergence. Further, the peak moisture convergence of ~0.013 kg^{-1} from the TIO-GFS experiment, simulated on December 01, is stronger than that from the Indo-Pacific-GFS experiment (0.007 kg^{-1}). This suggests that the local SST conditions in the BoB have contributed more to the observed moisture convergence as compared to the signals from the tropical Pacific. One needs to remember that some influence from the tropical Pacific may still be present through the atmospheric boundary conditions that have been prescribed. As the TIO-GFS simulation simulates the Chennai event qualitatively better than the Indo-Pacific-GFS experiment, we stick to the same domain as that in the TIO-GFS experiment for our further simulations reported in this thesis. We have, to be sure, also ascertained by repeating all experiments we report in the next two sub-sections with the Indo-pacific domain, that the findings are robust to the change of domain, just as in the current sub-section (results not shown).

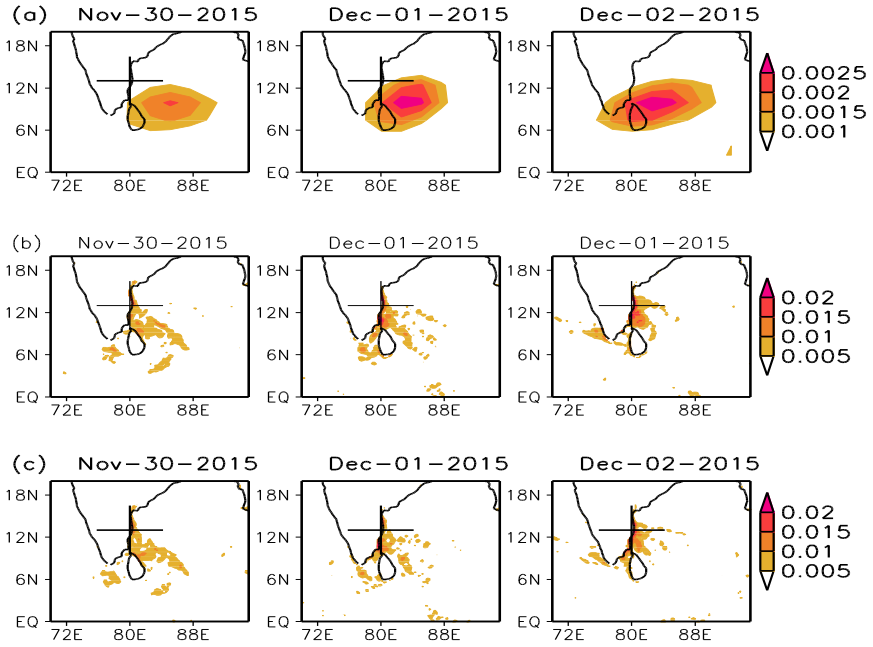

Figure 4.10: Daily moisture convergences (kg^{-1}) at 1000 hPa from (a) observed daily data from NCEP, (b) TIO-GFS experiment, and (c) Indo-Pacific-GFS experiment. Panels depict signals during November 30, December 01, and December 02, 2015 respectively, from left to right.

The experiment TIO-OISST-real, in which the observed OISST data for the November 29 through December 04, 2015 are used in the TIO domain, simulates a peak rainfall on December 01, 2015 (Figure 4.11), as observed (Figure 4.9). The simulated rainfall in this experiment, which is essentially our control experiment, is marginally less than that from the TIO-GFS experiment. Nonetheless, the experiment captures the evolution of the event reasonably.

Just to be sure that the occurrence and extremity of the Chennai event is associated with the low-frequency SST variability, we also conduct an experiment, namely, TIO-OISST-Clima. In this experiment, the WRF model has been forced by OISST daily climatology of 1986 to 2015, with other boundary forcing similar to the above experiments. The simulated rainfall from this experiment is weaker (Figure 4.11) than the corresponding rainfall from the control experiment. This critical result confirms that the Chennai event and its extremity are mainly due to the SST variability. As it is, the BoB was anomalously warm by above 1°C during 2015 (Figure 4.3), which favours an anomalous build-up of convection (Sikka et al., 1977; Prajeesh et al., 2013).

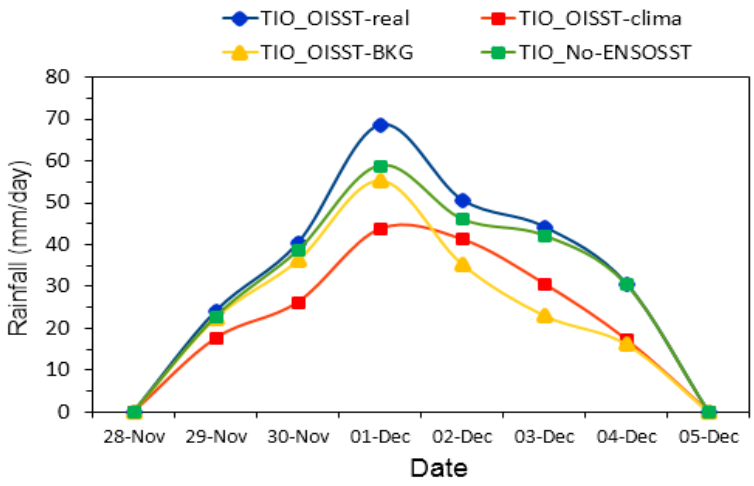

Figure 4.11: Time series of area-averaged (10°N - 14°N, 79°E - 82°E) of daily rainfall (mm/day) from different experiments with OISST dataset.

We conjectured elsewhere that the intensity of the Chennai event could be due to the strengthening warming trend in the BoB, or in other words, due to a changing background climate state in the BoB. To ascertain this, we carry out the TIO-OISST-BKG experiment. As mentioned in Table 4.2, the LBC SSTs in this experiment have been obtained by the following method: we first obtain the daily SST anomalies during the event by subtracting the (2006-2015) climatology from the observed SST. We add these anomalies to the SST climatology for the 1986-1995 period, i.e., the 'old' period when the SSTs were cooler in the tropical Indian Ocean, particularly the BoB. We see that the simulated rainfall from the TIO-OISST-BKG experiment is very less (Figure 4.11) as compared to that from the TIO-OISST-real experiment. This indicates that without the recent change in the background SST of the TIO - most likely in the BoB the Chennai event would have been much weaker in intensity as compared to what was observed.

As mentioned briefly in the introduction, when the ENSO occurs, it can influence the weather and seasonal climate in the NIO through two ways. The well-known understanding is that it anomalously modulates the atmospheric circulation in the equatorial Indian Ocean, which in turn will influence the atmospheric circulation over India and BoB. The ENSO-induced winds, however, also can influence the SST in the equatorial Indian Ocean (e.g., Alory et al., 2007), and portions of BoB (Figure 4.12a and 4.12b), as can be conjectured from the ENSO

correlations with the SST in the NIO. We shall explore these aspects in this sub-section

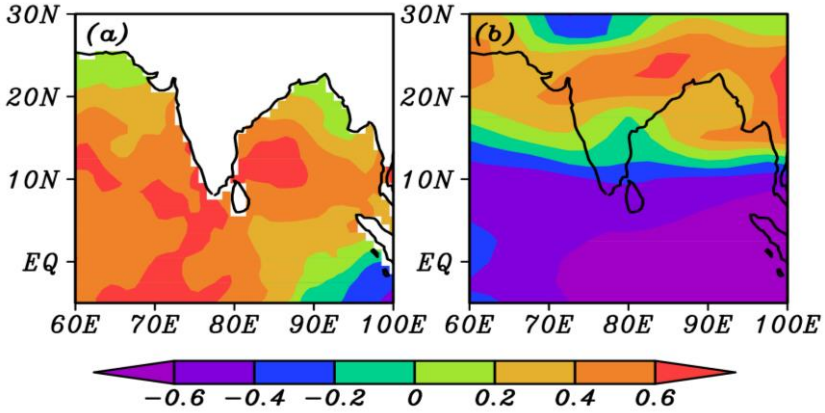

Figure 4.12: (a) Correlation between TIO SST anomalies and Niño3 index of SSTA, (b) correlation between zonal wind anomalies and Niño3 index of SSTA during the OND season for the period of 1986-2015.

The experiment TIO-No-ENSO-SST is similar to the control experiment, but only that the lower boundary SSTs have been obtained by regression out the concurrent El Niño signal in the SST through a regression analysis between the Niño3 index and the TIO SST from the daily OISST datasets. From Figure 4.9, it is clearly seen that the area-averaged rainfall evolution in this experiment is substantially lesser than about 21.5% that from the control experiment. Interestingly, the impact of the trends in the BoB seems to be slightly more relevant than the concurrent ENSO, of course subject to any limitations in our methodology.

Our final sensitivity experiment, TIO-No-ENSO-Winds is same as the TIO-OISST-real experiment, but differs in the atmospheric boundary conditions. Specifically, in this experiment, the concurrent El Niño-associated circulation at each level in the atmospheric circulation boundary conditions is regressed out just as in the TIO-No-ENSOSST experiment. The Figure 4.13 clearly shows that the area-averaged rainfall from this experiment during the event is less than that from the control experiment by about 10% - 12%. This indicates concurrent ENSO signal in the local SST in the BoB is more relevant to the correct simulation of the intensity of a synoptic event in the southwest BoB as compared to the signals through the atmospheric boundary conditions.

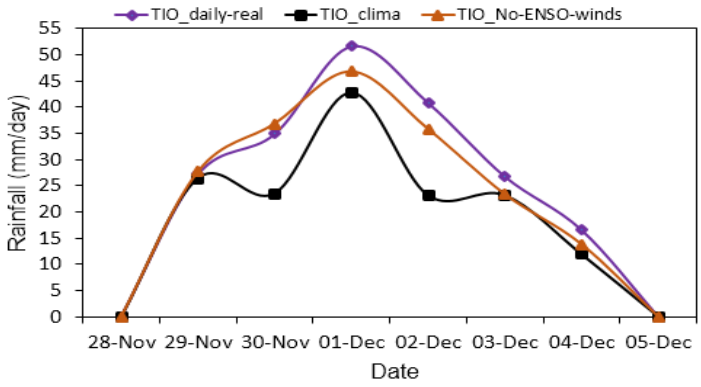

Figure 4.13: Time series of area averaged (10°N - 14°N, 79°E - 82°E) of daily rainfall (mm/day) from different experiments with winds.

4.5 Summary

In this chapter, using the gridded rainfall datasets of the HadISST (1901 - 2013) and IMD rainfall for the 1901 - 2013, we indeed find, through a linear correlation analysis, that any warming of the southern BoB has the propensity to cause above normal rainfall during NEM season in the southeast India at a statistically significant level. The correlation between the NEMR with the area-averaged SSTA have a magnitude comparable to that El Niño index. We evaluate the potential contribution of the concurrent El Niño as well as the background warming in the BoB to the intensity of the ERE on December 01, 2015. We start by conducting two exploratory numerical experiments with the WRF model. While both experiments are carried out on the November 29 - December 04, 2015, the first experiment, which we refer to as the TIO-GFS, covers the BoB domain (10°S - 30°N, 60°E - 100°E). The second experiment, named as the Indo-Pacific-GFS experiment, covers the broader tropical Indo-Pacific region (10°S - 30°N, 60°E - 90°W). Both experiments simulate the observed evolution of the location of the ERE of the Chennai adequately. However, while the life cycle of the TIO-GFS simulated extreme event is more or less comparable with the observations, the extreme event simulated in the Indo-Pacific-GFS experiment weakens rather faster as compared to the observations. Based on these results, we freeze the domain used in the TIO-GFS for our other experiments. Our control experiment is similar to the TIO-GFS but forced by OISST during November 29 to December 04, 2015, which are obviously more realistic compared to the GFS SST. Indeed, in

this experiment, we will get a more realistic evolution of the Chennai event with the peak rainfall occurring on December 01, as observed, though the simulated rainfall is marginally weaker TIO-GFS experiment.

We carried out several sensitive experiments with the WRF model to explore the relatively importance of the warming trend in the NIO, and the 2015 El Niño to the Chennai event. The area-averaged simulated rainfall from an experiment, in which the ENSO related signal from the lower boundary SST, has been a regressed out is lesser than that from the control experiment by about 21.5%. We also find, through several sensitivity experiment through in which the ENSO signals in the atmospheric boundary conditions have been regressed out, that the contribution of the concurrent ENSO to the rainfall during the Chennai event is 10% - 12%. This suggests that the SSTs in BoB associated with the El Niños are more important for the synoptic activity in the BoB as compared to the atmospheric circulation changes due to El Niños. This is reasonable because the local convection, which determines the rainfall intensity, is strongly connected to the SST. We have also carried out an experiment complementary to the control experiment by imposing a specially designed boundary SST. These special boundary conditions have been untainted by adding the SST anomalies from the current day climate (2006 - 2015) to the SST climatological two decades back, specifically (1986 - 1995). The simulated peak intensity of the Chennai event from this experiment is lesser than that from the control experiment by about 21%. This important result suggests that the impact of the recent warming trend in the BoB SST is comparable to that of the ENSO induced SST in BoB.

So far, we investigated the potential role of SST background changes to the ERE. Unlike the SST which is a large-scale field, the LULC has a very high spatial variation. Therefore, it is also very important to investigate the potential role of small/regional scale changes in LULC on the EREs. We addressed this problem using two different periods of LULC datasets with the WRF regional climate model and presented in the next chapter.

Chapter – 5

Explore the importance of LULC changes on extreme rainfall events in southern India using a regional model

In this chapter, I have investigated the impact of regional scale background mechanism of LULC changes on the intensity of extreme rainfall events over three southern Indian states using the regional climate model.

5.1 Introduction

Over the tropics, particularly over the Indian subcontinent, land-surface processes constitute an important driver of the weather and climate system (e.g., Nayak and Mandal, 2012; Saha et al., 2012, 2016; Nayak et al., 2019). As discussed in chapter 1, several recent studies suggest that, among other factors, the LULC/urbanization changes increase the heavy rainfall activity over India, at least at regional scales (Meehl and Washington, 1993; Niyogi et al., 2002; Kishtawal et al., 2010; Pielke et al., 2011; Cook et al., 2015; Jain et al., 2015; Paul et al., 2016; 2018, etc.). Most of such studies for other region in India have are case studies, i.e., they focused only on a single event (e.g., Sahoo et al., 2020b).

There have not been any studies, however, on the changes in the EREs in southern India. Several regions of southern part of India have been undergoing rapid LULC changes and urbanization in the last two decades (e.g., Agilan and Umamahesh, 2015; Aithal and Ramachandra, 2016; Garai and Narayana, 2018; also see our analysis and Figure 5.5). Therefore, an outstanding question is whether such changes in the LULC due to such rapid urbanization affect the rainfall intensity in southern India. This question is addressed in this study through an analysis of observational rainfall datasets as well as by conducting several sensitivity studies with a convection-resolving configuration of the WRF model. While we investigate twelve EREs (listed in Table 5.2), we mainly focus on the contribution of the changes in LULC through a detailed analysis of simulations pertaining to three representative EREs in southern India, one from each of the three southern Indian states namely; Tamil Nadu, Telangana and Kerala (see Figure 5.1 for the geographical locations). The reasons for selecting these three states are as follows. The state of Kerala on the southwest Indian coast off the Arabian Sea receives a copious amount of precipitation amounting to 1649.5 mm during ISM. In contrast, the state of Tamil Nadu is an eastern-coastal state off the BoB, and as mentioned earlier, receives a high amount of rainfall only during the NEM. Unlike the other two states, the state of Telangana is land-locked and relatively far off from the oceans. It receives the bulk of

its annual rainfall during the ISM. While this region receives moisture from the oceans, the importance of the LULC can be conjectured to be relatively higher owing to its location. Another distinction among the states is, because of the seasonality, the co-occurring El Niños have a propensity to exacerbate the rainfall in Tamil Nadu, unlike their detrimental effect on rainfall in the rest of India, including Telangana, and Kerala (Amat and Ashok, 2018; Ashok et al., 2019).

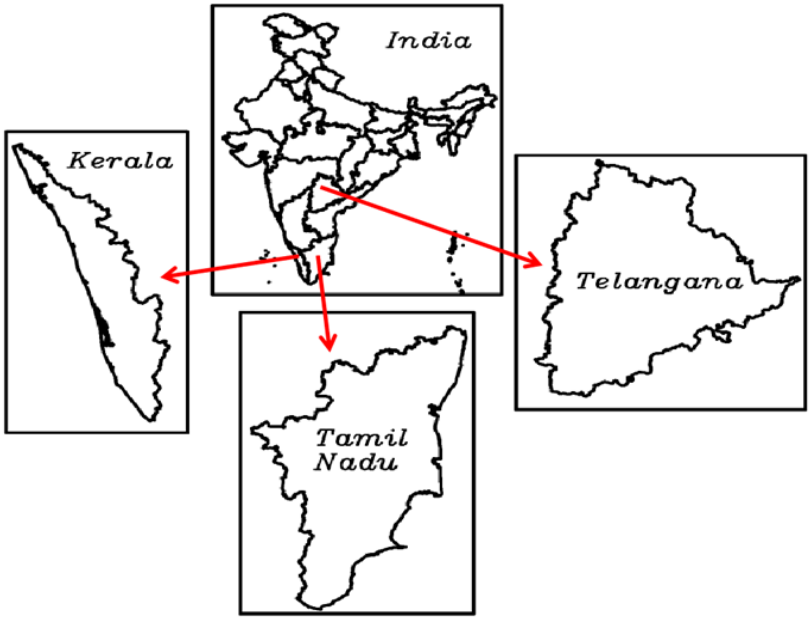

Figure 5.1: Geographical locations of the three studied extreme rainfall states.

5.2 Experimental design of sensitivity tests to investigate the relevance of LULC changes on extreme rainfall events over southern India using the WRF regional climate model

To study the impact of LULC changes on EREs, I have used the WRF regional climate model version 3.8.1 (Skamarock et al., 2008). The WRF model has configured with two-way interactive nested three domains with horizontal outer-to-inner resolutions of 18, 6, and 2 km (Figure 5.2). The regions of the first and second domains cover 45°E-115°E, 5°S-40°N and 65°E-95°E, 2°N-29°N (18 and 6 km resolutions) were the same for all three EREs. (see red color boxes in Figure 5.2). Based on the Srinivas et al., (2018), we selected physics options to include the Goddard Ensemble scheme for microphysics (Tao et al., 2016), the Dudhia for short-wave radiation scheme (Dudhia et al., 1989), the Rapid Radiation Transfer Model

(RRTM) for long-wave radiation (Mlawer et al., 1997), the Yonsei University (YSU) non-local scheme (Hong et al., 2006) for planetary boundary layer and the NOAH scheme (Tewari et al., 2004) for land surface processes. The Kain-Fritsch (KF) scheme (Kain, 2004) is used for the cumulus convection in the first and second domains. Adhering to the high resolution of the inner domains, no implicit cumulus scheme is used for the inner domain. The initial and lateral boundary meteorological conditions for the model are obtained from the National Centers for Environmental Prediction-Final Analysis (NCEP-FNL) data available for every six hours at 1°×1° resolution (NCEP, 2000). Simulations for each ERE start at 0000 UTC of the day prior to the heaviest rainfall day of the event, as catalogued by the IMD. For example, in the case of the Chennai ERE, as per the IMD, the peak rainfall occurred on December 01, 2015. Our corresponding simulations are initiated at 0000 UTC of November 30, 2015.

We analysed heavy rainfall events and their changes in the recent two decades during the primary rainfall season, i.e., ISM season for the Telangana and Kerala states, and the NEM season for Tamil Nadu state. We identify heavy rainfall events, from the gridded IMD rainfall datasets of 0.25°×0.25° resolution, following slightly modified the IMD categorized rainfall classifications. Accordingly, the heavy rainfall events are defined as those events for which the rainfall amount lies between ≥ 35.6 and ≤ 124.5 mm/day (Table 2.1). In addition to the daily IMD gridded rainfall datasets, two other observed daily gridded rainfall datasets, APHRODITE and TRMM, were also chosen for further analysis. At every grid point, we computed the linear trend in seasonal heavy rainfall events and the 99 percentile of rainfall magnitude. The statistical significance of the trends in the observed seasonal frequency of the heavy rainfall events and those in the 99 percentile of rainfall magnitude, in each region, are evaluated by a one-tailed Student's t-distribution test.

Based on the IMD dataset analysis results, we identify three EREs, one for each of the three states of the Tamil Nadu, Telangana, and Kerala, as representative cases that receive detailed attention. The selected events respectively occurred (i) on December 01, 2015 over

Tamil Nadu, (ii) September 24, 2016 over Telangana, and (iii) August 15, 2018 over Kerala.

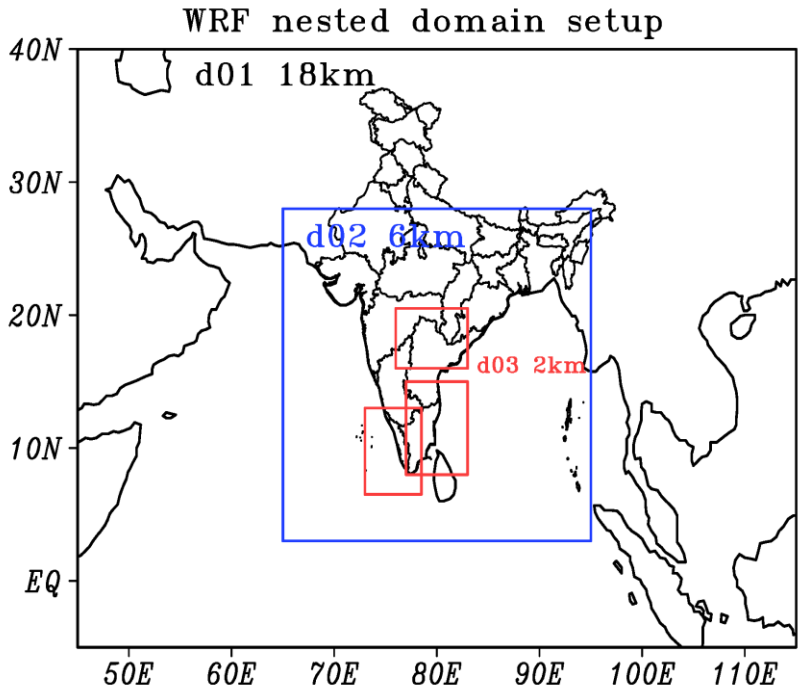

Figure 5.2: Model nested domains chosen for the simulation of extreme rainfall events three southern states.

We conduct various sensitivity experiments with the WRF model to evaluate the potential contribution of the recent LULC changes to the extremity of each of these representative events. In this study, the peak rainfall hours/stage, for each of these three representative events, are defined as the three to four contiguous heaviest rainfall hours, as deciphered from the time series of area-averaged GPM rainfall time-series; the area-averaging is done over the state in question. The next three hours after the peak rainfall is designated as the decaying stage. Similarly, we define the three hours before the peak stage as the developing stage, unless mentioned otherwise. The LULC dataset from the Moderate Resolution Imaging Spectroradiometer (MODIS) with 20 categories (Table 5.1) was based on the year 2001 (Ran et al., 2010; Bhati and Mohan, 2018) are used in the standard WRF model configuration. In addition, an option to use the United States of Geological Survey (USGS) LULC conditions of 1995 is also available. Notably, 24 categories (Table 5.1) at 30s resolution new LULC dataset for the over Indian continent was obtained from the Advanced Wide Field Sensor (AWiFS)

aboard the Indian Remote-Sensing Satellite (IRSP6) which was launched by the ISRO (Biswadip et al., 2014). Using the MM5 model, Badrinath et al. (2012) suggested that the Aila cyclone's track was better simulated over the Indian region with the ISRO LULC relative to that with the USGS LULC. Unnikrishnan et al., (2016) reported that an updated ISRO LULC in the dynamic model gives better weather prediction over India. More recently, Sahoo et al. (2020a) study suggests that using the 2013 ISRO LULC, as compared to the 2005 ISRO LULC, results in better simulation of the ERE. As the categories of the LULC from ISRO data are similar in-terms of number and types to those of the USGS LULC datasets, the ISRO LULC datasets can be used for simulations over India without any serious technical challenges. Equally important is the suggestion from the various case studies (e.g., Badrinath et al., 2012, Unnikrishnan et al., 2016; Sahoo et al., 2020a) that the simulations with concurrent ISRO LULC datasets exhibit better fidelity related to those with the MODIS and/or USGS LULC.

Therefore, we carried out three experiments by changing the LULC datasets. These are, (i) the control experiment, henceforth referred to as the 'MODIS' experiment, characterized by the LULC datasets of MODIS, (ii) the 'Old-ISRO' experiment with the ISRO LULC dataset for the year 2005, and (iii) the 'New-ISRO' experiment, with the LULC datasets of the year 2017. We also carry out similar simulations for nine more EREs to generate relevant statistics to understand the potential influences of the recent changes in the LULC on EREs.

We plan to carry out simulations at a relatively high horizontal resolution of 2 km; it is worth recalling a study by Bhaskarao et al. (2010). This study suggests that, for improved simulations of synoptic disturbances in the Indian region at a high horizontal resolution of 1~4 km, the vertical resolution should also be commensurately high. From this context, we carry out several preliminary sensitivity simulations with two vertical resolutions, namely, the standard 30 vertical levels that are default in WRF, and a higher 51 vertical levels we designed, comprising of 30 vertical levels in the lower troposphere (from the surface to 500 hPa), and the remaining 21 in the middle and upper troposphere (above 500 hPa to 10 hPa).

Table 5.1: List of LULC categories of ISRO and MODIS datasets.

S. No	**ISRO LULC categories**	**MODIS LULC categories**
1	Urban and Built-Up Land	Evergreen Needle leaf Forest
2	Dry land Cropland and Pasture	Evergreen Broadleaf Forest
3	Irrigated Cropland and Pasture	Deciduous Needle leaf Forest
4	Mixed Dry land/Irrigated Cropland and Pasture	Deciduous Broadleaf Forest
5	Cropland/Grassland Mosaic	Mixed Forests
6	Cropland/Woodland Mosaic	Closed Shrub lands
7	Grassland	Open Shrub lands
8	Shrub land	Woody Savannas
9	Mixed Shrub land/Grassland	Savannas
10	Savanna	Grasslands
11	Deciduous Broad leaf Forest	Permanent Wetlands
12	Deciduous Needle leaf Forest	Croplands
13	Evergreen Broad leaf	Urban and Built-Up
14	Evergreen Needle leaf	Cropland/Natural Vegetation Mosaic
15	Mixed Forest	Snow and Ice
16	Water Bodies	Barren or Sparsely Vegetated
17	Herbaceous Wetland	Water
18	Wooden Wetland	Wooded Tundra
19	Barren or Sparsely Vegetated	Mixed Tundra
20	Herbaceous Tundra	Barren Tundra
21	Wooded Tundra	
22	Mixed Tundra	
23	Bare Ground Tundra	
24	Snow or Ice	

5.3 Synoptic conditions of the extreme rainfall events

5.3.1 The Chennai event

Chennai (13.4°N, 80.1°E), the fourth largest city in India and capital city of Tamil Nadu located in the southeast coast of India with an estimated population of 8.7 million (Census, 2011). Chennai, as well as most of Tamil Nadu, experienced an extreme rainfall event during November 26 - December 02, 2015, reaching its peak rainfall above 300 mm/day on December, 01, 2015 (Figure 4). Several studies and reports have provided the details of the synoptic conditions for this event (India. Met. Dept. Rep., 2015; Chakarborty, 2016; Mishra, 2016; Narasimhan et al., 2016; Srinivas et al., 2018). As per these papers, a slow-moving low-pressure system was observed during November 27 - December 02, 2015 off the coast of Tamil

Nadu over southwest BoB, which resulted in extreme rainfall at 12°N - 14°N, 79°E - 80.1°E over the north coastal Tamil Nadu and the neighborhood regions.

5.3.2 The Telangana event

The state of Telangana experienced extreme rainfall of about 250 mm/day on September 24, 2016, which was 107% above the whole climatological rainfall for the month of September. As per the IMD reports, the maximum rainfall occurred over the northwest parts of Telangana, and was mainly associated with the formation of a well-marked low-pressure system over the central BoB and the adjoining area of coastal Andhra Pradesh, with cyclonic circulation extending from the surface up to 7.6 km on September 24, 2016. This surface low pressure system moved towards the interior of Andhra Pradesh. The system was then located further west over Vidarbha and Telangana regions on and September 24 and 25, 2016, contributing to the extreme rainfall over the north-western parts of Telangana during September 24 - 25, 2016. The highest amount of rainfall of 390 mm was recorded at a station called Armoor (18.79°N, 78.29°E) on September, 24 2016, with 320 mm and 270 mm of rainfall recorded at the neighboring Machareddy and Kamareddy on September, 24 2016. The details of synoptic and rainfall distributions are available at

https://www.aphrdi.ap.gov.in/documents/Trainings@APHRDI/2017/7_July/DRR/A%20case%20study%20on%20monsoon%20rainfall%20over%20Andhra%20Pradesh%20state%20in%20relation%20to%20synoptic%20systems.pdf.

5.3.3 The Kerala event

The state of Kerala, located on the southwest coast of India, experienced prolonged severe flood during August 01- 09, 2018, the heaviest ever recorded in 100 years. This extreme rainfall (50 mm/day to 480 mm/day) caused enormous damage and about 500 causalities. A detailed diagnostic study of this event was carried out by Viswanadhapalli et al. (2019) through an analysis of observations and high-resolution WRF model simulations. The extreme rainfall occurred in two spells over August 7-10 and August 14-18, 2018, with a southward movement

of rainfall bands from the northern mountain regions to the coastal areas of Kerala. The highest amount of rainfall during the first spell concentrated over the northeast mountain regions and a second spell with the maximum over central and south-central of Kerala. Extreme rainfall of 450 mm occurred during August 09-10 at Pookot station. Similarly, the Valparai station received about 950 mm of rainfall during August 14 - 15, 2018.

5.4 Changes in heavy rainfall events and LULC in southern India

Figures 5.3 and 5.4 show the distributions of linear trend in seasonally aggregated number of heavy rainfall events over the period of 2000-2017 in the three states of Tamil Nadu, Telangana and Kerala, and the corresponding trends in the 99 percentile of seasonal rainfall magnitude, from multiple rainfall datasets such as IMD, APHRODITE, and TRMM. Analysis of the IMD and APHRODITE datasets indicates an increase in the 99 percentile of rainfall magnitude over the northern Tamil Nadu during the NEM season, and northern part of Telangana as well as central part of Kerala during summer monsoon season (Figure 5.4). The 99 percentiles of the seasonal rainfall amounts, from the IMD and APHRODITE datasets show a significant (95% confidence level) trend over the northern part of Tamil Nadu during the NEM, and Telangana and central part of Kerala during the summer monsoon. The TRMM dataset, however, do not show a significant trend in the seasonal 99 percentiles of the rainfall over Telangana and Kerala. The positive trend observed in the frequency of heavy rainfall events in all three states (except in the TRMM dataset over Telangana) is, however, statistically not significant (Figure 5.3).

The distributions of LULC over the three different states of Tamil Nadu (Figures 5.5a, d, and g), Telangana (Figure 5.5b, f, and h), and Kerala (Figure 5.5c, e, and i) show an expansion of urbanization in recent periods. A significant reduction is observed in the crop/grass land in all states, which turned into a dry crop land and pasture. Water bodies and crop/wood lands have expanded in Tamil Nadu. Mixed shrub land/grass land became barren/sparsely vegetation in

Telangana, and a broad green fraction of mixed forests turned into deciduous needle/leaf forest over the Kerala.

The above results suggest that the heavy rainfall events and 99 percentile of rainfall magnitude in all three states are increasing in recent decades in potential conjunction with significant changes in the local LULC. However, at this stage, it is difficult to come up a final conclusion whether the LULC changes have unequivocally enhanced the rainfall. To this end, we carry out various sensitivity experiments with the WRF, as stated earlier.

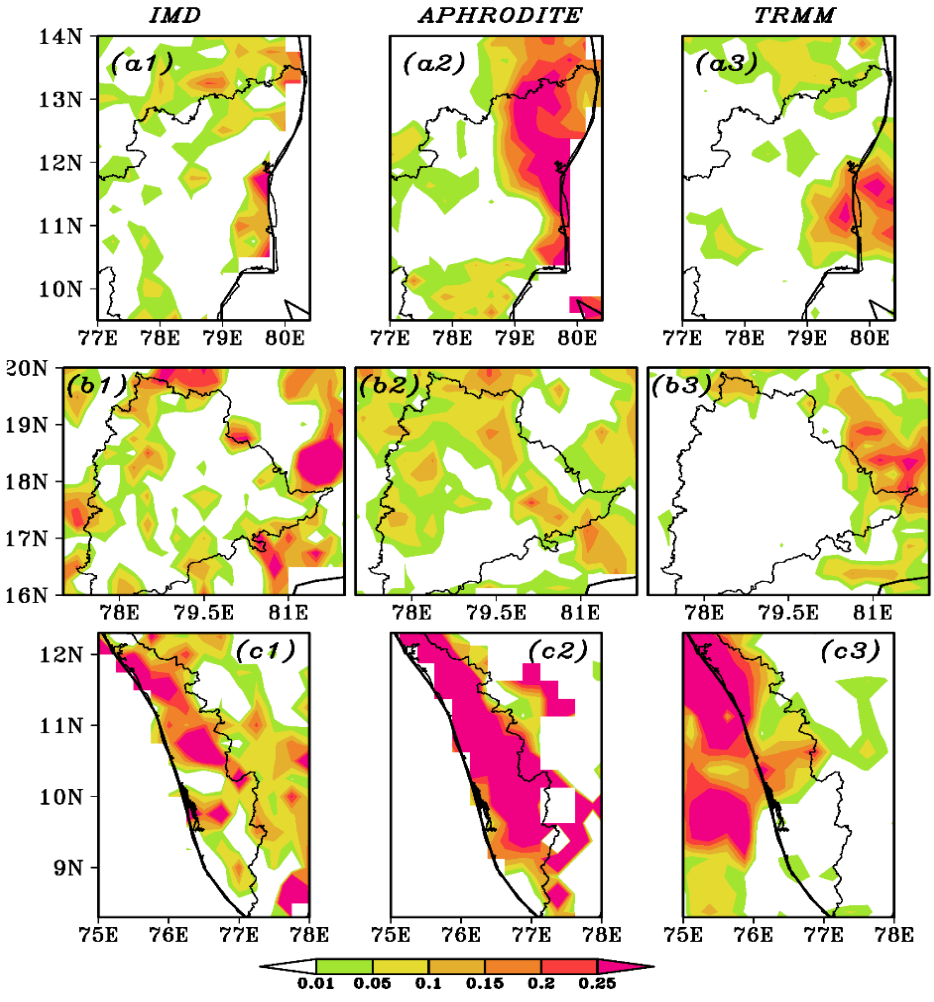

Figure 5.3: Spatial patterns of the linear trend in heavy rainfall events (those when the rainfall is ≥ 35.6 mm/day to ≤ 124.6 mm/day) during the OND season for Tamil Nadu, JJAS season for Telangana and Kerala for the period 2000-2017. Panels a1-a3, b1-b3, and c1-c3 are over Tamil Nadu, Telangana, and Kerala states, respectively. In all the three rows, the panels from left to right are based on the datasets from the IMD, APHRODITE and TRMM, respectively.

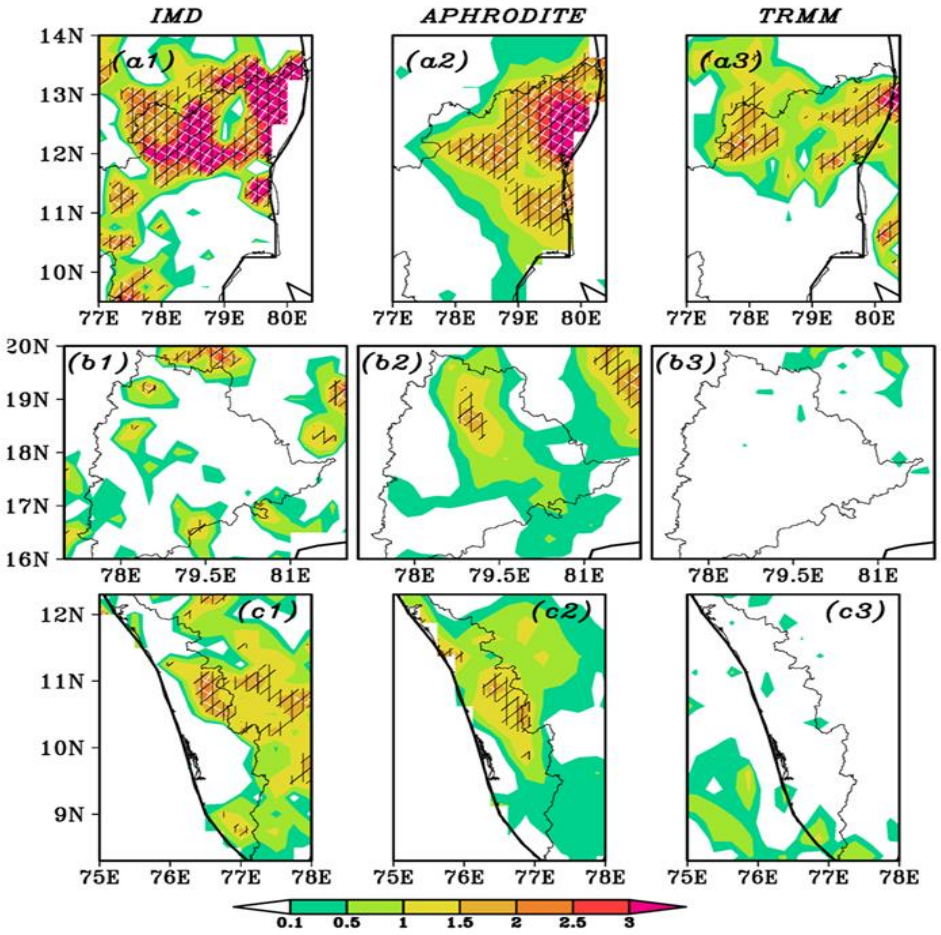

Figure 5.4: Same as Figure 5.3 but for the seasonal 99 percentile of rainfall magnitude. The white (black) color hatches show the increasing trends at 95% (90%) confidence level.

5.5 Sensitivity of the simulation to vertical resolution

This section reports results from the preliminary experiments conducted to ascertain the vertical resolution. To validate our simulations, we focus on specific features such as the location of the peak rainfall, orientation, magnitude and asymmetries of the rainfall distribution, among others features, which should be broadly captured by the relatively coarse observations as well. The model simulations (Figure 5.6) generally exhibit improved fidelity with the observed extreme rainfall with 51 vertical levels configuration. For example, the Chennai extreme rainfall simulated with 30 vertical levels resolution is oriented in the east-west direction (Figures 5.6d-f) and most of the rainfall magnitude concentrated over the ocean regardless of the used LULC data, which is different from that in the observations (Figures 5.6a-c).

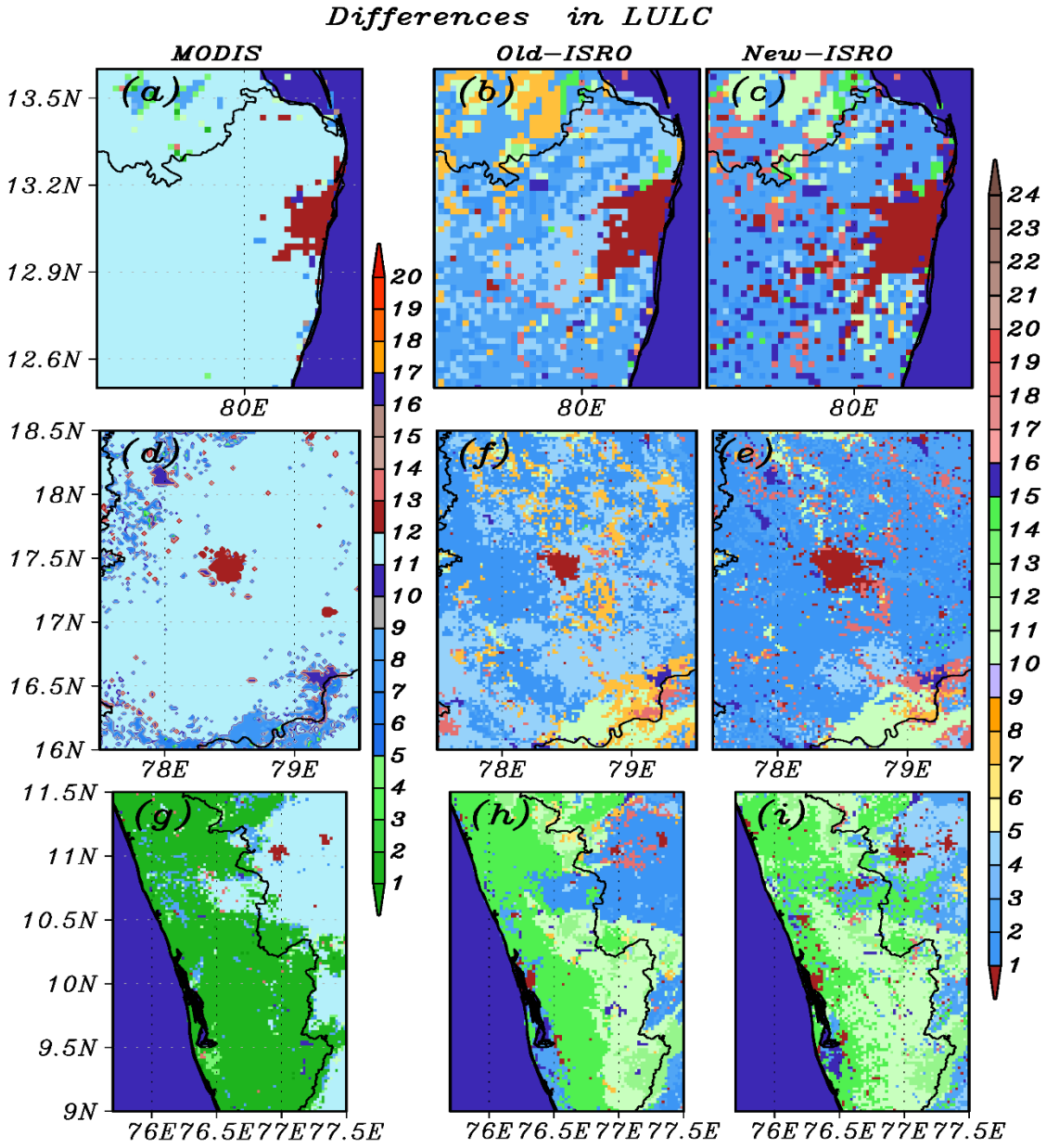

Figure 5.5: Spatial patterns of the LULC from three different datasets over three study regions. The regions shown are, Tamil Nadu (top panels), Telangana (middle panels), and Kerala (lower panels). The LULC with MODIS is shown in the first column (a, d, and g), the Old-ISRO LULC for the year 2004-05 is shown in the second column (b, e, and h), and New-ISRO LULC for the year 2016-17 shown in the third column (c, f, and I). The urbanization of LULC=1 in ISRO and LULC=13 in MODIS.

The corresponding simulations with 51 vertical levels resolution are, however, oriented south-north (Figures 5.6g-f) and the rainfall magnitude concentrated over the coastal land area, in agreement with the observations. The fine features of the model simulations are not artefacts of high resolution, as was evidenced by a companion study (Srinivas et al., 2018), which suggested that the features captured by the interpolated station observations data for the

Chennai extreme rainfall event in question have been well simulated. Therefore, we present our results from the simulations carried out with the 51 vertical levels configuration model.

5.6 Impact of changes in LULC on simulated extreme rainfall events

In this section, we present results from our nine simulations that examine the sensitivity of the simulated representative events, to different choices of the LULC, all of course generated with 51 vertical levels. Various panels in Figures 5.7 to 5.9 show the results of rainfall from nine different model simulations; also shown in these figures are the corresponding observed rainfall distributions from three different observed datasets.

In the case of the Chennai ERE, using a high-resolution Automatic Weather Gauge network over Chennai as well as rainfall derived from the Doppler Weather Radar data at the Chennai city, Srinivas et al. (2018) suggested that the observed rainfall over Chennai exhibited a high spatial variability with isolated extreme rainfall within the range of few kilometers. Figures 2a and 2b of Srinivas et al. (2018) are based on the automatic weather stations around Chennai and the IMD Doppler Weather Radar on 01 December 2015, the day of the maximum rainfall. These demonstrate that the 24-hour accumulated rainfall on this day extended southward from 13°N, ~12.7°N, at about 79.9°E. The IMD gridded rainfall datasets also show (Figure 5.7c) a high concentration of rainfall along the east coast of the Tamil Nadu, with a maximum between 12°N - 14°N, 79.5°E - 80.1°E, along a north-south oriented rainfall band. Similar patterns are seen (Figure 5.7a, b) from the other two observations datasets (TRMM and GPM-IMERG), with slight spatial differences, the analysis of high-resolution observations by Srinivas et al. (2018) gives a good opportunity to ascertain the fidelity of our simulations at high resolution.

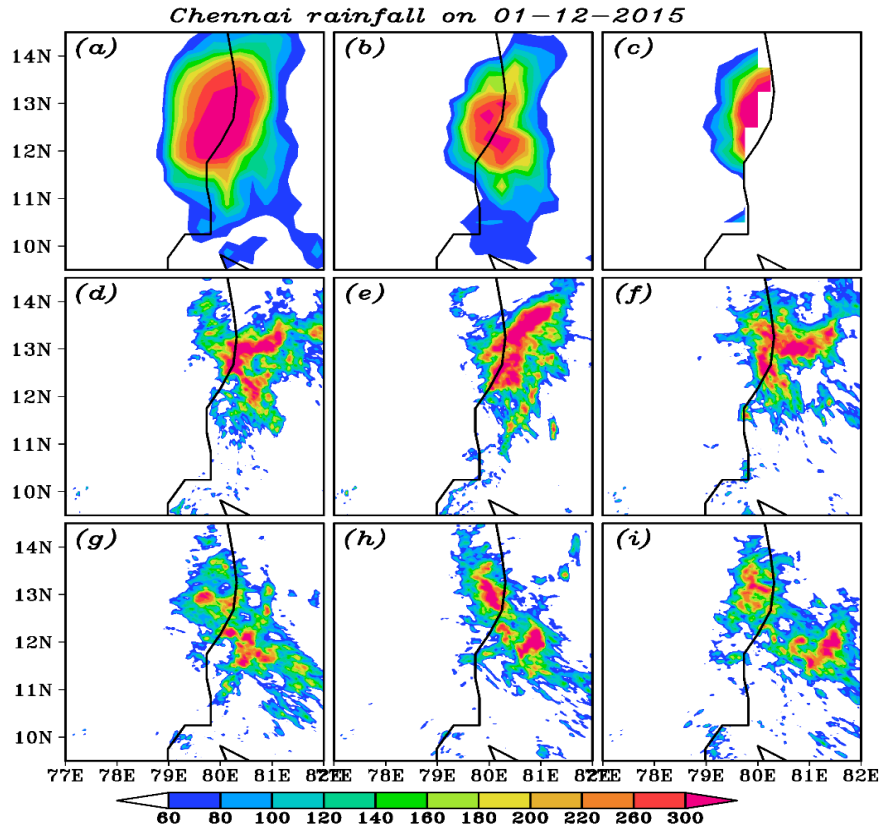

Figure 5.6: Spatial distributions of heavy rainfall over Tamil Nadu on 01 December 2015. Observations are shown in the top row panels, specifically, from (a) TRMM, (b) GPM-IMERG and (c) IMD daily rainfall (mm/day) observations datasets. The middle row panels show simulated daily accumulated rainfall (mm/day) from the simulations with (d) MODIS, (e) Old-ISRO, and (f) New-ISRO LULC lower boundary conditions with 30 vertical levels. The lower panes are same as those in middle row panels, but from corresponding simulations with 51 vertical levels.

The corresponding simulation of 24-hour accumulated rainfall on December 01, 2015 with the New-ISRO LULC simulation (Figure 5.7f) captures the location and the north-south orientation (shown with arrow mark) of the heaviest 24-hour rainfall and asymmetries (Figure 2a and 2b, respectively of Srinivas et al., 2018) reasonably well simulation with the New-ISRO LULC. However, the simulations with the MODIS and Old-ISRO LULC (Figure 5.7d, e) instead show a southeast-northwest orientation of the aforementioned rain band. All three simulations, though, simulate about 20% - 25% less rainfall that as reported by the Doppler Weather Radar as well as the automatic weather stations over Chennai.

For the Telangana ERE, the peak 24-hour accumulated rainfall was concentrated over the north-western part of Telangana (Figure 5.8a-c) on September 24, 2016. The area and magnitude of peak rainfall is slightly different across the three observational datasets (Figure

5.8a-c). The corresponding simulation with the New-ISRO LULC over Telangana state (Figure 5.8f) is comparable with the IMD observations in terms of the magnitude and area of the extreme rainfall. The simulated extreme rainfall with New-ISRO LULC is concentrated at 18.7°N and 78.2°E in conformation (shown with plus "+" mark) with the IMD observations (Figure 5.8c). It must, however, be mentioned that the simulated 24-hour accumulated rainfall with the New-ISRO LULC (Figure 5.8f) is an underestimate when compared with the corresponding GPM-IMERG rainfall estimate (Figure 5.8b). The MODIS and Old-ISRO LULCs (Figure 5.8d, e) simulations, to some extent, match better with the GPM-IMERG rainfall datasets in this case.

Figures 5.9a-c show the spatial extreme rainfall patterns over the Kerala state from the observational datasets of TRMM, GPM-IMERG and IMD. One can see that the heaviest rainfall is concentrated in the central and southern parts of Kerala on August 15, 2016 (Figure 5.9b and c), with a general westward extension of the rainfall into the Arabian Sea. All the three observational datasets look qualitatively similar (Figures 5.9a-c), though the magnitude of the maximum rainfall is much weaker in the TRMM rainfall. We find from Figures 5.9b and 5.9c that the maximum zone of rainfall (shown in circle) extended from around 10.9°N till 9.1°N in a narrow northwest-southeast direction (shown in arrow mark).

The corresponding simulations in general capture the general areal extent of the rainfall, including its extension into the Arabian Sea from the Kerala coast. However, the simulated the maximum rainfall is slightly weaker in than observations (Figure 5.9c) around 10.5°N (Figures 5.9d, e, and f). Importantly, the simulation with the New-ISRO LULC (Figure 5.9f) can be seen to extend up to 9.1°N, unlike the other two simulations.

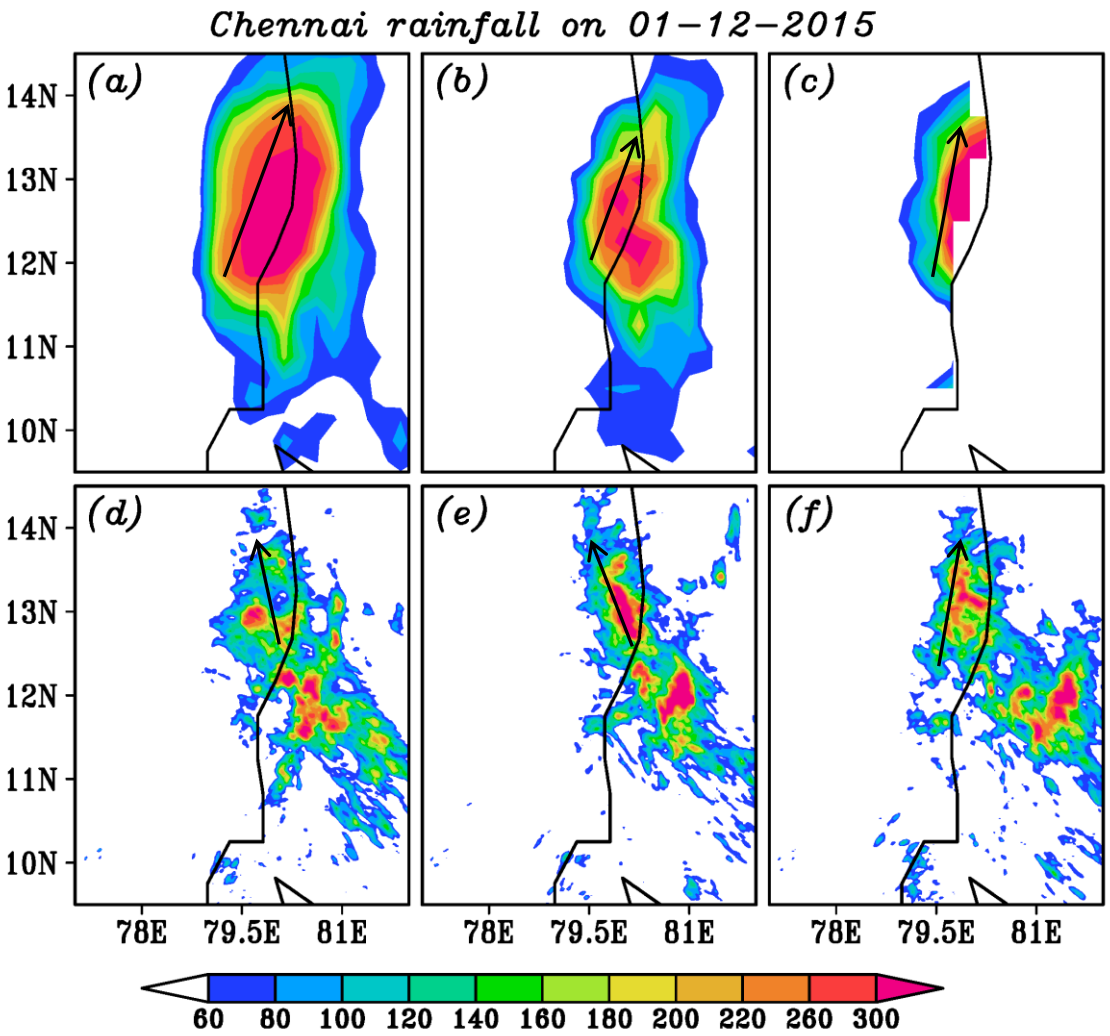

Figure 5.7: Spatial patterns of the rainfall over Tamil Nadu on December 01, 2015, during the Chennai heavy rainfall event. The first row shows the observed daily rainfall (mm/day) from (a) TRMM, (b) GPM-IMERG, and (c) IMD datasets. The second row shows the corresponding daily accumulated rainfall (mm/day) from the simulations with the LULC datasets of (d) MODIS, (e) Old-ISRO, and (f) New-ISRO. The arrows indicate the north-south orientation of the rainfall bands.

We have now computed the correlations between the hourly GPM-IMERG rainfall on the peak rainfall day, and that from relevant simulations, for the three representative events (Figure 5.10). The correlations are computed for eight hours (the peak hour and seven hours prior to that). Our analysis suggests that the areal extent of regions with positive correlations (0.72) that are significant at 95% confidence level is higher with the New-ISRO LULC. This particularly applies to the rainfall maxima regions.

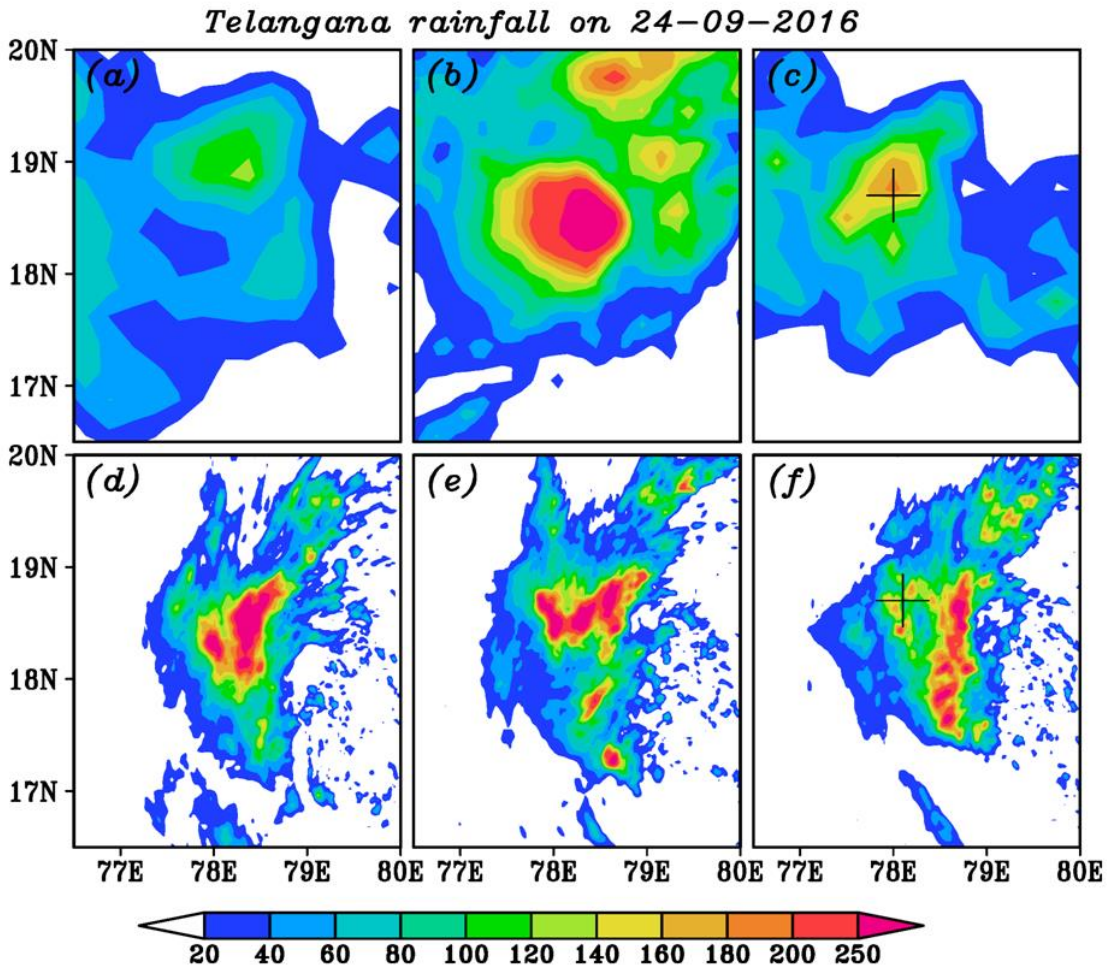

Figure 5.8: Same as Figure 5.7 but it is over Telangana, during the Telangana heavy rainfall event, on September 24, 2016. The plus (+) mark indicates the peak rainfall area in IMD observed and New-ISRO LULC simulated rainfall.

While ascertaining the significance levels for correlation values, we have confirmed that the observed hourly rainfall, over the eight hours over which the correlations are calculated, are subject to autocorrelation at many grid points for each of the case. Based on the resultant number of degrees of freedom, is coincidentally found to be 4 for all cases. Thus, a correlation magnitude of 0.72 (0.60) is significant at 95% (90%) confidence level from a one-tailed Student's t-test. All these suggest that the model performance improved with the updated LULC.

Based on our results so far, we can state that various simulated rainfall characteristics of the three representative EREs such as the spatial distribution and asymmetries somewhat better

simulated using the New-ISRO LULC, relative to those with the MODIS and Old-ISRO LULCs.

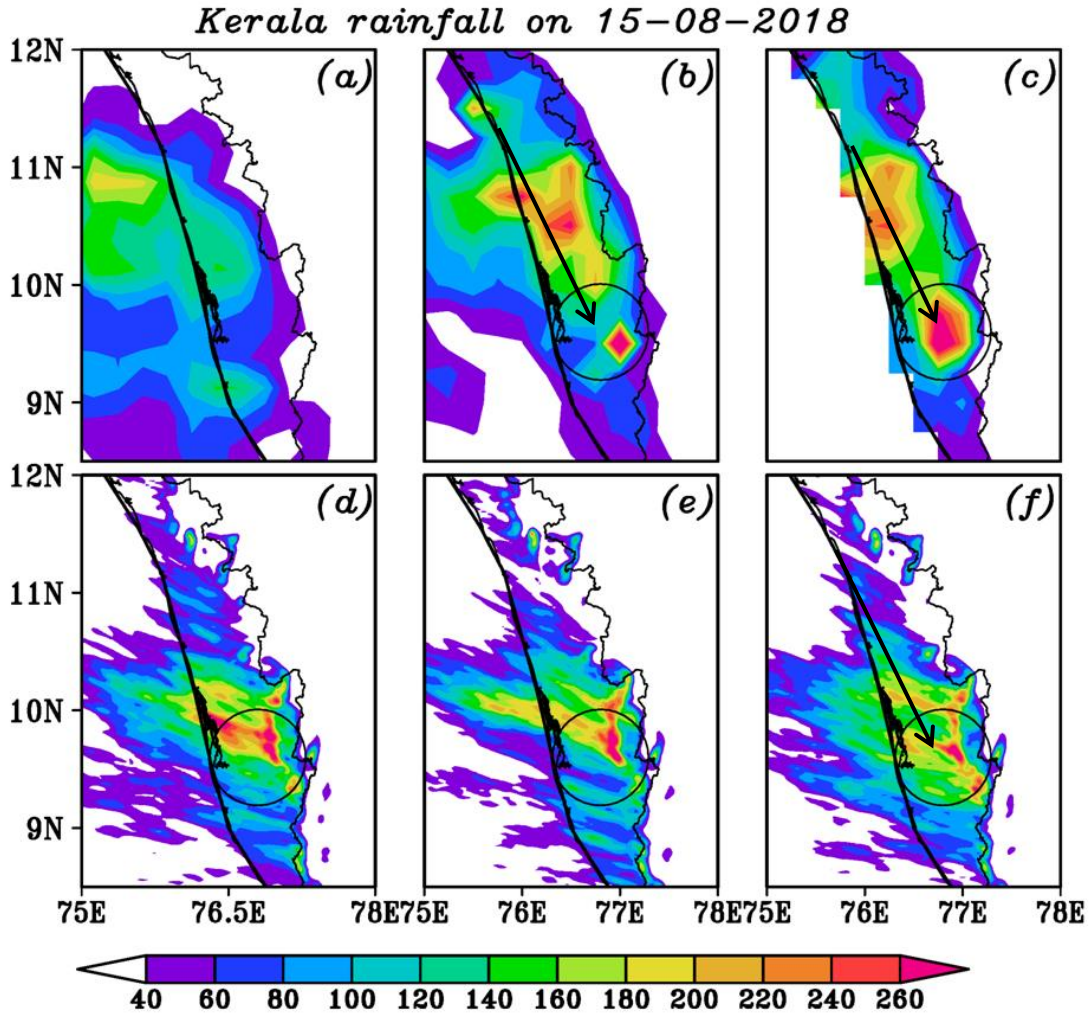

Figure 5.9: Same as Figure 5.7 but it is over Kerala, during the heavy rainfall event on August 15, 2018. The arrows indicate the northwest-southeast orientation of the rainfall band and the circle shows the high amount of rainfall concentrated area.

5.7 Simulated moisture, vorticity, zonal and vertical wind analysis

The available moisture in the atmosphere is a major factor in for any ERE (Brimelow and Reuter, 2005; Pathak et al., 2017; Yang and Smith, 2018). The dynamical and physical processes that facilitate the transport of the moisture are also important factor. A co-location of the maxima of simulated vertically integrated moisture, low level vorticity, and upward vertical motion with the location of the observed rainfall is a strong indication of the fidelity of the model. In this context, it is useful to examine the implications of any changes in the LULC to

the moisture pathways that contribute to the extreme rainfall. To this end, we have analyzed the simulated vertically integrated (integrated from surface to 300 hPa) moisture fluxes and their transport, these results are shown in Figures 5.11, 5.13 and 5.15. We also analyze the corresponding various kinematics to understand the spatial patterns of the large-scale circulation (Figures 5.12, 5.14, and 5.16) for all three extreme rainfall events with different LULCs.

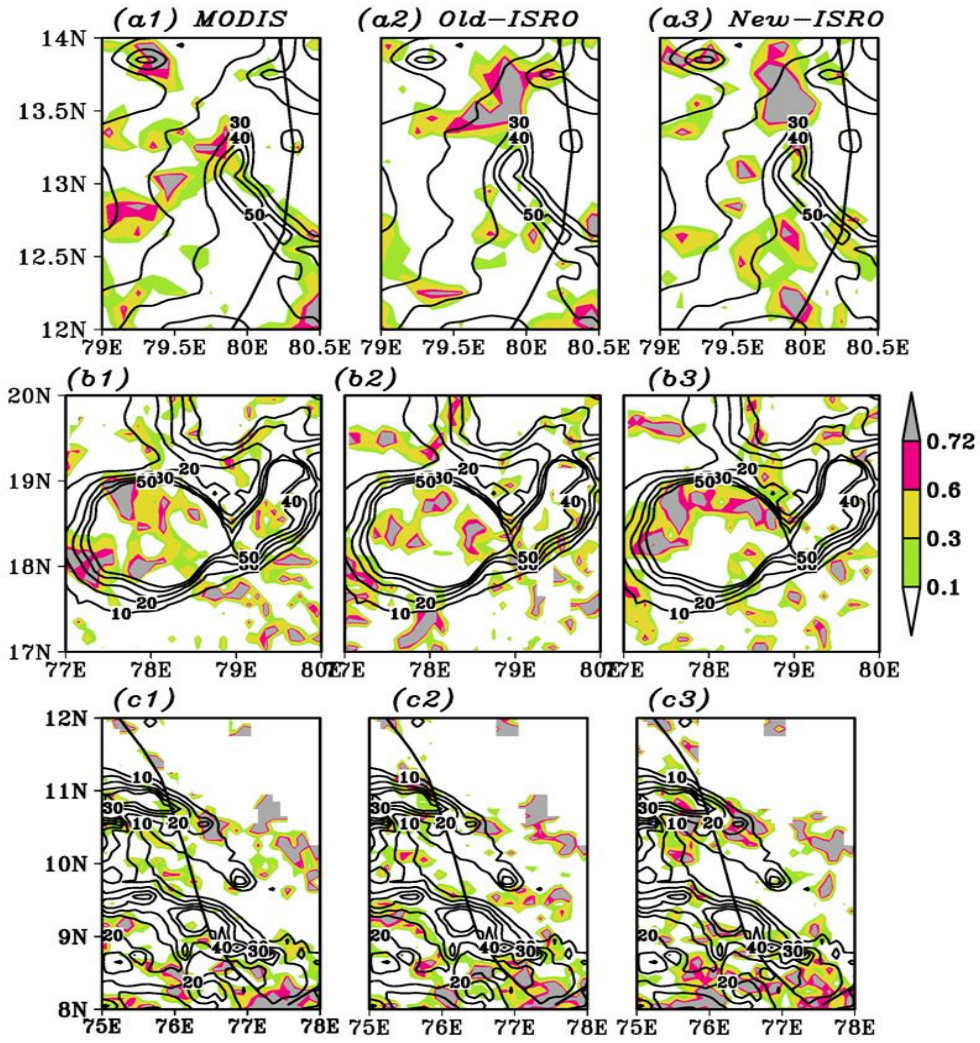

Figure 5.10: Correlation between the GPM-IMERG and model-simulated rainfall from the three experiments MODIS, Old-ISRO, and New-ISRO over Tamil Nadu (a1-a3), Telangana (b1-b3), and Kerala (c1-c3) during the eight rainfall hours. The shaded color shows the only the positive correlation values and the contour lines show the sum of eight rainfall (mm) hours from GPM-IMERG. The pink (gray) color indicates 90% (95%) confidence level from a one-tailed Student's t-test.

Our analysis of the hourly evolution of the vertically integrated moisture (VIM) from the ERA5 reanalysis for all three extreme rainfall events (Figures 5.11d, 5.13d, and 5.15d) suggest that the

moisture convergence regions are mostly smooth in ERA5, likely due to the relatively coarser resolution. In contrast, the corresponding model results are associated with asymmetries. Notwithstanding this, the large-scale directions of the moisture transport vectors (Figures 5.11, 5.13, and 5.15) as well other features such as the zones of moisture convergence in the observations and corresponding model simulations show relatively similar patterns.

We present a brief analysis of the moisture availability, and its transport during the peak of the Chennai extreme rainfall event, both from the ERA5 datasets and our simulations, in Figure 5.11. From the ERA5 datasets, we find the moisture from the adjoining BoB being transported towards the land region of the northern part of Tamil Nadu during the peak rainfall hours of the (Figure 5.11d) Chennai extreme rainfall event. The simulations (Figures 5.11a-c) broadly reflect these low-level wind moisture transport features. However, the spatial distributions of the VIM over Tamil Nadu from the all simulations (Figures 5.11a-d) are different from one another. During the peak rainfall hours, the VIM is concentrated around 12.5°N - 13.5°N in all the simulations (Figures 5.11a-d). Notably, the New-ISRO LULC simulation indicates a maximum zone of VIM oriented north-south over the coast along northern part of Tamil Nadu, and the adjoining BoB (Figure 5.11c). This is in agreement with not only the location and orientation of the simulated rainfall during the peak hours (Figure 5.7f), but to some extent with those of the observed rainfall (Figures 5.7a-c). The other two experiments with the MODIS and Old-ISRO LULC, on the other hand, simulate the VIM more over the inland. Furthermore, the corresponding simulated zonal wind, relative vorticity, and upward motion at 850 hPa during the peak rainfall hours of Chennai extreme rainfall event are shown in Figure 5.12. The experiments with MODIS and Old-ISRO LULC datasets (Figure 5.12a and b) simulate relatively weak low-level magnitudes of vorticity and vertical wind relatively over the north coastal Tamil Nadu as compared to that over more inland, which is associated with the shift of vertical moisture into inland (Figures 5.11a and b). The New-ISRO LULC experiment (Figure 5.12c) simulates a broad region of vertical wind concentrated over

the coastal area, which conform to the simulated as well as observed highest rainfall (Figures 5.7b and c).

Figures 5.13 and 5.15 show the reanalyzed as well as simulated VIM, and moisture transport for the Telangana and Kerala extreme rainfall events during the peak rainfall time, respectively. The corresponding low-level vorticity and circulation are shown in Figures 5.14 and 5.16, respectively. The ERA5 reanalysis datasets show two discrete spatial maxima of VIM over Telangana at 19°N - 20°N, 79°E, and 18°N - 19°N, 77.8°E regions during the peak rainfall hours in the ERA5 dataset (Figure 5.13d). The VIM is better simulated by the New-ISRO LULC in these regions (Figure 5.13c). The second peak at 19°N - 20°N, 79°E is not so well captured in the simulations with the MODIS and Old-ISRO LULCs (Figures 5.13a and 5.13b). Theses simulations also overestimate the areal extent of low-level vorticity and vertical velocity maximums (Figure 5.14a and b) as compared to the New-ISRO LULC (Figure 5.14c), and apparently hence the higher observed heavy rainfall zone (Figure 5.8b).

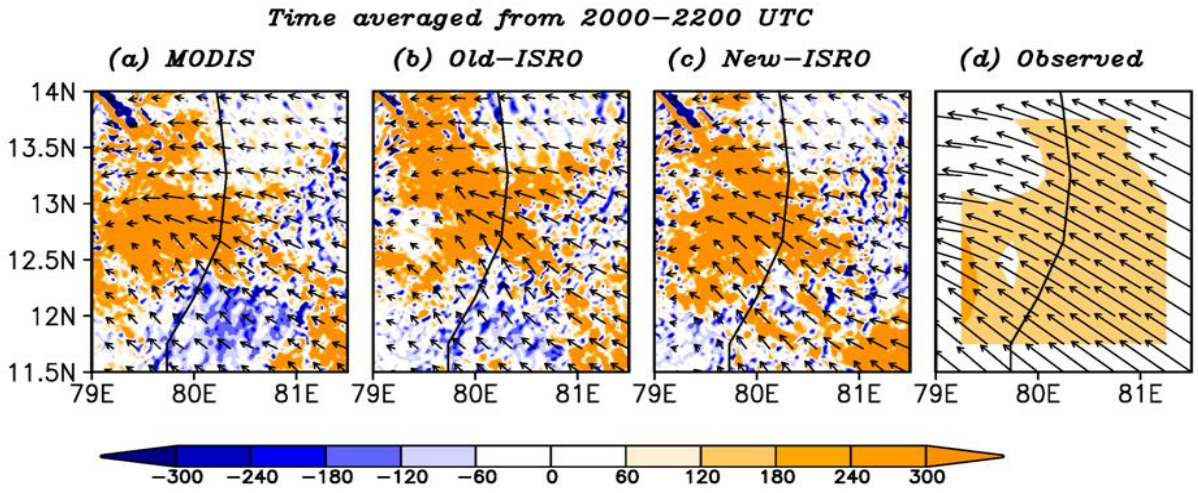

Figure 5.11: Spatial patterns of simulated vertically integrated moisture flux (10^{-6} kg m^{-2} s^{-1}) over Tamil Nadu during the Chennai heavy rainfall event. Positive and negative values indicate convergence and divergence, respectively. The wind vectors indicate moisture transport (kg m^{-1} s^{-1}). The panels (a), (b), (c), and (d) show results from simulations with the MODIS, Old-ISRO and New-ISRO LULC lower boundary conditions, and ERA5 observed datasets respectively, time averaged during the peak rainfall hours.

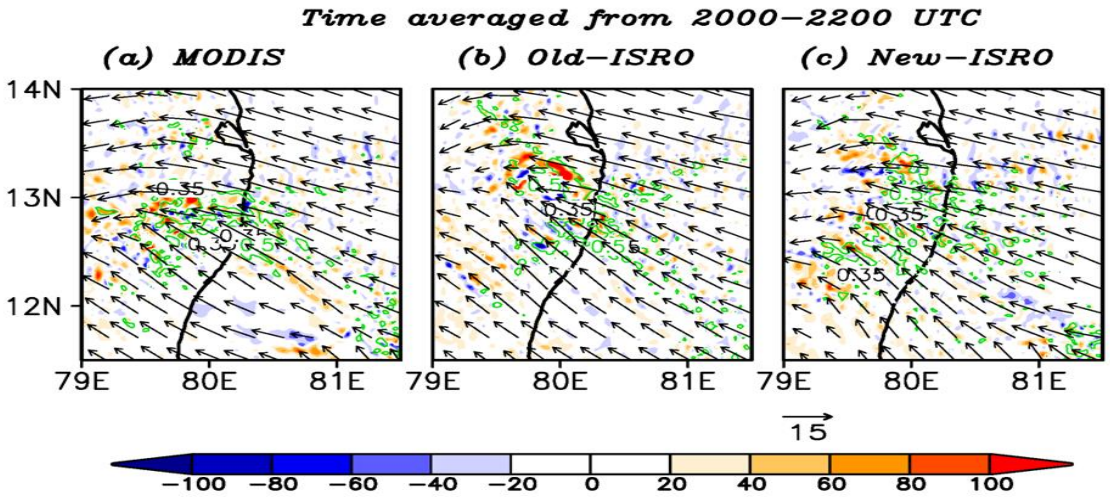

Figure 5.12: Spatial distribution of simulated vorticity (shaded), upward vertical wind (green contours) and zonal wind (vectors) at 850 hPa over Tamil Nadu during the Chennai rainfall event. The figures (a), (b), and (c) are from simulations with MODIS, Old-ISRO and New-ISRO LULC datasets, respectively, averaged during the peak rainfall hours.

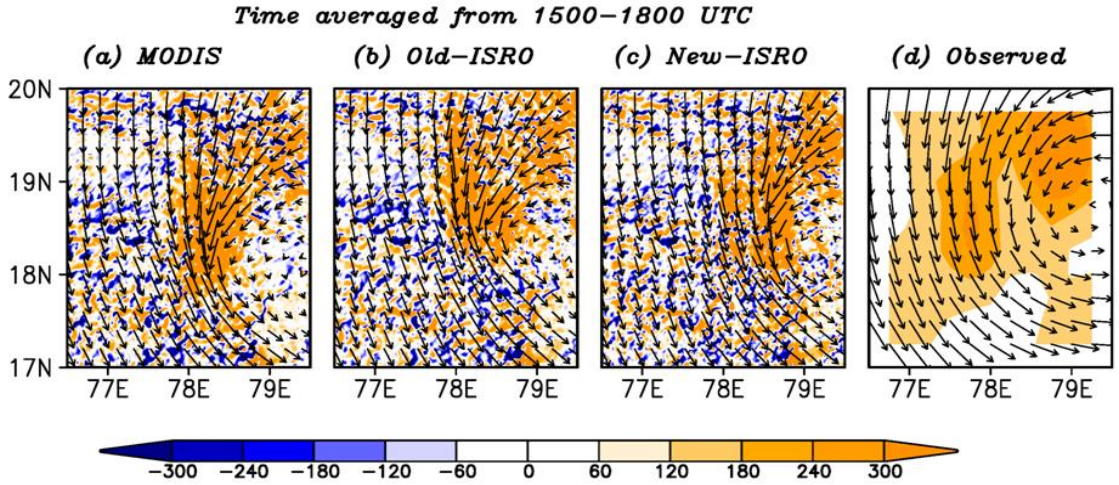

Figure 5.13: Same as Figure 5.11 but over Telangana during the Telangana heavy rainfall event.

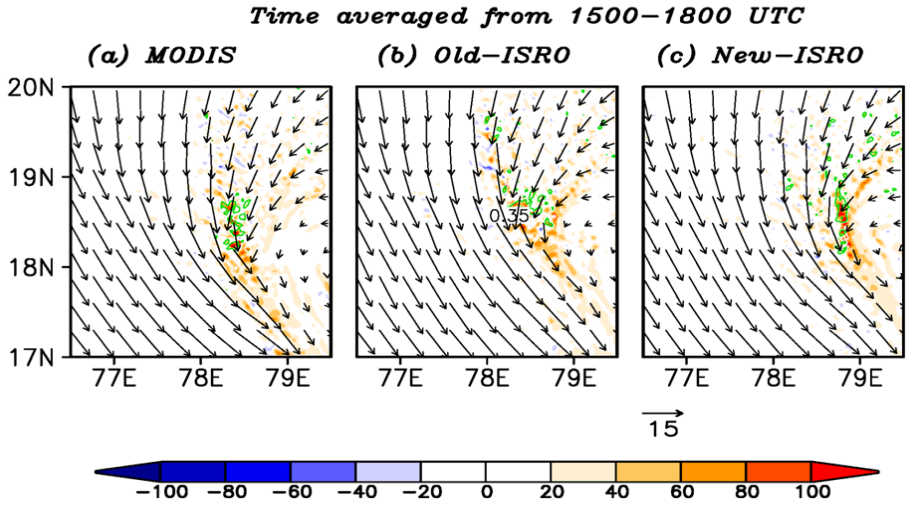

Figure 5.14: Same as Figure 5.12 but it is over Telangana during the Telangana heavy rainfall event.

For the Kerala heavy rainfall event, the VIM and its transport as deciphered from ERA5 dataset during the peak hour are shown in Figure 5.15d, and those from simulations in Figures 5.15a-c. The VIM is observed to be maximized at north and south of the coastal regions of Kerala during the peak rainfall hours, as per the ERA5 dataset (Figure 5.15d). The simulated vertically integrated moisture in the experiment with the New-ISRO LULC shows the simulated VIM extending from central through south coastal Kerala, but with an extension from into the Arabian Sea westward (Figure 5.15c). The northern peak of the VIM is not adequately simulated. Notwithstanding this, this simulated aspect is matching with the spatial rainfall maximum during the peak, which was observed over the South coastal Kerala (Figures 5.9b and c). The meridional width of the simulated VIM on the coastal Kerala in the corresponding of Old-ISRO LULC, just as the simulated rainfall is narrower than observed (Figure 5.15b). The MODIS LULC experiment is marginally better (Figure 5.15a). The simulated vertical wind and vorticity patterns are similar in all the respective LULC simulations for Kerala extreme rainfall event (Figures 5.16a-c).

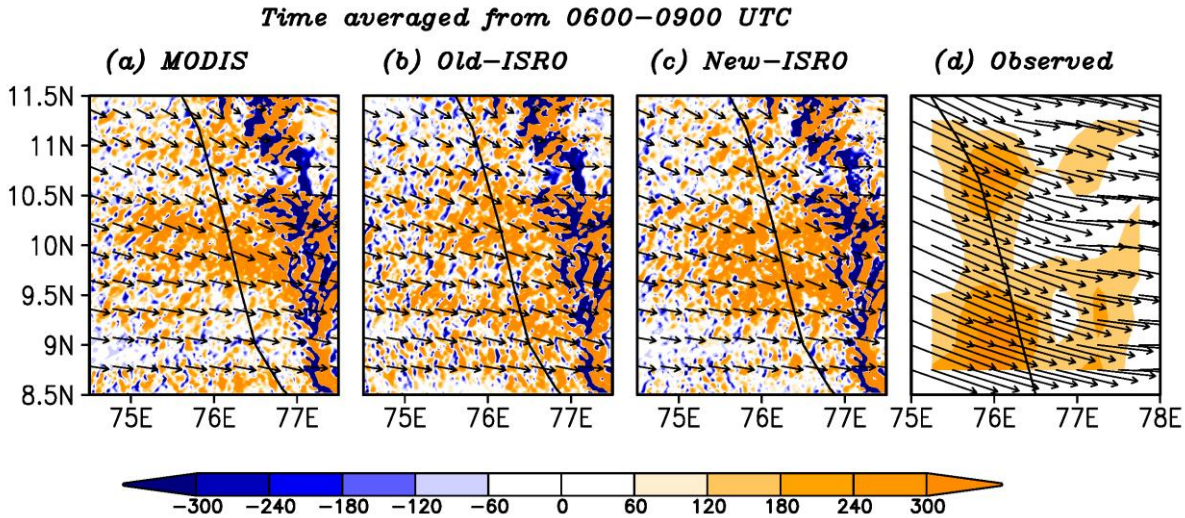

Figure 5.15: Same as Figure 5.11 but over Kerala during the Kerala heavy rainfall event.

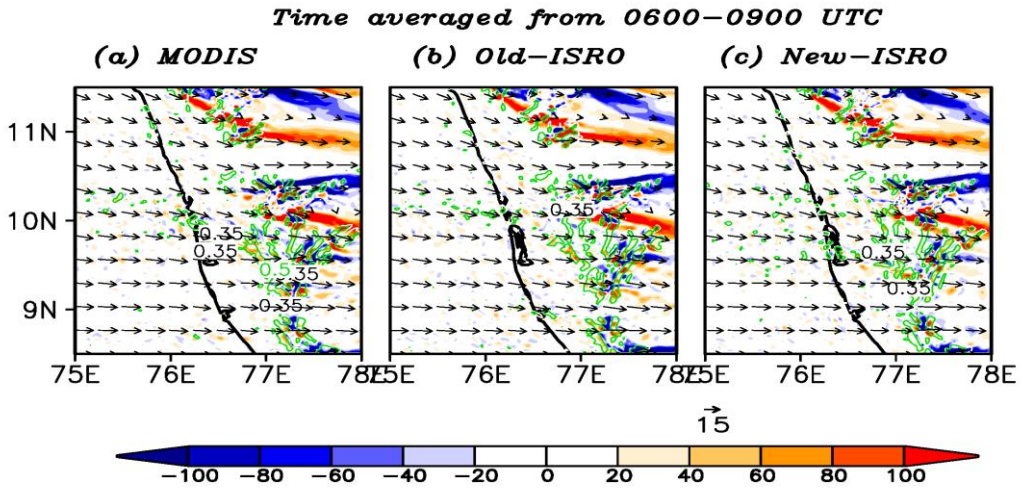

Figure 5.16: Same as Figure 5.12 but it is over Kerala during the Kerala heavy rainfall event.

The area averages of simulated vertical winds with height during the starting, peak and decaying stages of extreme rainfall hours of the three extreme rainfall events are shown in Figure 5.17. The vertical winds profiles over the three regions clearly show that a gradual increase in the vertical wind between the 800 hPa to 300 hPa levels with time. The maximum upward motion of the storm sustains for about 4 hours in all the cases, after which it starts decreasing, indicating the terminal stage of the life cycles of each of the systems. These higher vertical velocities at these levels are crucial for the vertical pumping of the moisture and deepening of the storm, thus for the extreme rainfall. These patterns are to some extent represented by the New-ISRO LULC based simulation relative to the other two experiments.

The above analysis suggests that the WRF model with New-ISRO LULC provides somewhat better realistic simulations of each of the three extreme rainfall events over southern India, as compared to the other two simulations with older LULC datasets. In the next sub-section, we investigate changes in the simulated physical processes associated with an updated representation of the LULC dataset, which result in relatively a better replication of the extremity of the rainfall as well as its temporal evolution.

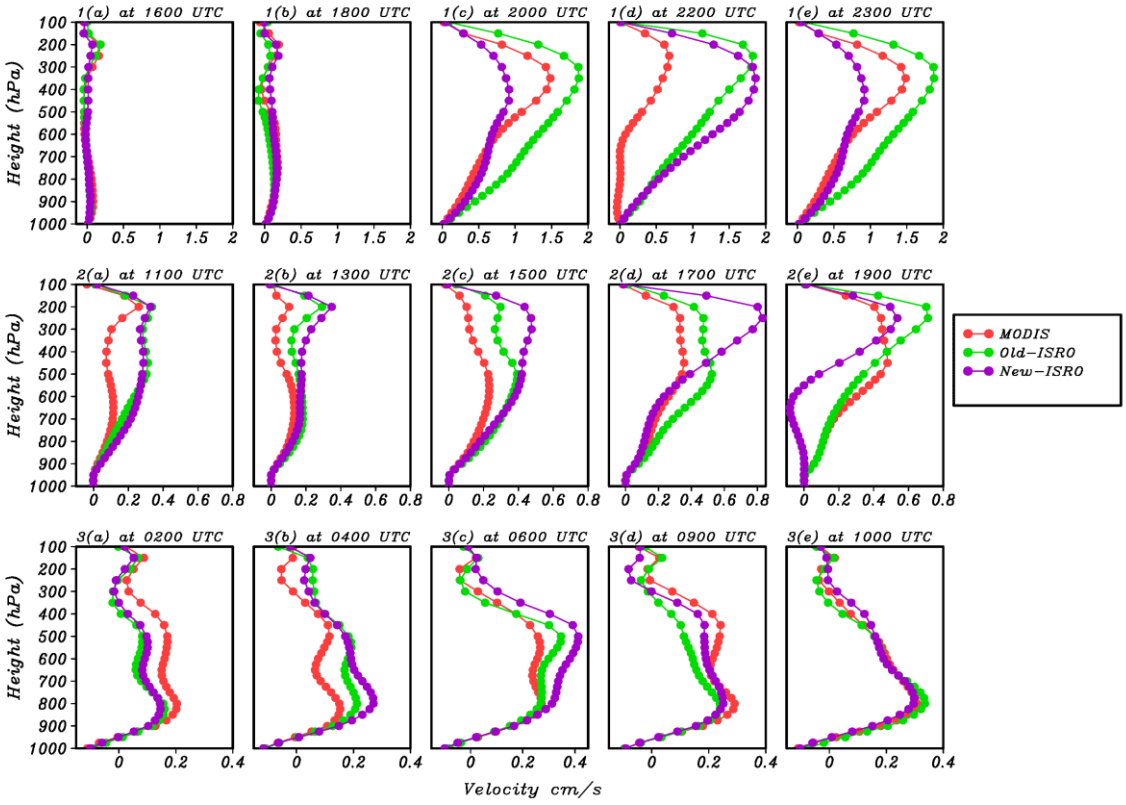

Figure 5.17: Area-averaged simulated vertical wind (cms^{-1}) profiles. The first row (1a-1e) pertains to the Chennai heavy rainfall event and values area-averaged over Tamil Nadu. The second (2a-2e) and third rows (3a-3e) are similar, but over Telangana and Kerala and pertain to respective representative events. The red, green and purple lines represent the simulations with MODIS, Old-ISRO and New-ISRO LULC lower boundary conditions, respectively. For a view of intra-stage evolution, these profiles are sampled twice during starting stage (1a-1b, 2a-2b, 3a-3b), thrice in peak (1c-1d, 2c-2d, 3c-3d), and thrice in decaying (1e, 2e, 3e) stages, respectively.

5.8 Implications of changes in LULC/Urbanization on the boundary layer processes during the extreme rainfall events

In the context of various studies that have suggested that the LULC changes resulted in increasing heavy rainfall events elsewhere through a change in the boundary layer processes and interactions (e.g., Zhang et al., 2007; Niyogi et al., 2017), we explore in detail the changes in the boundary layer processes associated with the changes in the LULC, which contributed to the extremity of the three EREs we discussed above. To do so, we analyze the differences in the simulated atmospheric variables such as the surface temperature, sensible heat flux, planetary boundary layer height (PBLH), water vapor, convective available potential energy (CAPE), and water vapor mixing ratio resulting from the Old-ISRO and New-ISRO LULC experiments, these results are presented in Figures 5.18 - 5.20.

For all the three extreme events, the New-ISRO LULC configuration simulates surface temperatures that are warmer by about 0.2°C to 0.5°C than those obtained with the Old-ISRO simulations (Figures 5.18a, 5.18a, and 5.20a). Such increases in surface temperatures result in increases in the corresponding sensible heat fluxes by about 20 - 40 W/m^2 (Figures 5.18b, 5.19b, and 5.20b). These higher surface temperature and sensible heat flux are associated with a deeper boundary layer height of about ~100 - 150 meters (Figures 5.17c, 5.18c, and 5.19c), higher water vapor mixing ratios of about ~0.2 - 0.5 g/kg^{-1} (Figures 5.18f, 5.19f, 5.20f), and high CAPE values around ~300 - 500 J/kg (Figures 5.18e, 5.19e, and 5.20e). The regions with lower surface temperature and sensible heat fluxes are, in contrast, associated with lower water vapor at the surface (Figures 5.18d, 5.19d, and 5.20d).

Importantly, for all three EREs, the regions with the higher surface temperature, sensible heat fluxes, boundary layer height, CAPE and water vapor mixing ratio are (Figures 5.18 - 5.20) seen with an increase in the urban/sub-urban zone (Figure 5.5c, 5.5f and 5.5i). The spatial distributions of the rainfall in the three cases also clearly indicate that the regions of extreme rainfall are located in/adjacent to the urban regions. This suggests that increasing urbanization in the peninsular India results in increased surface temperatures, sensible heat flux, PBLH, water vapor mixing ratio and CAPE, which, when released, results in the increased rainfall extremity (Figures 5.6, 5.7, 5.8). These results are in agreement with several recent case studies (e.g., Miao et al., 2011; Wan and Zhong, 2014; Yang et al., 2014; Zhong and Yang, 2015; Yu and Liu, 2015). This clearly suggests that the recent changes in LULC need to be accounted for in the advanced high-resolution mesoscale models reliably to predict the EREs.

To further substantiate our findings, in addition to the three representative EREs that we have discussed in detail so far, as mentioned earlier, we have performed several numerical simulations of the additional the earlier-mentioned nine additional EREs that had occurred over the three states (3 events over each state). The simulated area-average rainfall from these experiments, shown as the percentage of the corresponding observed IMD rainfall in Table 5.2,

varies from the observations by 20% - 25%. In contrast, the results from the Old-ISRO LULC experiments deviate substantially from the IMD observations. From this context, the simulations with the New-ISRO LULC can be deemed to be more realistic. We carry our further analysis to ascertain this point.

We investigated EREs from the IMD datasets, the area over which maximum rainfall, the peak day for each of the 12 considered cases (including the three sample cases), extends. We have then computed the area-averaged rainfall over these regions of maximum rainfall (Table 5.2). The corresponding values from all the simulations are also included. We have then calculated the correlations of the observational values with the corresponding simulations. While the correlation with the Old-ISRO LULC is 0.43, significant only at 90% confidence level, the corresponding correlation in the case of the New-ISRO LULC is a high 0.7 and significant at 99.95% level (Table 5.2). This strongly demonstrates that the use of the updated (New-ISRO) LULC has improved the simulation of extreme rainfall events.

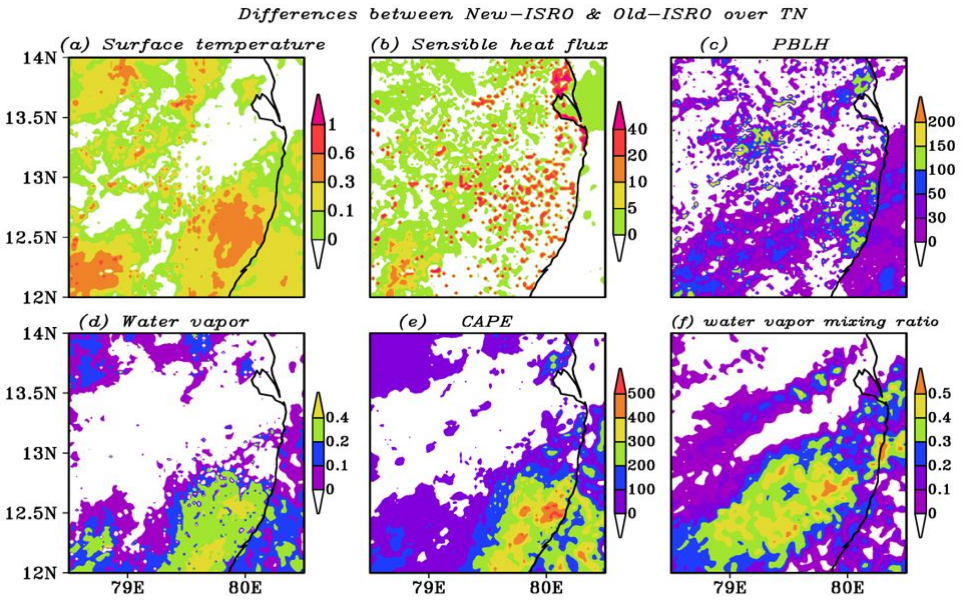

Figure 5.18: Difference plots over Tamil Nadu between Old-ISRO and New-ISRO LULC simulations, for the Chennai heavy rainfall event on 01-12-2015, of (a) surface temperature (°C), (b) sensible heat flux (W/m^2), (c) PBLH (m), (d) water vapor (g/kg), (e) CAPE (J/kg), and (f) water vapor mixing ratio (g/cm^2). The difference has been obtained by subtracting various parameters simulated in the experiment with the Old-ISRO LULC, from those from the corresponding New-ISRO LULC simulations.

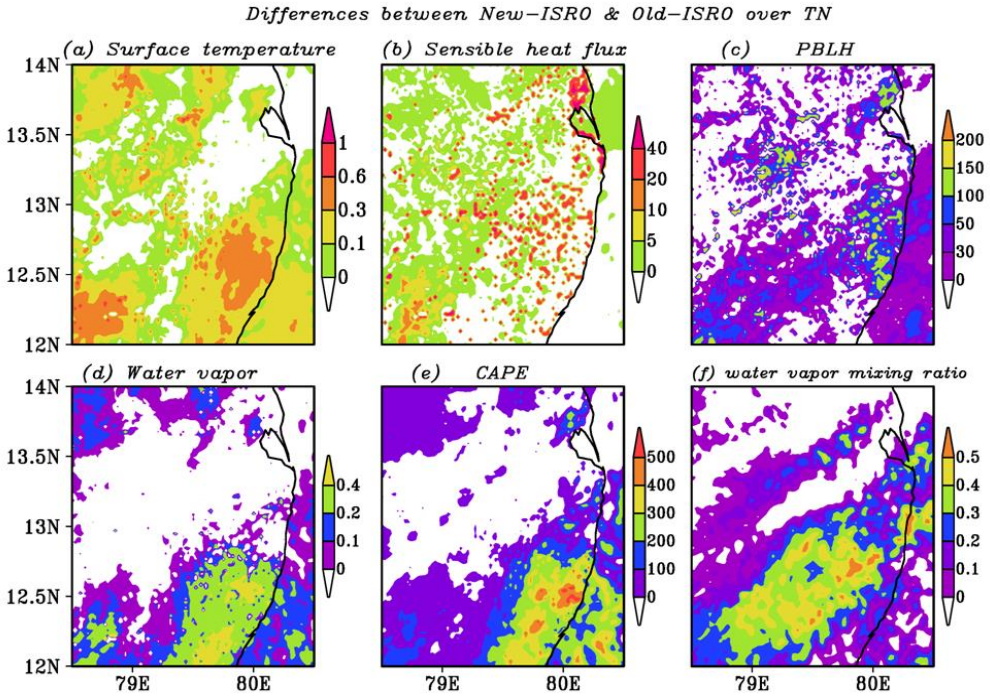

Figure 5.19: Same as Figure 5.16 but it is over Telangana, during the Telangana event on 24 -09-2016.

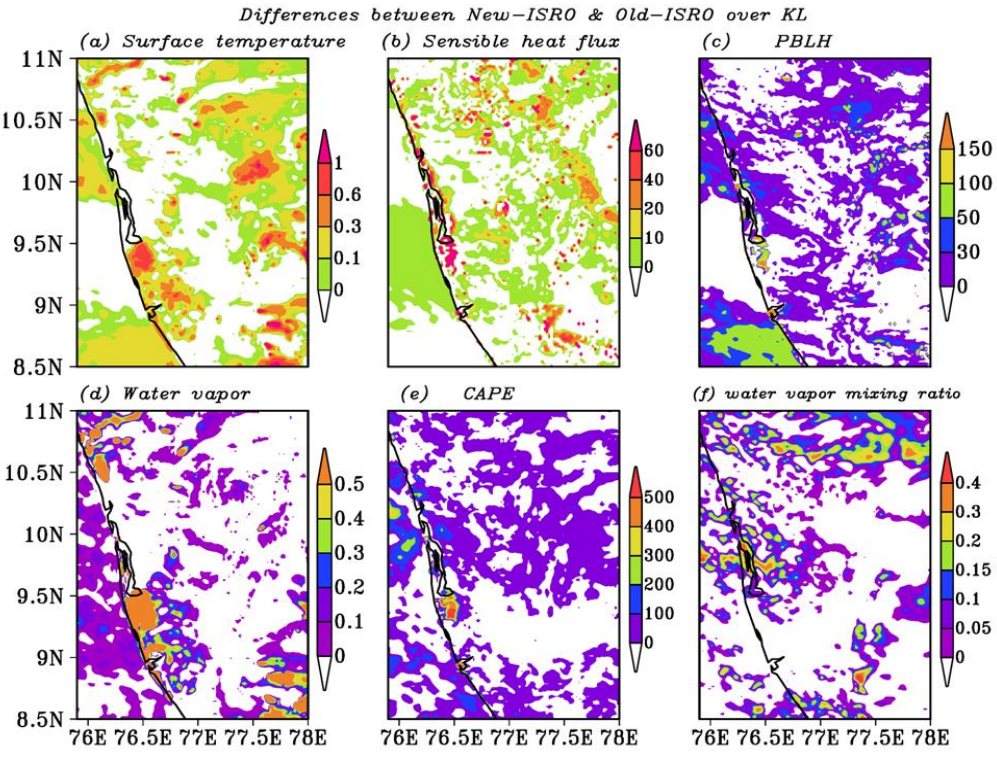

Figure 5.20: Same as Figure 5.16 but it is over Kerala, during the Kerala event on 15-08-2018.

Further analysis of the simulations for these nine heavy events also suggests that, just a for the three representative cases we presented in detail (Table 5.3), increasing urbanization has resulted in higher surface temperatures, larger sensible heat fluxes, and deeper boundary layer.

These changes in the boundary layer characteristics, mainly due to increased urbanization, can be deemed to have eventually led to increased extremity of the higher amount of rainfall of about 20% - 25%, as can be deciphered from the difference in simulated rainfall associated with the changed LULC (Table 5.2). Further, the analysis of these simulations clearly confirms that the changes in the LULC are critical for an accurate simulation, and potentially prediction, of an extreme rainfall event. This suggests that a realistic, updated LULC is important for the optimal simulations of extreme rainfall events, and presumably their prediction. More importantly, these results also clearly indicate that the recent changes in the local LULC are playing an important role in the local synoptic weather conditions over the three states.

Table 5.2: The area-averaged over the maximum rainfall (mm/day) of IMD observation and 12 experiments of Old-ISRO and New-ISRO over the regions of Tamil Nadu, Telangana and Kerala heavy rainfall events.

Events	IMD rainfall (mm/day)	Old-ISRO rainfall (mm/day)	New-ISRO rainfall (mm/day)
Oct-2017	125	29	75
Dec-2016	127	94	101
Dec-2015	180	54	83
Dec-2012	98	102	95
June-2016	75	53	60
Sept-2016	168	131	138
Aug-2013	36	61	42
Sept-2012	54	54	49
Aug-2018	99	91	99
Sept-2017	80	48	50
June-2016	49	39	44
Aug-2014	78	40	61
Mean value	**97.42**	**66.33**	**74.75**
Correlation with IMD values		**0.43 (90%)**	**0.79 (99.95%)**

Table 5.3: Shows the area-averaged values of surface temperature (°C), sensible heat flux (W/m^2) and PBLH (m) of New-ISRO and Old-ISRO LULC (in brackets) from 12 experiments for various Tamil Nadu, Telangana and Kerala heavy rainfall events.

Differences of New-ISRO and Old-ISRO over Tamil Nadu			
Events	Temperature (°C)	Sensible heat flux (W/m2)	PBLH (m)
Oct-2017	16.3 (15.2)	36 (30)	385 (359)
Dec-2016	24.7 (23.7)	24.7 (11.4)	524 (476)
Dec-2015	24.7 (24.3)	5 (2)	568 (506)
Dec-2012	23.5 (23)	22 (12)	562 (531)
Differences of New-ISRO and Old-ISRO over Telangana			
June-2016	27.8 (27.4)	55 (30)	673 (563)
Sept-2016	27.5 (26.8)	12 (-2)	556 (485)
Aug-2013	27.4 (26.4)	21 (-5)	520 (413)
Sept-2012	29 (28.5)	84 (64)	704 (667)
Differences of New-ISRO and Old-ISRO over Kerala			
Aug-2018	28.1 (27.7)	-3 (-8)	531 (495)
Sept-2017	23.5 (23)	-27 (-36)	364 (327)
June-2016	26.3 (26)	11 (8)	681 (635)
Aug-2014	25.5 (24.7)	46 (23)	566 (544)

5.9 Summary

In this chapter, through the analysis of observed datasets such as daily gridded rainfall datasets from of IMD, TRMM, and GPM-IMERG, we reported that the frequency of heavy rainfall events and 99 percentile of rainfall magnitude have significantly increased over three southern Indian states since year 2000. Also, we analyzed the available LULC data for the Indian region from the Advanced Wide Field Sensor (AWiFS) onboard the Indian satellite IRS P6 (IRS P6) for two years 2005 and 2017. An analysis of the IRSP6 LULC changes suggests that

urbanization has increased over the Hyderabad (Telangana), Chennai (Tamil Nadu) mega-city regions in addition to other LULC changes. The mixed forest turned into deciduous needle/leaf forest over Kerala, in addition to increased urbanization.

Such an LULC changes motivated us to explore whether the increasing urbanization has contributed to the extreme intensity of the rainfall events.

To this end, we identified twelve EREs, which have occurred in the last decade or so. Then, for each of these events, we carried out several numerical sensitivity experiments with the WRF. In all our experiments, we implemented a triple nesting configuration with a horizontal resolution of 2 km for the inner grid covering the state in question and neighborhood regions in order to capture fine features such as the rain bands, magnitude and location of the EREs.

For the sake of brevity, we focused on three representative EREs. The details of the three representative EREs have been well documented. These occurred, specifically, over (i) Tamil Nadu, mainly the Chennai city, with a peak on December 01, 2015, (ii) Telangana with a peak on September 24, 2016, (iii) and over Kerala with a peak on August 15, 2018. Several numerical experiments were performed using the WRF model in order to ascertain whether the recent LULC changes in these states have contributed to each of these three EREs.

Our numerical simulations suggest that the spatial rainfall patterns and asymmetries of extreme rainfall events are relatively better reproduced when the new LULC datasets of 2017 vintage provided by ISRO was used as a lower boundary condition instead of the default MODIS LULC of year 2001 vintage or even the ISRO 2005 LULC datasets. The simulations with the newest LULC lower boundary conditions facilitate realistic simulations of the observed extreme rainfall as well as that of fine features such as the asymmetric nature of rainfall distribution, concentrated rainfall over isolated regions, and meridional/zonal extension of rainfall, etc. The increase of the model resolution allowed resolving the urban effects more

accurately and further the asymmetries of extreme rainfall and higher intensity are likely occurred due to the accurate representation of LULC in the model.

The analysis of the simulations of twelve EREs, including the three focused events show that urbanization produces higher surface temperatures, larger sensible heat fluxes, a deeper boundary layer, higher water vapor, more water-vapor mixing in the boundary layer, and hence more convective available potential energy. The conducted sensitivity experiments suggest that about 20% - 25% of the rainfall in the recent EREs over southern India can be attributed to the changes in LULC/increased urbanization in the last decade. Our results also imply that up-to-date LULC boundary conditions, along with increased vertical levels, may also lead to an enhancement in the predictive skills of EREs over southern India.

In addition to investigate the impact of background mechanisms of SST and LULC changes on the extreme rainfall event, it is also import to explore the predictability of extreme rainfall events over southern India. In this context, I assimilated the satellite GPS RO refractivity profiles using WRF – 3DVar methods, and the findings are described in the following chapter.

Chapter - 6

Exploring the RO refractivity assimilation in improving prediction skills of extreme rainfall events in southern India in a regional climate model

In this chapter, we explored the importance of assimilating the observed GPS RO refractivity dataset in further improving the prediction skills of extreme rainfall events in southern part of India using a high resolution WRF-3Dimensional Variational (WRF-3DVar) technique.

6.1 Introduction

The ISM season has characterized by short duration EREs over various regions. To a certain extent, the vulnerability due to EREs can be mitigated by accurate prediction of EREs through the assimilation of observational data using advanced assimilation techniques in numerical weather prediction models (Mohanty et al., 2011). Several previous studies suggest that the predictability of EREs and their distributions can be improved by assimilating the synoptic, radiosonde, satellite based Global Positioning System Radio Occultation (GPS RO) datasets (Healy et al., 2005; Cucurull et al., 2006; Routray et al., 2010; Govindankutty and Chandrasekar, 2011; Srinivas et al., 2012; Kumar and Varma, 2016; Madhulatha et al., 2017).

Several researchers have used the WRF model to simulate EREs over various regions in India (Rao and Ratna, 2010; Srinivas et al., 2018; Boyaj et al., 2020). The 3DVar assimilation method has been widely used for assimilation of observational data due to its computational efficiency (Sugimoto et al., 2009). In various studies, the 3DVar method has been used to assimilate conventional non-conventional observations to improve the initial state of mesoscale models (Gao et al., 2004; Xiao et al., 2005; Xiao and Sun, 2007; Abhilash et al., 2007; Routray et al., 2013; Prasad et al., 2014; Thiruvengadam et al., 2019). However, there is ample scope for improvement. Notably, several frontline studies in the field of forecasting have demonstrated that the assimilation of satellite GPS RO refractivity data substantially enhances the ability to forecast regional and global weather predictions (e.g., Healy et al., 2005; Kuo et al., 2004, 2005; Huang et al., 2005; Cucurull et al., 2006; Chen et al., 2009). Cucurull et al. (2006) suggest that uncertainty in the model forecasts can be significantly reduced after assimilating GPS RO refractivity data. The assimilation of GPS RO refractivity data has led to significant improvements in weather prediction by improving the quality of initial water vapor and temperature fields (Kuo et al., 2000, 2005; Huang et al., 2007).

As far as the assimilation of the satellite GPS RO refractivity for the Indian weather is concerned, Huang et al. (2007) investigated the impact of assimilating GPS RO refractivity data

using the WRF-3DVar system to predict rainfall over the west coast of India. Their results suggest that the assimilation of GPS RO data improve predictions of both the amount and location of rainfall. In particular, no study has explored the potential impact of assimilating satellite GPS RO refractivity data on the prediction of EREs over southern India. To address this gap, in this study, we conducted retrospective weather prediction experiments by using a 3DVar technique to assimilate GPS RO refractivity data into the WRF model to forecast EREs over three southern Indian states, namely, Tamil Nadu, Telangana, and Kerala (to see the geographical location of these states, please refer Figure 5.1). The selection of these three states was briefly described in the Chapter 5, section 5.1. For this analysis, we selected three EREs, specifically: (i) the ERE over the state of Tamil Nadu centered around Chennai city on December 01, 2015; (ii) over Telangana on September 24, 2016; and (iii) over Kerala on August 15, 2018.

6.2. Experimental design

We used the WRF model version 3.8.1 (Skamarock et al., 2008) and its three-dimensional variational (3DVar) module for assimilating the GPS RO data (Barker et al., 2004). The study area, synoptic observation of three EREs, the model setup including model domains (Figure 5.2), resolutions, and physical parameterization schemes are followed that of Chapter 5, section 5.2 and 5.3, which was tuned for simulating three EREs over southern India. The initial and lateral boundary conditions to WRF are taken from the National Centres for Environmental Prediction-Global Forecasting System (NCEP-GFS, henceforth GFS) data available every six hours at a resolution of 0.25°×0.25° (NCEP, 2015). A satellite-based geographical LULC dataset available at 30s resolution for the year 2017 and measured by the AWiFS on-board the Indian Remote-Sensing Satellite launched by the ISRO was used for the lower-boundary conditions (Biswadip, 2014).

To study the impact of assimilating satellite GPS RO refractivity profiles data, upper-air and surface weather observations on the ability to realistically predict the features of the three EREs

over southern India. The details of the assimilated observations are presented in the Table 6.1. In this chapter, we carried out four different types of experiments, specifically: (i) the control experiments with initial conditions from the GFS forecast data, but without any assimilation (henceforth CTL), (ii) assimilating only the satellite GPS RO refractivity profiles (henceforth GPSRO), (iii) assimilating all observations discussed in Table 6.1, except GPS RO data (henceforth NOGPSRO), and (iv) assimilating all observations discussed in Table 6.1 (henceforth ALLOBS). The initial conditions for all the simulations started 24 hours before the extreme rainfall day. For instance, during the Chennai ERE, the heaviest rainfall occurred on 01 December 2015, and thus the corresponding experiments were initiated at 0000 UTC on 30 November 2015. In the GPSRO experiment, we assimilated the GPS RO data into the WRF model at 0000 UTC on November 30, 2015. After assimilation, the model was integrated for two more days without assimilation. The outputs of the sensitivity experiments with and without the assimilation of the GPS RO data were then compared with the observations.

6.3 Predicted spatial rainfall distributions

For each of the three extreme rainfall regions, the spatial distributions of the daily accumulated rainfall from observations, CTL, GPSRO, NOGPSRO, and ALLOBS experiments are presented in Figure 6.1. At a first glance, it looks like from Figure 6.1 that the heaviest magnitude of the rainfall maxima has not been very well captured in all the experiments. However, the predictions show good skill in predicting the distributions and location of the heaviest rainfall. From the three extreme rainfall simulations (Figure 6.1), one can see that the spatial distribution of rainfall location and magnitude improved better after assimilation (GPSRO, NOGPSRO, and ALLOBS) than without any assimilation (CTL). Briefly, the fidelity of the ALLOBS forecast for each study region is either better than that from the corresponding NOGPSRO forecast or similar, as discussed in more details below. In addition, to quantify the skills of the assimilation of the satellite GPS RO refractivity data, we calculated the BSS index (equations 2.10 and 2.11), which compares the predicted rainfall with that from the GPM

hourly gridded rainfall observations over the three extreme rainfall regions (Figure 6.2). The widespread positive BSS values shown in Figure 6.2 indicates that the rainfall forecast improved after assimilating the GPS RO refractivity and other observed datasets.

Figures 6.1a-6.1d show the spatial distributions of the daily accumulated rainfall from the four experiments (CTL, GPSRO, NOGPSRO, and ALLOBS) for the Chennai ERE on December 01, 2015, the peak rainfall day (e.g., Boyaj et al., 2018; Srinivas et al., 2018). For the Chennai case, the AWS and IMD rain-gauge observations, Srinivas et al. (2018) catalogued point observations of the peak daily accumulated rainfall; the data are shown in Figures 6.1a-6.1d (black dots). In this extreme rainfall event, the heaviest rainfall of 492 mm has occurred in the coastal region around 13.35°N, 80.2°E, where the city is also located. Importantly, we observed another peak of 320 mm around 40-50 km southwards along the coast. The northern margin of the rainfall is again observed on the coast about 50 km north of the rainfall peak at 13.7°N, 80.25°E. This is in agreement with Srinivas et al. (2018) who reported rainfall occurred in isolated patches along the coast during this event. The areal extent of predicted rainfall from GPSRO (Figure 6.1b) is reasonable spread around the peak rainfall area. However, the simulated rainfall shows further spreads south and southwest, e.g., 12.2°N on the coast and also over inland northwest of it, inland from 12.2°N-13.2°N, 79.1°E-79.8°E region, where heavy rainfall was not reported by rain-gauge observations (black dots in the Figure 6.1b). Moreover, the isolated rainfall peak at 13.7°N, 80.2°E is not captured in this experiment. The NOGPSRO experiment captures the observed extent of the heavy rainfall (Figure 6.1c). The heaviest rainfall from this experiment, however, is contiguous along the coast, and extends southward into the Bay of Bengal, rather than in isolated clusters (Srinivas et al., 2018). Importantly, the ALLOBS experiment (Figure 6.1d) predicts the observed isolated extreme rainfall patches. This is also apparent in the corresponding BSS distribution (Figure 6.2c), which shows positive scores mainly confined to regions of extreme rainfall. This indicates that assimilation of satellite GPS RO refractivity in addition to other observations helps to better predict the

distribution of the isolated extreme rainfall regions. Interestingly, all the three experiments do not indicate positive BSS score over the isolated extreme rainfall recorded at a station located at 13.12°N, 80.06°E.

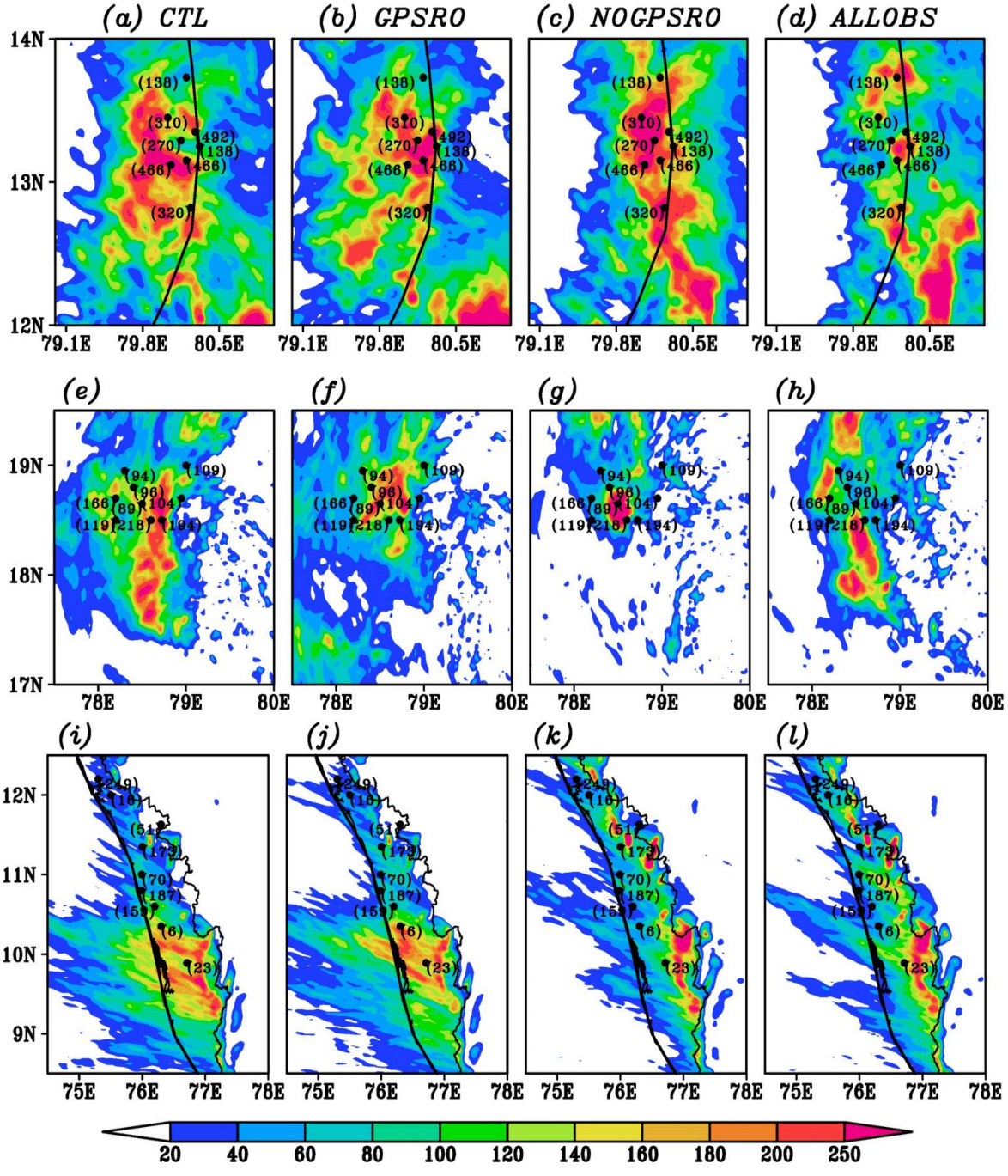

Figure 6.1: Spatial distribution of simulated and assimilated daily accumulated rainfall (mm/day), and AWS/rain-gauge stations rainfall magnitudes over the three study regions; Tamil Nadu (top panels), Telangana (middle panels), and Kerala (lower panels). The panels in first column (a), (e), (i), second column (b), (f), (j), third column (c), (g), (k), and fourth column (d), (h), (l) show rainfall resulting from CTL and GPSRO, NOGPSRO, and ALLOBS experiments, respectively over Tamil Nadu, Telangana, and Kerala.

Figures 6.1e-6.1h show the spatial distributions of the daily accumulated rainfall from the CTL, GPSRO, NOGPSRO, and ALLOBS experiments for the Telangana ERE on September 24, 2016. For the Telangana ERE, the IMD rain-gauge station rainfall data and Doppler weather radar datasets were not available. Fortunately, we had access to the rainfall data from the Bureau of Economics and Statistics, Government of Telangana. This Telangana AWS rainfall dataset shows that the heaviest rainfall on September 24, 2016 is concentrated over the north-western part of Telangana, between 78°E–79°E and 18.5°N–19°N (Figures 6.1e-6.1h, black dots). As seen in the Chennai case, similarly, in the Telangana ERE, the isolated extreme rainfall regions are better reproduced, with higher positive BSS values in ALLOBS (Figure 6.1h and Figure 6.2f) compared to GPSRO and NOGPSRO (Figures 6.1f, 6.1g and Figures 6.2d, 6.2e). For the Kerala extreme rainfall event, compared to GPSRO (Figure 6.1j), the spatial distributions of rainfall from the NOGPSRO and ALLOBS experiments (Figures 6.1k, 6.1l) are in much better agreement with the rain-gauge observations over the northern and central parts of Kerala where high rainfall was observed (black dots in Figures 6.1k, 6.1l). The spatial rainfall distribution in ALLOBS is only marginally better relative to the NOGPSRO experiment, and the BSS skills are similar (Figures 6.2h, and 6.2i). This is likely due to the fact that the satellite GPS RO profiles available for assimilation for this event are relatively less as compared to the other two extreme events (Table 6.1).

In all the three EREs, combining the satellite GPS RO refractivity profiles with the other observations lead to improved rainfall prediction skills in terms of isolated extreme rainfall regions, particularly for the Chennai and Telangana extreme events.

In the next subsection, we analyse the underlying mechanisms behind the improved prediction due to the assimilation of satellite GPS RO refractivity data.

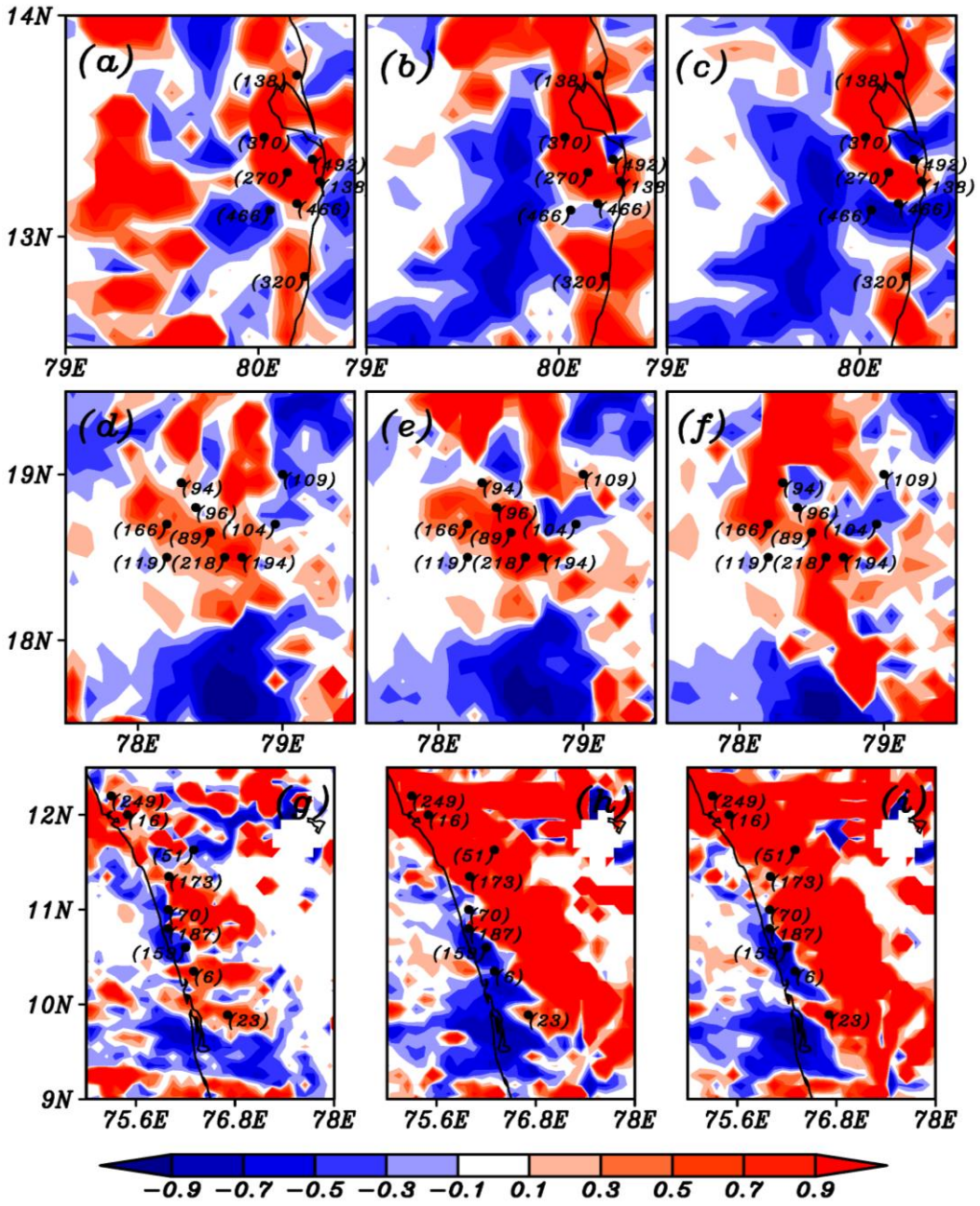

Figure 6.2: Spatial distributions of Brier Skill Score (BSS) between the GPM (observed), CTL, GPSRO, NOGPSRO, and ALLOBS experiments rainfall for the three extreme rainfall events over Tamil Nadu (top panels), Telangana (middle panels), and Kerala (lower panels). The first column shows BSS between the GPM, CTL, and GPSRO, the second column shows BSS between GPM, CTL, and NOGPSRO, and the third column shows the BSS between the GPM, CTL and ALLOBS experiments. The blue and red color shades represent positive and negative BSS values. The black dots indicate the location of AWS/rain-gauge station and corresponding rainfall magnitude over three respective extreme rainfall regions.

6.4 Diagnosis of mechanism behind improvements due to assimilation of GPS RO data

In this subsection, we analyze the underlying mechanisms behind the improved prediction due to the assimilation of GPS RO data. At the location of the heaviest observed daily accumulated rainfall in each of the three cases, the height–longitude and height–latitude distributions of the

differences in temperature and water vapor between the ALLOBS and NOGPSRO experiments are plotted in Figures 6.3 and 6.4. We show the temporal variations of wind shear, time-height sections of vertical winds, and relative humidity at the maximum rainfall locations recorded over the three regions in Figures 6.5 and 6.6. In addition, we investigated the dynamic mechanisms behind the EREs using the vorticity tendency equation (Figures 6.7, 6.8, and 6.9). We also determined the locations of the heat sink and source flux regions (Figure 6.10) for the three EREs. Finally, we analysed Skew-T Log-P diagram (Figure 6.11), and calculated the predicted mixing ratios at the mature stage of each ERE (Figure 6.12).

6.4.1 Chennai extreme rainfall event

The two cross-sections of the differences between the temperature profiles from the NOGPSRO and ALLOBS experiments for the Chennai extreme rainfall are shown in Figures 6.3a and 6.3d. The ALLOBS experiment predicts warmer temperatures in the 800 ~ 650 hPa, and 450 – 350 hPa layers with cooler temperatures in the lower and mid-troposphere, that is, in the 1000 – 850 hPa and 650 – 500h Pa layers (Figures 6.3a and 6.3d), compared to the NOGPSRO experiment. The ALLOBS experiment also shows a higher water vapor in the 900 – 800 hPa and 650 – 600 hPa layers, and signatures of lower water vapor in a narrow vertical extent at 700 hPa (Figures 6.4a and 6.4d). The ALLOBS experiment shows a relatively higher wind shear than NOGPSRO over the heaviest rainfall area (13.3°N, 80.2°E) during mature stage of the storm from 2000 UTC on December 01, 2015 (Figure 6.5a). Moreover, the time-height section of vertical wind at the location of the highest rainfall shows a strong vertical wind between 1000 to 400 hPa at 0000 to 0600 UTC, and during the mature stage of the storm i.e., from 2000 UTC in ALLOBS (Figure 6.6d, shaded) than the NOGPSRO (Figure 6.6a, shaded). The lower tropospheric relative humidity in ALLOBS just prior to the mature stage of the storm (Figure 6.6d, contours) is higher than that simulated by NOGPSRO (Figure 6.6a contours). These are the one of important reason for the heavier and realistic rainfall predicted by ALLOBS.

Furthermore, as mentioned earlier, we compute the contributions to the vorticity tendencies,

following Equation (1), over the heaviest rainfall locations (13°N–13.4°N, 79.9°E–80.3°E) at each vertical level on the peak rainfall day (December 01, 2015) for both NOGPSRO and ALLOBS. Figure 6.7 displays the time–height sections of these terms. In ALLOBS, the vorticity tendency (Figure 6.7f) shows higher cyclonic vorticity after 1900UTC. The vertical advection term (Figure 6.7h) from ALLOBS show higher values from 1900 UTC on December 01 relative to those from NOGPSRO (Figure 6.7c). The vertical advection is crucial for modeling the intensification of cyclonic vorticity (Dasari et al., 2017; Srinivas et al., 2018). The higher contribution to the vertical advection in the lower and middle troposphere, associated with the higher vertical velocity (Figure 6.6d), resulted in deep convection and extreme rainfall over that region. The stretching term (Figure 6.7i) is the representative of the vertical extension/stretching of the vortex show higher values from 1900 UTC in ALLOBS than NOGPSRO (Figure 6.7d). The horizontal advection (Figure 6.7b) and tilting (Figure 6.8e) terms are stronger in NOGPSRO. The reduction in strength of the tilting term in lower troposphere in the ALLOBS indicates that the vortex associated with the extreme events is relatively tilted less than it is in NOGPSRO, and tends to move towards the positive vorticity regions. The horizontal (vertical) advection terms show somewhat lower negative (higher positive) values in the lower troposphere from 1800 UTC onwards (Figure 6.7g, 6.7h), suggesting that the simultaneous occurrence of weak horizontal and strong vertical advection leads to the ascension of the vertical motion, resulting in a deepening of the storm.

The vertical profile of the rainfall distribution depends on the available moisture through the water vapor condensation (Yanai et al., 1973; Schumacher et al., 2007; Shige et al., 2007) and the associated heat source flux (Wong et al., 2011). We computed the vertically integrated (1000–300hPa) heat sink and source flux regions using Equation (2) from both NOGPSRO and ALLOBS for December 01, 2015 (Figures 6.10a, 6.10d). The vectors in Figure 6.10a and 6.10d are the vertically integrated heat source flux, which, in this case, travels from the Bay of Bengal into the land region in both experiments. The heat sink regions from ALLOBS (Figure 6.10d)

are consistent with the distribution of heaviest rainfall locations over Tamil Nadu (Figure 6.1d) relative to NOGPSRO (Figure 6.10a).

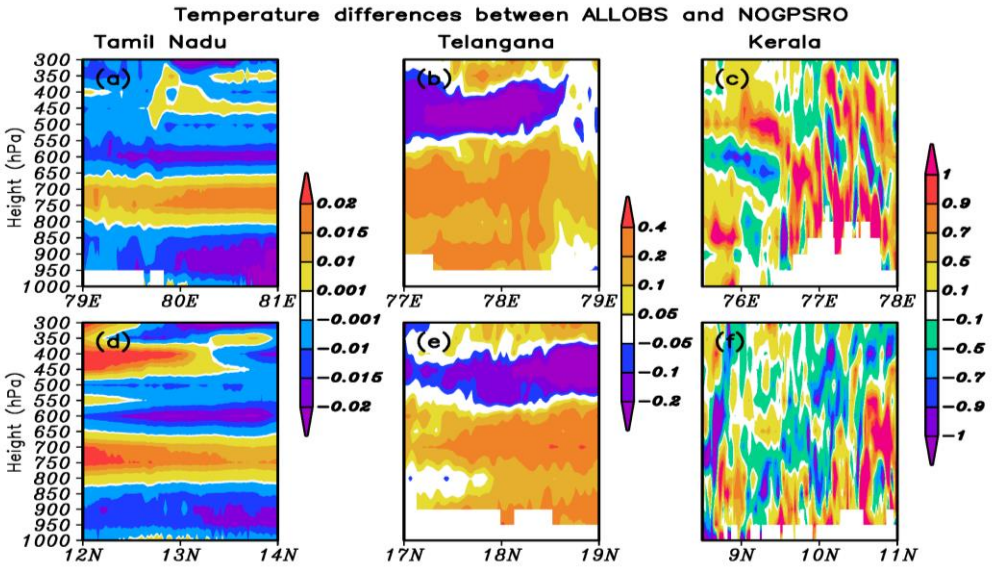

Figure 6.3: Vertical profile of temperature (°C) difference between ALLOBS and NOGPSRO (ALLOBS-NOGPSRO) experiments at the model initial time step for the three extreme rainfall events. The first column (a and d) shows the temperature differences over Tamil Nadu, along with longitude from 79°N to 81°N and at particular latitude of 13.3°N (a) and along with latitude from 12°N to 14°N and at particular longitude of 80.2°E (d). The second column (b and e) shows the temperature difference over Telangana, along with longitude from 77°E to 79°E and at particular latitude of 18.5°N (b) and along with latitude from 17°N to 19°N at particular longitude of 78.6°E (e). The third column (c and f) shows the temperature difference over Kerala, along with longitude from 75.5°E to 78°E and at particular latitude of 10.8°N (c) and along with latitude from 8.5°N to 11°N at particular longitude of 76.6°E (f).

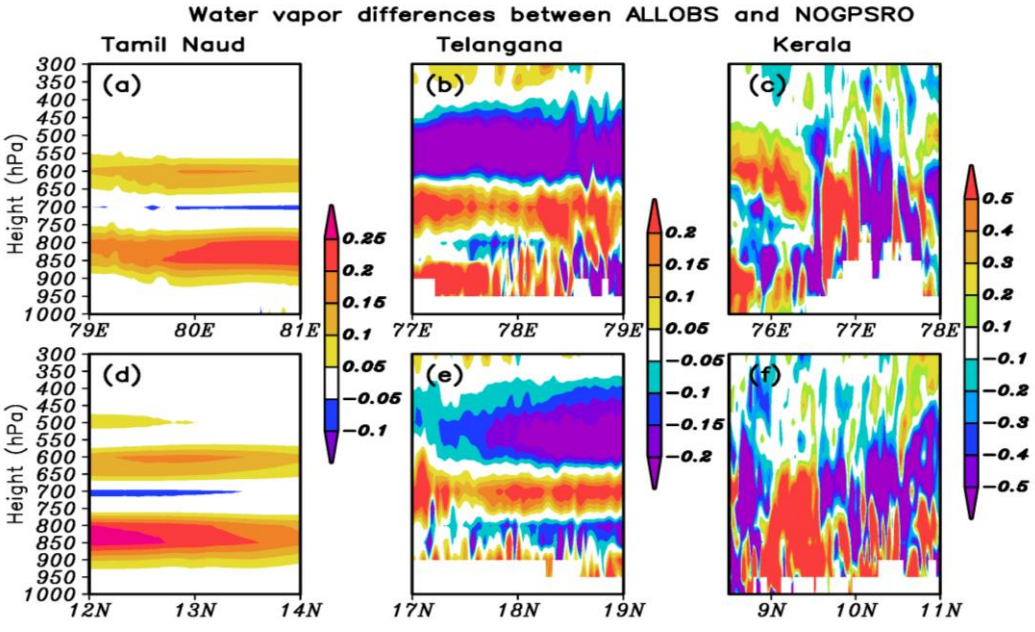

Figure 6.4: Same as Figure 6.3 but it is for water vapor (g/kg) over the three respective extreme rainfall regions.

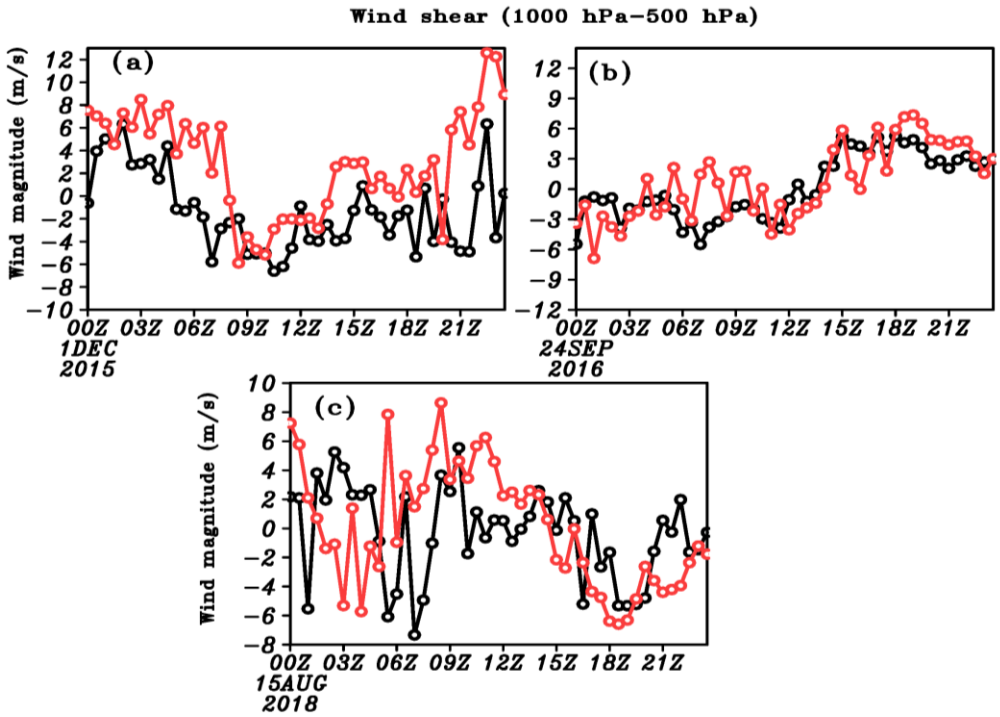

Figure 6.5: Time-series of vertical wind shear (m/s) during peak rainfall day over the three extreme rainfall regions. The total wind subtracted from 1000hPa-500hPa over (a) Tamil Nadu at 13.3°N, 80.2°E, (b) over Telangana at 18.5°N, 78.6°E, and (c) over Kerala at 10.8°N, 76.6°E. The black (red) color line indicates the NOGPSRO (ALLOBS) wind shears.

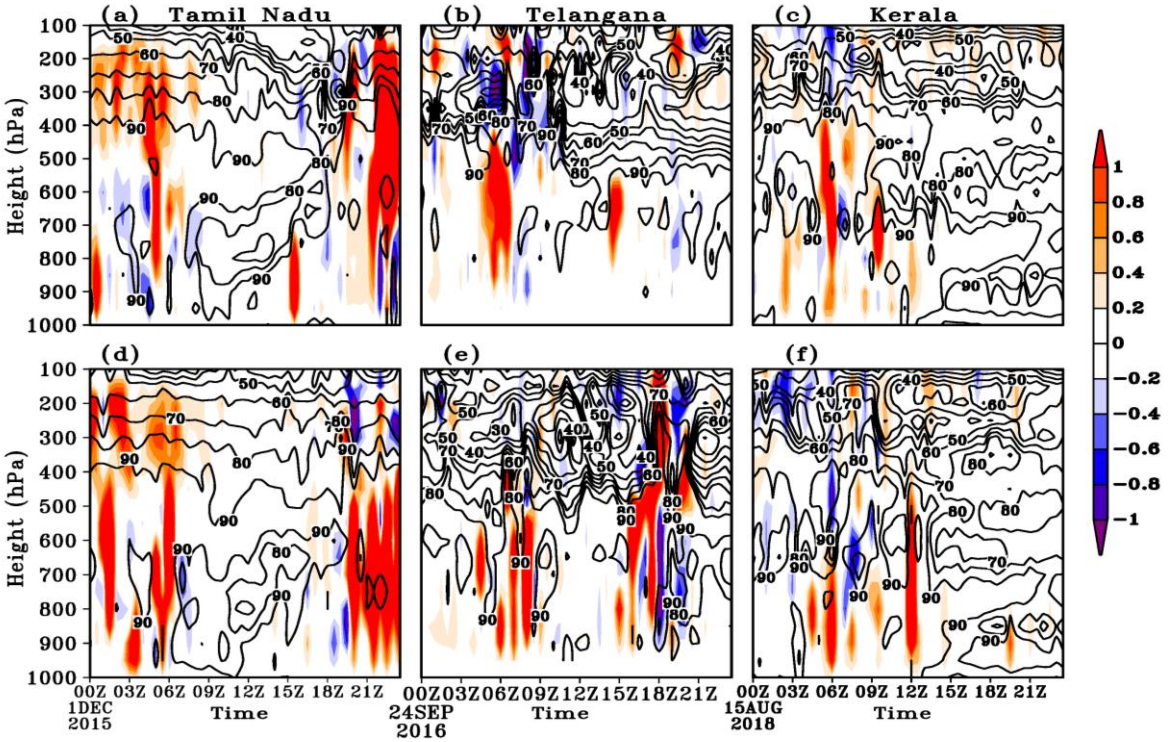

Figure 6.6: Time-height section of vertical wind (shaded) and relative humidity (contours) over Tamil Nadu at 13.3°N, 80.2°E (a, d), Telangana 18.5°N, 78.6°E (b, e), and Kerala 10.8°N, 76.6°E (c, f) regions on extreme rainfall day. First row (a, b, c) shows NOGPSRO and the second row (d, e, f) with ALLOBS experiments over the three regions.

6.4.2 Telangana extreme rainfall event

For the Telangana ERE, the temperature and water vapor differences between NOGPSRO and ALLOBS are shown in Figures 6.3b, 6.3e and 6.4b, 6.4e. The vertical distributions of temperature and water vapor differences over the Telangana region indicate the warmer (colder) temperatures and higher (lower) water vapor differences can be observed in the lower and mid (upper) troposphere in the ALLOBS experiment (Figure 6.3b, 6.3e, and 6.4b, 6.4e). The wind shear during the mature stage, which is between 0500 and 0900 UTC over the heaviest rainfall location (18.5°N, 78.6°E), is relatively stronger in ALLOBS (Figures 6.5b). Moreover, the time-height sections of vertical wind (Figure 6.6e, shaded) show stronger upward motion and marginally more relative humidity (Figure 6.6e, contours) in ALLOBS relative to those from NOGPSRO (Figure 6.6b) during the mature stage of the storm at 0500 – 0900 UTC, also it shows higher upward motion at 1600 – 2100 UTC.

In the ALLOBS experiment of the Telangana event, the corresponding time-height sections of vorticity, horizontal, vertical advection, stretching, and tilting terms (Figures 6.9f-j) over the heaviest rainfall location (18.3°N–19°N, 78.3°E–78.8°E) show, in general, processes similar to those seen in the Chennai case. However, the maximum values of verticity, vertical advection, and stretching terms (Figures 6.8f, h, and i) are higher from 800 hPa in this case, suggesting that the assimilation of satellite GPS RO data results in a stronger deepening of the storm. The vertically integrated heat source flux vectors show (Figure 6.10b, e, vectors) that the heat is transported from the north-western part of Telangana in the two experiments. The heat sink regions were slightly stronger in ALLOBS (Figure 6.10e, shaded) than in NOGPSRO (Figure 6.10b, shaded) experiment at 18.5°N, 78.6°E, which is consistent with the heaviest rainfall location in Telangana.

6.4.3 Kerala extreme rainfall event

Over Kerala, unlike in the other two cases, the temperature and water vapor differences between NOGPSRO and ALLOBS do not show uniform spatial patterns. The temperature

(Figures 6.3c, 6.3f) and water vapor (Figures 6.4c, 6.4f) analyses suggest that warmer temperatures and the presence of water vapor are concentrated over narrow regions. These sharp features are mostly associated with the orographic uplifting of convection due to eastward winds from the Arabian Sea. In this Kerala event, the temperature and water vapor in lower troposphere show relatively higher values in ALLOBS than NOGPSRO experiment (Figure 6.3c, 6.3f, and 6.4c, 6.4f). The wind shear from ALLOBS (Figure 6.5c) is slightly stronger during the mature stage of the storm i.e., at 0500 – 0900 UTC over the heaviest rainfall location (10.8°N, 76.6°E). The time-height section of vertical wind and relative humidity in ALLOBS (Figure 6.6f, shaded and contours) shows marginally strong vertical wind higher relative humidity between 1000 and 600 hPa during the mature stage of the storm. The time-height section of different terms in the vorticity budget analysis over the heaviest rainfall location (10.3°N - 11.3°N, 76.0°E - 77.0°E) in Kerala is shown in Figure 6.9. The contributions to the generation of vorticity from various vorticity budget terms in ALLOBS experiment are slightly higher (Figure 6.9f-j) than those from NOGPSRO (Figure 6.9a-e). In this case, these features persist longer than those of the other two events (Chennai and Telangana), in agreement with the fact that the rainfall over Kerala during this event was of longer duration (e.g., Viswandhapalli et al., 2019). Figures 6.10c and 6.10f plot the vertically integrated heat source (shown as arrows) coming from the Arabian Sea into the land region from both experiments. There is not much difference in the apparent heat sink/source flux over the Kerala region between the two experiments (Figures 6.10c and f, shaded).

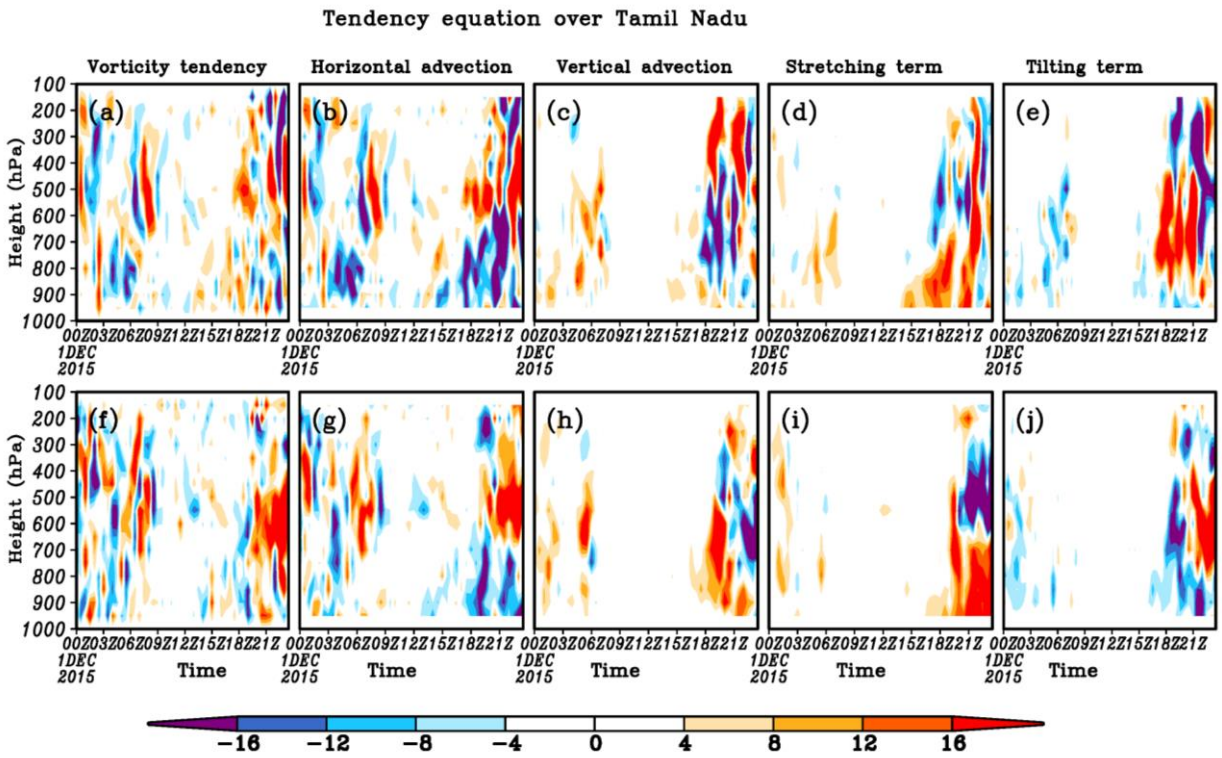

Figure 6.7: Time-height sections of area-average horizontal advection, vertical advection, vorticity tendency, stretching and tilting terms during the Tamil Nadu extreme rainfall event on December 01, 2015. As they result from NOGPSRO (first row) and ALLOBS (second row). The positive (negative) values represent the cyclonic (anti-cyclonic) vorticity.

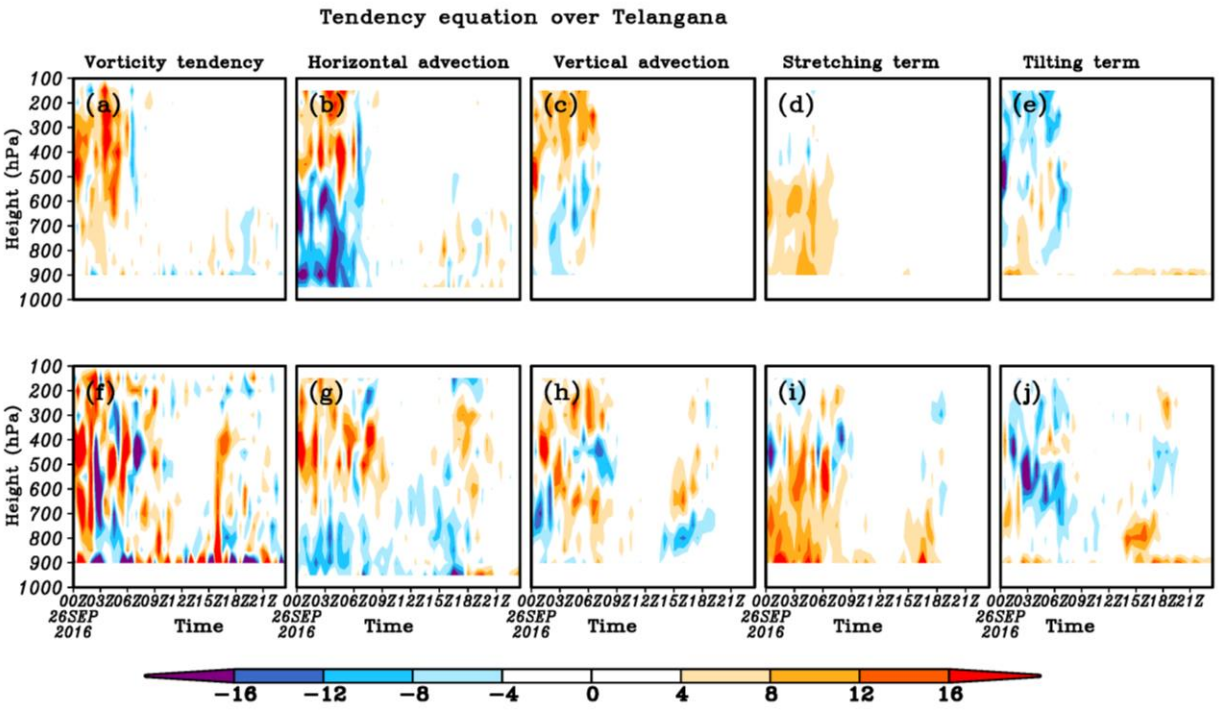

Figure 6.8: Same as Figure 6.7 but for the Telangana event on September 24, 2016.

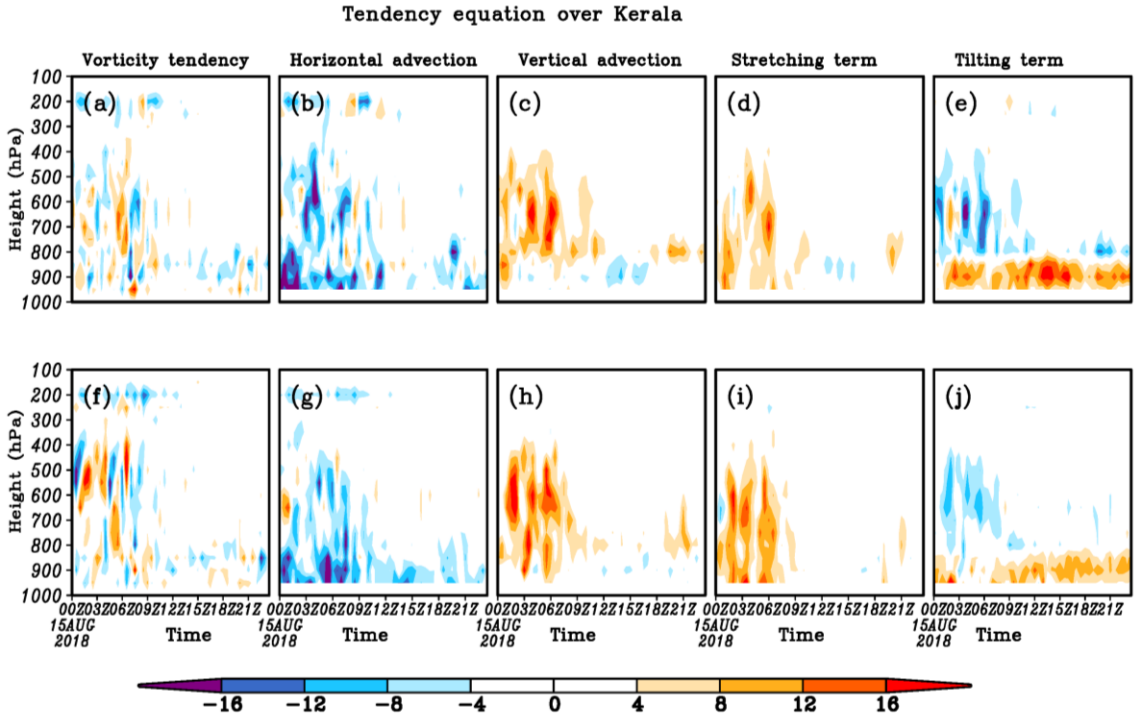

Figure 6.9: Same as Figure 6.7 but for the Kerala event on August 15, 2018.

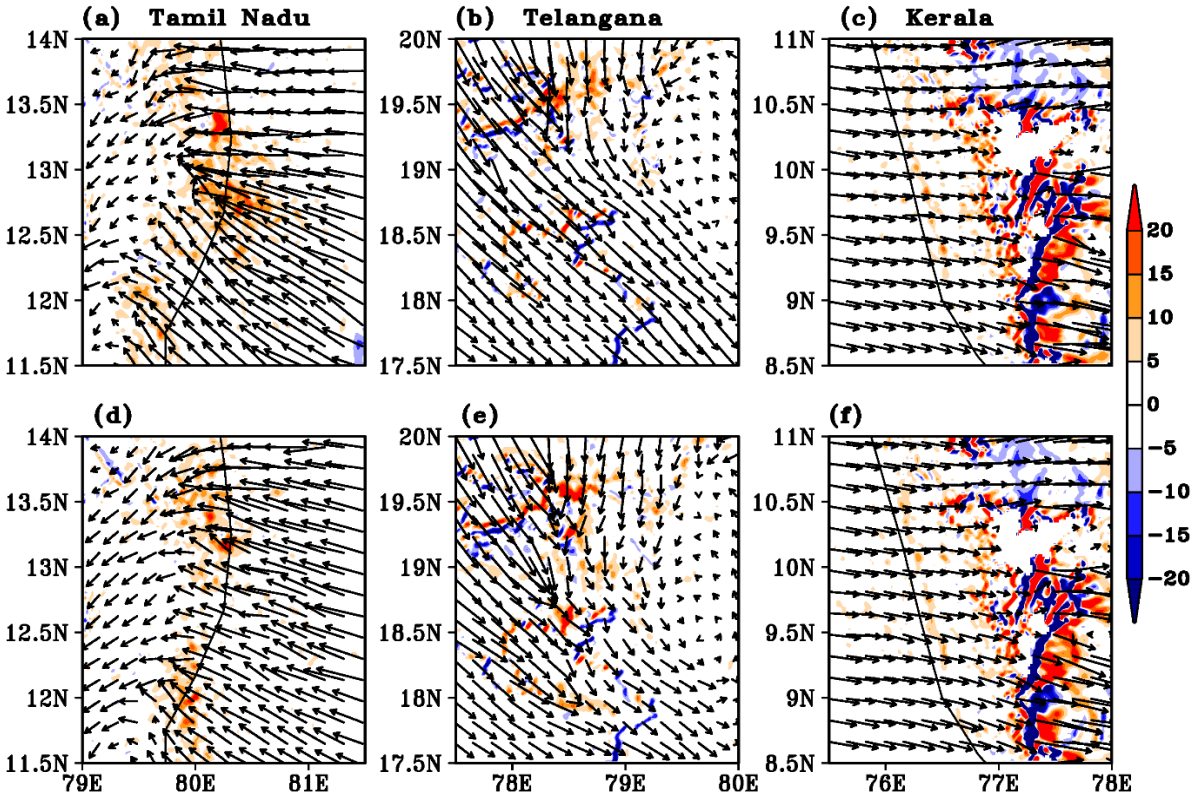

Figure 6.10: Vertically integrated (1000 to 300hPa) heat (°C) sink and source flux over Tamil Nadu (a, d), Telangana (b, e), and Kerala (c, f) regions on the respective extreme rainfall day. As they result from CTL (first row) and GPSRO (second row) over three regions. The positive values indicate the heat sink regions and vectors representing the heat source.

6.4.4 Analysis of Skew-T Log-P and mixing ratios for three extreme rainfall cases

The Skew-T Log-P diagram plotted over the heaviest rainfall locations one hour before the mature stages of the three EREs for NOGPSRO and ALLOBS are presented in Figure 6.11. In all three cases, the air-parcel temperature is ambient, indicating that the air parcel is forced to move upwards as moisture condenses out of the parcel. This warms the parcel and causes the saturation adiabat from the LCL to trend upward until the parcel becomes warmer than the surrounding air. The CAPE values resulting from the ALLOBS experiments for the Chennai, Telangana, and Kerala events are 1726 (J), 4140 (J), and 1102 (J), respectively (Table 6.2). These values are about 15%–25% higher than those from the corresponding NOGPSRO experiments. The LCLs from all three ALLOBS experiments are lower than those from the corresponding NOGPSRO experiments by 1-6 hPa, and the CCL are relatively higher (not shown). The higher CAPE values in the ALLOBS experiments are due to the convection of low-level warm (Figures 6.3d-6.3f) and moist (Figures 6.4d-6.4f) air. This causes the air parcels in the assimilation experiments to rise higher and consequently form higher vertical convective clouds demonstrates that the assimilation of satellite GPS RO data produces stronger convective clouds. The vertical distributions of wind exhibit somewhat similar patterns between the ALLOBS and NOGPSRO experiments for all three cases (Figure 6.11).

The vertical distributions of different mixing ratios from ALLOBS and NOGPSRO at the mature stage of each storm (Figure 6.12) indicate minor differences in water vapor. In the ALLOBS experiments show larger amounts of ice at the upper levels (Figures 6.12), cloud water at the middle level, and rain water at the lower levels suggests that the improvements in rainfall distributions with the assimilation of satellite GPS RO refractivity are mainly associated with changes in the vertical profiles of the hydrometers. This is mainly because deeper convection allows the water vapor to condense and reach higher levels, forming ice crystals and liquid water in clouds before triggering extreme rainfall. These changes in the dynamics and thermodynamics due to the assimilation of the satellite GPS RO data are critical

for the changes in the vertical distributions of the hydrometeor mixing ratios (e.g., water vapor, ice, clouds, and rainwater), which ultimately translate into better rainfall predictions for the three events.

Table 6.1 Types and number of observations assimilated for each of the three studied extreme rainfall events.

Observation type	Chennai event	Telangana event	Kerala event
Sound	61	75	74
synop	726	736	789
Pilot	24	28	20
geoamv	6315	7269	9388
gpsrf	2099	3834	774
metar	155	159	169
ships	25	35	31
buoy	34	33	16
sonde_sfc	61	75	74

Table 6.2: The CAPE and LCL from model simulations retrieved using the Skew-T diagrams.

Attributes	Chennai		Telangana		Kerala	
	NOGPSRO	ALLOBS	NOGPSRO	ALLOBS	NOGPSRO	ALLOBS
Convective Available Potential Energy (J)	1452	1726	3920	4140	850	1102
Pressure of the lifting condensation level (hPa)	999	995	966	960	999	964

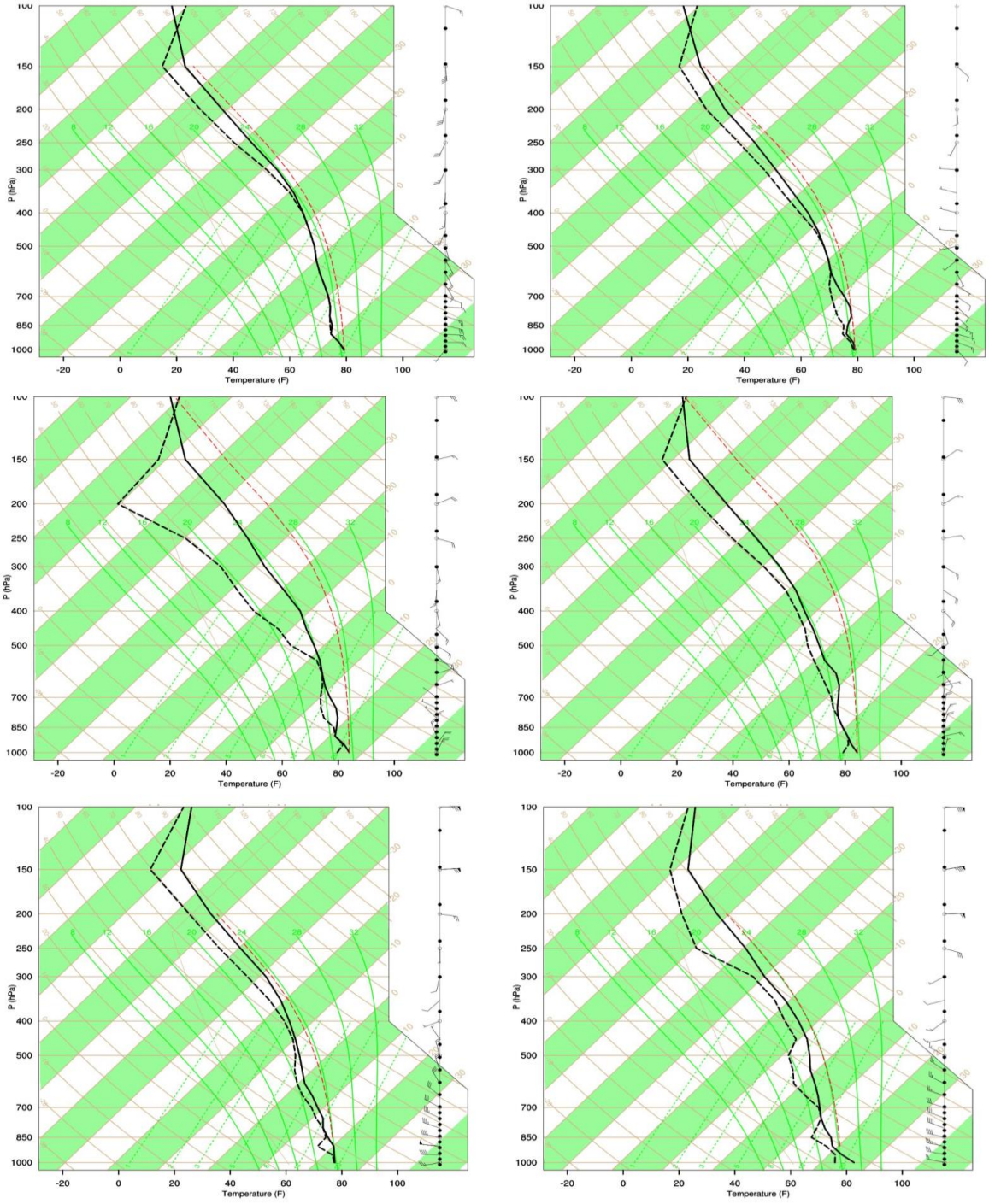

Figure 6.11: Skew-T Log-P diagrams from the NOGPSRO and ALLOBS experiments over the heaviest rainfall locations before (one-hour) the mature stages of the three extreme rainfall events. The top, middle, and bottom panels Skew-T plots represent for Chennai, Telangana, and Kerala respectively. The first column plots result from NOGPSRO and second column plots from ALLOBS experiments. The solid and dotted black lines represent the temperature and dew-point temperatures. The barbs on the right side of each Skew-T plot shows the wind speed (knots) and direction. The red dotted line represents the atmospheric lapse rate.

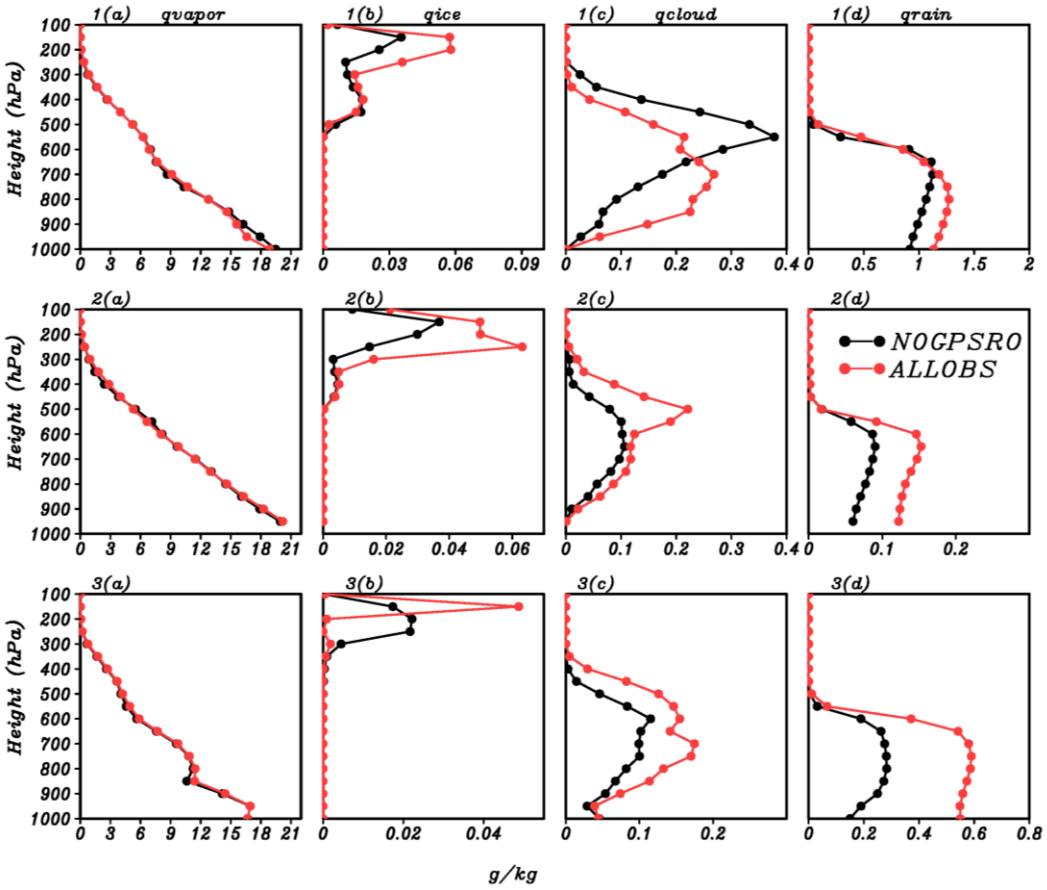

Figure 6.12: The first, second, third, and fourth columns display the water vapor, ice, cloud, and rain mixing ratios (g/kg) respectively during peak rainfall hours over the three respected extreme rainfall regions. The first, second, and third rows plots show the results from the Tamil Nadu at 13.3°N, 80.2°E, Telangana at 18.5°N, 78.6°E, and Kerala at 10.8°N, 76.6°E regions, respectively.

6.5 Summary

This study evaluated the impact of the assimilation of satellite product of GPS RO refractivity profiles data on the prediction of peak rainfall locations and magnitudes during three EREs that occurred over southern India. These three events occurred over (i) the state of Tamil Nadu on December 01, 2015, (ii) Telangana on September 24, 2016, and (iii) Kerala on August 15, 2018. We began with an analysis of the high resolution (~10 km) GPM gridded rainfall datasets and available IMD rain-gauge and AWS rainfall datasets for the three EREs. At the outset, we carried out simulation of the events using the state-of-art Advanced Weather Research and Forecasting (WRF) model (configured at 2 km resolution in the inner domain). We then carry out complementary experiments, in which we assimilated the satellite product of GPS RO refractivity profiles data and other available observations using the 3DVar assimilation

technique. These experiments were carried out to evaluate if the assimilation of satellite GPS RO data improves the ability of the model to predict the locations and magnitudes of the three EREs.

The results demonstrate that the assimilation of satellite GPS RO refractivity profiles somewhat better improves the predictive ability of the WRF model. Specifically, the spatial distributions of the isolated extreme rainfall locations over the three regions are better predicted after including the satellite GPS RO refractivity profiles data with other observations.

We further diagnosed the changes in the underlying dynamical and thermodynamic mechanisms that are associated with the enhanced prediction skills in the ALLOBS experiments. This included the analysis of the complete vorticity budget and vertically integrated heating rates. Our analysis indicate that the assimilation of GPS RO data enables deeper convection due to warmer conditions at lower levels, leading to a higher concentration of water vapor due to excess evaporation. Stronger vertical motion at the lower troposphere, which triggers unstable air, is observed in WRF simulations after the assimilation of GPS RO data. Further, these features are closely associated with changes in the vertical shear of horizontal wind, indicating that the GPS RO refractivity profiles assimilation enhances the dynamical and thermo-dynamical features of the model. The analysis of the vorticity tendency equation also shows an increase in vertical advection in the lower and middle layers of the troposphere causing deep convection. These improvements in the vertical extension/stretching of the vortex after assimilation contribute to higher extreme rainfall and associated extreme conditions. Especially, in the Chennai and Telangana cases, assimilation of the GPS RO refractivity profiles resulted in higher water vapor, stronger low-level convergence, and associated enhanced vertical motions, all of which in turn led to deep convection and heavier rainfall relative to the corresponding NOGPSRO simulations. The heat sink regions coincide with the regions with heavy rainfall in these experiments, suggesting the higher heating due to the strong ascending motions and the surplus moisture caused the excess amount of rainfall.

In summary, this study demonstrates that the assimilation of satellite GPS RO refractivity in a high-resolution version of the WRF model improves the ability to predict the dynamic features associated with the EREs in the southern part of India. Our results, based on the three prediction experiments, emphasize that the assimilation of satellite GPS RO refractivity profiles into the model improves the predictability of all three EREs, in terms associated isolated extreme rainfall locations. While the results are based on only three cases, similar improvements in the skills and associated dynamics and thermodynamics qualitatively support our conclusions. More numerical experiments need to be performed for different EREs over India to statistically authenticate our findings. Such studies will be performed in the future. We are aware that sophisticated assimilation methods such as four-dimensional data assimilation, Ensemble Kalman filter, etc. are available. Based on our results, we can postulate that assimilation of satellite GPS RO will continue to improve the predictive skills of the extreme events in southern India even with such schemes.

Chapter – 7

Summary and future scope of the thesis

The complete summary of this thesis and conclusions from it, along with a brief perspective on future scope, are provided in this chapter.

7.1 Summary

The goal of the thesis is to investigate the potential roles of background changes in the tropical Indo-Pacific sea surface temperatures and those in land-use land-cover on the intensity/frequency of the extreme rainfall events (EREs), and/or heavy rainfall events as the case may be, in southern India. An offshoot of this goal is to explore the importance of such changes in improving the prediction skills of EREs using a state-of-the-art regional climate model. To this end, , I have used the various observed and reanalyzed ocean and atmospheric gridded hourly, daily, and monthly datasets mainly from 1901 to 2019, which are briefly described in Chapter 2. The main results of this thesis are summarized below.

I adopted a slightly modified rainfall categorizations of the IMD to define the extreme rainfall events (ERE) over India. My results on the changes in the frequency and intensity of extreme and heavy rainfall, reported in the Chapter 3, are, however, not sensitive to this re-classification. At the outset, I have documented the changes in various statistics of characteristics of the summer monsoon EREs for the 2000-2019 period from those during the 1980-1999 period over all major regions of India. My results show that the number of rainy days and the frequencies of various categories of rainfall events and magnitudes have increased by ~10% - 30% mainly over northwestern region of India and the east coastal Indian state of Odisha during the Post-1999 period compared to the Pre-2000 period. Interestingly, the frequency of EREs has increased by ~ 40% over the western state of Gujarat, some places in central India, and Odisha. It is well-known that the interannual variability (IAV) of ISMR is highly influenced by the tropical ocean climate drivers such as canonical ENSO, ENSO Modoki, Indian Ocean Dipole (IOD), and the Atlantic Zonal Mode (AZM), whose variability has been represented in my study by the Niño3 index, EMI, IODMI and AZM index, respectively. Among this, the IODMI and AZM index show significantly increasing trends in intensity at 99% and 94% confidence level since the year 2000. In this context, the results of my composite and partial correlation analyses show that, in the last two decades, the positive

IOD events have most significantly associated with the aforementioned significant increase in the frequency and intensity of the monsoon EREs over the northwestern state of Gujarat, western central, and Odisha regions of India. The relevance of other three oceanic drivers is relatively less prominent. The possible reason for raising the frequency of EREs and magnitudes over these regions may be the observed basin wide warming in the tropical Indian Ocean in the last 3-4 decades (Alory et al., 2010). This increasing SST in the equatorial Indian Ocean, particularly in the west, apparently results in increasing the extremity of the positive IOD events (Cai et al., 2014). Increasing strength of the positive IOD strengthens the convergence over western Indian Ocean, resulted in anomalous increase in the rainfall along the monsoonal trough and north western regions of the Indian subcontinent (e.g., Ashok et al., 2004).

The summer monsoon EREs in the peninsular India do not seem to be as much affected by the trends in the strength of the aforementioned tropical Indo-Pacific drivers as the northern and central regions of India and the coastal state of Odisha are. However, many states in southern India are urbanizing fast. Importantly, the distance to the sea, and seasonal cycle of the rainfall, across the peninsular states are not uniform.

The southeastern peninsular region of India, mainly the Tamil Nadu state and the Rayalaseema sub-region of the neighboring Andhra Pradesh, mainly receives the rain during the northeast monsoon (NEM) season, which lasts from October-December. The IAV of NEMR is highly influenced by the SSTs over eastern Bay of Bengal (BoB) and Niño3 index. Due to the matching of anomalous El Niño circulation with the seasonal mean wind pattern during September to October over the region, El Niños exacerbate the seasonal local rainfall. Consequently, the frequency of heavy rainfall events is higher during the El Niño years in this season (Sanap et al., 2018). Moreover, we find that the positive SSTA over eastern BoB has a positive association with the NEMR (Yadav, 2013). Importantly, the strengthening trend in these SST has been shown to be intensifying the tropical cyclones in the BoB (Balaguru et al.,

2014). Notably, during early December 2015, the Tamil Nadu region received extreme rainfall, which resulted in ~350 deaths and heavy loss of property. This was a year of an extreme El Niño, as shown in this thesis. The eastern BoB also experienced strong above normal SSTs during November-December 2015. Therefore, it was pertinent to understand and explore the potential importance of relative contributions of the strong El Niño, and the strengthening eastern BoB SSTs to the intensity of this ERE over Tamil Nadu, centered over its capital city of Chennai. My results in this context were presented in Chapter 4. My correlation analysis establishes that the NEMR over the Chennai region is positively correlated (at 90% confidence level) with eastern BoB SST and Niño3 index for the period 1901-2013. Equipped with this information, we carried out several sensitive experiments with the WRF model. The experiments have been designed with a hypothesis that the ENSO impacts on the intensity of the synoptic events in the Tamil Nadu during NEM manifested through the local SST off Tamil Nadu as well as its anomalous signature in the local atmospheric circulations. Our experiments, carried out at 25 km resolution suggest that, while the strong concurrent El Niño conditions contributed to about 21.5% (~10%) of the intensity of the extreme Chennai rainfall through its signals in the local SST (atmospheric circulation), the warming trend in BoB SST also contributed equally to the extremity of the event. Further, the El Niño southern oscillation (ENSO) impacts on the intensity of the synoptic events in the BoB during the northeast monsoon are manifested largely through the local SST in the BoB as compared through its signature in the atmospheric circulations over the BoB.

In addition to investigating the potential role of large-scale impacts such as background SST changes to the EREs, it is also very important to understand and investigate the impact of small/regional scale background changes in the LULC on the EREs, particularly in the regions away from the coast. For this analysis, we selected three major southern Indian states, namely Tamil Nadu, Telangana, and Kerala. The latter two receive the peak rainfall in summer monsoon, but the state of Telangana is way from both Bay of Bengal and Arabian Sea by about

300-400 km, unlike the other two, which are coastal states. Using the WRF model in a nested mode with 2 km resolution, in Chapter 5, we examined the sensitivity of twelve extreme events in these states, which occurred during 2014-2018 period to the LULC changes. In this regard, we primarily used the 30s resolution of Indian Space Research Organization (ISRO) derived LULC datasets for the years of 2005 (old) and 2017 (new). We notice from observations that that the frequency of heavy rainfall events and 99 percentile rainfall magnitudes significantly increases over these three states. Considerable rapid urbanization in these three states, particularly Tamil Nadu and Telangana has been occurring in the last wo decades, with reduction in the crop/grass-land which turned into dry cropland and pasture in Tamil Nadu and Telangana, mixed shrub-land/grass-land became barren/sparsely vegetation in Telangana, and a broad green fraction of mixed forests turned into deciduous needle/leaf forest in Kerala in the last two decades. Of the simulations for the twelve EREs over three southern Indian states (four events from each state), we study in more detail three representatives EREs that occurred, specifically, over the Chennai city on December 01, 2015, over Telangana on September 24, 2016 and over Kerala on August 15, 2018. Several numerical experiments were performed using the WRF model to ascertain whether the recent LULC changes in these states have contributed to each of these three EREs.

Our numerical simulations suggest that the spatial rainfall patterns and asymmetries of EREs are relatively better reproduced with the new LULC dataset of 2017 than the 2005 ISRO LULC dataset. The simulations with the newest LULC lower boundary conditions facilitate realistic simulations of the observed extreme as well as that of fine features such as the asymmetric nature of rainfall distribution, concentrated rainfall over isolated regions, and meridional/zonal extension of rainfall, etc. The analysis of the simulations of twelve EREs, including the three focused events shows that urbanization produces higher surface temperatures, larger sensible heat fluxes, a deeper boundary layer, more water-vapor, more water-vapor mixing in the boundary layer, and hence more convective available potential

energy. The conducted sensitivity experiments suggest that about 20%-25% of the rainfall in the recent EREs over southern India can be attributed to the changes in LULC/increased urbanization in the last decade. Our results also imply that up-to-date LULC boundary conditions also lead to an enhancement in the predictive skills of EREs over southern India. Therefore, the background mechanism of LULC also playing the curtail role for the intensity of the extreme rainfall activity.

Of course, potential improvement of the prediction skills of the ERE should be possible even after taking the realistic SST and updated LULC into consideration. Therefore, in Chapter 6, we evaluated the impact of assimilation satellite-based product of GPS RO refractivity data on the prediction of peak rainfall locations and magnitudes of the aforementioned three major EREs that occurred over southern India. We conducted several numerical sensitivity experiments, specifically: (i) the control experiments with initial conditions from the GFS forecast data, but without any assimilation. (ii) by assimilating only, the satellite GPS RO refractivity profiles, (iii) by assimilating all observations, except GPS RO data, and (iv) by assimilating all observations including satellite GPS RO refractivity data. Our results demonstrate that assimilation of GPS RO refractivity profiles into the model in addition to assimilating all other standard observations further improves the predictability of all three EREs in terms of isolated extreme rainfall locations, and associated extreme conditions through improvement in vertical velocities.

7.2 Future scope of the study

This thesis reveals the importance of background mechanism of SST and LULC changes to the frequency and intensity of the EREs. The outstanding issues mentioned below need further attention.

- As we presented in Chapter 3, the strengthening positive IODs in the last two decades are associated with the increased occurrence of high intensity of rainfall events over Gujarat, west central, and Odisha regions of India. This can be further validated by

conducting the several sensitivity studies using coupled climate models. The relevance of the negative IOD events for trends in the EREs has also not been explored in a non-linear sense.

Using a fully coupled atmospheric-ocean model with SST assimilation and using latest LULC would be necessary for improving the ERE prediction weather scales and beyond. Assimilation of the moisture signatures, through assimilation of the GPS RO into such a model will potentially improve the lead period of skillful predictions of the EREs in peninsular India.

- As we tend to use higher resolution models, it may be worth exploring whether incorporating aerosols, which affect not only the radiation but also play a major role in rainfall formation, would improve the prediction.
- Lack of rainfall observations with resolutions finer than 10 km is a challenge. Fortunately, many state governments have started deploying their own automatic weather stations. We have presented an example of how data from such agency in the state of Telangana helped us to validate our simulations. These new datasets may be used to develop high resolution rainfall observation data sets across the data, complementing the IMD rainfall observations.

References

Abhilash, S., Das, S., Kalsi, S. R., Gupta, M. D., Mohankumar, K., George, J. P., Banargee, S. K., Thampi, S. B., and Pradhan, D. (2007). Impact of Doppler radar wind in simulating the intensity and propagation of rainbands associated with mesoscale convective complexes using MM5-3DVAR system. Pure Appl. Geo. Phys., 164, 1–19.

Agilan, V., and Umamahesh, N. V. (2015). Detection and attribution of non-stationarity in intensity and frequency of daily and 4-h extreme rainfall of Hyderabad, India. Journal of Hydrology, 530, 677-697.

Aithal, B. H., and Ramachandra, T. V. (2016). Visualization of Urban Growth Pattern in Chennai Using Geoinformatics and Spatial Metrics. J. Indian Soc. Remote Sens., 44, 617–633.

Ajayamohan, R. S., and Rao, S. A. (2007). Indian Ocean Dipole modulates the number of extreme rainfall events in a warming environment. J. Meteorol. Soc. Jpn., 86, 245–252.

Alam, M. M., Hussain, M. A., and Shafee, S. (2003). Frequency of Bay of Bengal cyclonic storms and depressions crossing different coastal zones. Inter. J. Clima., 23, 1119–1125.

Ali, H., and Mishra, V. (2017). Contrasting response of rainfall extremes to increase in surface air and dewpoint temperatures at urban locations in India. Sci. Rep., 7, 1228.

Alory, G., Wijffels, S., and Meyers, G. (2007). Observed temperature trends in the Indian Ocean over 1960 – 1999 and associated mechanisms. Geophys. Research Lett., 34, L02606.

Amat, H. B., and Ashok, K. (2018). Relevance of Indian Summer Monsoon and its Tropical Indo-Pacific Climate Drivers for the Kharif Crop Production. Pure Appl. Geophys., 175, 2307–2322.

Anthes, R. A., and Co-authors. (2008). The COSMIC/FORMOSAT-3 mission: Early results. Bull. Amer. Meteor. Soc., 89, 313-333.

Arnfield, A. J. (2003). Two decades of urban climate research: a review of turbulence, exchanges of energy and water, and the urban heat is land. Int. J. Clima., 23, 1-26.

Ashok, K., and Saji, N. H. (2007). Impacts of ENSO and Indian Ocean Dipole Events on the Sub-Regional Indian Summer Monsoon Rainfall. J. Nat. Hazards, 42, 273–285.

Ashok, K., Behera, S. K., Rao, S. A., Weng, H., and Yamagata, T. (2007). El Niño Modoki and its possible teleconnection. J. Geophys. Res., 112, C11007.

Ashok, K., Feba, F., and Tejavath, C. T. (2019). The Indian summer monsoon rainfall and ENSO. Mausam, 70(3), 443–452.

Ashok, K., Guan, Z., and Yamagata, T. (2001). Impact of the Indian Ocean Dipole on the relationship between the Indian Monsoon rainfall and ENSO. Geophys. Res. Lett., 28, 4499–4502.

Ashok, K., Guan. Z., Saji, N. H., and Yamagata, T. (2004). Individual and combined influences of the ENSO and Indian Ocean Dipole on the Indian summer monsoon. J. Climate. 17, 3141-3155.

Badarinath, K. V. S., Mahalakshmi, D. V., and Ratna S. B. (2012). Influence of Land Use Land Cover on Cyclone Track Prediction-A Study During Aila Cyclone. Open Atmos. Sci. J., 6, 33–41.

Balaguru, K., Taraphdar, S., Leung, L. R., Foltz, G. R. (2014). Increase in the intensity of postmonsoon Bay of Bengal tropical cyclones. Geophys. Res. Lett., 41(10), 3594–3601.

Barker, D. M., Huang, W., Guo, Y. R., Bourgeois, A. J., and Xiao, Q. N. (2004). A three-dimensional variational data assimilation system for use with MM5: Implementation and initial results. Mon. Weather Rev., 132, 897–914.

Behera, S. K., Krishnan, R., and Yamagata, T. (1999). Unusual ocean-atmosphere conditions in the tropical Indian Ocean during 1994. Geophys. Res. Lett., 26, 3001–3004.

Bhanu Kumar, O. S. R. U., Suneetha, P., Ramalingeswara Rao, S., Satya Kumar, M. (2012). Simulation of Heavy Rainfall Events during Retreat Phase of Summer Monsoon Season over Parts of Andhra Pradesh. Inter. J. Geosciences, 3(4), 737-748.

Bhaskar Rao, D. V., and Ratna, S. B. (2010). Mesoscale characteristics and prediction of an unusual extreme heavy rainfall event over Mumbai city. India. Atmos. Res., 95, 255–269.

Bhaskar Rao, D. V., Srinivas, D., Dasari, H. P., and Gubbala, C. S. (2016). Prediction of tropical cyclone over North Indian Ocean using WRF model: sensitivity to scatterometer winds, ATOVS and ATMS radiances. Proc. SPIE 9882, Remote Sensing and Modeling of the Atmosphere, Oceans, and Interactions, VI, 988213.

Bhaskar, Rao, D. V, and Ashok, K. (1999). Simulation of Tropical Cyclone Circulation over the Bay of Bengal, Part I - Description of the Model, initial data & results of the control experiment. Pure Applied Geophysics, 156, 525-542.

Bhatla, R., Verma, S., Ghosh, S., and Mall, R. K. (2020). Performance of regional climate model in simulating Indian summer monsoon over Indian homogeneous region. Theor. Appl. Climatol., 139, 1121–1135.

Bhowmik, S. K. R., Roy, S. S., Srivastava, K., Mukhopadhay, B., Thampi, S. B., Reddy, Y. K., Singh, H., Venkateswarlu, S., and Adhikary, S. (2011). Processing of Indian doppler weather radar data for mesoscale applications. Meteorol. Atmos. Phys., 111, 133–147.

Biswadip, G. (2014). IRS-P6 AWiFS derived gridded land use/land cover data compatible to Mesoscale Models (MM5 and WRF) over Indian Region. NRSC Technical Document No. NRSC-ECSA-ACSGOCT-2014-TR-651, 1–11.

Bjerknes, J. (1969). Atmospheric teleconnections from the equatorial Pacific. Mon. Weather Rev., 97, 163-172.

Boyaj, A., Ashok, K., Ghosh, S., Devanand, A., Dandu, G. (2018). The Chennai extreme rainfall event in 2015: the Bay of Bengal connection. Clim. Dyn., 50, 2867–2879.

Boyaj, A., Dasari, H. P., Hoteit, I., and Ashok, K. (2020). Increasing heavy rainfall events in south India due to changing land use and land cover. Q. J. R. M. S., 146, 1–22.

Brimelow, J. C., and Reuter, G. W. (2005). Transport of atmospheric moisture during three extreme rainfall events over the Mackenzie River Basin. J. Hydrometeorol, 6, 423–440.

Chakraborty, A. (2016). A synoptic-scale perspective of heavy rainfall over Chennai in November 2015. Current Science. 111, 201–207.

Charney, J. G., FjÖrtoft, R., and Neumann, J. V. (1950). Numerical Integration of the Barotropic Vorticity Equation. Tellus. 2(4), 237– 254.

Chatterjee, P., and Goswami, B. N. (2004). Structure, genesis and scale selection of the tropical quasi-biweekly mode. Q. J. R. M. S., 130, 1171–1194.

Chawla, I., Osuri, K., Mujumdar, P., and Niyogi, D. (2018). Assessment of the Weather Research and Forecasting (WRF) model for simulation of extreme rainfall events in the upper Ganga Basin. Hydrol. Earth Syst. Sci., 22, 1095–1117.

Chen, S. Y., Huang, C. Y., Kuo, Y. H., Guo, Y. P., and Sokolovskiy, S. (2009). Assimilation of GPS refractivity from FORMOSAT-3/COSMIC using a nonlocal operator with WRF 3DVAR and its impact on the prediction of a typhoon event. Terr. Atmos. Oceanic Sci., 20, 133–154.

Chen, S. Y., Huang, C. Y., Kuo, Y. H., Guo, Y. R., and Sokolovskiy, S. (2009). Assimilation of GPS refractivity from FORMOSAT-3/COSMIC using a nonlocal operator with WRF 3DVAR and its impact on the prediction of a typhoon event. Terr. Atmos. Ocean Sci., 20, 133–154.

Coniglio, M. C., Hwang, J. Y., and Stensrud, D. J. (2010). Environmental Factors in the Upscale Growth and Longevity of MCSs Derived from Rapid Update Cycle Analyses. Mon. Wea. Rev., 138, 3514–3539.

Cook, B. I., Shukla, S. P., Puma, M. J., and Nazarenko, L. S. (2015). Irrigation as an historical climate forcing. Climate Dynamics, 44, 1715–1730.

Cruz, F. T., and Narisma, G. T. (2016). WRF simulation of the heavy rainfall over Metropolitan Manila, Philippines during tropical cyclone Ketsana: a sensitivity study. Meteorology and Atmospheric Physics, 128(4), 415–428.

Cucurull, L., Kuo, Y. H., Barker, D., and Rizvi, S. R. H. (2006). Assessing the impact of simulated COSMIC GPS radio occultation data on weather analysis over the Antarctic: a case study. Mon. Wea. Rev., 134, 3283–3296.

Cucurull, L., Kuo, Y. H., Barker, D., and Rizvi, S. R. H. (2006). Assessing the impact of simulated COSMIC GPS radio occultation data on weather analysis over the Antarctic: a case study COSMIC project. Mon. Weather Rev., 134, 3283–3296.

Daley, R. (1991). Atmospheric data analysis. Cambridge atmospheric and space science series, Cambridge University Press, pp 457.

Dasari, H. P., Rao, V. B., Ramakrishna, S., Gunta, P., and Kumar, R. (2017). On the movement of tropical cyclone LEHAR. Earth Systems and Environment, 1(2), 21.

Dash, S. K., Kulkarni, M. A., Mohanty, U. C. and Prasad, K. (2009). Changes in the characteristics of rain events in India. J. Geophys. Res. Atmos., 114, D10109.

Dash, S. K., Nair, A. A., Kulkarni, M. A., and Mohanty, U. C. (2011). Characteristic changes in the long and short spells of different rain intensities in India. Theor. Appl. Climatol. 105, 563–570.

Dave, H., James, M. E., and Ray, K. (2017). Trends in intense rainfall events over Gujarat state (India) in the warming environment using gridded and conventional data. Inter. J. Applied Environmental Sci., 12, 977–998.

De Sales, F., and Xue, Y. (2010). Assessing the dynamic downscaling ability over South America using the intensity-scale verification technique. Int. J. Climatol., 31, 1205–1221.

De, U. S., and Mukhopadhyay, R. K. (1999). The effect of ENSO/Anti ENSO on northeast monsoon rainfall. Mausam, 50, 343–354.

Desamsetti, S., Dasari, H. P., Langodan, S., Titi, E. S., Knio, O., and Hoteit, I. (2018). Efficient dynamical downscaling of general circulation models using continuous data assimilation. Q. J. R. M. S., 145, 3175-3194.

Dhar, O. N., and Rakhecha, P. R. (1983). Forecasting northeast monsoon rainfall over Tamil Nadu, India. Monsoon Weather Review, 111, 109–112.

Di Luca, A., de Elia, R., and Laprise, R. (2011). Potential for added value in precipitation simulated by high resolution nested Regional Climate Models and observations. Clim. Dyn. 38, 1229–1247.

Dudhia, J. (1989). Numerical study of convection observed during the winter monsoon experiment using a mesoscale two-dimensional model. J. Atmos. Scie. 46, 3077–3107.

Duncombe, J. (2018). Making sense of landslide danger after Kerala's floods. Eos. 99.

Feba, F., Ashok, K., and Ravichandran, M. (2017). Role of changed Indo-Pacific atmospheric circulation in the recent disconnect between the Indian summer monsoon and ENSO. Clim. Dyn., 52, 1461–1470.

Findlater, J. (1969). A major low-level air current near the Indian Ocean during the northern summer. Q. J. R. M. S., 95, 362-380.

Francis, P., and Gadgil, S. (2006). Intense rainfall events over the west coast of India. Meteorol. Atmos. Phys., 94, 27–42.

Gadgil, S. (2003). THE INDIAN MONSOON AND ITS VARIABILITY. Annual Review of Earth and Planetary Sciences, 31. 429-467.

Gadgil, S., Joseph, P. V., and Joshi, N. V. (1984). Ocean-atmosphere coupling over monsoon regions. Nature., 312, 141-143.

Gadgil, S., Vinaychandran, P. N., Francis, P. A., and Gadgil, S. (2004). Extremes of Indian summer monsoon rainfall, ENSO, equatorial Indian Ocean Oscillation. Geophys. Res. Lett., 31, L12213.

Gao, J., Xue, M., Brewster, A. K., and Droegemeier, K. (2004). A three-dimensional variational data analysis method with recursive filter for Doppler radars. J. Atmos. Oceanic Technol., 21, 457–469.

Garai, D., and Narayana, A. C. (2018). Land use/land cover changes in the mining area of godavari coal fields of southern India. The Egyptian J. Remote Sensing and Space Sci., 2, 375–381.

Geethalakshmi, V., Akiyo Yatagai, K., Palanisamy, and Chicko Umetsu. (2009). Impact of ENSO and the Indian Ocean Dipole on the Northeast Monsoon rainfall of Tamil Nadu State in India. Hydrol. Process, 23, 633-647.

George, G., Charlotte, G. B., and Ruchith, R. D. (2011). Interannual variation of northeast monsoon rainfall over southern peninsular India. Indian J. Marine Sci., 40, 98–104.

Ghosh, S., Das, D., Kao, S. C., Ganguly, A. R. (2012). Lack of uniform trends but increasing spatial variability in observed Indian rainfall extremes. Nature Clim. Change, 2, 86–91.

Ghosh, S., Luniya, V., and Gupta, A. (2009). Trend analysis of Indian summer monsoon rainfall at different spatial scales. Atmos. Sci. Lett., 10, 285–290.

Girishkumar, M. S., and Ravichandran, M. (2012). The influences of ENSO on tropical cyclone activity in the Bay of Bengal during October-December. J. Geophys. Res. Oceans, 117, 2033.

Gogoi, P. P., Vinoj, V., Swain, D., Roberts, G., Dash, J., and Tripathy, S. (2019). Land use and land cover change effect on surface temperature over eastern India. Sci. Rep., 9, 1–10.

Goswami, B. N., and Chakravorty, S. (2017). Dynamics of the Indian Summer Monsoon Climate. Climate Science, https://doi.org/10.1093/acrefore/9780190228620.013.613.

Goswami, B. N., Venugopal, V., Sengupta, D., Madhusoodanan, M. S., and Xavier, P. K. (2006). Increasing trend of extreme rain events over India in a warming environment. Science, 314, 1442–1445.

Goswami, P., Himesh, S., Goud, B. S. (2010). Impact of urbanization on tropical mesoscale events: investigation of three heavy rainfall events. Meteorologische Zeitschrift, 19, 385-397.

Govindankutty, M., and Chandrasekar, A. (2011). Impact of assimilation of ATOVS temperature and humidity and SSM/I total precipitable water on the simulation of a monsoon depression, Natural Hazards, 59, 1647-1669.

Guhathakurta, P., Sreejith O. P., and Menon, P. A. (2011). Impact of climate change on extreme rainfall events and flood risk in India. J. Earth Syst. Sci., 120(3), 359–373.

Ha, J., Kang, J., and Choi, S. (2017). The Impact of Vertical Resolution in the Assimilation of GPS Radio Occultation Data. Wea. Forecasting, 33, 1033–1044.

Halder, S., Saha, S. K., Dirmeyer, P. A., Chase, T. N., and Goswami, B. N. (2016). Investigating the impact of land-use land-cover change on Indian summer monsoon daily rainfall and temperature during 1951–2005 using a regional climate model. Hydrol. Earth Syst. Sci., 20, 1765–1784.

Hari prasad, D., Venkata Srinivas, C., Venkata Bhaskar Rao, D., and Anjaneyulu, Y. (2011). Simulation of Indian monsoon extreme rainfall events during the decadal period 2000–2009 using a high resolution mesoscale model. Adv. Geosci., A6, 31–48.

Hastenrath, S. (1985). Climate and circulation of the tropics. Springer Publications, 8, 464.

Healy, S. B., and Thépaut, J. N. (2006). Assimilation experiments with CHAMP GPS radio occultation measurements. Q. J. R. M. S., 132, 605–623.

Healy, S. B., Jupp, A. M., and Marquardt, C. (2005). Forecast impact experiment with GPS radio occultation measurements. Geophys. Res. Lett., 32, L03804.

Hersbach, H., and Dee, D. (2016). ERA5 reanalysis is in production, ECMWF Newsletter 147, ECMWF, Reading, UK.

Hong, Song You, Yign Noh, Jimy Dudhia. (2006). A new vertical diffusion package with an explicit treatment of entrainment processes. Mon. Wea. Rev., 134, 2318-2341.

Huang, C. Y., Kuo, Y. H., Chen, S. H., and Vandenberghe, F. (2005). Improvements on typhoon forecast with assimilated GPS occultation refractivity. Wea. Forecas., 20, 931–953.

Huang, C. Y., Kuo, Y. H., Chen, S. Y., Anisetty, S. K. A. V. Prasad Rao., and Chien, J. W. (2007). The assimilation of GPS radio occultation data and its impact on rainfall prediction along the west coast of India during monsoon 2002. Pure Appl. Geophys., 164, 1577–1591.

Huffman, G., 2015: GPM IMERG Late Precipitation L3 Half Hourly 0.1 degree x 0.1 degree V05, Greenbelt, MD, Goddard Earth Sciences Data and Information Services Center (GES DISC), https://disc.gsfc.nasa.gov/datasets/GPM_3IMERGHHE_06/summary?keywords=%22IMERG%20Early%22. Accessed on December 01, 2015; September 24, 2016; August 15, 2018.

Huffman, G., Adler, R., Bolvin, D., and Nelkin, E. (2010). The TRMM Multi-Satellite Precipitation Analysis (TMPA), in: Satellite Rainfall Applications for Surface Hydrology. Gebremichael, M. and Hossain, F., 3–22, Springer Netherlands.

Jain, S. K., and Kumar, V. (2012). Trend analysis of rainfall and temperature data for India. Curr. Sci., 102, 37–49.

Jayanthi, N., and Govindachari, S. (1999). El Nino and northeast monsoon rainfall over Tamilnadu. Mausam, 50(2), 217.

Jenamani, R. K., Bhan, S. C., and Kalsi, S. R. (2006). Observational/forecasting aspects of the meteorological event that caused a record highest precipitation in Mumbai. Current Science, 90, 1344–1362.

Jones, R. G., Murphy, J. M., Noguer, M. (1995). Simulation of climate change over Europe using a nested regional climate model. 1: assessment of control climate, including sensitivity to location of lateral boundaries. Q. J. R. M. S., 121, 1413–1449.

Joseph, P. V., and Raman, P. L. (1966). Existence of low level westerly jet-stream over peninsular India during July. Indian J. Meteor. Geophys., 17, 407-410.

Kain John, S. (2004). The Kain–Fritsch convective parameterization: An update. J. Appl. Meteor., 43, 170–181.

Kalnay, E., and co-authors. (1996). The NCEP/NCAR 40-year reanalysis project. Bull. American Meteo. Society., 77, 437-470.

Kanase, R., and Salvekar, P. (2014). Study of Weak Intensity Cyclones over Bay of Bengal Using WRF Model. Atmospheric and Climate Sciences, 4, 534-548.

Keshavamurty, R. N. (1982). Response of the atmosphere to sea surface temperature anomalies over the equatorial Pacific and teleconnections of the Southern Oscillation. J. Atmos. Sci., 39, 1241-1259.

Keshavamurty, R. N., and Awade, S. T. (1970). On the maintenance of the mean monsoon trough over north India. Mon. Wea. Rev., 98, 315-320.

Khole, M., and De, U. S. (2003). A study on north-east monsoon rainfall over India. Mausam, 54(2), 419–426.

Kirtsaeng, S., Chantara, S., and Kreasuwun, J. (2010). Mesoscale simulation of a very heavy rainfall event over Mumbai, using the weather research and forecasting (wrf) model. Chiang Mai Journal of Science, 37(3), 429–442.

Kishtawal, C. M., Niyogi, D., Tewari, M., Pielke, R. A., Shepherd Sr, J. M. (2010). Urbanization signature in the observed heavy rainfall climatology over India. Int. J. Climatol., 30, 19081916.

Koteswara Rao, K., Patwardhan, S. K., Kulkarni, A., Kamala, K., Sabade, S. S., and Kumar, K. K. (2014). Projected changes in mean and extreme precipitation indices over India using PRECIS, Global Planet. Change., 113, 77–90.

Koteswaram, P. (1958). The easterly jet stream in the tropics. Tellus. 10(1), 43–57.

Kripalani, R. H., and Kulkarni, A. (1997). Rainfall variability over south-east Asia Connections with Indian monsoon and ENSO extremes: New perspectives. Int. J. Climatol., 17, 155–1168.

Kripalani, R. H., and Kulkarni, A. (2001). Monsoon rainfall variations and teleconnections over South and East Asia. Int. J. Climatol., 21, 603–616.

Kripalani, R. H., and Kumar, P. (2004). Northeast monsoon rainfall variability over south peninsular India vis-??-vis the Indian Ocean dipole mode. Int. J. Climat., 24, 1267–1282.

Krishna Kumar, K., Rajagopalan, B., and Cane, M. A. (1999). On the weakening relationship between the Indian monsoon and ENSO. Science, 284, 2156–2159.

Krishnamurti, T. N., and Bhalme, H. N. (1976). Oscillations of a Monsoon System. Part I. Observational Aspects. J. Atmos. Sci., 33, 1937–1954.

Krishnaswamy, J., Vaidyanathan, S., Rajagopalan, B., Bonell, M., Sankaran, M., Bhalla, R. S., Badiger, S. (2014). Non-stationary and non-linear influence of ENSO and Indian Ocean Dipole on the variability of Indian monsoon rainfall and extreme rain events. Clim. Dyn., 45, 175-184.

Kucharski, F., Bracco, A., Yoo, J. H., and Molteni, F. (2007). Low-frequency variability of the Indian monsoon–ENSO relationship and the tropical Atlantic: the "weakening" of the 1980s and 1990s. J. Clim., 20, 4255–4266.

Kumar, A., Dudhia, J., Rotunno, R., Niyogi, D., and Mohanty, U. C. (2008). Analysis of the July 26, 2005 heavy rain event over Mumbai, India using the Weather Research and Forecasting (WRF) model. Q. J. R. M. S., 134, 1897–1910.

Kumar, K. K., Rajagopalan, B., Hoerling, M., Bates, G., and Cane, M. (2006). Unraveling the mystery of Indian monsoon failure during El Niño. Science, 314, 115–119.

Kumar, P. A., and Varma, K. (2016). Assimilation of INSAT-3D hydro-estimator method retrieved rainfall for short-range weather prediction. Q. J. R. M. S. 143, 384–394.

Kumar, P., Rupa Kumar, K., Rajeevan, M., Sahai, A. K. (2007). On the recent strengthening of the relationship between ENSO and northeast monsoon rainfall over South Asia. Clim. Dyn., 28, 649–660.

Kuo, Y. H., Schreiner, W. S., Wang, J., Rossiter, D. L., & Zhang, Y. (2005). Comparison of GPS radio occultation soundings with radiosondes, Geophys. Res. Lett. 32, L05817. doi:10.1029/2004GL021443.

Kuo, Y. H., Sokolovskiy. S. V., Anthes, R. A., and Vandenberghe, F. (2000). Assimilation of GPS radio occultation data for numerical weather prediction. Terr. Atmos. Oceanic Sci., 11, 157–186.

Kuo, Y. H., Wee, T. K., Sokolovskiy, S., Rocken, C., Schreiner, W., Hunt, D., and Anthes, R. A. (2004). Inversion and error estimation of GPS radio occultation data. J. Meteor. Soc. Japan, 82, 507–531.

Kursinski, E. R., Hajj, G. A., Leroy, S. S., and Herman, B. (2000). The GPS radio occultation technique. Terr. Atmos. Oceanic Sci., 11, 53–114.

Lei, M., Niyogi, D., Kishtawal, C., Pielke, R., Sr, Beltrán-Przekurat, A., Nobis, T., and Vaidya, S. (2008). Effect of explicit urban land surface representation on the simulation of the 26 July 2005 heavy rain event over Mumbai, India. Atmos. Chemistry and Physics., 8, 8773–8816.

Lübbecke, J. F., Böning, C. W., Keenlyside, N. S., Xie. S. P. (2010). On the connection between Benguela and equatorial Atlantic Niños and the role of the South Atlantic anticyclone. J. Geophys. Res., 115, C09015.

Luong, T. M., Dasari, H. P., and Hoteit, I. (2020). Impact of urbanization on the simulation of extreme rainfall in the city of Jeddah, Saudi Arabia. J. Appl. Meteo. and Climat., 59, 953–971.

Madhulatha, A., Rajeevan, M., Bhowmik, S. K. R., and Das, A. K. (2017). Impact of assimilation of conventional and satellite radiance GTS observations on simulation of mesoscale convective system over Southeast India using WRF-3DVar. Pure and Applied Geophysics, 175, 479–500.

Malik, N., Bookhagen, B., and Mucha, P. J. (2016). Spatiotemporal patterns and trends of Indian monsoonal rainfall extremes. Geophys. Res. Lett., 43, 1710–1717.

Marathe, S., Ashok, K., Swapna, P., and Sabin, T. P. (2015). Revisiting El Nino Modoki. Climate Dynamics, 45, 3527–3545.

Meehl, G. A., and Washington, W. M. (1993). South Asian summer monsoon variability in a model with doubled atmospheric carbon dioxide concentration. Science, 260, 1101–1104.

Miao, S. G., Chen, F., Li, Q. C., and Fan, S. Y. (2011). Impacts of urban processes and urbanization on summer precipitation: A case study of heavy rainfall in Beijing on 1 August 2006. J. Appl. Meteorol. Climatol., 50, 806– 825.

Mishra, A. K. (2016). Monitoring Tamil Nadu flood of 2015 using satellite remote sensing. Nat. Hazars, 82, 1431–1434.

Mitra, A. K., Bohra, A. K., Rajeevan, M. N., Krishnamurti, T. N. (2009). Daily Indian precipitation analysis formed from a merge of rain-gauge data with the TRMM TMPA satellite-derived rainfall estimates. J. Meteorological Society of Japan, 87A, 265-279.

Mlawer., Eli. J., Steven, Taubman, J., Patrick, Brown, D., Iacono, M. J., and Clough, S. A. (1997). Radiative transfer for inhomogeneous atmospheres: RRTM, a validated correlated–k model for the longwave. J. Geophys. Res., 102, 16663–16682.

Mohanty, U. C., Routray, A., Krishna, O. K., and Prasad, S. K. (2011). A Study on Simulation of Heavy Rainfall Events over Indian Region with ARW-3DVAR Modeling System. Pure and Applied Geophysics, 169, 381–399.

Mohapatra, P. K., and Singh, R. D. (2003). Flood Management in India. Nat. Hazards, 28, 131–143.

Mooley, D. A., and Parthasarathy, B. (1984). Fluctuations in all-India summer monsoon rainfall during 1871–1978. Clim. Change., 6, 287–301.

Mooley, D. A., and Shukla, J. (1989). Index of activity of the monsoon trough over India. Mausam, 40, 247-258.

Mukherjee, S., Aadhar, S., Stone, D., and Mishra, V. (2018). Increase in extreme precipitation events under anthropogenic warming in India. Wea. and Climate Extremes, 20, 45–53.

Mukhopadhyay, P., Taraphdar, S., Goswami, B. N., Krishnakumar, K. (2010). Indian Summer Monsoon Precipitation Climatology in a High-Resolution Regional Climate Model: Impacts of Convective Parameterization on Systematic Biases. Wea. Forecasting, 25, 369– 387.

Murtugudde, R., McCreary, J. P., and Busalacchi, A. J. (2000). Oceanic processes associated with anomalous events in the Indian Ocean with relevance to 1997–1998. J. Geophysical Research, Oceans, 105(C2), 3295–3306.

Narasimhan, B., S. M. Bhallamudi, A. Mondal, S. Ghosh, and P. Mujumdar, 2016: Chennai floods 2015 – A rapid assessment. Interdisciplinary Centre for Water Research, Indian Institute of Science, Bangalore, 49p.

National Centers for Environmental Prediction/National Weather Service/NOAA/U.S. Department of Commerce, 2008: NCEP ADP Global Upper Air and Surface Weather Observations (PREPBUFR format). Research Data Archive at the National Center for Atmospheric Research, Computational and Information Systems Laboratory, Boulder, Colo. Accessed on December 01, 2015; September 24, 2016; August 15, 2018.

National Centers for Environmental Prediction/National Weather Service/NOAA/U.S. Department of Commerce, 2015: NCEP GDAS/FNL 0.25 Degree Global Tropospheric Analyses and Forecast Grids. Research Data Archive at the National Center for Atmospheric Research, Computational and Information Systems Laboratory, Boulder, Colo. Accessed on December 01, 2015; September 24, 2016; August 15, 2018.

Nayak, H. P., Palash Sinha., Satyanarayana, A. N. V., Bhattacharya. A., and Mohanty, U. C. (2019). Performance Evaluation of High-Resolution Land Data Assimilation System (HRLDAS) Over Indian Region. Pure Appl. Geophys., 176, 389–407.

Nayak, S., and Mandal, M. (2012) Impact of land use and land cover change on temperature trends over Western India. Current Science, 102, 1166–1173.

Nikumbh, A. C., Chakraborty, A., and Bhat, G. S. (2019). Recent spatial aggregation tendency of rainfall extremes over India. Sci. Rep., 9, 1–7.

Niyogi, D., Kishtawal, C., Tripathi, S., and Govindaraju, R. S. (2010). Observational evidence that agricultural intensification and land use change may be reducing the Indian summer monsoon rainfall. Water Resour., Res., 46, W03533.

Niyogi, D., Lei, M., Kishtawal, C., Schmid, P., and Shepherd, M. (2017). Urbanization Impacts on the Summer Heavy Rainfall Climatology over the Eastern United States. Earth Interactions, 21, 1–17.

Niyogi, D., Pielke Sr, R. A., Alapaty, K., Eastman, J., Holt, T., Mohanty, U. C., Raman, S., Roy, T. K., and Xue, Y. K. (2002). Challenges of representing land surface processes in weather and climate models over Tropics: Examples over the Indian subcontinent, in Weather and Climate Modeling, edited by S. V. Singh, S. Basu, and T. N. Krishnamurti, New Age Int., New Delhi, 132–145.

Pai, D. S., Sridhar, L., Rajeevan, M., Sreejith, O. P., Satbhai, N.S., and Mukhopadyay, B. (2014). Development of a new high spatial resolution (0.25° × 0.25°) long period (1901–2010) daily gridded rainfall dataset over India and its comparison with existing data sets over the region. Mausam, 65, 1–18.

Pankaj, K., Rupa Kumar, K., Rajeevan, M. (2007). On the recent strengthening of the relationship between ENSO and northeast monsoon rainfall over South Asia. Clim. Dyn., 28, 649–660.

Pant, G. B., and Parthasarathy, B. (1981). Some aspects of an association between the southern oscillation and Indian summer monsoon. Arch. Meteorol. Geophys. Bioclimatology, 1329, 245-252.

Pant, G. B., and Rupa Kumar, K. (1998). Climates of South Asia. J. Wiley and Sons: Chichester, Keith.

Parthasarathy, B., Munot, A. A., and Kothawale, D. R. (1994). All India monthly and seasonal rainfall series: 1871-1993. Theo. and Appl. Climatol., 49, 217-224.

Pathak, A., Ghosh, S., Martínez, J. A., Domínguez, F., and Kumar, P. (2017). Role of Oceanic and Land Moisture Sources and Transport in the Seasonal and Interannual Variability of Summer Monsoon in India. J. Climate, 30, 1839–1859.

Pattanaik, D. R., and Rajeevan, M. (2010). Variability of extreme rainfall events over India during southwest monsoon season. Meteorol. Appl, 17, 88–104.

Paul, S., Ghosh, S., Mathew, M., Devanand, A., Karmakar, S., and Niyogi, D. (2018). Increased spatial variability and intensification of extreme monsoon rainfall due to urbanization. Sci Rep., 8(1), 3918.

Paul, S., Ghosh, S., Oglesby, R., Pathak, A., Chandrasekharan, A., and Ramsankaran, R. (2016). Weakening of Indian summer monsoon rainfall due to changes in land use land cover. Sci. Rep., 6, 32177.

Pielke Sr, R., Pitman, A., Niyogi, D., Mahmood, R., McAlpine, C., Hossain, F., and Fall, S. (2011). Land use/land cover changes and climate: modeling analysis and observational evidence. Climate Change, 2, 828–850.

Pielke, R. A., Marland Sr, G., Betts, R. A., Chase, T. N., Eastman, J. L., Niles, J. O., Niyogi, D., and Running, S. (2002). The influence of land-use change and landscape dynamics on the climate system: Relevance to climate change policy beyond the radiative effect of greenhouse gases. Philos. Trans. R. Soc. London Ser. A., 360, 1705–1719.

Pottapinjara, V., Girishkumar, M. S., Sivareddy, S., and Ravichandran, M. (2016). Relation between the upper ocean heat content in the equatorial Atlantic during boreal spring and the Indian monsoon rainfall during June–September. Int. J. Climatol. 36, 2469–2480.

Prajeesh, A. G., Ashok, K., and Rao, D. V. B. (2013). Falling monsoon depression frequency: a Gray-Sikka condition perspective. Sci. Report, 3, 1–8.

Prakash, S. M. C., Sathiyamoorthy, V., and Gairola, R. M. (2013). Increasing trend of northeast monsoon rainfall over the equatorial Indian Ocean and peninsular India. Theo. and App. Clim., 112, 185–191.

Pramanik, S. K., Jagannathan, P. (1954). Climate change in India–I rainfall. Indian J. Meteorol. Geophys., 4, 291–309.

Prasad, K. S., Mohanty, U. C., Routray, A., Osuri, K. K., Ramakrishna, S. S. V. S., and Niyogi, D. (2014). Impact of Doppler weather radar data on thunderstorm simulation during STORM pilot phase-2009. Nat. Hazards, 74, 1403–1427.

Rajeevan, M., Bhate, J., and Jaswal, A. K. (2008). Analysis of variability and trends of extreme rainfall events over India using 104 years of gridded daily rainfall data. Geophys. Res. Lett., 35, L18707.

Rajendran, K., and Kitoh, A. (2008). Indian summer monsoon in future climate projection by a super high-resolution global model. Current Science, 95, 2–11.

Ramage, C. S. (1971). Monsoon Meteorology. Academic press, New York, pp296.

Ran, L., Pleim, J., and Gilliam, R. (2010). Impact of high resolution land-use data in meteorology and air quality modeling systems. In: Steyn GD, Rao TS (eds) Air pollution modeling and its application, vol XX. Springer Netherlands, Dordrecht, pp 1–108.

Rao Krishna, P. R., and Jagannathan, P. (1953). A study of the northeast monsoon rainfall of Tamil Nadu. Indian J. meteorology and Geophysics, 4, 22.

Rao, B. D. V., and Ratna, S. B. (2010). Mesoscale characteristics and pre- diction of an unusual extreme heavy rainfall event over Mumbai city, India. Atmos. Res., 95, 255–269.

Rao, D. V. B., Hari Prasad, D., Srinivas, D., and Anjaneyulu, Y. (2010). Role of vertical resolution in numerical models towards the intensification, structure and track of tropical cyclones. Marine Geod., 33, 338–355.

Rao, K. K., Patwardhan, S. K., Kulkarni, A., Kamala, K., Sabade, S. S., and Kumar, K. K. (2014). Projected changes in mean and extreme precipitation indices over India using PRECIS Glob. Planet. Change, 113, 77-90.

Rao, K. N., and Raghavendra, V. K. (1971). Time series analysis of 158 years rainfall of Madras (India) (period 1813–1970). Scientific report., 163.

Rao, V. B. D., and Ashok, K. (1991). Simulation of Tropical Cyclone Circulation over Bay of Bengal Using the Arakawa-Schubert Cumulus Parametrization. Part I-Description of the Model, Initial Data and Results of the Control Experiment. Pure appl. geophys., 156, 525–542.

Rao, V. V. M. J., Venkat Ratnam, M., Durga Santhi, Y., Roja Raman, M. and Rajeevan, M. (2013). On the detection of onset and activity of the Indian summer monsoon using GPS RO refractivity profiles. Mon. Weather Rev., 141, 2096-2106.

Rao, Y. P. (1976). Southwest monsoon. Synoptic Meteorology, IMD Meteor., Monogr., No.1/1976, Delhi, pp367.

Rasmussen, E. M., and Carpenter, T. H. (1983). The relationship between the eastern equatorial Pacific sea surface temperatures and rainfall over India and Sri Lanka. Mon. Wea. Rev. 111, 517–528.

Rayner, N. A., Parker, D. E., Horton, E. B., Folland, C. K., Alexander, L. V., Rowell, D. P., Kent, E. C., and Kaplan, A. (2003). Global analyses of sea surface temperature, sea ice, and night marine air temperature since the late nineteenth century. J. Geophy. Resea., 108, 4407.

Reddy, R. D., Sreenivas, G., Mahadevappa, S. G., Madhavi Lata, A., Rao, S. B. S. N., and Varma, N. R. G. (2007). Rainfall variability and its impact on agriculture in North Telangana regions of Andhra Pradesh. J. Agrometeorology, 9, 253-258.

Revadekar, J. V., and Kulkarni. A. (2007). The El Niño-Southern Oscillation and winter precipitation extremes over India. Int. J. Climatol, 28, 1445-1452.

Reynolds, Richard, W., Thomas, M., Smith, Chunying Liu, Dudley, B., Chelton, Kenneth, S., Casey, Michael, G., and Schlax. (2007). Daily High-Resolution-Blended Analyses for Sea Surface Temperature. J. Climate, 20, 5473-5496.

Rocken, C., Anthes, R., Exner, M., Hunt, D., Sokolovskiy, S., Ware, R., Gorbunov, M., Schreiner, W., Feng, D., Herman, B., Kuo, Y., and Zou, X. (1997). Analysis and validation of GPS/MET data in the neutral atmosphere. J. Geophys. Res., 102, 29849–29866.

Rocken, C., Kuo, Y. H., Schreiner, W. S., Hunt, D., Sokolovskiy, S., and Mccormick, C. (2000). COSMIC system description. Terr. Atmos. Oceanic Sci., 11, 21–52.

Routray, A., Mohanty, U. C., Osuri, K. K., and KiranPrasad, S. (2013). Improvement of monsoon depressions forecast with assimilation of Indian DWR data using WRF-3DVAR analysis system. Pure Appl. Geophys., 170, 2329–2350.

Routray, A., Mohanty, U. C., Rizvi, S. R. H., Niyogi, D., Osuri, K. K., and Pradhan, D. (2010). Impact of Doppler weather radar data on simulation of Indian monsoon depressions. Q. J. R. M. S. 136, 1836–1850.

Roxy, M. K., Ghosh, S., Pathak, A., Athulya, E., Mujumdar, M., Murtugudde, R., Terray, P., and Rajeevan, M. (2017). A threefold rise in widespread extreme rain events over central India. Nat. Commun., 8, 708.

Rupa Kumar, K., Pant, G. B., Parthasarathy, B., and Sontakke, N. A. (1992). Spatial and sub-seasonal patterns of the long-term trends of Indian summer monsoon rainfall. Int. J. Climatol., 12, 257–268.

Saha, S. K., Dirmeyer, P. A., and Chase, T. N. (2016). Investigating the impact of land-use land-cover change on Indian summer monsoon daily rainfall and temperature during 1951–2005 using a regional climate model. Hydrology and Earth System Sciences, 20, 1765–1784.

Saha, S. K., Halder, S., Rao, A. S., and Goswami, B. N. (2012). Modulation of ISOs by land–atmosphere feedback and contribution to the interannual variability of Indian summer monsoon. J. Geophys. Res., 117, D1301.

Sahany, S., Venugopal,V., and Nanjundiah, R. S. (2010). The 26 July 2005 heavy rainfall event over mumbai: numerical modeling aspects. Meteorology and Atmospheric Physics, 109, 115–128.

Sahoo, S. K., Ajilesh, P. P., Gouda, K. C., and Himesh, S. (2020a). Impact of land-use changes on the genesis and evolution of extreme rainfall event: A case study over Uttarakhand, India. Theor. Applied Climatology, 140, 915–926.

Sahoo, S. K., Himesh, S., and Gouda, K. C., (2020b) Impact of Urbanization on Heavy Rainfall Events: A Case Study over the Megacity of Bengaluru, India. Pure Appl. Geophys., 177, 6029–6049.

Saji, N. H., Goswami, B. N., Vinayachandran, P. N., and Yamagata, T. (1999). A dipole mode in the tropical Indian Ocean. Nature. 401, 360–363.

Sanap, S. D., Priya, P., Sawaisarje, G. K., and Hosalikar, K. S. (2019). Heavy rainfall events over southeast peninsular India during northeast monsoon: Role of El Niño and easterly wave activity. Int. Journal of Climatology, 39(4), 1954–1968.

Sardeshmukh, P. D., and Hoskins, B. J. (1988). The generation of global rotational flow by steady, idealized tropical divergence. J. Atmos. Sci., 45, 1228–1251.

Sarika Jain. (2015), WRF model analysis of land-surface processes over Jaipur Region. Inte. J. Scientific & Engineering Research, 6, 2229-5518.

Schumacher, C., Zhang, M. H., and Ciesielski, P. E. (2007). Heating structures of the TRMM field campaigns. J. Atmos. Sci. 64, 2593–2610.

Shige, S., Takayabu, Y. N., Tao, W. K., and Shie, C. L. (2007). Spectral retrieval of latent heating profiles from TRMM PR data. Part II: Algorithm improvement and heating estimates over tropical ocean regions. J. Appl. Meteor. Climatol., 46, 1098–1124.

Shukla, J., and Paolina, D. A. (1983). The southern oscillation and long range forecasting of the summer monsoon rainfall over India. Mon. Weather Rev., 111, 1830–1837.

Shweta Bhati., and Manju Mohan. (2018). WRF-urban canopy model evaluation for the assessment of heat island and thermal comfort over an urban airshed in India under varying land use/land cover conditions. Geosci. Lett., 5, 27.

Sikka, D. R. (1977). Some aspects of the life history, structure and movement of monsoon depressions. Pure and Applied Geophysics. 115, 1501–1529.

Sikka, D. R. (1980). Some aspects of the large scale fluctuations of summer monsoon rainfall over India in relation to fluctuations in the planetary and regional scale circulation parameters. Earth Planet. Sci., 89, 179-195.

Singh, D., Ghosh, S., Roxy, M. K., and Mc Dermid, S. (2019). Indian summer monsoon: extreme events, historical changes, and role of anthropogenic forcings. Climate Change, 10, E571.

Singh, D., Tsiang, M., Rajaratnam, B., and Diffenbaugh, N. S. (2014). Observed changes in extreme wet and dry spells during the South Asian summer monsoon season. Nat. Clim., 4(6), 456–461.

Skamarock, W. C., Klemp, J. B., Dudhia, J., Gill, D. O., Barker. D. M., Duda, M. G., Huang, X. Y., Wang, W., and Powers, J. G. (2008). A Description of the Advanced Research WRF Version 3. NCAR Tech. Note NCAR/TN-475+STR, pp113.

Slingo, J. M., and Annamalai, H. (2000). The El Niño of the century and the response of the Indian summer monsoon. Mon. Weather Rev., 128, 1778–1797.

Sreekala, P. P., Rao, S. V. B., and Rajeevan, M. (2012). Northeast monsoon rainfall variability over south peninsular India and its teleconnections. Theor. Appl. Climatol., 108, 73–83.

Srinivas, C. V., Hariprasad, D., Bhaskar Rao, D. V., Anjaneyulu, Y., Baskaran, R., and Venkatraman, B. (2013). Simulation of the Indian summer monsoon regional climate using advanced research WRF model. Inter. J. Climatology., 33, 1195–1210.

Srinivas, C. V., Yesubabu, V., Hari Prasad, K. B. R. R., Venkatraman, B., and Ramakrishna, S. S. V. S. (2012). Numerical simulation of cyclonic storms FANOOS, NARGIS with assimilation of conventional and satellite observations using 3-DVAR. Natural Hazards, 63, 867-889.

Srinivas, C. V., Yesubabu, V., Prasad, D. H., Prasad, K. B. R. R. H., Greeshma, M. M., Baskaran, R., and Venkataman, B. (2018). Simulation of an extreme heavy rainfall event over Chennai, India using WRF: sensitivity to grid resolution and boundary layer physics. Atmos. Res., 210, 66-82.

Srinivasan, V., and Ramamurthy, K. (1973). Comprehensive articles on selected topics, Northeast monsoon. FMU Rep. of India Meteorological Department, 6, 18.

Srivastava, K., Bhowmik, S. K. R., Roy, S. S., Thampi, S. B., and Reddy, Y. K. (2010). Simulation of high impact convective events over Indian region by ARPS model with assimilation of Doppler weather radar radial velocity and reflectivity. Atmosfera, 23, 53–73.

Subbaramayya, I., and Ram Mohan Rao, S. (1984). Frequency of Bay of Bengal cyclones in the post–monsoon season. Monthly Weather Review, 112, 1640–1642.

Subbaramayya, I., Subba Rao, M. (1981). Cyclone climatology of north Indian seas. Indian J. Marine Sciences, 10, 1195-1210.

Sugimoto, S., Crook, N. A., Sun, J., Xiao, Q., and Barker, D. M. (2009). An examination of WRF 3DVAR radar data assimilation on its capability in retrieving unobserved variables and forecasting precipitation through observing system simulation experiments. Mon. Weather Rev., 137, 4011–4029.

Tao, W. K., Wu, D., Lang, S., Chern, J. D., Peters-Lidard, C., Fridlind, A., and Matsui, T. (2016). High-resolution NU-WRF simulations of a deep convective-precipitation system during MC3E: further improvements and comparisons between Goddard microphysics schemes and observations. J. Geophysical Research, Atmospheres, 121, 1278–1305.

Taylor, C. M., Belušić, D., Guichard, F., Parker, D. J., Vischel, T., Bock, O., Harris, P. P., Janicot, S., Klein, C., and Panthou, G. (2017). Frequency of extreme Sahelian storms tripled since 1982 in satellite observations. Nature, 544, 475– 478.

Taylor, C. M., Fink, A. H., Klein, C., Parker, D. J., Guichard, F., Harris, P. P., and Knapp, K. R. (2018). Earlier seasonal onset of intense Mesoscale Convective Systems in the Congo Basin since 1999. Geophys. Res. Lett., 45, 13458–13467.

Tewari, M., Chen, F., Wang, W., Dudhia, J., LeMone, M.A., Mitchell, K., Ek. M., Gayno, G.G., Wegiel, J., and Cuenca, R. H. (2004). Implementation and verification of the unified NOAH land surface model in the WRF model. 20th conference on weather analysis and forecasting/16th conference on numerical weather prediction, pp11–15.

Thiruvengadam, P., Indu, J., and Ghosh, S. (2019). Assimilation of Doppler weather radar data with a regional WRF-3DVAR system: Impact of control variables on forecasts of a heavy rainfall case. Advances in Water Resources. 126, 24–39.

Titchner, H., Rayner, N. (2014). The Met Office Hadley Centre sea ice and sea surface temperature data set, version 2:1. Sea ice concentrations. J. Geophysical Research Atmospheres, 119, 2864–2889.

Trenberth, K. E., Dai, A., Rasmussen, R. M., and Parsons, D. B. (2003). The changing character of precipitation. Bull. Am. Meteorol. Soc. 84, 1205–1217.

Unnikrishnan, C. K., Gharai, B., Mohandas, S., Mamgain, A., Rajagopal, E. N., Gopal, R. I. and Rao, P. V. N. (2016). Recent change on land use/land cover over Indian region and its impact on the weather prediction using Unified Model. Atmos. Sci. Lett., 17(4), 294–300.

Van Oldenborgh, G. J., Friederike, E. L. O., Karsten Haustein, and Krishna Achuta Rao, (2016), THE HEAVY PRECIPITATION EVENT OF DECEMBER 2015 IN CHENNAI, INDIA, (DECEMBER 2015). J. Bull. Amer. Meteo. Society, 97, S87–S91.

Varikoden, H., Kumar K. K., Babu C. A. (2013). Long term trends of seasonal and monthly rainfall in different intensity ranges over Indian subcontinent. Mausam, 64, 481-488.

Varikoden, H., Preethi, B. (2013). Wet and dry years of Indian summer monsoon and its relation with Indo-Pacific sea surface temperatures. Int. J. Climatol., 33, 1761–1771.

Vishnu, C. L., Sajinkumar, K. S., Oommen, T., Coffman, R. A., Thrivikramji, K. P., Rani, V. R., and Keerthy. S. (2019). Satellite-based assessment of the August 2018 flood in parts of Kerala, India. Geomatics, Natural Hazards and Risk, 10, 758-767.

Vishnu, C. R., and Sridharan. R. (2016). A Case Study on Impact of Chennai Floods: Supply Chain Perspective. Industrial Engineering Journal, 9, 12–16.

Viswanadhapalli, Y., Srinivas, C. V., Basha, G., Dasari, H. P., Langodan, S., Venkat Ratnam, M., and Hoteit, I. (2019). A diagnostic study of extreme precipitation over Kerala during August 2018. Atmospheric Science Letters, 20(12), e941.

Von Storch, H., and Zwiers, F. W. (1999). Statistical Analysis in Climate Research. Cambridge University Press: Cambridge, UK.

Wan, H. C., and Zhong, Z. (2014). Ensemble simulations to investigate the impact of large scale urbanization on precipitation in the lower reaches of Yangtze River Valley, China. Q. J. R. M. S., 140, 258– 266.

Wang, B., Wu, R., and Fu, X. (2000). Pacific–east Asian teleconnection: How does ENSO affect east Asian climate? J. Clim., 13, 1517–1536.

Wang, C., Kucharski, F., Barimalala, R., and Bracco, A. (2009). Teleconnections of the tropical Atlantic to the tropical Indian and Pacific Oceans: a review of recent findings. Meteorologische Zeitschrift, 18(4), 445-454.

Ware, R., Exner, M., Feng, D., Gorbunov, M., Hardy, K., Herman, B., Kuo, Y., Meehan, T., Melbourne, W., Rocken, C., Schreiner, W., Sokolovskiy, W., Solheim, F., Zou, X., Anthes, R., Businger, S., and Trenberth, K. (1996). GPS sounding of the atmosphere from low Earth orbit: Preliminary results. Bull. Amer. Met. Soc., 77, 19-40.

Webster, P. J., Moore, A., Loschnigg, J., and Leban, M. (1999). Coupled dynamics in the Indian Ocean during 1997–1998. Nature, 401, 356–360.

Webster., and Peter, J. (1987). The elementary monsoon. Wiley, New York.

Wilks, D. S. (2006). Statistical methods in the atmospheric sciences, Second edition. International Geophysics Series 91. Academic Press.

Wong, S., Fetzer, E. J., Tian, B., Lambrigtsen, B., and Ye, H. (2011). The Apparent Water Vapor Sinks and Heat Sources Associated with the Intraseasonal Oscillation of the Indian Summer Monsoon. J. Climate. 24, 4466–4479.

Xavier, P. K., and Joseph, P. V. (2000). Vertical wind shear in relation to frequency of monsoon depressions and tropical cyclones of Indian seas. Proceedings of TROPMET-2000, Kochi, India. pp 242–245.

Xiao, Q., and Sun, J. (2007). Multiple-radar data assimilation and short-range quantitative precipitation forecasting of a squall line observed during IHOP_2002. Mon. Weather Rev. 135, 3381–3404.

Xiao, Q., Kuo, Y. H., Sun, J., Lee, W. C., Lim, E., Guo, Y. R., and Barker, D. M. (2005). Assimilation of Doppler radar observations with a regional 3dvar system: impact of Doppler velocities on forecasts of a heavy rainfall case. J. Appl. Meteorol. 44, 768–788.

Yadav, R. K. (2012). Why is ENSO influencing Indian northeast monsoon in the recent decades? Inter. J. Climatology, 32(14), 2163–2180.

Yadav, R. K. (2013). Emerging role of Indian Ocean on Indian northeast monsoon. Clim. Dyn. 41, 105–116.

Yadav, R. K. (2017). On the relationship between east equatorial Atlantic SST and ISM through Eurasian wave. Climate Dyn., 48, 281–295.

Yadav, R. K., Yoo, J. H., Kucharski, F., and Abid, M. A. (2010). Why is ENSO influencing northwest India winter precipitation in recent decades?. J. Clim., 23, 1979–1993.

Yamagata, T., Behera, S. K., Rao, S. A., Guan, Z., Ashok, K., and Saji, N. H. (2003). Comments on Dipoles, temperature gradients, and tropical climate anomalies. Bull. Amer. Meteor. Soc. 84, 1418–1421.

Yanai, M., Esbensen, S., and Chu, J. H. (1973). Determination of bulk properties of tropical cloud clusters from large scale heat and moisture budgets. J. Atmos. Sci., 30, 611–627.

Yang, L., and Smith, J. (2018). Sensitivity of extreme rainfall to atmospheric moisture content in the arid/semiarid southwestern United States: Implications for probable maximum precipitation estimats. J. Geophysical Research, Atmospheres, 123, 1638–1656.

Yang, L., Tian, F.Q., Smith, J.A, and Hu, H.P. (2014). Urban signatures in the spatial clustering of summer heavy rainfall events over the Beijing metropolitan region. J. Geophys. Res. Atmos, 119, 1203– 1217.

Yatagai, A., Kamiguchi, K., Arakawa, O., Hamada, A., Yasutomi, N., and Kitoh, A. (2012). APHRODITE: Constructing a long-term daily gridded precipitation dataset for Asia based on a dense network of rain gauges. Bull. Am. Meteorol. Soc, 93, 1401–1415.

Yu, M., and Liu, Y. (2015). The possible impact of urbanization on a heavy rainfall event in Beijing. Geophys. Res. Atmos., 120, 8132-8143.

Yunck, T. P., Liu, C. H., and Ware, R. (2000). A history of GPS sounding. Terrestrial Atmospheric and Oceanic Sciences, 11, 1-20.

Zebiak, S. E. (1993). Air–sea interaction in the equatorial Atlantic region. J. Climate, 6, 1567–1586.

Zeng, X. M., Wu, Z. H., Song, S., Xiong, S. Y., Zheng, Y. Q., Zhou, Z. G., and Liu, H. Q. (2012). Effect of land surface schemes on the simulation of a heavy rainfall event by WRF. Chin. J. Geophys., 55, 16–28.

Zhang, C. L., Chen, F., Miao, S. G., Li, Q. C., and Xuan, C. Y. (2007). Influences of urbanization on precipitation and water resources in the metropolitan Beijing area. In Proceedings of the 21st American Metrological Society Conference on Hydrology, San Antonio, TX, USA.

Zhong, S., and Yang, X. Q. (2015). Ensemble simulations of the urban effect on a summer rainfall event in the Great Beijing Metropolitan Area. Atmos. Res., 153, 318– 334.

Zubair, L., and Ropelewski, C. F. (2006). The strengthening relationship between ENSO and northeast monsoon rainfall over Sri Lanka and southern India. J. Clim., 19, 1567–1575.

Deciphering the relevance of background changes to extreme rainfall events in southern India

by Boyaj Alugula

Submission date: 20-Apr-2021 02:54PM (UTC+0530)
Submission ID: 1564528453
File name: boyaj_thesis_V1.9.pdf (11.83M)
Word count: 36972
Character count: 191406

Deciphering the relevance of background changes to extreme rainfall events in southern India

ORIGINALITY REPORT

40%	17%	27%	4%
SIMILARITY INDEX	INTERNET SOURCES	PUBLICATIONS	STUDENT PAPERS

PRIMARY SOURCES

1	Alugula Boyaj, Hari Prasad Dasari, Ibrahim Hoteit, Karumuri Ashok. "Increasing heavy rainfall events in South India due to changing land use land cover", Quarterly Journal of the Royal Meteorological Society, 2020 Publication	13%
2	link.springer.com Internet Source	11%
3	Alugula Boyaj, Hari P. Dasari, Ibrahim Hoteit, Karumuri Ashok. "Increasing heavy rainfall events in south India due to changing land use and land cover", Quarterly Journal of the Royal Meteorological Society, 2020 Publication	6%
4	mafiadoc.com Internet Source	1%
5	worldwidescience.org Internet Source	<1%

Student paper from the thesis
K. Ash 20 April'21

Student paper from the thesis
K. Ash 20 April'21

Student paper from the thesis
20 April'21

Karumuri Ashok 20 April, 2021
Prof. KARUMURI ASHOK
Centre for Earth, Ocean & Atmospheric Sciences
University of Hyderabad
Hyderabad-500 046, INDIA.

6	"Assessment of Climate Change over the Indian Region", Springer Science and Business Media LLC, 2020 Publication	<1 %
7	Ji-Hyun Ha, Gyu-Ho Lim, Suk-Jin Choi. "Assimilation of GPS Radio Occultation Refractivity Data with WRF 3DVAR and Its Impact on the Prediction of a Heavy Rainfall Event", Journal of Applied Meteorology and Climatology, 2014 Publication	<1 %
8	tiikijiten.jp Internet Source	<1 %
9	Hemadri Bhusan Amat, Maheswar Pradhan, C. T. Tejavath, Avijit Dey, Suryachandra A. Rao, A. K. Sahai, Karumuri Ashok. "Value Addition to Forecasting: Towards Kharif Rice Crop Predictability Through Local Climate Variations Associated With Indo-Pacific Climate Drivers.", Research Square, 2021 Publication	<1 %
10	www.science.gov Internet Source	<1 %
11	hdl.handle.net Internet Source	<1 %
12	Alugula Boyaj, Karumuri Ashok, Subimal Ghosh, Anjana Devanand, Govardhan Dandu	<1 %

20 Apr, 21

Prof. KARUMURI ASHOK
Centre for Earth, Ocean & Atmospheric Sciences
University of Hyderabad
Hyderabad-500 046, INDIA.